Methodological developments for single-cell mass spectrometry imaging

Cumulative dissertation

by

Max Alexander Müller

Submitted to the

Faculty of Biology and Chemistry (FB08)

and prepared at the

Institute of Inorganic and Analytical Chemistry

for the degree of

Doctor rerum naturalium (Dr. rer. nat.)

Justus Liebig University Giessen, Germany

Giessen 2023

This thesis was accepted as a doctoral dissertation in fulfillment of the requirements for the degree of Doctor rerum naturalium by the Faculty of Biology and Chemistry, Justus Liebig University Giessen, Germany.

1. Referee: Prof. Dr. Bernhard Spengler

2. Referee: Prof. Dr. Sven Heiles

Table of content

Publication list

1) Atmospheric-Pressure MALDI Mass Spectrometry Imaging at 213 nm Laser Wavelength

   Sven Heiles, Mario Kompauer, Max A. Müller & Bernhard Spengler
   Journal of the American Society for Mass Spectrometry, **2020**, 31, 2, 326-335
   https://doi.org/10.1021/jasms.9b00052

2) Implementation of a High-Repetition-Rate Laser in an AP-SMALDI MSI System for Enhanced Measurement Performance

   Max A. Müller, Mario Kompauer, Kerstin Strupat, Sven Heiles & Bernhard Spengler
   Journal of the American Society for Mass Spectrometry, **2021**, 32, 2, 465-472
   https://doi.org/10.1021/jasms.0c00368

3) Matrix-Free High-Resolution Atmospheric-Pressure SALDI Mass Spectrometry Imaging of Biological Samples Using Nanostructured DIUTHAME Membranes

   Max A. Müller, Dhaka R. Bhandari & Bernhard Spengler
   Metabolites, **2021**, 11, 9, 624
   https://doi.org/10.3390/metabo11090624

4) Lipid Signatures and Inter-Cellular Heterogeneity of Naïve and Lipopolysaccharide-Stimulated Human Microglia-like Cells

   Max A. Müller, Norman Zweig, Bernhard Spengler, Maria Weinert & Sven Heiles
   Analytical Chemistry, **2023**, 95, 31, 11672-11679
   https://doi.org/10.1021/acs.analchem.3c01533

The doctoral thesis is based on publications 3 and 4.

List of abbreviations

CRM	charge residue model
DESI	desorption electrospray ionization
DG	diglyceride
DHB	2,5-dihydroxybenzoic acid
DIUTHAME	desorption ionization using through-hole alumina membrane
ESI	electrospray ionization
FT-ICR	Fourier transform ion cyclotron resonance
FWHM	full width at half maximum
HPLC	high-performance liquid chromatography
IEM	ion evaporation model
IR	infrared
LAESI	laser ablation electrospray ionization
LDI	laser desorption/ionization
LPS	lipopolysaccharide
m/*z*	mass-to-charge-number ratio
MALDI	matrix-assisted laser desorption/ionization
MALDI-2	MALDI with laser-based post-ionization
MS	mass spectrometry
MS^2	tandem mass spectrometry
MS/MS	tandem mass spectrometry
MSI	mass spectrometry imaging
NAPA	nanopost array
PA	phosphatidic acid
PBS	phosphate-buffered saline
PC	phosphatidylcholine
PE	phosphatidylethanolamine
PFA	paraformaldehyde
PI	phosphatidylinositol
ppm	parts per million
PS	phosphatidylserine
SALDI	surface-assisted laser desorption/ionization
TG	triglyceride
ToF	time of flight
UV	ultraviolet

Abstract

The work presented in this doctoral thesis addresses the development of mass spectrometry imaging (MSI) methods and focuses on their application to biological samples for analysis on the single-cell level. For this purpose, a home-built MSI ion source was developed and optimized for high lateral resolution in the low micrometer range. Sample preparation had to be optimized and multiple approaches were evaluated in order to fulfill the special requirements posed by high-lateral-resolution MSI at the single-cell level.

In a first project, an approach alternative to the widely employed matrix-assisted laser desorption/ionization (MALDI) MSI was evaluated, involving a matrix-free sample preparation method using nanostructured membranes, so-called DIUTHAME (desorption ionization using through-hole alumina membrane). With this method, the MS image quality regarding contrast and signal homogeneity could be improved compared to MALDI MSI while employing a simpler and faster sample preparation workflow. DIUTHAME membranes were successfully demonstrated as useful ionization-assisting materials on a variety of tissue types. However, signal intensities were found to be reduced by about one order of magnitude compared to MALDI MSI and thereby the number of analytes detected with the DIUTHAME method was reduced. Sub-cellular resolution MSI was demonstrated to be possible with a lateral resolution down to 5 µm using DIUTHAME, but better lateral resolutions were impeded by low ionization efficiency.

In a second project, the MALDI MSI sample preparation workflow was optimized for microglia single cells grown on glass slides for high-lateral-resolution MSI down to 1.5 µm. Separate workflows have been developed for bulk lipidomics analysis and for high-lateral-resolution MSI to extend the usability of the method in general. It was possible to statistically differentiate multiple microglia cell lines from each other and find molecular markers for inflammatory stimulation. By employing an imaging approach, the cell morphology could be resolved in high detail while simultaneously pinpointing cellular heterogeneity on the level of distinct molecules. Intra-cellular heterogeneity involving the formation and varying composition of lipid droplets was observed and the influence of inflammatory stimulation was investigated. Further, inter-cellular phospholipid heterogeneity was described and visualized for the first time in microglia cells grown under identical conditions.

In summary, the methods and home-built instrumentation described in this doctoral thesis successfully enabled single-cell mass spectrometry imaging at sub-cellular lateral resolution and fundamentally improved its application to biological samples. In an outlook, further possible applications of single-cell MSI are showcased. Lipidomic differences in rested and sleep-deprived *Drosophila melanogaster* brains were identified and a potential localization to sleep-related neurons was investigated in a multimodal approach involving fluorescence microscopy.

Zusammenfassung

Die in dieser Doktorarbeit vorgestellten Arbeiten beschäftigen sich mit der Weiterentwicklung von Methoden der bildgebenden Massenspektrometrie (MSI) und deren Anwendung auf biologische Proben. Eine eigens dafür entwickelte Ionenquelle ermöglicht räumlich hochaufgelöste Messungen im Mikrometerbereich, um einzelne biologische Zellen zu untersuchen und deren räumliche Molekülverteilung bildlich darzustellen. Des Weiteren wurden Probenvorbereitungsmethoden optimiert und verschiedene methodische Ansätze evaluiert, um den hohen Anforderungen von hochauflösender MSI auf Einzelzellebene gerecht zu werden.

In einem ersten Projekt wurde eine Alternative zur weit verbreiteten Matrix-unterstützten Laserdesorption/-ionisation (MALDI) MSI evaluiert, die auf einer matrixfreien Probenvorbereitung mit nanostrukturierten Membranen, sogenannten DIUTHAME (engl.: desorption ionization using through-hole alumina membrane), basiert. Mit dieser Methode konnten im Vergleich zu MALDI MSI Kontrast und Homogenität der erhaltenen Verteilungsbilder gesteigert werden, während die notwendigen Arbeitsschritte reduziert oder vereinfacht werden konnten. Die erhaltenen Signalintensitäten jedoch waren im Vergleich zu MALDI MSI um etwa eine Größenordnung reduziert, was eine verringerte Anzahl detektierbarer Moleküle zur Folge hatte. Die DIUTHAME Membranen wurden erfolgreich auf einer Vielzahl von verschiedenartigen biologischen Gewebeproben angewendet. Eine subzelluläre räumliche Auflösung konnte in MSI Experimenten gezeigt werden, die jedoch durch die geringe Ionisationseffizienz der Methode auf 5 µm begrenzt wurde.

Ein zweites Projekt fokussierte sich auf die Optimierung der Probenvorbereitung und Instrumentierung für MALDI MSI, um einzelne Mikrogliazellen auf Glasobjektträgern bildgebend mit bis zu 1.5 µm Auflösung zu vermessen. Dedizierte Methoden für hochauflösende Bildgebung oder optimierte Signalintensität von Lipiden wurden entwickelt, um eine vielseitigere Anwendungsmöglichkeit von MALDI MSI zu erreichen. Mit den entwickelten Methoden war es möglich, Zelllinien und Stimulationsstatus der Zellen basierend auf massenspektrometrischen Daten statistisch zu unterscheiden und molekulare Marker zu identifizieren. Die hohe räumliche Auflösung der Bildgebung ermöglichte es, die Morphologie der Zellen detailliert darzustellen und die Heterogenität einzelner Zellen auf molekularer Ebene zu identifizieren. Beispielsweise konnte die heterogene Verteilung von Lipidtropfen sowie deren veränderte Zusammensetzung und Verteilung nach Stimulation beobachtet werden. Des Weiteren konnte eine zelluläre Heterogenität auf Basis von Phospholipiden zwischen ansonsten ununterscheidbaren Zellen zum ersten Mal für Mikroglia gezeigt werden.

Zusammenfassend kann gesagt werden, dass die in dieser Doktorarbeit entwickelte Methodik und Instrumentierung erfolgreich die Anwendung von MSI in biologischen Proben auf Einzelzellebene ermöglicht hat. Als Ausblick werden weitere Anwendungsmöglichkeiten präsentiert und erste Ergebnisse zum Einfluss von Schlafentzug auf die Lipidzusammensetzung des Gehirns von *Drosophila melanogaster* gezeigt. Einzelne Lipidmoleküle konnten identifiziert werden, deren Intensität sich nach Schlafentzug verändert hat. Ein räumlicher Zusammenhang mit schlafassoziierten Neuronen, die aufgrund genetischer Modifikationen durch Fluoreszenzmikroskopie identifizierbar sind, wurde untersucht.

Chapter I - Synopsis

Introduction

Mass spectrometry

Mass analyzers

Mass spectrometry (MS) is a modern analytical technique to elucidate molecular information from organic or inorganic samples by determining the mass-to-charge-number ratio (*m*/*z*) of analytes. In mass spectra, the *m*/*z* values are plotted against signal intensities, which in combination allows for qualitative and quantitative investigation of the sample. High sensitivity, low limit of detection, fast data acquisition, precision and label-free analysis even of complex samples are key-factors, that enabled MS to reach outstanding importance and wide-spread application in the life sciences.[1]

MS is generally relying on the generation of ions from the sample by various ionization techniques in an ion source. Ions are subsequently manipulated in high vacuum by electrical or magnetic fields in a mass analyzer. Most mass spectrometers can perform well with positively-charged or negatively-charged ions. The polarity can be chosen individually before an experiment depending on the use case.

Magnetic fields have first been used in a mass analyzer in 1918 by A. J. Dempster.[2] Such analyzers, which are also used in modern-day sector field analyzers, can divert an initially linear ion beam onto a circular trajectory. The radius of the ion path is described in equation (1) and is dependent on the ion's *m*/*z* value. By either varying the magnetic field strength or the position of the detector, ions can be separately detected based on their individual *m*/*z*.

$$r = \frac{mv}{zeB} \tag{1}$$

r = radius
m = mass
v = velocity
z = charge number
e = elementary charge

Mass spectrometers applying electric fields have first been described by A. E. Cameron and D. F. Eggers Jr. in 1948.[3] They claimed that earlier magnetic-field-based mass spectrometers are too slow to describe rapidly changing samples due to multiple ion packages being necessary for a single spectrum. In their so-called "ion velocitron", whose modern-day counterparts are known as "time-of-flight" (ToF) mass spectrometers, Cameron and Eggers applied a locally defined electric field to accelerate ions inside a high-vacuum field-free drift tube. All ions experience the same potential energy input, which is translated into kinetic energy, but following equation (3) their velocity will be dependent on their *m*/*z* value. By time-resolved detection of the ion package, a mass spectrum can be constructed.

$$E_{kin} = \frac{1}{2}mv^2 = zeU = E_{pot} \tag{2}$$

$$v = \sqrt{\frac{2zeU}{m}} \tag{3}$$

E_{kin} = kinetic energy of the ion
E_{pot} = potential energy of the electric field
m = mass
v = velocity
z = charge number
e = elementary charge
U = voltage

In 1953, W. Paul and H. Steinwedel first described the quadrupole ion trap.[4] This concept is based on calculations, for which ions can be trapped in-between four rod-shaped electrodes, on which superimposed static and dynamic electric fields are applied. The fields can be carefully adjusted in a way to create a stable trapping potential for a given *m*/*z* range. Variation of the fields enables to selectively destabilize selected ions with given *m*/*z* values, which can then exit the trap to reach a detector. A systematic emptying of the trap, so called "scanning", results in a complete mass spectrum of the initially trapped ions.

Ion traps have since then appeared in multiple variants. In so-called Penning traps,[5] the cyclotron frequency of ions circulating in an magnetic field can be precisely measured. This is directly dependent on the *m*/*z* value of the ion, which is utilized in so-called Fourier-transform ion cyclotron resonance (FT-ICR) mass spectrometers.[6] As the name suggests, the overlap of the cyclotron frequencies of all ions is measured at once and translated into *m*/*z* values via Fourier transformation.

While trapping techniques were becoming increasingly popular over time, A. Makarov described a new design of an ion trap in the year 2000, the so-called "Orbitrap", which consists of an outer barrel-shaped and an inner spindle-like electrode, between which ions can orbit on stable trajectories.[7] Due to a decentral injection of ions, not only an orbital motion is induced, but also an axial movement along the central electrode. The harmonic frequency of this oscillation is dependent on an ion's *m*/*z* value and can be measured as a transient for all ions in the trap. Through Fourier transformation, individual components and thereby *m*/*z* values of the ions can be determined.

For most applications in the life sciences, a precise measurement of the *m*/*z* value of ions is key to identify molecules and understand biological or biochemical processes. Key quality markers for mass spectrometers are the mass resolution and mass accuracy that the system can deliver. Mass resolution describes the ability of a mass analyzer to discriminate ions having minimal *m*/*z* differences and can be calculated using equation (4), e.g. following the "full width at half maximum" (FWHM) definition. Mass spectrometers able to achieve high mass resolution results are called to have a high mass resolving power.[8]

$$R = \frac{m}{\Delta m} \tag{4}$$

R = mass resolution
m = mass of a selected, singly charged ion
Δm = width of peak at 50% intensity

Mass accuracy on the other hand describes the deviation of the accurate mass, which is measured by the mass spectrometer in an experiment, from the theoretically calculated exact mass, which is a true value per definition, and is usually given in parts per million (ppm) as in equation (5).[8]

$$\Delta = \frac{m_{accurate} - m_{exact}}{m_{exact}} \cdot 10^6 \tag{5}$$

Δ = mass accuracy in parts per million (ppm)
$m_{accurate}$ = measured mass of an ion with known charge
m_{exact} = theoretically calculated mass of an ion

The higher the mass resolution of a mass spectrometer, the higher is its ability to individually detect ions of similar mass as separate peaks. The highest mass resolution can be achieved with FT-ICR instruments with up to *R* = 2,000,000 and an accuracy of < 1 ppm in recent approaches,[9,10] which enables for example the differentiation of isotopologues of very similar masses like ^{57}Fe-heme and ^{56}Fe-heme^{13}C, differing by only Δ(*m/z)* = 0.0029.[11] Similarly, with a mass resolution of up to *R* = 480,000

on commercial and up to *R* = 2,000,000 on experimental setups[12,13] while simultaneously achieving a mass accuracy of < 1 ppm, recent Orbitrap instruments can offer performances comparable to FT-ICR instruments while having greatly reduced expenses, complexity and size.[14,15]

Despite their lower mass resolution, ToF analyzers are dominantly used due to their unprecedented speed and high versatility.[16,17] Nevertheless, the share of ion-trapping analyzers has been growing constantly over the last decade, mainly driven by an increased need for high mass resolution and mass accuracy for molecular identification in complex samples.[18–20] In the last ten years, the relative amount of publications using Orbitrap technology has doubled (Figure 1).

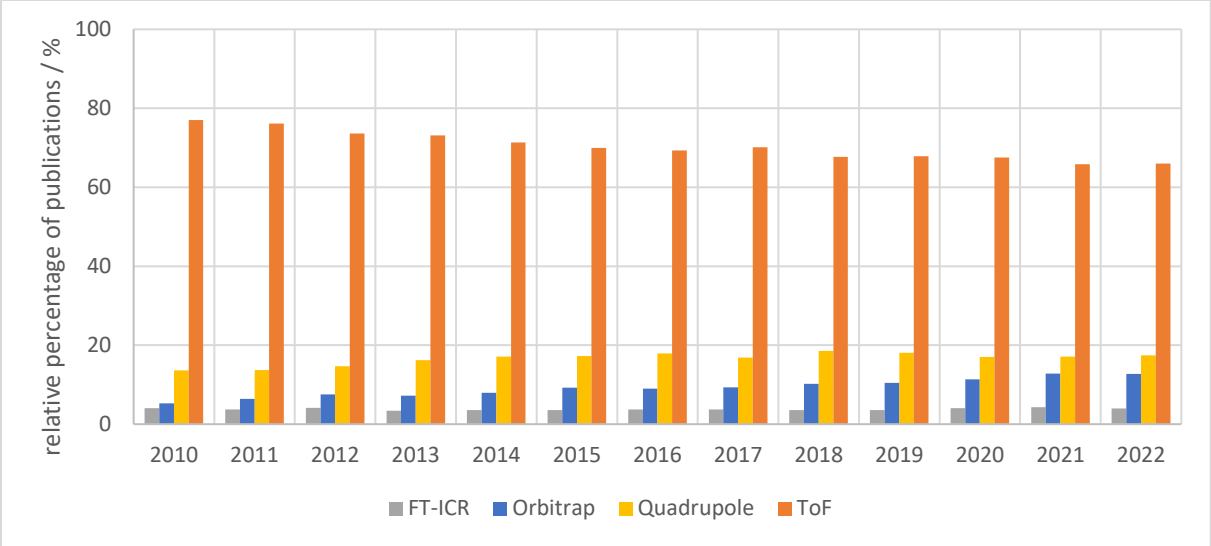

Figure 1: Relative percentage of publications listed in the Clarivate Web of Science upon searching for either FT-ICR (grey), Orbitrap (blue), quadrupole (yellow) or ToF (orange) analyzers per year in the MS research field without restriction in application. Results are normalized to 100%.

Analyte identification and fragmentation

In mass spectrometry, measuring the accurate mass of an ion is one way to designate a molecular identity. Based on the increasingly high mass accuracy and resolving power of modern mass spectrometers, the sum formula of an ion can be calculated from a peak or annotated using databases.[21–24] Furthermore, the characteristic isotopic pattern of a molecular species observable in a mass spectrum can give additional information or validation of an analyte annotation and elemental composition. It must be considered, however, that charge carriers also contribute to the pattern of mass signals of one molecular species. In bioanalytical research, charge carriers are usually monoatomic or molecular ions of salts initially present in the biological environment which can attach to the analyte or substitute exchangeable protons of the molecule. Thereby, multiple signals in a mass spectrum can arise from one analyte with different charge carriers.

However, multiple biological entities can usually be annotated to one *m/z* signal based on accurate mass alone. Molecules with identical sum formulae but different chemical structure, so-called isobaric ions, cannot be directly differentiated in accurate mass spectra. As an everyday example, the well-known carbohydrates sucrose and lactose share the sum formula $C_{12}H_{22}O_{11}$ and thereby would be measured with the same *m/z* values, but they are structurally different from each other, which is the background behind the clinically important selective intolerance for lactose but not glucose in some humans.[25]

To elucidate the structural features of molecules or ions using mass spectrometry, fragmentation experiments are typically performed. One of the benefits of ion trap mass spectrometers is their ability to not only measure but also store selected ions for further manipulation. Tandem-MS, also denoted as MS/MS or MS^2, utilizes this ability for structural elucidation. In general, a narrow *m/z* range, putatively containing only the ion-species of interest, is selectively collected in the ion trap while other ions are discarded. The selected ion-species is then subjected to a high energy input, for example by gas collision[26,27] or laser irradiation,[28–30] which induces characteristic and predictable fragmentation of the ions. Subsequently, the fragment ions themselves are subjected to MS analysis, giving vital insights into the initial molecular structure through characteristic fragment ions. On suitable instruments, the process of isolation and fragmentation can be repeated several times on the resulting fragments (MS^n), enabling a more and more elaborated structural analysis of the ion of interest.[31]

Mass spectrometry Imaging

Since mass spectrometry is a relatively fast process in obtaining a single mass spectrum (typically taking less than a second per spectrum), a high throughput of samples is feasible. In mass spectrometry imaging (MSI), first introduced in 1967 by H. Liebl[32] and made available to bioanalytical research by B. Spengler in 1994,[33] a multitude of MS measurements is performed repeatedly from a sample surface in an organized pattern, usually a rectangle.[33] Signal acquisition by a probe, e.g. a focused laser, is restricted to a confined area on the sample per spectrum, resulting in a pixel-wise scanning of the surface. Since mass spectra are available for every pixel, an image can be reconstructed through data evaluation, resembling the distribution of a single ion over the sample surface.[34–37]

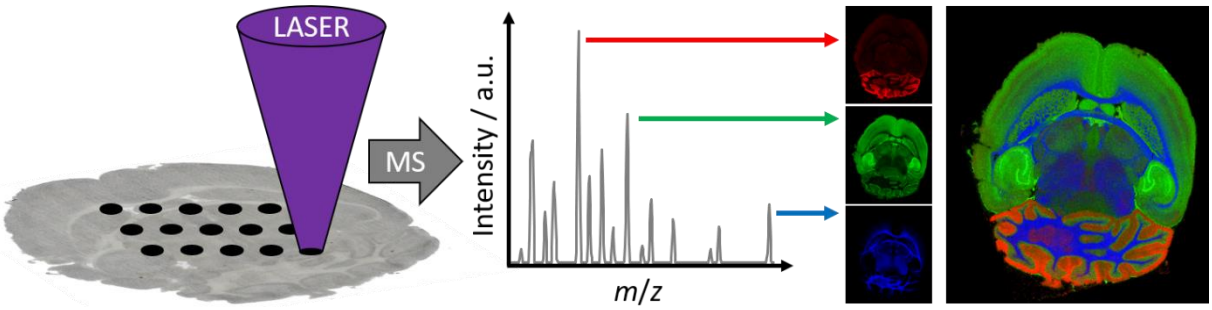

Figure 2: Schematic workflow of a laser-based MSI experiment. Confined and ordered areas of the sample are sequentially ionized and subjected to MS analysis. The intensity distribution of selected peaks can be visualized as images after data evaluation. Up to three ion images can be overlaid to a loss-less RGB image.

A key factor for MSI analysis is the achievable lateral resolution, represented by the pixel size, which is directly linked to the size of the sampling probe. In principle, it is desirable to achieve a preferably small sampling probe while retaining a sufficient ion signal intensity, which naturally drops with decreasing sampling area.[38] This is in line with the trend in bioanalytical research towards small model organisms or cells cultures, that are easier to study than e.g. rodent animals, due to shorter reproduction cycles, low cost or ethical reasons,[39] making high-lateral-resolution MSI an important and active field of research.

Commonly, imaging in bioanalytical research is performed by optical or fluorescence microscopy, often enhanced by staining techniques. However, classical histological staining is comparably unspecific, since it is only targeting a molecule class instead of giving defined molecular information.[40] Immunostaining techniques on the other hand are very precise but limited to one particular analyte per staining reagent and require at least some knowledge about the sample prior to investigation.[41,42] The same is true for *in vivo* imaging of organisms, that were genetically modified to selectively express

a fluorophore in targeted cells.[43–45] MSI overcomes these shortcomings by being able to analyze any sample, even unknown ones, in an untargeted approach while simultaneously acquiring distinct molecular information for hundreds or thousands of analytes at the same time.[34–37]

Ionization

An important step of any MS analysis, independent of the analyzer, is the ionization of the analyte, for which a variety of methods exist. The analyte can be transferred to the gas phase and ionized through thermal, electric, kinetic, ionic or photonic energy input. Individual methods are classified into the categories "soft" and "hard", depending on their tendency of fragmenting the analyte during ionization. Whereas a general fragmentation might be useful for example in structure elucidation of reaction products in organic chemistry,[46] it would overcomplicate the already very complex spectra in modern biochemical research. Thereby, "soft" ionization methods are usually preferred in the life sciences for the analysis of intact biomolecules. These methods introduce charges by adding or removing charge carriers (X), yielding adducts with the analyte (M) that are commonly notated as $[M \pm X]^{\pm}$. For example, a proton (H^+) can be added ($[M+H]^+$) or subtracted ($[M-H]^-$) from an analyte to introduce a charge without triggering fragmentation processes. Other charge carriers such as Na^+, K^+, NH_4^+ or Cl^- are naturally found in biological samples and therefore can also form adducts with the analyte, e.g. $[M + Na]^+$.

Electrospray ionization

One of the most widely used ionization techniques is electrospray ionization (ESI), which was first described by M. Yamashita and J. B. Fenn in 1984.[47] For ESI, the analyte has to be dissolved in some form of solvent, e.g. a mixture of water and methanol, which can be individually tuned to the experimental objective. The solution is then pumped through a fine capillary with an inner diameter in the micrometer range using a flow rate of a few microliters per minute. To create an electrospray, a high voltage of a few kilovolts is applied between the mass spectrometer inlet, which is usually on ground potential, and the ESI spray capillary. Charge separation occurs by charge carriers, e.g. protons, being enriched either on the capillary wall or at the capillary tip, depending on the applied polarity and their charge. From the capillary tip, a so-called Taylor-cone is formed, from which a liquid jet is ejected that decays into a spray of charged droplets due to electrostatic repulsion. As stated in equation (6), a stable electrospray can only be formed, if the force generated by the electric field is stronger than the surface tension of the solvent. Using a heated capillary or an assisting gas flow can support the ionization process.

$$F_{repulsion} = \frac{2Uq}{r \cdot \ln(\frac{4d}{r})} > \sigma_{surface} \qquad (6)$$

$F_{repulsion}$ = force generated by the electric field
U = voltage applied to the capillary
q = charge
r = radius of the capillary
d = distance between capillary tip and mass spectrometer inlet
$\sigma_{surface}$ = surface tension

On the way to the mass spectrometer, the solvent gets vaporized and the charge density inside the droplets rises until it reaches the Rayleigh limit[48] and the droplet gets split into smaller droplets repeatedly. The process of final ionization can be explained by two mechanisms. Smaller and highly

charged molecules tend to follow the "ion evaporation model" (IEM),[49,50] which claims that ions are ejected from the droplets directly due to the high charge density inside the droplets. Larger molecules tend to follow the "charge residue model" (CRM),[51,52] which assumes that the solvent is vaporized completely until only the analyte and charge carriers remain.

One of the major benefits of ESI, which also contributes to its widespread use, is the possibility to seamlessly couple it with liquid chromatography, e.g. high-performance liquid chromatography (HPLC).[53,54] In HPLC, a small amount of the sample is pumped through a column, the so-called stationary phase, using ultra-pure solvents as a mobile phase. Samples must be soluble in the mobile phase and are usually extracts from biological tissue or cells. Depending on the interaction of the individual analyte molecule with the mobile and stationary phase, e.g. due to its size or polarity, a chromatographic separation into multiple fractions can be achieved. The time an analyte takes to pass the stationary phase, the so-called retention time, is distinctive under given experimental conditions. For optimal separation, stationary and mobile phase have to be carefully tuned and optimized. Nevertheless, a perfect separation of all analytes in a complex biological sample usually cannot be achieved due to similarities in the large ensemble of bioactive compounds, limiting the chromatographic resolution. The mass spectrometer can serve as the detector here, not only detecting the presence of an analyte for determining its retention time, but additionally separating analytes by their *m*/*z* values. The interconnection of HPLC-MS enables to better elucidate the molecular structure or identity by physically separating individual molecules and thereby deconvoluting resulting mass spectra. Additionally, tandem-MS experiments can be conducted more reliably, since HPLC can partially eliminate co-isolation of multiple molecules.

Desorption electrospray ionization

Similar to ESI, the method of desorption electrospray ionization (DESI)[55–57] is utilizing an electrospray with solvent to ionize the sample. The analyte, however, is not dissolved in the electrospray solvent, but is residing on a sample surface on which the electrospray is directed at. Charged droplets are ejected from a small capillary and accelerated by a gas stream to hit the sample surface, from which analytes are subsequently desorbed, ionized and transported towards the mass spectrometer inlet by secondary droplets.[58] The lack of sample pretreatment and the ability to investigate virtually any sample under ambient conditions are key factors, that make DESI an attractive bioanalytical method. Extracting and dissolving the analyte, which would be an additional sample preparation step employing ESI analysis, is already incorporated into the DESI process. Additionally, microdroplets as utilized in DESI are ideally suited reaction vessels to derivatize analytes during desorption and ionization by mixing derivatization agents into the solvent, so-called reactive DESI.[59] Thereby, charge carriers or polar groups, which are usually inevitable for efficient ionization with soft ionization methods, can be chemically introduced into an apolar target molecule. For example, Wu and coworkers were able to investigate cholesterol with reactive DESI,[60] whereas underivatized cholesterol is hard to ionize due to its low proton affinity and low acidity.[61] DESI can also be employed as an imaging technique, since the solvent jet can be selectively steered over the surface to scan a sample.[57,62] Depending on the size of the capillary used, a lateral resolution of around 10 µm can be achieved.[63,64]

Matrix-assisted laser desorption/ionization

By using light as a sampling probe, matrix-assisted laser desorption/ionization (MALDI) is, besides ESI, one of the most widely used ionization techniques in MS.[65–68] First described by M. Karas and F. Hillenkamp in 1987, MALDI utilizes a focused ultraviolet (UV) laser beam directed to a sample, which was covered with an ionization-assisting matrix.[69] Despite laser desorption/ionization (LDI) was already described for the use of small molecules, particles or elemental analysis,[70–72] only the introduction of

an organic matrix enabled the technique to also be applicable to larger biomolecules.[73] Especially for imaging applications, MALDI MSI has become one of the most valuable and widely used techniques in the life sciences today.[33,34,36,74] Nevertheless, the actual ionization mechanism of MALDI is still a matter of debate.[75] Recent research has focused on secondary ionization processes in the dense desorption plume, that are responsible for analyte ion formation, whereas the primary source of matrix ionization remains unclear.[76]

As matrices, various organic acids or bases can be utilized for positive- or negative-ion mode, respectively.[65] Nevertheless, matrices should be mostly inert towards the sample or oxidation, be in solid state under ambient conditions, have a low vapor pressure, absorb the wavelength of the laser employed and ideally produce minimal background signal.[77–81] In the early days of the method, matrix application was performed via the "dried droplet" method. A sample is spotted onto a surface, e.g. a purified authentic standard on a glass slide, and subsequently covered by a small amount of matrix solution. While the solvent is vaporized after some time, the matrix incorporates the analyte inside large crystals in a process called co-crystallization.[73] This method is still applied today due to its ease of use,[82] but cannot be used for quantitative approaches since the distribution of the analyte in the spot after drying is far from homogeneous, resulting in hotspots of higher signal intensities.[83] Also, imaging applications would not be possible with dried droplet matrix preparation protocols.

To achieve a homogeneous matrix layer over the sample suitable for imaging applications, e.g. on tissues or cells, sublimation and spray-coating methods were developed. However, careful method optimization is a crucial step in MALDI MSI sample preparation, since even slight changes to the protocol can lead to reduced reproducibility and validity of the results.[84–86] In general, the matrix layer should consist of small, homogeneously distributed matrix crystals and efficiently incorporate the analyte of interest. For spray-coating, the matrix is therefore dissolved in a suitable solvent mixture and then nebulized by a gas flow towards the sample. Small solvent droplets hit the sample surface and dissolve some of the analytes to form matrix-analyte cocrystals after solvent evaporation. Careful adjustments of the solvent mixture, spray volume and spray duration are inevitable to efficiently dissolve analyte molecules while avoiding wash-out effects and analyte delocalization on the sample.[87] For sublimation, a matrix substance is placed in a vacuum chamber and heated. Matrix is transferred to the gas phase and subsequently resublimates on the sample, which is mounted on a cold finger at the top of the vacuum chamber.[88] The analytes of the sample will not only be covered with small matrix crystals, but to some extent will also diffuse into the matrix crystals.[89,90] However, analyte incorporation and therefore signal intensity is usually higher using spray-coating methods due to solvent use.[38,85]

Surface-assisted laser desorption/ionization

Since matrix application is such a crucial step in MALDI MS(I) experiments, efforts have been made to eliminate organic matrices from the workflow. Around the same time as MALDI emerging as an ionization technique, K. Tanaka described the use of inorganic particles to assist ionization in a process later called surface-assisted laser desorption/ionization (SALDI).[91,92] A surface, however, can be made of a large variety of nanomaterials. A nanostructured material, ranging from randomly oriented nanoparticles or colloidal materials[93–95] to highly engineered nanoposts,[96–98] nanotubes,[99] nanowires[100,101] or nanoholes,[102,103] is usually made up of metals[104] or their oxides,[93–95,99] silicon[101,105] or inorganic carbon, e.g. graphene[91,106].

The mechanism taking place on the surface of a material during desorption and ionization is highly debated. Since the analytical performance of a SALDI experiment is dependent on many material characteristics like shape, size, nanostructure, thermal conductivity, melting point, photoabsorption

efficiency or chemical surface properties, finding a general mechanism for all materials is tough if not impossible.[107,108] However, thermal and non-thermal processes both seem to play a role when the rapid and sharp increase in surface temperature induced by the laser has to be efficiently transferred to the analyte.[109]

The desorption process is assumed to be driven by the rapid heating of the material surface and subsequent phase transfer.[108,110] Due to heat confinement effects in the nanostructures and low thermal conductivity of the material, a locally restricted high temperature spike is produced upon laser irradiation.[111] Through this heat spike, material residing on the surface of the material will be thermally desorbed.[107]

For ionization, however, multiple proposed mechanisms and potential pathways exist.[112] For example, the so-called "hot electron" mechanism proposal assumes, that laser-induced electron ejection leads to surface charges and subsequent fragmentation of the charge-separated SALDI material through Coulomb explosion, as a main cause of analyte ionization.[113] Later, this mechanism was extended on remaining electron-holes after electron ejection, which are considered to be possible contributors to ionization.[114] Another proposed mechanism claims that the SALDI material is quickly heated until a laser-induced plasma is formed. Through a shockwave from the rapidly expanding material, analytes are desorbed from the surface and ionized through gas-phase interactions with the plasma.[115] Beyond those examples, a high number of further mechanistic proposals exist.[112] Due to the highly diverse nature of the different materials and nanostructures, multiple mechanistic approaches might be relevant.[109]

Post-ionization

In surface-based ionization techniques such as MALDI, DESI or SALDI, desorption and ionization are typically concerted processes initialized by the sampling probe. In this process, many more analyte molecules are desorbed than actually ionized, resulting in highly reduced ion yields. It is estimated that for MALDI, less than 0.1 % of the desorbed molecules are actually ionized.[116,117] Especially for high-lateral-resolution MSI experiments, that are naturally limited in the number of available molecules due to the small sampling area, the low ionization efficiency may become a limiting factor.

However, to boost signal intensities and increase ion yield, techniques have been developed to additionally assist ionization. So-called post-ionization approaches implement a secondary ionization step into the system, that is performed on the already desorbed material. Post-ionization can for example be performed by electrospray, plasma or irradiation using a second laser.[118]

One example for spray-based post-ionization is laser ablation electrospray ionization (LAESI), where the sample is ablated using an infrared (IR) laser. The resulting desorption plume is then intercepted with an electrospray plume. Post-ionization is achieved due to the fusion of electrospray droplets with ablated neutral molecules or particles, resulting in doping of the electrospray with analyte, which is then measured by the mass spectrometer.[119,120]

In another approach called MALDI-2, a laser is utilized to enhance ionization in a MALDI experiment.[121] Here, a second laser with higher intensity is precisely timed to intersect the desorption plume ejected from the sample surface by the primary laser. For example, an increase in signal intensity by up to two orders of magnitude was observed for some lipid species, whereas on other lipid species the effect was lower or miniscule, showing an efficiency dependence on the actual ion species.[121] The mechanistic background of the process is still a matter of active research, but it is suggested that a two-photon process on desorbed molecules as well as a classical MALDI process in ejected material clusters play an important role in laser-based post-ionization.[122]

High-resolution laser-based mass spectrometry imaging

Laser sampling probe

The use of laser systems as sampling probes in mass spectrometry imaging applications is the basis of both, MALDI and SALDI MSI. One of the main advantages of using lasers here is their versatility, ease of use and wide-spread availability. A laser can be easily controlled using optical elements like lenses, filters or mirrors, which are, as the laser sources themselves, available in a large variety and already widely applied in numerous scientific, medical or industrial settings.

To achieve high lateral resolution in MSI, the laser has to be focused to a small spot on the sample surface. Commercially available ion sources typically operate at laser spot sizes between 5 µm and 20 µm.[34] However, smaller ablation spot diameters around 1 µm have been shown in experimental setups as proofs-of-principle.[38,121,123,124] From a mechanistic point of view, the development towards high lateral resolution is not only appreciated for its increasingly detailed analysis of the sample morphology, but also in regard to ionization efficiency. For example, it has been found that ionization efficiency in MALDI is strongly dependent on laser fluence, which is the employed laser energy per irradiated area.[125–127] Despite that smaller ablation spots naturally reduce signal intensities due to a reduced sampling area, the increased laser fluence is counteracting this behavior to some extent.

In the MSI community, the terms “pixel size” and “spot size” are often used synonymously to describe the measurement characteristics of an MSI experiment. However, when talking about high lateral resolution, the difference between the terms should be made clear. “Pixel size” is referring to the size of the picture elements in a digital image and is equivalent to the distance the sample or the laser spot is moved between two consecutive desorption/ionization events on the sample surface. It thus defines the size of the area represented by a pixel in an MS image. The pixel size is directly set by the experimenter. “Spot size” on the other hand refers to the actual size of the ablation spot crater produced by a single desorption/ionization event, which is dependent on the objective lens used to focus the laser and can be additionally controlled via the laser energy input. The lower the laser energy, the smaller is the spot size for a given (near) gaussian laser spot intensity profile. However, the actual size of the ablation spot is also dependent on surface and sample characteristics and should thereby be confirmed by microscopy techniques for each experiment.

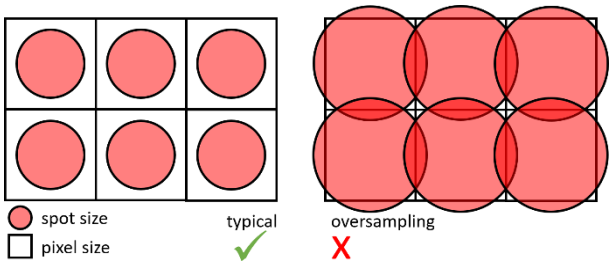

Figure 3: Schematic representation of pixel size and spot size for a typical MSI measurement and for oversampling approaches.

The achievable minimal pixel size and thereby level of detail for the MSI measurements is dependent on the ablation spot diameter, since the laser should be directed to a completely untouched area of the sample surface for each pixel to ensure authentic and reproducible MSI results (“non-oversampling conditions”). Therefore, the spot size should be smaller than the pixel size. However, by using so-called oversampling conditions, a pixel size smaller than the ablation spots can be employed. In this case it is assumed that 100% of the sample material is desorbed during a laser irradiation event. For the next pixel, only the not-yet irradiated part of the sample surface under the laser spot is desorbed and ionized, resulting in the pixel size becoming independent of the laser ablation spot size. However, the assumption on which oversampling is based is not necessarily true, especially at the low laser energy settings that are required for achieving small ablation spots. Therefore, when using oversampling, some material of the previous pixel is always co-analyzed, resulting in measurement artifacts and washout effects. For achieving authentic and reproducible MSI results, oversampling should be avoided.[37] All results in this work are produced without oversampling.

Single-cell and subcellular mass spectrometry imaging

The required lateral resolution of an MSI experiment is linked to the kind of sample to be investigated. Larger samples like tissue sections can easily be investigated with commercially available ion sources. However, research on the single-cell level is becoming increasingly important.[34,128–133] Genetically identical cells, which were grown under the same environmental conditions from the same ancestor can express different phenotypes.[129] In this context, a phenotype is defined as a subset from a set of genetically identical cells, which have distinct observable characteristics, e.g. the expression of a specific molecule.[134] Phenotype heterogeneity has been found to play an important role in health and disease[135–138] and even switching phenotypes, e.g. upon stimulation or a changing environment, has been observed for cells.[139]

To obtain information from single cells, multiple approaches have been developed over the last years involving mass spectrometry. If spatial information is not necessary, single-cells can be collected from a culture medium and sampled as individual entities using microfluidic devices.[140,141] Cells can for example be separated in micrometer-sized droplets of water in oil or a combination of other immiscible fluids.[141] Therefore, a highly diluted cell suspension is inserted into a flow of an immiscible fluid, creating microdroplets that encapsulate single cells. From a statistical point of view, each microdroplet should include one or no cell due to the low concentration of cells in the suspension. The microdroplets can then be transported to an analyzer, for example an ESI source coupled to a mass spectrometer. Besides that, a large variety of trapping[142,143] or encapsulation[144] methods for single cells have been demonstrated, based on microfluidics.

However, spatial information is usually not neglectable due to the influence neighboring cells have on each other, especially in multicellular organisms. If cells are of sufficient size, samples can be taken manually using mechanical probes like nanopipettes.[145–147] By extracting the cell interior, analysis can be directly performed with an ESI MS approach. However, this manual extraction is labor intensive and only gives limited spatial information.

For smaller cells, laser radiation can serve as a viable probe. Even for cells smaller than the laser focus, different multimodal approaches guided or aided by optical or fluorescence microscopy have been developed. In an approach called microMS,[148] an optical microscopy image of the cells spatially separated on a glass slide is acquired prior to matrix application and the MALDI MS measurement. Software-based cell-detection identifies individual cells on the surface and handles their location to the MALDI MS system. The laser is then triggered to sample from the preselected position and mass spectra of single cells are recorded. Based on the microscopy image, which recorded the physical boundaries of the cells, an image can be created by extrapolating the MS information from one sample spot over the whole cell body. By only targeting actual cells, this approach saves a lot of time compared to a classical MSI approach, which would also measure the empty space in-between cells. Inter-cellular heterogeneity within a sample can be detected and correlated to optical or fluorescence microscopy measurements of the sample to yield advanced biological insights.[149] However, a potential intra-cellular heterogeneity would be missed and cells have to be reasonably separated for reliable identification.

Approaching the problem the other way, the SpaceM[150] method measures a fixed sample area of cells grown on glass slides in a native environment, avoiding biochemical distortion due to cell sorting and cell separation. By an automated overlay of pre- and post-MALDI MSI microscopy images, the mass spectrometric information can be extrapolated within the detected cell boundaries, even if the lateral resolution achievable by the MALDI MSI instrument would not be sufficient otherwise. The system makes use of the ablation marks the laser produces on the cells to precisely and reliably co-align MALDI MSI and microscopy data.

An even more versatile approach on single-cell MALDI MSI would be to achieve a laser ablation spot size significantly smaller than the cell itself. With modern MALDI MSI instrumentation, this can be achieved for some types of cells. For example, human fibroblast cells have been investigated utilizing commercially available instruments with a pixel size of down to 5 µm, which is significantly smaller than the cell size of >100 µm.[151] The detected cellular heterogeneity in MALDI MSI was in line with fluorescence microscopy, but was acquired independently.

However, cells come in a large variety of sizes, even inside one organism.[152] While MALDI MSI of zebrafish embryos, around 600 µm in diameter, can also be called single-cell imaging,[153] most cells of biological interest are much smaller than that. In humans, for example, adipocytes (fat cells) or fibroblasts (skin cells) can be 100 µm or larger in diameter,[151,154,155] whereas pancreatic beta cells (insulin production) or enterocytes (intestinal cells) are usually around 10 µm or 15 µm in diameter,[156,157] respectively, and red blood cells have a diameter of around 8 µm with a thickness of around 2 µm.[158] Thereby, using commercially available MALDI MSI instrumentation, only a hand-full of pixels could be obtained per cell in most cases, which is neither sufficient to outline the cell's morphology, nor to distinguish its inter- or intra-cellular heterogeneity from random signal fluctuations. The investigation of small cells though requires an even smaller laser spot size to sufficiently resolve the cellular structures and outlines.

Instrumentation

In recent years, single-cell MALDI MSI has gained in popularity.[34] However, application of the technique to not only the largest of cells is usually combined with specialized instrumental developments of the ion source. While the working principle of MALDI MSI remains largely the same, different technical approaches have been developed over the years. Most ion sources are equipped with lasers utilizing UV light, which can be well focused due to its short wavelength and is widely absorbed by organic matrices. The minimal focal diameter is restricted by the Abbe limit, which is, besides the physical and technical characteristics of the focusing lens, dependent on the laser wavelength.[159,160] The shorter the wavelength, the smaller is the possible laser focus. Alternatively, some approaches utilize IR-lasers, which come with the benefit that the intrinsic water of a biological sample can perform as the matrix due to its IR-absorbing characteristics.[161,162] Thereby, it is not necessary to apply a matrix onto the sample. However, achievable lateral resolution and ion yield are greatly reduced compared to UV-MALDI approaches.[37,163]

In general, the laser is guided through filters or attenuators to precisely control the output laser energy reaching the sample surface, since this has direct influence on the ablation spot diameter and ionization efficiency.[125] Beam-steering mirrors are used to guide the laser beam to an objective lens, which is used to focus the laser beam to its final diameter. The sample is either placed on a conductive glass slide, e.g. indium tin oxide (ITO) glass, or placed in front of a conducting metal plate on a regular glass slide to apply a high voltage of 3 – 5 kV to the sample, which is accelerating the ions away from the sample surface to the MS inlet. MALDI ion sources can be realized in multiple, vendor-specific geometries, that come with individual advantages and disadvantages.

In angled geometry (Figure 4a), the objective lens is placed at some angle < 90° to the sample surface, which is placed directly in front of the MS inlet.[164] Commercially available microscope objectives can be used. This approach is comparably easy to realize mechanically, but ionization efficiency and lateral resolution are reduced due to the angle. In MALDI MSI, the ions are preferably desorbed and ejected from the surface towards the laser beam.[165] Thereby in this approach, ions are initially guided away from the mass spectrometer inlet, resulting in the loss of ions. Also, the laser spot is geometrically enlarged due to hitting the sample at an angle.

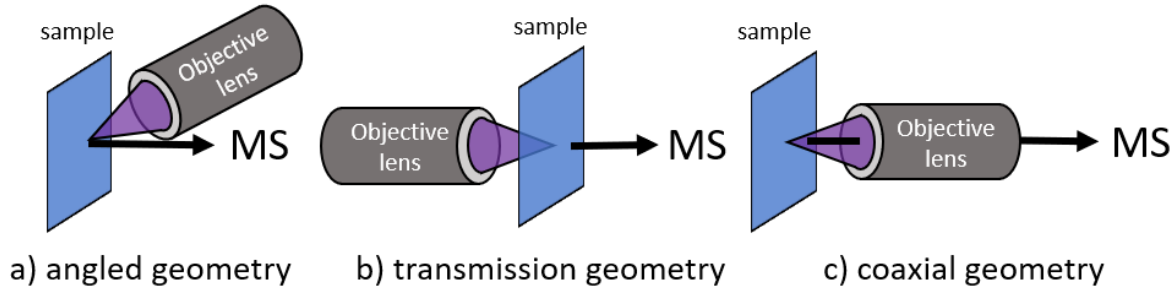

Figure 4: Schematic overview of possible geometries for laser-based ion sources.

Transmission geometry (Figure 4b) realizes laser irradiation from the sample backside, which means that the laser has to be focused through the sample itself onto the matrix layer.[123,166] The ions then have no other possibility than to desorb into the direction of the MS inlet. However, ionization efficiency here is linked to the local transparency of the sample. For example, a cell's nucleus, which is less transparent than the cytoplasm, partly blocks the laser radiation and thereby reduces ionization efficiency and measured ion intensity.[123] This results in measurement artifacts and can mislead data interpretation. However, this approach is technically easy to realize and can also benefit from well-established microscopic objectives.

A third approach utilizes a coaxial geometry (Figure 4c), where the laser radiation and the mass spectrometer inlet are both having a 90° angle to the sample surface, which comes with some spatial constraints.[38,167,168] To realize this approach, a highly specialized objective lens with a central bore has to be realized, to be pulled over a prolonged ion-transfer tube. The ions are then transferred through the center of the objective lens. While this approach overcomes the shortcomings or problems of the previously presented methods and combines high ion-transfer efficiency without the problems caused by varying sample transparency, it comes with technical complexity and needs specifically tailored objective lenses. The coaxial approach is used in this work (Figure 5).

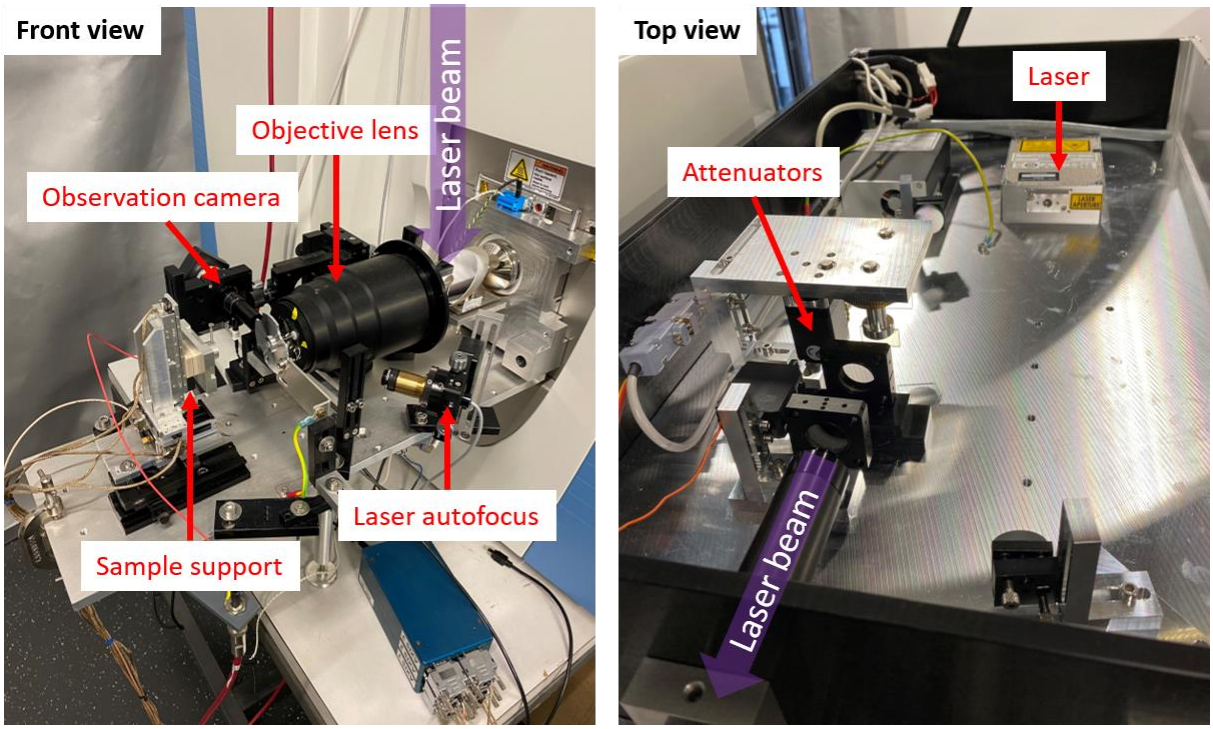

Figure 5: Photo of the home-built ion source developed and used for this doctoral thesis. The ion source is mounted to the front and on the top of a Q Exactive mass spectrometer (Thermo Fisher Scientific, Bremen, Germany).

Motivation and aim of this work

The goal of this work was to improve the performance of MSI methods and instrumentation to a point, where it can be applied to single-cell investigation. Using MSI, cells could be identified, localized and characterized while overcoming the limitations of classical histology. Precisely, MSI enables to unravel cellular characteristics and heterogeneity down to the molecular level with minimal or no prior knowledge about the sample. Due to the small size of cells as the building blocks of life as we know it, the lateral resolution of MSI techniques had to be improved fundamentally compared to commercially available state-of-the-art technology. To pinpoint mass spectrometry features to single molecules, mass spectrometers employing Orbitrap technology were chosen for these projects due to their high mass resolving power of up to 240,000.[7]

First, the achievable lateral resolution of MS imaging sources had to be improved. Therefore, a home-built ion source in coaxial geometry with a highly specialized centrally bored objective lens was constructed and optimized by fine-tuning laser setting and instrument geometry. On a red-dye coating, which was used as a simple model system, an ablation spot size of < 1 µm was achieved while simultaneously achieving signal intensities comparable to commercially available instruments at 5 µm spot size. To translate the high lateral resolution achieved on a red-dye model system to real biological samples, sample preparation had to be optimized to yield a highly homogeneous coverage with the ionization-assisting matrix. Due to the low focal depth of the new objective lens, surface homogeneity, especially regarding height variations, is becoming a limiting factor. Matrix application for MALDI MSI, however, is prone to such imperfections and optimization is challenging.

In the first project, DIUTHAME membranes were applied to tissue sections to characterize their applicability in high-lateral-resolution MSI and compare them to classical MALDI matrices. DIUTHAME membranes had so-far only been demonstrated as a proof-of-concept by the manufacturer. The near-perfect surface homogeneity of DIUTHAME membranes is a promising feature for MSI applications, since it promises to improve image quality regarding homogeneity and contrast compared to MSI employing matrix application. Further, it is easier to use and could therefore accelerate the adoption of high-lateral-resolution MSI as an established tool in the life sciences. However, DIUTHAME has never been used before for high-lateral-resolution MSI. It was found that individual cells in tissue could be resolved using DIUTHAME MSI with greater contrast and higher signal homogeneity compared to MALDI MSI, but the signal intensities using MALDI MSI were superior.

In a second project, the lipidome of microglia cells was investigated using MALDI MSI at subcellular lateral resolution. Microglia were chosen due to their high clinical significance and their variety of phenotypes, which could be resolved using MALDI MSI. The lipidome of microglia has been investigated before, but spatial distribution of lipids was never investigated in high detail. Sample preparation, including matrix application and cell pretreatment, were optimized for a high ion yield and a high lateral resolution. With an optimized sample preparation protocol and home-built instrumentation, it was possible to visualize the lipid distribution of microglia cells at 1.5 µm lateral resolution without oversampling. The heterogeneous distribution of individual lipids gave vital insights into microglia phenotyping, and statistical analysis of the lipid signatures of microglia cells enabled cell-line and cell-status differentiation based on MS data.

The results of this work highlight how MSI at high lateral resolution can be utilized facing bioanalytical problems and give new insights over established methods. The scientific tools developed in this work might help to achieve a better understanding of single-cell processes like phenotyping or cell-to-cell interaction due to the high lateral resolution available now.

Matrix-Free High-Resolution Atmospheric-Pressure SALDI Mass Spectrometry Imaging of Biological Samples Using Nanostructured DIUTHAME Membranes

The importance and trouble of sample preparation for MSI applications

One of the major bottlenecks for increasing the lateral resolution achievable with MALDI MSI is sample preparation, since inhomogeneities like matrix-crystal clusters, holes or variations in the thickness of the matrix layer negatively impact the practically achievable resolution and analyte signal intensity.[38,77,84,169] More precisely, the matrix application on a sample has to fulfill higher requirements in regard of homogeneity and ionization efficiency with increasing lateral resolution. Optimizing the sample-preparation workflow is a tedious and time-consuming challenge, that has to be faced again for every new matrix. Even between different sample types, some tweaking of the parameters might be necessary, while matrix can either be applied by spray-coating or sublimation.[170,171] Spray-coating captivates with an efficient formation of matrix-analyte cocrystals due to solvent use, while sublimation techniques are limited to diffusion for analyte migration into the matrix resulting in an over-all lower analyte ion signal.[38] However, solvent use can also have a delocalization effect on the analytes, which should be minimized for high-lateral-resolution MSI.[169]

Inhomogeneities in the matrix layer like the formation of clustered matrix crystals can obstruct the sample underneath and prevent effective analyte ionization. Especially for single-cell applications, where the samples can be of similar size as the inhomogeneities, a negative impact on the image authenticity can be expected. Further, variations in matrix thickness should be avoided in order to obtain a homogeneous and undistorted desorption and ionization of analytes from the sample. Matrix thickness directly influences the signal intensity of the analytes of interest, since analyte incorporation into the matrix is decreasing with distance from the sample surface. If the matrix layer becomes too thick, the laser cannot penetrate to analyte-rich regimes thus reducing analyte signal. If the matrix layer is too thin or even incomplete, not enough material would be incorporated into the matrix, which also results in a lowered analyte signal. On the other hand, a varying thickness has negative impact on the diameter of the laser focus on the surface. The smaller the laser focus an objective lens produces, the smaller its focal depth usually becomes. This becomes obvious when comparing the two objective lenses used in the projects of this thesis, which are capable of producing 5 µm or 1.5 µm focal diameter with a focal depth of ≈ 40 µm or < 6 µm, respectively.[38,172] Thereby, single-cell applications at high lateral resolution have increasingly high requirements for matrix-layer homogeneity throughout the sample and an optimization of the preparation protocol is inevitable.

Hence, the perfect sample preparation would captivate with high ionization efficiency, prevent analyte delocalization and be a universal and easy-to-use process. One of the benefits of SALDI MSI is that, unlike for MALD MSI, it is possible to premanufacture ionization-assisting materials with a near-perfect surface homogeneity, which can then be then placed over or under the sample.[96,98,102] One of those premanufactured SALDI materials is DIUTHAME (Desorption Ionization Using Through-Hole Alumina Membrane, Figure 6[173]), which is a promising candidate to provide an improved sample preparation compared to a classical MALDI-matrix application. The DIUTHAME membrane consists of a 5 µm thin alumina membrane, which is nanostructured with 200 nm wide capillary-like through-holes and was first described in 2018.[103] A sample, for example a standard in solution, can be applied on the DIUTHAME membrane and ionized through laser radiation.[103,174,175] First imaging applications on tissue were presented

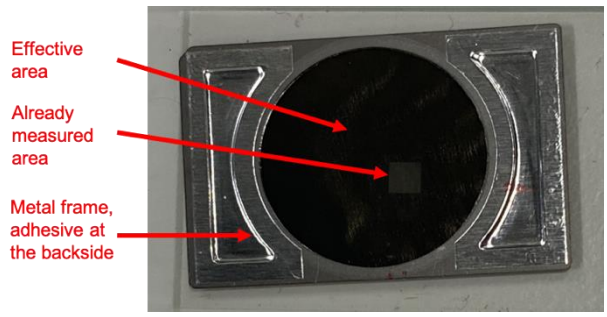

Figure 6: Optical image of the DIUTHAME membrane attached to mouse brain tissue after an MSI measurement.

shortly after for mouse brain tissue[102] or plants[176] at comparably low lateral resolutions between 50 µm and 300 µm. The reproducibility of mass accuracy and signal intensity was found to be higher for DIUTHAME compared to 2,5-dihydroxybenzoic acid (DHB), a wide-spread MALDI matrix, using authentic standards or mouse brain tissue sections.[177] This effect is directly linked to the near-perfect surface homogeneity of the DIUTHAME membrane and will be highly beneficial for high-lateral-resolution MSI. Despite the promising characteristics, no attempt on achieving high-lateral-resolution MSI data using DIUTHAME membranes has been published before.

Similarly, the development of other SALDI MSI techniques has not been focusing on achieving high lateral resolution yet. For example, another premanufactured SALDI material on which tissue sections can simply be placed, nanopost arrays (NAPA), has only been shown to achieve pixel sizes of around 100 µm.[97,178] The smallest pixel size shown for SALDI MSI in general is 5 µm for silver-sputtered mouse brain tissue,[179] whereas bioanalytical applications are usually performed at larger pixel sizes.[109,180,181] However, 5 µm pixel size could only be achieved by performing oversampling with 20 µm wide ablation spots, resulting in wash-out effects and measurement artifacts reducing the MS image quality.[179] No ablation spot sizes smaller than 20 µm were reported in literature for SALDI MSI yet.

Comparison between DIUTHAME membrane and classical MALDI MS

As a first step to implement the DIUTHAME membrane into a high-lateral-resolution MSI workflow, its physical properties were investigated. Using optical microscopy, the surface of the DIUTHAME membrane was found to be more homogeneous than typical MALDI matrices. Sample preparation was reduced to placing the membrane on a frozen tissue section and slowly warming it up, which stands in contrast to the multi-stepped workflow of applying a MALDI matrix. However, tissue sections have to be at least 50 µm thick for an efficient adhesion of the DIUTHAME membrane to the thawing sample section. To evaluate the performance of the DIUTHAME membrane and its potential as a substitute or supplement to well established organic matrices, a comparison of methods was performed. In particular, DIUTHAME MS was compared to MALDI MS to investigate benefits and drawbacks of the DIUTHAME membrane. Further, a comparison with LDI MS on the unaltered sample was performed to prove the ionization-assisting effects of the DIUTHAME membranes.

First, all three methods were applied to mouse brain tissue sections, which are a widely used and well understood model system for method development. Due to the large mechanistical differences between the methods, a normalization method for better comparison had to be developed. In particular, keeping the laser energy constant between measurements, like it is usually done when comparing among several MALDI methods,[182] was not suitable here and resulted in differently sized ablation spots for MALDI and DIUTHAME, respectively. The laser energy input necessary to achieve efficient desorption and ionization is directly linked to the absorption characteristics of the sample or its ionization-assisting material and can even differ between MALDI matrices. A large ablation spot from a too high laser intensity naturally leads to increased signal intensity, since more material is desorbed and ionized, impeding a fair comparison. However, keeping the ablation spot diameter constant has proven to be a valuable method to compare MALDI, DIUTHAME and LDI signal intensities, especially with respect to potential imaging applications. It was found that the laser energy required to produce small ablation spots of ≈5 µm and information-rich mass spectra for DIUTHAME MS (≈1300 J/m^2) was similar to MALDI MS with DHB matrix (≈2500 J/m^2), but far-off the vastly higher laser energy settings required to get any ablation spots or signal in LDI experiments (≈500,000 J/m^2).

When comparing mass spectra in the phospholipid mass range between *m*/*z* 600 – 1000 from mouse brain tissue between MALDI MS and DIUTHAME MS, both methods showed similar signals. Measurements performed with LDI, however, did only result in low-intensity and noisy mass spectra.

This confirms the previous reports of the ionization-assisting properties of DIUTHAME.[102,103] Background or off-tissue signals, that are commonly present from ionized matrix clusters in MALDI MS, especially in the lower mass range, have not been observed for DIUTHAME. However, signal intensities were about one order of magnitude lower for DIUTHAME than for MALDI, resulting in a low number of individual analytes being detected, about 10% compared to MALDI. Molecular annotations[23] based on accurate mass further revealed that the analytes found by DIUTHAME MS are mostly a subset of those found by MALDI MS. This might be a direct consequence of the lower signal intensities, leading to low abundant signals falling under the limit of detection. These findings were confirmed by others after the publication of this project.[183]

Performance and limits of DIUTHAME MSI applications

To utilize the potential DIUTHAME has shown as an ionization-assisting substrate, it was applied to mouse brain tissue sections, which were then investigated by MSI. Comparative measurements with MALDI and LDI were performed on consecutive tissue sections. First, samples were measured on a commercially available AP-SMALDI[5] AF ion source by TransMIT GmbH, which is specified to achieve pixel sizes down to 5 µm. After that, a home-built ion source was utilized, that has been shown to be capable of MALDI MSI measurements at 1.4 µm lateral resolution.[38] Due to the lower ion yield when using DIUTHAME, the lowest usable lateral resolution was 5 µm on both instrumentations. To achieve smaller ablation spots, the laser energy would have to be lowered, which resulted in a total loss of ion signal on DIUTHAME-covered samples. On matrix-coated samples, however, smaller ablation spots were feasible with sufficient ion signal. Nevertheless, the ablation spot size achieved here was at least 4x smaller than in previously published work on SALDI MSI.[179] When comparing the MSI results from DIUTHAME and MALDI at 5 µm pixel size, tissue borders, e.g. between white matter and granular layer of the cerebellum, were visualized sharper and with higher contrast using DIUTHAME. Especially the Purkinje cells, which are separated single cells interlaced between the grey matter and the granular layer of the cerebellum, were better resolved.[184] Despite that DIUTHAME is unable to generate distinctive ions from these cells due to the low ionization efficiency, their morphology could be sharply visualized by the absence of signals from their surrounding tissue. In MALDI MSI, however, distinct signals for Purkinje cells could be detected, but the single cells were not visualized as clearly as with DIUTHAME. Especially in denser regions, the individual cell's signals spatially overlapped to be visualized as a continuous layer, which was not observed using DIUTHAME. This is directly linked to the solvent-free methodology of the DIUTHAME applications, which stands in contrast to spray-coating samples with a MALDI matrix, where the used solvent can lead to small washout effects. Also, the pixel-to-pixel reproducibility of DIUTHAME was found to be higher than when using MALDI MSI, which leads to less signal variations in homogeneous parts of the tissue and subsequently a more regular representation in the MS image. The high reproducibility described for DIUTHAME compared to DHB matrix was later confirmed by another research group after publication of this project.[177] DIUTHAME was successfully applied to tissue sections from mouse brain, mouse kidney, rape seed and *Spodoptera littoralis* caterpillar at different lateral resolutions, always resulting in high-quality MSI images while being in line with previous studies of these samples.[185]

In conclusion, the DIUTHAME membrane was found to be a viable ionization-assisting material for high-lateral-resolution MSI down to 5 µm pixel size and even at the single-cell level. It captivates with a higher pixel-to-pixel reproducibility and a higher contrast compared to MALDI MSI measurements while simultaneously being easier and faster to use. However, the lower ion yield of DIUTHAME compared to MALDI hampers its wide-spread use and needs improvement in the future to utilize its full potential, especially for even higher lateral resolution in MSI applications < 5 µm.

Lipid Signatures and Inter-Cellular Heterogeneity of Naïve and Lipopolysaccharide-Stimulated Human Microglia-like Cells

The role of lipids in biological systems

Lipids are a highly abundant class of molecules in every living system. In general, lipids are defined as biomolecules, that are soluble in apolar solvents, which sets them into contrast to generally water-soluble biomolecules such as proteins, saccharides or nucleic acids.[186] Lipids are further divided into subclasses based on their molecular structure. Among those, glycero- and glycerophospholipids are the most prominent, since they are a main component of the cellular membrane. Therefore, they are the main focus of this work. In general, glycerolipids consist of up to 3 fatty acids attached to a glycerol backbone. In glycerophospholipids, one reaction site of the glycerol is linked to a polar headgroup via a phosphate group. Typical lipid classes in mammals include phosphatidylcholines (PC, Figure 7a), phosphatidylethanolamines (PE, Figure 7b), phosphatidic acids (PA), phosphatidylinositols (PI, Figure 7c), phosphatidylserines (PS), triglycerides (TG, Figure 7d) or diglycerides (DG). Commonly, individual lipids are noted by their headgroup abbreviation followed by the number of carbons and double bonds in their fatty acids.[187,188] If the fatty acid composition is not known in detail, both fatty acids can be summarized. For example, PC 38:1 would stand for a phosphatidylcholine (PC) lipid, which has 38 carbon atoms and 1 double bond in its fatty acid chains with unknown distribution.

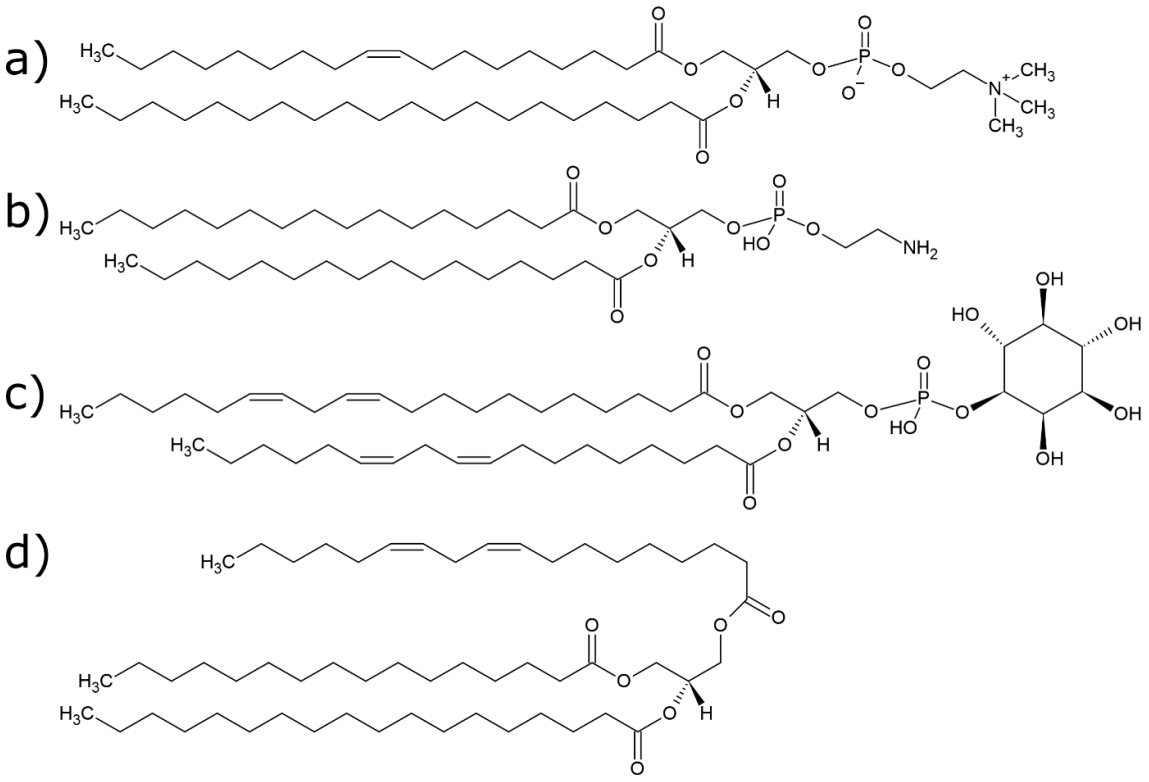

Figure 7: Examples of lipids typically to be expected in microglia cells. Each structure represents one isomer of a) PC 38:1, b) PE 32:0, c) PI 38:4, d) TG 52:2.

Lipids, however, are also known to have multiple bioactive functions and can therefore serve as a valid discriminator of cell status, phenotype or health and disease, making them a major target in bioanalytical research.[189–191] For example, it has been found using MSI tools, that breast cancer tissue can be identified on a molecular basis due to its increased expression of PI 38:3 compared to the surrounding tissue. The stroma around the cancerous tissue, however, was found to increasingly express PI 38:4.[192] This study highlights, how miniscule changes in the lipid composition, here one double bond, can make the difference between healthy and cancerous tissue and how lipids can serve

as a discriminator of cell states. It is thereby of high interest to better understand the function of lipid biomarkers. Another example for the importance of lipid signaling is the apoptosis mechanism of cells, in which PS lipids play an important role. In healthy cells, PS species are present only on the inside of the cellular membrane bilayer and this status is maintained by specialized enzymes. During cell death, however, PS is actively flipped to the outside of the cell, serving as a signal that the cell is ready to undergo apoptosis and is thereby attacked by macrophages, a part of the immune system.[193,194]

Microglia cells as a target for sub-cellular lipidomics

Microglia are often referred to as the immune cells of the central nervous system.[195,196] They are non-neuronal cells residing in the brain and spinal cord and are for example involved in brain maintenance, homeostasis or immune response, but also play a major role in neurodegenerative diseases like Alzheimer's disease, Parkinson's disease or multiple sclerosis.[197–204]

New literature reports suggest that microglia can change their form and function as a response to a changing micro-environment,[205–208] but morphological cell changes are not sole descriptors for a changing cell function.[209] For example, microglia preferably catabolize glucose to fuel cell maintenance and growth, but can switch to fatty acyl digestion when in a nutrition-deprived environment.[210] Cell-internal storages in the form of lipid droplets, consisting of mostly neutral lipids,[211] can be depleted to satisfy energy needs, whereas an increased abundance of them seems to be a survival benefit.[212] At the same time, however, lipid droplet formation can also be a sign of cell-aging and dysfunction,[213] making them an ambiguous descriptor of the cell status using histology alone.

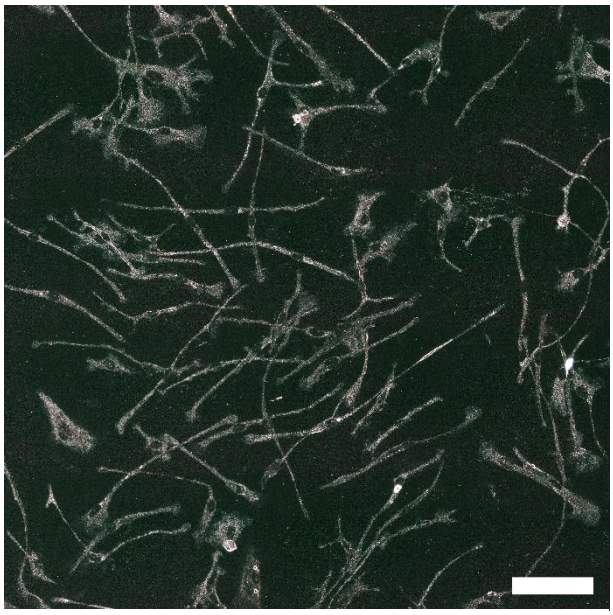

Figure 8: Microscopic image of naïve microglia cells grown on a glass slide after fixation and before MALDI MSI measurement. Scale bar: 100 µm.

While single proteins can be identified and localized by staining with specifically designed antibody dyes and subsequent fluorescence microscopy, this is not easily performed for lipids. Lipids come in a large variety, but individual species are very similar to each other and can differ by as little as one double bond in the alkyl chain while fulfilling completely different functions.[191] Lipid droplets, again for example, are usually identified by staining based on their enrichment with apolar neutral lipids.[211,214] However, it is neither possible with this technique to differentiate between lipid class, e.g. triglycerides or cholesterol esters, nor to identify lipid species. Mass spectrometry imaging tools, especially MALDI MSI, can assist here to give a better insight into the cell's function since it is possible to differentiate individual lipid molecules.[191] Analyses of the lipidome of microglia have already been conducted using mass spectrometry,[215–217] but due to technical limitations or experimental design no study was able to perform spatially resolved lipidomics on microglia cells yet. The small size of microglia presents a major challenge to commonly used MALDI MSI instrumentation. Especially the fine projections, which are typical for microglia morphology and are usually < 5 µm in diameter (Figure 8), could not be authentically represented with commercially available instruments. However, MALDI MSI investigations of fibroblast cells, which are significantly larger (≈100 µm) than microglia, already found cellular heterogeneity, identified cellular subpopulations and characterized the function of some lipids.[151]

Lipidomic signatures of microglia cell lines

To characterize the lipidome of microglia cells by MALDI MSI, a high lateral resolution would be necessary to retrieve sub-cellular information. All experiments on microglia therefore had to be performed on a home-built ion source, which was equipped with a specialized objective lens. The laser beam was focused onto the sample in orthogonal reflective geometry, while the ions had to be transferred via a prolonged inlet capillary through the central bore of the objective lens. The geometry, in particular the laser beam path and the distance between the laser focus and the tip of the inlet capillary, was carefully optimized for highest ion yield while retaining homogeneously round and reproducible ablation spots. An oversampling-free lateral resolution of 1.5 µm was achieved using this setup, which is in accordance with other state-of-the-art MALDI MSI setups.[38,123,169,218] However, most approaches on high-lateral-resolution single-cell MALDI MSI rely on post-ionization techniques to achieve the sensitivity needed for small ablation spots.[123,169,218] In this work, it was possible to optimize the geometry of the ion source and the laser-setup in a way, that enables high lateral resolution without the need for additional post-ionization, reducing complexity.

Microglia cells of four individual cell lines were investigated in positive- and negative-ion mode, respectively. Each cell line was investigated in naïve state and upon stimulation with lipopolysaccharide (LPS), which is commonly used to induce an inflammatory response of cells. Sample preparation was optimized, which included washing steps, matrix application protocol and cell pretreatment. It was found that a fixation of cells using paraformaldehyde (PFA) for 1 minute and storage at +4°C in phosphate-buffered saline (PBS) resulted in a better preservation of the original cell's morphology, whereas skipping fixation and storage at -80°C after flash-freezing improved the analyte ion signal. Hence, fixed cells were used for high-lateral-resolution MALDI MSI experiments, whereas flash-frozen cells were devoted for lipidomic research and statistical evaluation between cell populations.

Using MALDI MSI data, it was possible to differentiate cell lines based only on their lipidomic profile by statistical analysis. Further, the same approach allowed to identify differences in lipid expression between naïve and LPS-stimulated cells. Here, especially triglyceride species were found to be increased in signal intensities and variety upon LPS-stimulation. These findings were confirmed by the MS images of these compounds, where more triglyceride-containing lipid droplets were found in LPS-stimulated compared to naïve samples, which is in line with previous studies.[219,220] One of the benefits using high-lateral-resolution MALDI MSI compared to other single-cell MALDI approaches is, that each pixel can be seen as a technical replicate measurement of a cell or its cell population. The higher the lateral resolution, the more technical replicates can be performed per cell and therefore the significance of findings is increased. With this setup, hundreds of individual measurements can be performed from a single microglia cell.

High lateral resolution MALDI MSI of microglia cells

To further characterize the capability of the method, the data quality of experiments utilizing high-lateral-resolution MALDI MSI compared to a more moderate lateral resolution had to be evaluated. Therefore, MALDI MSI measurements at 5 µm, 2 µm and 1.5 µm were compared regarding signal intensity, number of detected lipid analytes and pixel coverage, which is the ratio between signal-containing and blank pixels on a cell. It was found that an increase in lateral resolution from 5 µm to 1.5 µm decreases the sensitivity of the method by a factor of 3x to 5x, which was expected due to the 11x smaller ablation spot area. Despite the significantly smaller amount of sample material, the quality of the MS images remained high, judged by the high pixel coverage of 75% - 96% and by comparison

with microscopy images. With this method, it was possible to visualize the distribution of single lipids species and their spatial interaction throughout microglia cells in yet unachieved detail.

As mentioned earlier, microglia are known to differentiate into multiple phenotypes. With the sub-cellular lateral resolution, it was possible to characterize the molecular makeup of individual cells. It was found, that despite the similar environment, some cells form lipid droplets while others do not. Upon LPS-stimulation, their numbers increase but their distribution remains heterogeneous. It can be shown that lipid droplets accumulate favorably in the bulkier part of the cells, while the fine projections usually are free of lipid droplets. This intra-cellular heterogeneity is in line with other studies based on staining techniques,[211,214] but their distinct molecular makeup was investigated for the first time using this setup. Individual triglyceride species were identified as main components of lipid droplets and compared between cell lines.

Also, phospholipids were found to be heterogeneously distributed between cells. Other than triglyceride heterogeneity in lipid droplets, phospholipid heterogeneity was affecting the whole cell body uniformly. Neighboring or even overlapping cells were found to express different phospholipids, potentially in their cellular membrane, despite a similar environment. For example, some cells were found to have an up- or downregulated production of certain PI lipid species, that differ by the degree of unsaturation in their alkyl chain. While all cells were found to homogeneously express PI 38:4, one phenotype increasingly expressed PI 38:5 while the other identified phenotype increasingly expressed PI 38:3.

In conclusion, it can be said that MALDI MSI at high lateral resolution down to 1.5 µm helped to identify lipid signatures of human microglia cells, while simultaneously being able to localize and identify heterogeneity on a molecular level in yet unachieved detail. These findings contribute to a better understanding of microglia phenotyping and the involvement of lipids in this process.

Conclusion

The aim of the work presented in this thesis was to improve mass spectrometry imaging of single cells and make it therefore applicable to a wider range of users. To achieve a higher lateral resolution, a new home-built ion source was constructed, optimized and evaluated. Ablation spots of < 1 µm were observed on red-dye model systems.

With DIUTHAME membranes, high lateral resolution of up to 5 µm on tissue sections could be achieved, which is sufficient to localize single cells inside the tissue. In particular, the Purkinje cell layer could be visualized in mouse brain cerebellum tissue sections. The contrast between different tissue regions and the homogeneity in the resulting MS images were improved in comparison to classical MALDI MSI with an organic matrix. Due to the lack of solvents in the sample preparation process, analyte delocalization was efficiently prevented. The applicability of DIUTHAME has been demonstrated on multiple tissue sections like mouse brain, mouse kidney, rape seed or a larva. However, signal intensity using DIUTHAME was reduced compared to MALDI at constant ablation spot size by about one order of magnitude. Thereby, the number of individual analytes detectable was also reduced for DIUTHAME. The results were evaluated with respect to the SALDI mechanism, where phase transitions of the membrane seem to play an important role in the desorption mechanism, as indicated by microscopy on the DIUTHAME membrane after the MSI measurement. Charge carriers, however, appear to result rather from the sample itself than from the DIUTHAME material, since they do not include ionic adducts of the membrane material but are rather adducts comparable to those found using MALDI MSI. The ease of use of the method makes it a reliable tool for high-throughput applications, even on the single-cell level, despite tradeoffs in signal intensity.

However, MALDI MSI appeared more promising for the investigation of single cells at highest lateral resolution, due to its higher ionization efficiency. Therefore, an improved matrix application protocol was developed to fit the high requirements of single-cell analysis on surface homogeneity and ionization efficiency for positive- and negative-ion mode. The pretreatment of the cells, which were grown in PBS, a medium incompatible to MALDI MSI due to its high salt content, was separately optimized for bulk lipidomics and single-cell MSI to adapt the method to a broader range of scientific needs. By analyzing the lipidomic signatures of the cells, multiple cell lines as well as stimulation states could be statistically differentiated. Further, high-lateral-resolution oversampling-free MALDI MSI of down to 1.5 µm pixel size was achieved on microglia cells. The morphology as visualized by MALDI MSI was precisely in line with microscopy results. This enabled to visualize inter- and intra-cellular heterogeneity of microglia cells grown under identical conditions while simultaneously pinpointing the molecules responsible for the heterogeneity. Triglycerides were found to be heterogeneously increased in some microglia cells upon inflammatory stimulation and distinct phospholipid species were found to be heterogeneously expressed independent of stimulation.

In summary, the methods developed and improved here allow to investigate the lipidome of single cells using MALDI MSI at a high lateral resolution of up to 1.5 µm, which is suitable for most cell types. Sample preparation protocols for high-throughput applications, bulk lipidomics and spatial lipidomics have been developed and evaluated.

Outlook

As presented in this work, the instrumental setup and preparation protocol enables high-lateral-resolution MSI on the single-cell level. Future projects could revisit the DIUTHAME membrane to increase the ionization efficiency of the method based on the mechanistical insights given in this work. Technical development, both in the manufacturing process of DIUTHAME and in ion-transfer efficiency of mass spectrometers might enable the method to achieve even higher lateral resolution in MSI experiments than presented here. Also, as the field of SALDI MSI is still in its beginnings, multiple alternatives to the DIUTHAME membranes using different materials or nanostructures might be accessible in the future, which might make it more competitive to the classical MALDI MSI approach.

In MALDI MSI, the methodology can be seen as ready for application on bioanalytical projects focusing on single-cell analysis in cell culture or in tissue. However, matrix application protocols could be improved for more matrices, in addition to the ones presented in this work.

As an example for further application of high-lateral-resolution MALDI MSI, experiments on dissected *Drosophila melanogaster* brains have been conducted with the goal to achieve insights into the lipidomic changes and processes involved in sleep deprivation. Sleep is known to be controlled by the circadian rhythm, basically the 24-hour cycle of day and night, which is well understood.[221] However, the reaction of an organism to sleep deprivation, so-called homeostatic sleep control, is a matter of active research.[222,223] It has been found in the *D. melanogaster* model organism applying optogenetics, that a small set of neurons in the dorsal fan-shaped body of the brain is responsible for sleep control.[224,225] While being able to fluorescently label these neurons through genetic modification, a detailed molecular investigation on the lipidome has not been performed yet. Identifying molecular changes in single neurons is challenging, but the results presented in this work encourage to apply MALDI MSI at high lateral resolution on this bioanalytical problem.

After adapting and optimizing a protocol to the embedding and sectioning of fragile and small samples,[226] thin tissue sections of dissected *D. melanogaster* brains were produced. Fluorescence microscopy was employed to identify sections through the dorsal fan-shaped body, which were subsequently subjected to MALDI MSI (Figure 9).

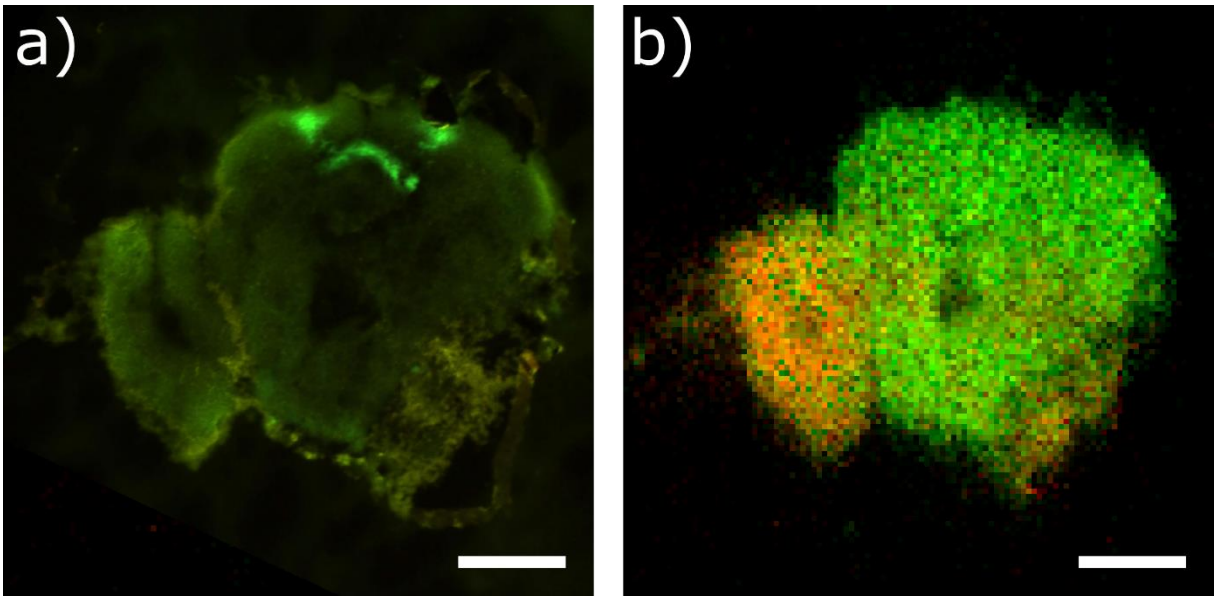

Figure 9: a): Fluorescence microscopy image of a D. melanogaster brain section, highlighting the fluorescently labelled dorsal fan-shaped body in bright green. b): MALDI MS image of the same D. melanogaster brain section as in (a), indicating heterogeneity between optic lobe (red, m/z 762.6018, $[PC\ 34:0 + H]^+$) and central brain region (green, m/z 865.5782, $[PI\ 36:1 + H]^+$). Scale bars: 100 µm.

As a compromise between high signal intensity and high lateral resolution, a pixel size of 5 µm was chosen for the experiments, which would be sufficient to resolve the structures of interest. It was possible to visualize individual brain regions of *D. melanogaster* brains, for example the optic lobe, by distinct lipid expression using MALDI MSI (Figure 9b).

Lipids found by MALDI MSI in multiple replicates of rested and sleep-deprived *D. melanogaster* brains were compared using a statistical approach. Molecular markers for resting and sleep deprivation were identified, and the two conditions individually grouped in a principal component analysis based on their lipidomic signatures. To confirm molecular annotations based on exact mass measurements in MALDI MSI, validation experiments were performed using HPLC MS^2 on a lipid extract of ≈1300 individually dissected rested or sleep-deprived *D. melanogaster* brains, respectively.

Table 1: Lipid species found exclusively in rested or sleep-deprived Drosophila melanogaster brain sections, respectively, by MALDI MSI. Annotations are candidates validated by HPLC-MS^2 of Drosophila melanogaster brain extracts. Bold annotations indicate the candidate with the lowest mass deviation to the MALDI MSI peak.

Rested		Sleep-deprived	
m/z	Annotation	*m/z*	Annotation
695.4621	PA 36:5, **PA 34:2**	618.4110	**PE 27:2**
697.4780	PA 36:4, **PA 34:1**	728.5586	**PE O-36:3**, PE O-34:0
719.4615	PA 38:7, **PA 36:4**	742.5378	**PC 33:3, PE 36:3**, PC 31:0, PE 34:0
721.4775	PA 38:6, **PA 36:3**	744.5536	**PC 33:2, PE 36:2**
723.4932	PA 38:5, **PA 36:2**	788.6140	**PC 36:1**
728.5190	PC 32:3, PE 35:3, **PC 30:0, PE 33:0**		
745.4777	**PA 38:5**		
751.5261	**PA 40:5**		
758.4709	**PE 36:6**		
778.5345	PC 36:6, **PC 34:3, PE 37:3**		
794.5655	**PC 35:2, PE 38:2**		
826.4618	**PS 38:8**		
887.5612	PI 38:5, **PI 36:1**		

In rested brains, multiple highly unsaturated phospholipids were identified, that were not detected in sleep-deprived brains (Table 1). Similarly, a high number of PA lipids was only detected in rested *D. melanogaster* brains. It is assumed, that sleep deprivation results in oxidative stress and that highly unsaturated lipid species should be degraded first.[227] While oxidation products are usually hard to detect using MS methods due to their lability, the absence of highly unsaturated lipid species in sleep-deprived samples still might be a hint that oxidative stress plays a major role in sleep deprivation. Further, it is interesting to note that PA lipid species are assumed to play a major role in cell fission or fusion, since their small polar headgroup allows for negative membrane curvatures of the cells.[228,229] Cell division might thereby be hindered or restricted upon sleep deprivation.

It was found, however, that those molecular changes identified between rested and sleep-deprived *D. melanogaster* brains were not limited to the dorsal fan-shaped body as anticipated. Sleep deprivation rather affected the lipidome of the whole brain uniformly and did not only occur in distinct neurons, which could have been resolved by the high lateral resolution of the method (Figure 10). The spatial lipidomics abilities of MALDI MSI were a key factor here to make unanticipated findings on the effect of sleep deprivation in *D. melanogaster* brains, which might not have been possible with established methods like HPLC MS alone. For future projects on this topic, MALDI MSI might be used on other biomolecular classes than lipids, that might be affected differently by sleep deprivation. Further, *D. melanogaster* could be genetically modified to express an alternative oxidase found in plants,[230] that could prevent oxidative stress to some extent and therefore reduce the oxidation process of highly unsaturated lipid species.

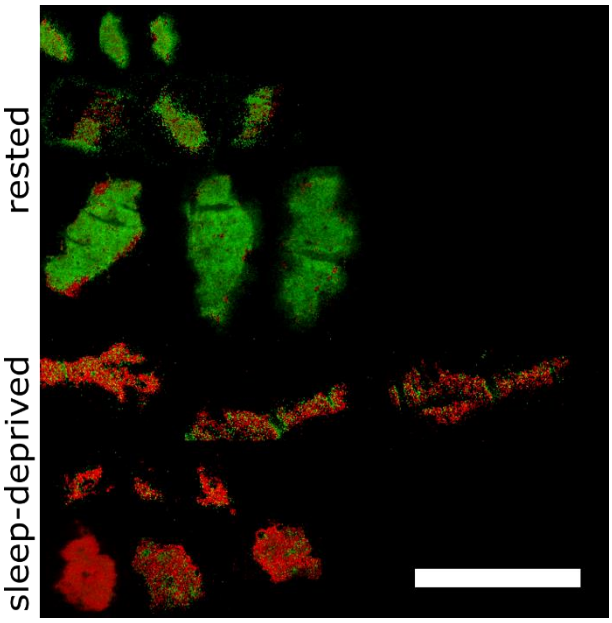

Figure 10: Composed MALDI MS image of 18 individual MALDI MSI measurements of rested or sleep-deprived Drosophila melanogaster brain sections. Brain sections in a row are replicate measurements of the same brain. Sectioning plains might differ between samples. Color coding: red: [PE 36:3 + H]$^+$ (m/z 742.5384), green: [PA 36:3 + Na]$^+$ (m/z 721.4779). Annotations are confirmed by HPLC MS^2 experiments. Scale bar: 1 mm.

References

(1) Griffiths, J. A brief history of mass spectrometry. *Anal. Chem.* **2008**, *80*, 5678–5683.
(2) Dempster, A. J. A new Method of Positive Ray Analysis. *Phys. Rev.* **1918**, *11*, 316–325.
(3) Cameron, A. E.; Eggers, D. F. An Ion "Velocitron". *Rev. Sci. Instrum.* **1948**, *19*, 605–607.
(4) Paul, W.; Steinwedel, H. Notizen: Ein neues Massenspektrometer ohne Magnetfeld. *Z. Naturforsch. A* **1953**, *8*, 448–450.
(5) Penning, F. M. Die Glimmentladung bei niedrigem Druck zwischen koaxialen Zylindern in einem axialen Magnetfeld. *Physica* **1936**, *3*, 873–894.
(6) Comisarow, M. B.; Marshall, A. G. Fourier transform ion cyclotron resonance spectroscopy. *Chem. Phys. Lett.* **1974**, *25*, 282–283.
(7) Makarov. Electrostatic axially harmonic orbital trapping: a high-performance technique of mass analysis. *Anal. Chem.* **2000**, *72*, 1156–1162.
(8) Murray, K. K.; Boyd, R. K.; Eberlin, M. N.; Langley, G. J.; Li, L.; Naito, Y. Definitions of terms relating to mass spectrometry (IUPAC Recommendations 2013). *Pure Appl. Chem.* **2013**, *85*, 1515–1609.
(9) Hendrickson, C. L.; Quinn, J. P.; Kaiser, N. K.; Smith, D. F.; Blakney, G. T.; Chen, T.; Marshall, A. G.; Weisbrod, C. R.; Beu, S. C. 21 Tesla Fourier Transform Ion Cyclotron Resonance Mass Spectrometer: A National Resource for Ultrahigh Resolution Mass Analysis. *J. Am. Soc. Mass Spectrom.* **2015**, *26*, 1626–1632.
(10) Tiquet, M.; La Rocca, R.; Kirnbauer, S.; Zoratto, S.; van Kruining, D.; Quinton, L.; Eppe, G.; Martinez-Martinez, P.; Marchetti-Deschmann, M.; Pauw, E. de; Far, J. FT-ICR Mass Spectrometry Imaging at Extreme Mass Resolving Power Using a Dynamically Harmonized ICR Cell with 1ω or 2ω Detection. *Anal. Chem.* **2022**, *94*, 9316–9326.
(11) Kihara, M.; Matsuo-Tezuka, Y.; Noguchi-Sasaki, M.; Yorozu, K.; Kurasawa, M.; Shimonaka, Y.; Hirata, M. Visualization of 57Fe-Labeled Heme Isotopic Fine Structure and Localization of Regions of Erythroblast Maturation in Mouse Spleen by MALDI FTICR-MS Imaging. *J. Am. Soc. Mass Spectrom.* **2017**, *28*, 2469–2475.
(12) Denisov, E.; Damoc, E.; Lange, O.; Makarov, A. Orbitrap mass spectrometry with resolving powers above 1,000,000. *Int. J. Mass Spectrom.* **2012**, *325-327*, 80–85.
(13) Denisov, E.; Damoc, E.; Makarov, A. Exploring frontiers of orbitrap performance for long transients. *Int. J. Mass Spectrom.* **2021**, *466*, 116607.
(14) Eliuk, S.; Makarov, A. Evolution of Orbitrap Mass Spectrometry Instrumentation. *Annu. Rev. Anal. Chem.* **2015**, *8*, 61–80.
(15) Perry, R. H.; Cooks, R. G.; Noll, R. J. Orbitrap mass spectrometry: instrumentation, ion motion and applications. *Mass Spetrom. Rev.* **2008**, *27*, 661–699.
(16) Brais, C. J.; Ibañez, J. O.; Schwartz, A. J.; Ray, S. J. Recent advances in instrumental approaches to time-of-flight mass spectrometry. *Mass Spetrom. Rev.* **2021**, *40*, 647–669.
(17) Mamyrin, B. A. Time-of-flight mass spectrometry (concepts, achievements, and prospects). *Int. J. Mass Spectrom.* **2001**, *206*, 251–266.
(18) DeLaney, K.; Phetsanthad, A.; Li, L. Advances in high-resolution MALDI mass spectrometry for neurobiology. *Mass Spetrom. Rev.* **2022**, *41*, 194–214.
(19) Junot, C.; Fenaille, F.; Colsch, B.; Bécher, F. High resolution mass spectrometry based techniques at the crossroads of metabolic pathways. *Mass Spetrom. Rev.* **2014**, *33*, 471–500.
(20) Züllig, T.; Köfeler, H. C. High resolution mass spectrometry in lipidomics. *Mass Spetrom. Rev.* **2021**, *40*, 162–176.
(21) Aimo, L.; Liechti, R.; Hyka-Nouspikel, N.; Niknejad, A.; Gleizes, A.; Götz, L.; Kuznetsov, D.; David, F. P. A.; van der Goot, F. G.; Riezman, H.; Bougueleret, L.; Xenarios, I.; Bridge, A. The SwissLipids knowledgebase for lipid biology. *Bioinformatics* **2015**, *31*, 2860–2866.

(22) Degtyarenko, K.; Matos, P. de; Ennis, M.; Hastings, J.; Zbinden, M.; McNaught, A.; Alcántara, R.; Darsow, M.; Guedj, M.; Ashburner, M. ChEBI: a database and ontology for chemical entities of biological interest. *Nucleic Acids Res.* **2008**, *36*, D344-50.
(23) Sud, M.; Fahy, E.; Cotter, D.; Brown, A.; Dennis, E. A.; Glass, C. K.; Merrill, A. H.; Murphy, R. C.; Raetz, C. R. H.; Russell, D. W.; Subramaniam, S. LMSD: LIPID MAPS structure database. *Nucleic Acids Res.* **2007**, *35*, D527-32.
(24) Wishart, D. S.; Tzur, D.; Knox, C.; Eisner, R.; Guo, A. C.; Young, N.; Cheng, D.; Jewell, K.; Arndt, D.; Sawhney, S.; Fung, C.; Nikolai, L.; Lewis, M.; Coutouly, M.-A.; Forsythe, I.; Tang, P.; Shrivastava, S.; Jeroncic, K.; Stothard, P.; Amegbey, G.; Block, D.; Hau, D. D.; Wagner, J.; Miniaci, J.; Clements, M.; Gebremedhin, M.; Guo, N.; Zhang, Y.; Duggan, G. E.; Macinnis, G. D.; Weljie, A. M.; Dowlatabadi, R.; Bamforth, F.; Clive, D.; Greiner, R.; Li, L.; Marrie, T.; Sykes, B. D.; Vogel, H. J.; Querengesser, L. HMDB: the Human Metabolome Database. *Nucleic Acids Res.* **2007**, *35*, D521-6.
(25) Büller, H. A.; Grand, R. J. Lactose intolerance. *Annu. Rev. Med.* **1990**, *41*, 141–148.
(26) Cooks, R. G. Special feature: Historical. Collision-induced dissociation: Readings and commentary. *J. Mass Spectrom.* **1995**, *30*, 1215–1221.
(27) Mitchell Wells, J.; McLuckey, S. A. *Methods Enzymol.* **2005**, 402, 148-185.
(28) Little, D. P.; Speir, J. P.; Senko, M. W.; O'Connor, P. B.; McLafferty, F. W. Infrared multiphoton dissociation of large multiply charged ions for biomolecule sequencing. *Anal. Chem.* **1994**, *66*, 2809–2815.
(29) Ly, T.; Julian, R. R. Ultraviolet photodissociation: developments towards applications for mass-spectrometry-based proteomics. *Angew. Chem., Int. Ed. Engl.* **2009**, *48*, 7130–7137.
(30) R Julian, R. The Mechanism Behind Top-Down UVPD Experiments: Making Sense of Apparent Contradictions. *J. Am. Soc. Mass Spectrom.* **2017**, *28*, 1823–1826.
(31) Vaniya, A.; Fiehn, O. Using fragmentation trees and mass spectral trees for identifying unknown compounds in metabolomics. *Trends Anal. Chem.* **2015**, *69*, 52–61.
(32) Liebl, H. Ion Microprobe Mass Analyzer. *J. Appl. Phys.* **1967**, *38*, 5277–5283.
(33) Spengler, B.; Hubert, M.; Kaufmann, R. MALDI ion imaging and biological ion imaging with a new scanning UV-laser microprobe. *Proceedings of the 42nd ASMS Conference on Mass Spectrometry and Allied Topics, Chicago, IL, USA, 29 May - 3 June* **1994**, 1041.
(34) Gilmore, I. S.; Heiles, S.; Pieterse, C. L. Metabolic Imaging at the Single-Cell Scale: Recent Advances in Mass Spectrometry Imaging. *Annu. Rev. Anal. Chem.* **2019**, *12*, 201–224.
(35) Goodwin, R. J. A.; Takats, Z.; Bunch, J. A Critical and Concise Review of Mass Spectrometry Applied to Imaging in Drug Discovery. *SLAS Discovery* **2020**, *25*, 963–976.
(36) Römpp, A.; Spengler, B. Mass spectrometry imaging with high resolution in mass and space. *Histochem. Cell Biol.* **2013**, *139*, 759–783.
(37) Spengler, B. Mass spectrometry imaging of biomolecular information. *Anal. Chem.* **2015**, *87*, 64–82.
(38) Kompauer, M.; Heiles, S.; Spengler, B. Atmospheric pressure MALDI mass spectrometry imaging of tissues and cells at 1.4-µm lateral resolution. *Nat. Methods* **2017**, *14*, 90–96.
(39) Leonelli, S.; Ankeny, R. A. What makes a model organism? *Endeavour* **2013**, *37*, 209–212.
(40) Javaeed, A.; Qamar, S.; Ali, S.; Mustafa, M. A. T.; Nusrat, A.; Ghauri, S. K. Histological Stains in the Past, Present, and Future. *Cureus* **2021**, *13*, e18486.
(41) Buchwalow, I. B.; Böcker, W. *Immunohistochemistry: Basics and Methods*; Springer: Berlin, Heidelberg, **2010**, ISBN 978-3-642-04609-4.
(42) Chu, P. *Modern Immunohistochemistry*; Cambridge University Press: Cambridge, **2014**, ISBN 978-1-10704-015-1.

(43) Deisseroth, K.; Feng, G.; Majewska, A. K.; Miesenböck, G.; Ting, A.; Schnitzer, M. J. Next-generation optical technologies for illuminating genetically targeted brain circuits. *J. Neurosci.* **2006**, *26*, 10380–10386.
(44) Feng, G.; Mellor, R. H.; Bernstein, M.; Keller-Peck, C.; Nguyen, Q. T.; Wallace, M.; Nerbonne, J. M.; Lichtman, J. W.; Sanes, J. R. Imaging Neuronal Subsets in Transgenic Mice Expressing Multiple Spectral Variants of GFP. *Neuron* **2000**, *28*, 41–51.
(45) Young, P.; Feng, G. Labeling neurons in vivo for morphological and functional studies. *Curr. Opin. Neurobiol.* **2004**, *14*, 642–646.
(46) Wyllie, S. G.; Amos, B. A.; Tökés, L. Electron impact induced fragmentation of cholesterol and related C-5 unsaturated steroids. *J. Org. Chem.* **1977**, *42*, 725–732.
(47) Yamashita, M.; Fenn, J. B. Electrospray ion source. Another variation on the free-jet theme. *J. Phys. Chem.* **1984**, *88*, 4451–4459.
(48) Rayleigh, J. W. S. On the equilibrium of liquid conducting masses charged with electricity. *London, Edinburgh, and Dublin Phil. Mag. J. Sci.* **1882**, *14*, 184–186.
(49) Iribarne, J. V. On the evaporation of small ions from charged droplets. *J. Chem. Phys.* **1976**, *64*, 2287.
(50) Thomson, B. A.; Iribarne, J. V. Field induced ion evaporation from liquid surfaces at atmospheric pressure. *J. Chem. Phys.* **1979**, *71*, 4451–4463.
(51) Dole, M.; Mack, L. L.; Hines, R. L.; Mobley, R. C.; Ferguson, L. D.; Alice, M. B. Molecular Beams of Macroions. *J. Chem. Phys.* **1968**, *49*, 2240–2249.
(52) Wilm, M. S.; Mann, M. Electrospray and Taylor-Cone theory, Dole's beam of macromolecules at last? *Int. J. Mass Spectrom. Ion Processes* **1994**, *136*, 167–180.
(53) Dong, M. New HPLC, MS, and CDS Products Introduced in 2021–2022: A Brief Review. *LCGC North Am.* **2022**, *40*, 165–173.
(54) Games, D. E. High-performance liquid chromatography/mass spectrometry (HPLC/MS). *Adv. Chromatogr.* **1983**, *21*, 1–39.
(55) Badu-Tawiah, A. K.; Eberlin, L. S.; Ouyang, Z.; Cooks, R. G. Chemical aspects of the extractive methods of ambient ionization mass spectrometry. *Annu. Rev. Phys. Chem.* **2013**, *64*, 481–505.
(56) Takáts, Z.; Wiseman, J. M.; Gologan, B.; Cooks, R. G. Mass spectrometry sampling under ambient conditions with desorption electrospray ionization. *Science* **2004**, *306*, 471–473.
(57) Tillner, J.; Wu, V.; Jones, E. A.; Pringle, S. D.; Karancsi, T.; Dannhorn, A.; Veselkov, K.; McKenzie, J. S.; Takats, Z. Faster, More Reproducible DESI-MS for Biological Tissue Imaging. *J. Am. Soc. Mass Spectrom.* **2017**, *28*, 2090–2098.
(58) Takáts, Z.; Wiseman, J. M.; Cooks, R. G. Ambient mass spectrometry using desorption electrospray ionization (DESI): instrumentation, mechanisms and applications in forensics, chemistry, and biology. *J. Mass Spectrom.* **2005**, *40*, 1261–1275.
(59) Girod, M.; Moyano, E.; Campbell, D. I.; Cooks, R. G. Accelerated bimolecular reactions in microdroplets studied by desorption electrospray ionization mass spectrometry. *Chem. Sci.* **2011**, *2*, 501–510.
(60) Wu, C.; Ifa, D. R.; Manicke, N. E.; Cooks, R. G. Rapid, direct analysis of cholesterol by charge labeling in reactive desorption electrospray ionization. *Anal. Chem.* **2009**, *81*, 7618–7624.
(61) Johnson, D. W.; Brink, H. J. ten; Jakobs, C. A rapid screening procedure for cholesterol and dehydrocholesterol by electrospray ionization tandem mass spectrometry. *J. Lipid Res.* **2001**, *42*, 1699–1705.
(62) Wu, C.; Dill, A. L.; Eberlin, L. S.; Cooks, R. G.; Ifa, D. R. Mass spectrometry imaging under ambient conditions. *Mass Spetrom. Rev.* **2013**, *32*, 218–243.
(63) Laskin, J.; Heath, B. S.; Roach, P. J.; Cazares, L.; Semmes, O. J. Tissue imaging using nanospray desorption electrospray ionization mass spectrometry. *Anal. Chem.* **2012**, *84*, 141–148.

(64) Yin, R.; Burnum-Johnson, K. E.; Sun, X.; Dey, S. K.; Laskin, J. High spatial resolution imaging of biological tissues using nanospray desorption electrospray ionization mass spectrometry. *Nat. Protoc.* **2019**, *14*, 3445–3470.
(65) Baker, T. C.; Han, J.; Borchers, C. H. Recent advancements in matrix-assisted laser desorption/ionization mass spectrometry imaging. *Curr. Opin. Biotechnol.* **2017**, *43*, 62–69.
(66) Fuchs, B.; Süss, R.; Schiller, J. An update of MALDI-TOF mass spectrometry in lipid research. *Prog. Lipid Res.* **2010**, *49*, 450–475.
(67) Greco, V.; Piras, C.; Pieroni, L.; Ronci, M.; Putignani, L.; Roncada, P.; Urbani, A. Applications of MALDI-TOF mass spectrometry in clinical proteomics. *Expert Rev. Proteomics* **2018**, *15*, 683–696.
(68) Israr, M. Z.; Bernieh, D.; Salzano, A.; Cassambai, S.; Yazaki, Y.; Suzuki, T. Matrix-assisted laser desorption ionisation (MALDI) mass spectrometry (MS): basics and clinical applications. *Clin. Chem. Lab. Med.* **2020**, *58*, 883–896.
(69) Karas, M.; Bachmann, D.; Bahr, U.; Hillenkamp, F. Matrix-assisted ultraviolet laser desorption of non-volatile compounds. *Int. J. Mass Spectrom. Ion Processes* **1987**, *78*, 53–68.
(70) Honig, R. E.; Woolston, J. R. Laser-induced emission of electrons, ions and neutral atoms from solid surfaces. *Appl. Phys. Lett.* **1963**, *2*, 138–139.
(71) Kaufmann, R.; Wiesner, P. Laser microprobe mass analysis (LAMMA) in particle analysis. *Proceedings of the Particle Analysis Session of the 13th Annual Conference of the Microbeam Analysis Society*, Ann Arbor, Michigan, **1978**, 199-223.
(72) Posthumus, M. A.; Kistemaker, P. G.; Meuzelaar, H. L. C.; Noever de Brauw, M. C. ten. Laser desorption-mass spectrometry of polar nonvolatile bio-organic molecules. *Anal. Chem.* **1978**, *50*, 985–991.
(73) Karas, M.; Hillenkamp, F. Laser desorption ionization of proteins with molecular masses exceeding 10,000 daltons. *Anal. Chem.* **1988**, *60*, 2299–2301.
(74) Addie, R. D.; Balluff, B.; Bovée, J. V. M. G.; Morreau, H.; McDonnell, L. A. Current State and Future Challenges of Mass Spectrometry Imaging for Clinical Research. *Anal. Chem.* **2015**, *87*, 6426–6433.
(75) Zenobi, R.; Knochenmuss, R. Ion formation in MALDI mass spectrometry. *Mass Spectrom. Rev.* **1998**, *17*, 337–366.
(76) Knochenmuss, R. Ion formation mechanisms in UV-MALDI. *Analyst* **2006**, *131*, 966–986.
(77) Calvano, C. D.; Monopoli, A.; Cataldi, T. R. I.; Palmisano, F. MALDI matrices for low molecular weight compounds: an endless story? *Anal. Bioanal. Chem.* **2018**, *410*, 4015–4038.
(78) Horneffer, V.; Dreisewerd, K.; Lüdemann, H.-C.; Hillenkamp, F.; Läge, M.; Strupat, K. Is the incorporation of analytes into matrix crystals a prerequisite for matrix-assisted laser desorption/ionization mass spectrometry? A study of five positional isomers of dihydroxybenzoic acid. *Int. J. Mass Spectrom.* **1999**, *185-187*, 859–870.
(79) Robinson, K. N.; Steven, R. T.; Bunch, J. Matrix Optical Absorption in UV-MALDI MS. *J. Am. Soc. Mass Spectrom.* **2018**, *29*, 501–511.
(80) Smirnov, I. P.; Zhu, X.; Taylor, T.; Huang, Y.; Ross, P.; Papayanopoulos, I. A.; Martin, S. A.; Pappin, D. J. Suppression of alpha-cyano-4-hydroxycinnamic acid matrix clusters and reduction of chemical noise in MALDI-TOF mass spectrometry. *Anal. Chem.* **2004**, *76*, 2958–2965.
(81) Soltwisch, J.; Jaskolla, T. W.; Hillenkamp, F.; Karas, M.; Dreisewerd, K. Ion yields in UV-MALDI mass spectrometry as a function of excitation laser wavelength and optical and physico-chemical properties of classical and halogen-substituted MALDI matrixes. *Anal. Chem.* **2012**, *84*, 6567–6576.
(82) O'Rourke, M. B.; Djordjevic, S. P.; Padula, M. P. The quest for improved reproducibility in MALDI mass spectrometry. *Mass Spetrom. Rev.* **2018**, *37*, 217–228.
(83) Nishikaze, T.; Okumura, H.; Jinmei, H.; Amano, J. Correlation between Sweet Spots of Glycopeptides and Polymorphism of the Matrix Crystal in MALDI Samples. *Mass Spectrom.* **2012**, *1*, A0006.

(84) Goodwin, R. J. A. Sample preparation for mass spectrometry imaging: small mistakes can lead to big consequences. *J. Proteomics* **2012**, *75*, 4893–4911.
(85) Hermann, J.; Noels, H.; Theelen, W.; Lellig, M.; Orth-Alampour, S.; Boor, P.; Jankowski, V.; Jankowski, J. Sample preparation of formalin-fixed paraffin-embedded tissue sections for MALDI-mass spectrometry imaging. *Anal. Bioanal. Chem.* **2020**, *412*, 1263–1275.
(86) Veličković, D.; Zhang, G.; Bezbradica, D.; Bhattacharjee, A.; Paša-Tolić, L.; Sharma, K.; Alexandrov, T.; Anderton, C. R. Response Surface Methodology As a New Approach for Finding Optimal MALDI Matrix Spraying Parameters for Mass Spectrometry Imaging. *J. Am. Soc. Mass Spectrom.* **2020**, *31*, 508–516.
(87) Caldwell, R. L.; Caprioli, R. M. Tissue profiling by mass spectrometry: a review of methodology and applications. *Mol. Cell. Proteomics* **2005**, *4*, 394–401.
(88) Hankin, J. A.; Barkley, R. M.; Murphy, R. C. Sublimation as a method of matrix application for mass spectrometric imaging. *J. Am. Soc. Mass Spectrom.* **2007**, *18*, 1646–1652.
(89) Li, H.; Wu, R.; Hu, Q.; Chen, X.; Dominic Chan, T.-W. A Matrix Sublimation Device with an Integrated Solvent Nebulizer for MALDI-MSI. *J. Am. Soc. Mass Spectrom.* **2022**, *33*, 11–16.
(90) van Nuffel, S.; Elie, N.; Yang, E.; Nouet, J.; Touboul, D.; Chaurand, P.; Brunelle, A. Insights into the MALDI Process after Matrix Deposition by Sublimation Using 3D ToF-SIMS Imaging. *Anal. Chem.* **2018**, *90*, 1907–1914.
(91) Sunner, J.; Dratz, E.; Chen, Y. C. Graphite surface-assisted laser desorption/ionization time-of-flight mass spectrometry of peptides and proteins from liquid solutions. *Anal. Chem.* **1995**, *67*, 4335–4342.
(92) Tanaka, K.; Waki, H.; Ido, Y.; Akita, S.; Yoshida, Y.; Yoshida, T.; Matsuo, T. Protein and polymer analyses up to m/z 100 000 by laser ionization time-of-flight mass spectrometry. *Rapid Commun. Mass Spectrom.* **1988**, *2*, 151–153.
(93) McLean, J. A.; Stumpo, K. A.; Russell, D. H. Size-selected (2-10 nm) gold nanoparticles for matrix assisted laser desorption ionization of peptides. *J. Am. Chem. Soc.* **2005**, *127*, 5304–5305.
(94) Sekuła, J.; Nizioł, J.; Rode, W.; Ruman, T. Gold nanoparticle-enhanced target (AuNPET) as universal solution for laser desorption/ionization mass spectrometry analysis and imaging of low molecular weight compounds. *Anal. Chim. Acta* **2015**, *875*, 61–72.
(95) Watanabe, T.; Kawasaki, H.; Yonezawa, T.; Arakawa, R. Surface-assisted laser desorption/ionization mass spectrometry (SALDI-MS) of low molecular weight organic compounds and synthetic polymers using zinc oxide (ZnO) nanoparticles. *J. Mass Spectrom.* **2008**, *43*, 1063–1071.
(96) Fincher, J. A.; Dyer, J. E.; Korte, A. R.; Yadavilli, S.; Morris, N. J.; Vertes, A. Matrix-free mass spectrometry imaging of mouse brain tissue sections on silicon nanopost arrays. *J. Comp. Neurol.* **2019**, *527*, 2101–2121.
(97) Fincher, J. A.; Korte, A. R.; Yadavilli, S.; Morris, N. J.; Vertes, A. Multimodal imaging of biological tissues using combined MALDI and NAPA-LDI mass spectrometry for enhanced molecular coverage. *Analyst* **2020**, *145*, 6910–6918.
(98) Walker, B. N.; Stolee, J. A.; Pickel, D. L.; Retterer, S. T.; Vertes, A. Tailored Silicon Nanopost Arrays for Resonant Nanophotonic Ion Production. *J. Phys. Chem. C* **2010**, *114*, 4835–4840.
(99) Lo, C.-Y.; Lin, J.-Y.; Chen, W.-Y.; Chen, C.-T.; Chen, Y.-C. Surface-assisted laser desorption/ionization mass spectrometry on titania nanotube arrays. *J. Am. Soc. Mass Spectrom.* **2008**, *19*, 1014–1020.
(100) Dutkiewicz, E. P.; Su, C.-H.; Lee, H.-J.; Hsu, C.-C.; Yang, Y.-L. Visualizing vinca alkaloids in the petal of Catharanthus roseus using functionalized titanium oxide nanowire substrate for surface-assisted laser desorption/ionization imaging mass spectrometry. *Plant J.* **2021**, *105*, 1123–1133.
(101) Go, E. P.; Apon, J. V.; Luo, G.; Saghatelian, A.; Daniels, R. H.; Sahi, V.; Dubrow, R.; Cravatt, B. F.; Vertes, A.; Siuzdak, G. Desorption/ionization on silicon nanowires. *Anal. Chem.* **2005**, *77*, 1641–1646.
(102) Kuwata, K.; Itou, K.; Kotani, M.; Ohmura, T.; Naito, Y. DIUTHAME enables matrix-free mass spectrometry imaging of frozen tissue sections. *Rapid Commun. Mass Spectrom.* **2020**, *34*, e8729.

(103) Naito, Y.; Kotani, M.; Ohmura, T. A novel laser desorption/ionization method using through hole porous alumina membranes. *Rapid Commun. Mass Spectrom.* **2018**, *32*, 1851–1858.
(104) Hansen, R. L.; Dueñas, M. E.; Lee, Y. J. Sputter-Coated Metal Screening for Small Molecule Analysis and High-Spatial Resolution Imaging in Laser Desorption Ionization Mass Spectrometry. *J. Am. Soc. Mass Spectrom.* **2019**, *30*, 299–308.
(105) Chen, Y.; Vertes, A. Adjustable fragmentation in laser desorption/ionization from laser-induced silicon microcolumn arrays. *Anal. Chem.* **2006**, *78*, 5835–5844.
(106) Chen, Y.-C.; Shiea, J.; Sunner, J. Thin-layer chromatography–mass spectrometry using activated carbon, surface-assisted laser desorption/ionization. *J. Chromatogr. A* **1998**, *826*, 77–86.
(107) Ng, K.-M.; Chau, S.-L.; Tang, H.-W.; Wei, X.-G.; Lau, K.-C.; Ye, F.; Ng, A. M.-C. Ion-Desorption Efficiency and Internal-Energy Transfer in Surface-Assisted Laser Desorption/Ionization: More Implication(s) for the Thermal-Driven and Phase-Transition-Driven Desorption Process. *J. Phys. Chem. C* **2015**, *119*, 23708–23720.
(108) Picca, R. A.; Calvano, C. D.; Cioffi, N.; Palmisano, F. Mechanisms of Nanophase-Induced Desorption in LDI-MS. A Short Review. *Nanomaterials* **2017**, *7, 75*.
(109) Müller, W. H.; Verdin, A.; Pauw, E. de; Malherbe, C.; Eppe, G. Surface-assisted laser desorption/ionization mass spectrometry imaging: A review. *Mass Spetrom. Rev.* **2022**, *41*, 373–420.
(110) Lai, S. K.-M.; Tang, H.-W.; Lau, K.-C.; Ng, K.-M. Nanosecond UV Laser Ablation of Gold Nanoparticles: Enhancement of Ion Desorption by Thermal-Driven Desorption, Vaporization, or Phase Explosion. *J. Phys. Chem. C* **2016**, *120*, 20368–20377.
(111) Stolee, J. A.; Walker, B. N.; Zorba, V.; Russo, R. E.; Vertes, A. Laser-nanostructure interactions for ion production. *Phys. Chem. Chem. Phys.* **2012**, *14*, 8453–8471.
(112) Song, K.; Cheng, Q. Desorption and ionization mechanisms and signal enhancement in surface assisted laser desorption ionization mass spectrometry (SALDI-MS). *Appl. Spectrosc. Rev.* **2020**, *55*, 220–242.
(113) Kamat, P. V.; Flumiani, M.; Hartland, G. V. Picosecond Dynamics of Silver Nanoclusters. Photoejection of Electrons and Fragmentation. *J. Phys. Chem. B* **1998**, *102*, 3123–3128.
(114) Cheng, Y.-H.; Ng, K.-M. The Hidden Heroes: Holes in Charge-Driven Desorption Mass Spectrometry. *Anal. Chem.* **2020**, *92*, 5645–5649.
(115) Zeng, X.; Mao, X. L.; Greif, R.; Russo, R. E. Experimental investigation of ablation efficiency and plasma expansion during femtosecond and nanosecond laser ablation of silicon. *Appl. Phys. A: Mater. Sci. Process.* **2005**, *80*, 237–241.
(116) Knochenmuss, R.; Zhigilei, L. V. What determines MALDI ion yields? A molecular dynamics study of ion loss mechanisms. *Anal. Bioanal. Chem.* **2012**, *402*, 2511–2519.
(117) Mowry, C. D.; Johnston, M. V. Simultaneous detection of ions and neutrals produced by matrix-assisted laser desorption. *Rapid Commun. Mass Spectrom.* **1993**, *7*, 569–575.
(118) Ding, X.; Liu, K.; Shi, Z. Laser desorption/ablation postionization mass spectrometry: Recent progress in bioanalytical applications. *Mass Spetrom. Rev.* **2021**, *40*, 566–605.
(119) Nemes, P.; Vertes, A. Laser ablation electrospray ionization for atmospheric pressure, in vivo, and imaging mass spectrometry. *Anal. Chem.* **2007**, *79*, 8098–8106.
(120) Taylor, M. J.; Liyu, A.; Vertes, A.; Anderton, C. R. Ambient Single-Cell Analysis and Native Tissue Imaging Using Laser-Ablation Electrospray Ionization Mass Spectrometry with Increased Spatial Resolution. *J. Am. Soc. Mass Spectrom.* **2021**, *32*, 2490–2494.
(121) Soltwisch, J.; Kettling, H.; Vens-Cappell, S.; Wiegelmann, M.; Müthing, J.; Dreisewerd, K. Mass spectrometry imaging with laser-induced postionization. *Science* **2015**, *348*, 211–215.
(122) Potthoff, A.; Dreisewerd, K.; Soltwisch, J. Detailed Characterization of the Postionization Efficiencies in MALDI-2 as a Function of Relevant Input Parameters. *J. Am. Soc. Mass Spectrom.* **2020**, *31*, 1844–1853.

(123) Niehaus, M.; Soltwisch, J.; Belov, M. E.; Dreisewerd, K. Transmission-mode MALDI-2 mass spectrometry imaging of cells and tissues at subcellular resolution. *Nat. Methods* **2019**, *16*, 925–931.
(124) Spivey, E. C.; McMillen, J. C.; Ryan, D. J.; Spraggins, J. M.; Caprioli, R. M. Combining MALDI-2 and transmission geometry laser optics to achieve high sensitivity for ultra-high spatial resolution surface analysis. *J. Mass Spectrom.* **2019**, *54*, 366–370.
(125) Guenther, S.; Koestler, M.; Schulz, O.; Spengler, B. Laser spot size and laser power dependence of ion formation in high resolution MALDI imaging. *Int. J. Mass Spectrom.* **2010**, *294*, 7–15.
(126) Qiao, H.; Spicer, V.; Ens, W. The effect of laser profile, fluence, and spot size on sensitivity in orthogonal-injection matrix-assisted laser desorption/ionization time-of-flight mass spectrometry. *Rapid Commun. Mass Spectrom.* **2008**, *22*, 2779–2790.
(127) Steven, R. T.; Race, A. M.; Bunch, J. Probing the Relationship Between Detected Ion Intensity, Laser Fluence, and Beam Profile in Thin Film and Tissue in MALDI MSI. *J. Am. Soc. Mass Spectrom.* **2016**, *27*, 1419–1428.
(128) Ali, A.; Davidson, S.; Fraenkel, E.; Gilmore, I.; Hankemeier, T.; Kirwan, J. A.; Lane, A. N.; Lanekoff, I.; Larion, M.; McCall, L.-I.; Murphy, M.; Sweedler, J. V.; Zhu, C. Single cell metabolism: current and future trends. *Metabolomics* **2022**, *18*, 77.
(129) Altschuler, S. J.; Wu, L. F. Cellular heterogeneity: do differences make a difference? *Cell* **2010**, *141*, 559–563.
(130) Borland, L. M.; Kottegoda, S.; Phillips, K. S.; Allbritton, N. L. Chemical analysis of single cells. *Annu. Rev. Anal. Chem.* **2008**, *1*, 191–227.
(131) Guo, S.; Zhang, C.; Le, A. The limitless applications of single-cell metabolomics. *Curr. Opin. Biotechnol.* **2021**, *71*, 115–122.
(132) Lanni, E. J.; Rubakhin, S. S.; Sweedler, J. V. Mass spectrometry imaging and profiling of single cells. *J. Proteomics* **2012**, *75*, 5036–5051.
(133) Zenobi, R. Single-cell metabolomics: analytical and biological perspectives. *Science* **2013**, *342*, 1243259.
(134) Prasun, P.; Pradhan, M.; Agarwal, S. One gene, many phenotypes. *J. Postgrad. Med.* **2007**, *53*, 257–261.
(135) Cunningham, C.; Dunne, A.; Lopez-Rodriguez, A. B. Astrocytes: Heterogeneous and Dynamic Phenotypes in Neurodegeneration and Innate Immunity. *Neuroscientist* **2019**, *25*, 455–474.
(136) Fatoba, O.; Itokazu, T.; Yamashita, T. Microglia as therapeutic target in central nervous system disorders. *J. Pharmacol. Sci.* **2020**, *144*, 102–118.
(137) Marusyk, A.; Almendro, V.; Polyak, K. Intra-tumour heterogeneity: a looking glass for cancer? *Nat. Rev. Cancer* **2012**, *12*, 323–334.
(138) Yuan, Y.; Wu, C.; Ling, E.-A. Heterogeneity of Microglia Phenotypes: Developmental, Functional and Some Therapeutic Considerations. *Curr. Pharm. Des.* **2019**, *25*, 2375–2393.
(139) Tosh, D.; Slack, J. M. W. How cells change their phenotype. *Nat. Rev. Mol. Cell Biol.* **2002**, *3*, 187–194.
(140) Dusny, C.; Grünberger, A. Microfluidic single-cell analysis in biotechnology: from monitoring towards understanding. *Curr. Opin. Biotechnol.* **2020**, *63*, 26–33.
(141) Luo, T.; Fan, L.; Zhu, R.; Sun, D. Microfluidic Single-Cell Manipulation and Analysis: Methods and Applications. *Micromachines* **2019**, *10*.
(142) Di Carlo, D.; Wu, L. Y.; Lee, L. P. Dynamic single cell culture array. *Lab Chip* **2006**, *6*, 1445–1449.
(143) Gebreyesus, S. T.; Siyal, A. A.; Kitata, R. B.; Chen, E. S.-W.; Enkhbayar, B.; Angata, T.; Lin, K.-I.; Chen, Y.-J.; Tu, H.-L. Streamlined single-cell proteomics by an integrated microfluidic chip and data-independent acquisition mass spectrometry. *Nat. Commun.* **2022**, *13*, 37.
(144) Collins, D. J.; Neild, A.; deMello, A.; Liu, A.-Q.; Ai, Y. The Poisson distribution and beyond: methods for microfluidic droplet production and single cell encapsulation. *Lab Chip* **2015**, *15*, 3439–3459.

(145) Saha-Shah, A.; Weber, A. E.; Karty, J. A.; Ray, S. J.; Hieftje, G. M.; Baker, L. A. Nanopipettes: probes for local sample analysis. *Chem. Sci.* **2015**, *6*, 3334–3341.
(146) Yin, R.; Prabhakaran, V.; Laskin, J. Quantitative Extraction and Mass Spectrometry Analysis at a Single-Cell Level. *Anal. Chem.* **2018**, *90*, 7937–7945.
(147) Yu, R.-J.; Ying, Y.-L.; Gao, R.; Long, Y.-T. Confined Nanopipette Sensing: From Single Molecules, Single Nanoparticles, to Single Cells. *Angew. Chem., Int. Ed. Engl.* **2019**, *58*, 3706–3714.
(148) Comi, T. J.; Neumann, E. K.; Do, T. D.; Sweedler, J. V. microMS: A Python Platform for Image-Guided Mass Spectrometry Profiling. *J. Am. Soc. Mass Spectrom.* **2017**, *28*, 1919–1928.
(149) Neumann, E. K.; Comi, T. J.; Rubakhin, S. S.; Sweedler, J. V. Lipid Heterogeneity between Astrocytes and Neurons Revealed by Single-Cell MALDI-MS Combined with Immunocytochemical Classification. *Angew. Chem., Int. Ed. Engl.* **2019**, *58*, 5910–5914.
(150) Rappez, L.; Stadler, M.; Triana, S.; Gathungu, R. M.; Ovchinnikova, K.; Phapale, P.; Heikenwalder, M.; Alexandrov, T. SpaceM reveals metabolic states of single cells. *Nat. Methods* **2021**, *18*, 799–805.
(151) Capolupo, L.; Khven, I.; Lederer, A. R.; Mazzeo, L.; Glousker, G.; Ho, S.; Russo, F.; Montoya, J. P.; Bhandari, D. R.; Bowman, A. P.; Ellis, S. R.; Guiet, R.; Burri, O.; Detzner, J.; Muthing, J.; Homicsko, K.; Kuonen, F.; Gilliet, M.; Spengler, B.; Heeren, R. M. A.; Dotto, G. P.; La Manno, G.; D'Angelo, G. Sphingolipids control dermal fibroblast heterogeneity. *Science* **2022**, *376*, eabh1623.
(152) Ginzberg, M. B.; Kafri, R.; Kirschner, M. On being the right (cell) size. *Science* **2015**, *348*, 1245075.
(153) Dueñas, M. E.; Essner, J. J.; Lee, Y. J. 3D MALDI Mass Spectrometry Imaging of a Single Cell: Spatial Mapping of Lipids in the Embryonic Development of Zebrafish. *Sci. Rep.* **2017**, *7*, 14946.
(154) Jernås, M.; Palming, J.; Sjöholm, K.; Jennische, E.; Svensson, P.-A.; Gabrielsson, B. G.; Levin, M.; Sjögren, A.; Rudemo, M.; Lystig, T. C.; Carlsson, B.; Carlsson, L. M. S.; Lönn, M. Separation of human adipocytes by size: hypertrophic fat cells display distinct gene expression. *FASEB J.* **2006**, *20*, 1540–1542.
(155) Qin, Z.; Balimunkwe, R. M.; Quan, T. Age-related reduction of dermal fibroblast size upregulates multiple matrix metalloproteinases as observed in aged human skin in vivo. *Br. J. Dermatol.* **2017**, *177*, 1337–1348.
(156) Ho, M.-C. D.; Ring, N.; Amaral, K.; Doshi, U.; Li, A. P. Human Enterocytes as an In Vitro Model for the Evaluation of Intestinal Drug Metabolism: Characterization of Drug-Metabolizing Enzyme Activities of Cryopreserved Human Enterocytes from Twenty-Four Donors. *Drug Metab. Dispos.* **2017**, *45*, 686–691.
(157) Marchetti, P.; Bugliani, M.; Tata, V. de; Suleiman, M.; Marselli, L. Pancreatic Beta Cell Identity in Humans and the Role of Type 2 Diabetes. *Front. Cell Dev. Biol.* **2017**, *5*, 55.
(158) Diez-Silva, M.; Dao, M.; Han, J.; Lim, C.-T.; Suresh, S. Shape and Biomechanical Characteristics of Human Red Blood Cells in Health and Disease. *MRS Bull.* **2010**, *35*, 382–388.
(159) Abbe, E. Beiträge zur Theorie des Mikroskops und der mikroskopischen Wahrnehmung. *Arch. Mikrosk. Anat.* **1873**, *9*, 413–468.
(160) Rayleigh, J. W. S. On the theory of optical images, with special reference to the microscope. *London, Edinburgh, and Dublin Phil. Mag. J. Sci.* **1896**, *42*, 167–195.
(161) Berkenkamp, S.; Kirpekar, F.; Hillenkamp, F. Infrared MALDI mass spectrometry of large nucleic acids. *Science* **1998**, *281*, 260–262.
(162) Li, Y.; Shrestha, B.; Vertes, A. Atmospheric pressure molecular imaging by infrared MALDI mass spectrometry. *Anal. Chem.* **2007**, *79*, 523–532.
(163) Joignant, A. N.; Bai, H.; Manni, J. G.; Muddiman, D. C. Improved Spatial Resolution of Infrared Matrix-Assisted Laser Desorption Electrospray Ionization (IR-MALDESI) Mass Spectrometry Imaging (MSI) Using a Reflective Objective. *Rapid Commun. Mass Spectrom.* **2022**, *36*, e9392.

(164) Feenstra, A. D.; Dueñas, M. E.; Lee, Y. J. Five Micron High Resolution MALDI Mass Spectrometry Imaging with Simple, Interchangeable, Multi-Resolution Optical System. *J. Am. Soc. Mass Spectrom.* **2017**, *28*, 434–442.
(165) Aksouh, F.; Chaurand, P.; Deprun, C.; Della-Negra, S.; Le Beyec, Y.; Hoyes, J.; Pinho, R. R. Influence of the laser beam direction on the molecular ion ejection angle in matrix-assisted laser desorption/ionization. *Rapid Commun. Mass Spectrom.* **1995**, *9*, 515–518.
(166) Galicia, M. C.; Vertes, A.; Callahan, J. H. Atmospheric pressure matrix-assisted laser desorption/ionization in transmission geometry. *Anal. Chem.* **2002**, *74*, 1891–1895.
(167) Chaurand, P.; Schriver, K. E.; Caprioli, R. M. Instrument design and characterization for high resolution MALDI-MS imaging of tissue sections. *J. Mass Spectrom.* **2007**, *42*, 476–489.
(168) Spengler, B.; Hubert, M. Scanning microprobe matrix-assisted laser desorption ionization (SMALDI) mass spectrometry: Instrumentation for sub-micrometer resolved LDI and MALDI surface analysis. *J. Am. Soc. Mass Spectrom.* **2002**, *13*, 735–748.
(169) Bien, T.; Bessler, S.; Dreisewerd, K.; Soltwisch, J. Transmission-Mode MALDI Mass Spectrometry Imaging of Single Cells: Optimizing Sample Preparation Protocols. *Anal. Chem.* **2021**, *93*, 4513–4520.
(170) Shimma, S.; Sugiura, Y. Effective Sample Preparations in Imaging Mass Spectrometry. *Mass Spectrom.* **2014**, *3*, S0029.
(171) Yang, J.; Caprioli, R. M. Matrix sublimation/recrystallization for imaging proteins by mass spectrometry at high spatial resolution. *Anal. Chem.* **2011**, *83*, 5728–5734.
(172) Kadesch, P.; Quack, T.; Gerbig, S.; Grevelding, C. G.; Spengler, B. Tissue- and sex-specific lipidomic analysis of Schistosoma mansoni using high-resolution atmospheric pressure scanning microprobe matrix-assisted laser desorption/ionization mass spectrometry imaging. *PLoS Neglected Trop. Dis.* **2020**, *14*, e0008145.
(173) Müller, M. A.; Bhandari, D. R.; Spengler, B. Matrix-Free High-Resolution Atmospheric-Pressure SALDI Mass Spectrometry Imaging of Biological Samples Using Nanostructured DIUTHAME Membranes. *Metabolites* **2021**, *11*.
(174) Fouquet, T. N. J.; Cody, R. B.; Nakamura, S.; Sato, H.; Ohmura, T.; Kotani, M.; Naito, Y. Rapid Fingerprinting of High-Molecular-Weight Polymers by Laser Desorption-Ionization Using Through-Hole Alumina Membrane High-Resolution Mass Spectrometry. *Anal. Chem.* **2020**, *92*, 7399–7403.
(175) Naito, Y.; Kotani, M.; Ohmura, T. Feasibility of Acetylcholinesterase Reaction Assay Monitoring in DIUTHAME-MS. *J. Am. Soc. Mass Spectrom.* **2020**, *31*, 2154–2160.
(176) Enomoto, H.; Kotani, M.; Ohmura, T. Novel Blotting Method for Mass Spectrometry Imaging of Metabolites in Strawberry Fruit by Desorption/Ionization Using Through Hole Alumina Membrane. *Foods* **2020**, *9*.
(177) Hasan, M. M.; Eto, F.; Mamun, M. A.; Sato, S.; Islam, A.; Waliullah, A. S. M.; Chi, D. H.; Takahashi, Y.; Kahyo, T.; Naito, Y.; Kotani, M.; Ohmura, T.; Setou, M. Desorption ionization using through-hole alumina membrane offers higher reproducibility than 2,5-dihydroxybenzoic acid, a widely used matrix in Fourier transform ion cyclotron resonance mass spectrometry imaging analysis. *Rapid Commun. Mass Spectrom.* **2021**, *35*, e9076.
(178) Fincher, J. A.; Korte, A. R.; Dyer, J. E.; Yadavilli, S.; Morris, N. J.; Jones, D. R.; Shanmugam, V. K.; Pirlo, R. K.; Vertes, A. Mass spectrometry imaging of triglycerides in biological tissues by laser desorption ionization from silicon nanopost arrays. *J. Mass Spectrom.* **2020**, *55*, e4443.
(179) Dufresne, M.; Thomas, A.; Breault-Turcot, J.; Masson, J.-F.; Chaurand, P. Silver-assisted laser desorption ionization for high spatial resolution imaging mass spectrometry of olefins from thin tissue sections. *Anal. Chem.* **2013**, *85*, 3318–3324.
(180) Huang, H.; Ouyang, D.; Lin, Z.-A. Recent Advances in Surface-Assisted Laser Desorption/Ionization Mass Spectrometry and Its Imaging for Small Molecules. *J. Anal. Test.* **2022**, *6*, 217–234.

(181) Müller, W. H.; Pauw, E. de; Far, J.; Malherbe, C.; Eppe, G. Imaging lipids in biological samples with surface-assisted laser desorption/ionization mass spectrometry: A concise review of the last decade. *Prog. Lipid Res.* **2021**, *83*, 101114.
(182) Müller, M. A.; Kompauer, M.; Strupat, K.; Heiles, S.; Spengler, B. Implementation of a High-Repetition-Rate Laser in an AP-SMALDI MSI System for Enhanced Measurement Performance. *J. Am. Soc. Mass Spectrom.* **2021**, *32*, 465–472.
(183) Müller, W. H.; McCann, A.; Arias, A. A.; Malherbe, C.; Quinton, L.; Pauw, E. de; Eppe, G. Imaging Metabolites in Agar-Based Bacterial Co-Cultures with Minimal Sample Preparation using a DIUTHAME Membrane in Surface-Assisted Laser Desorption/Ionization Mass Spectrometry. *ChemistrySelect* **2022**, *7*, e20220073.
(184) Schiebler, T. H.; Korf, H.-W. *Anatomie, 10th Ed.*; Steinkopff: Heidelberg, **2007**, ISBN-10: 3798517703.
(185) Bhandari, D. R.; Wang, Q.; Friedt, W.; Spengler, B.; Gottwald, S.; Römpp, A. High resolution mass spectrometry imaging of plant tissues: towards a plant metabolite atlas. *Analyst* **2015**, *140*, 7696–7709.
(186) Moss, G. P.; Smith, P. A. S.; Tavernier, D. Glossary of class names of organic compounds and reactivity intermediates based on structure (IUPAC Recommendations 1995). *Pure Appl. Chem.* **1995**, *67*, 1307–1375.
(187) Liebisch, G.; Fahy, E.; Aoki, J.; Dennis, E. A.; Durand, T.; Ejsing, C. S.; Fedorova, M.; Feussner, I.; Griffiths, W. J.; Köfeler, H.; Merrill, A. H.; Murphy, R. C.; O'Donnell, V. B.; Oskolkova, O.; Subramaniam, S.; Wakelam, M. J. O.; Spener, F. Update on LIPID MAPS classification, nomenclature, and shorthand notation for MS-derived lipid structures. *J. Lipid Res.* **2020**, *61*, 1539–1555.
(188) Liebisch, G.; Vizcaíno, J. A.; Köfeler, H.; Trötzmüller, M.; Griffiths, W. J.; Schmitz, G.; Spener, F.; Wakelam, M. J. O. Shorthand notation for lipid structures derived from mass spectrometry. *J. Lipid Res.* **2013**, *54*, 1523–1530.
(189) Divecha, N.; Irvine, R. F. Phospholipid signaling. *Cell* **1995**, *80*, 269–278.
(190) Hannun, Y. A.; Obeid, L. M. Principles of bioactive lipid signalling: lessons from sphingolipids. *Nat. Rev. Mol. Cell Biol.* **2008**, *9*, 139–150.
(191) Hu, T.; Zhang, J.-L. Mass-spectrometry-based lipidomics. *J. Sep. Sci.* **2018**, *41*, 351–372.
(192) Tian, H.; Sparvero, L. J.; Anthonymuthu, T. S.; Sun, W.-Y.; Amoscato, A. A.; He, R.-R.; Bayır, H.; Kagan, V. E.; Winograd, N. Successive High-Resolution (H2O)n-GCIB and C60-SIMS Imaging Integrates Multi-Omics in Different Cell Types in Breast Cancer Tissue. *Anal. Chem.* **2021**, *93*, 8143–8151.
(193) Leventis, P. A.; Grinstein, S. The distribution and function of phosphatidylserine in cellular membranes. *Annu. Rev. Biophys.* **2010**, *39*, 407–427.
(194) Segawa, K.; Nagata, S. An Apoptotic 'Eat Me' Signal: Phosphatidylserine Exposure. *Trends Cell Biol.* **2015**, *25*, 639–650.
(195) Lawson, L. J.; Perry, V. H.; Dri, P.; Gordon, S. Heterogeneity in the distribution and morphology of microglia in the normal adult mouse brain. *Neuroscience* **1990**, *39*, 151–170.
(196) Loving, B. A.; Bruce, K. D. Lipid and Lipoprotein Metabolism in Microglia. *Front. Physiol.* **2020**, *11*, 393.
(197) Block, M. L.; Hong, J.-S. Microglia and inflammation-mediated neurodegeneration: multiple triggers with a common mechanism. *Prog. Neurobiol.* **2005**, *76*, 77–98.
(198) Butovsky, O.; Weiner, H. L. Microglial signatures and their role in health and disease. *Nat. Rev. Neurosci.* **2018**, *19*, 622–635.
(199) Cartier, N.; Lewis, C.-A.; Zhang, R.; Rossi, F. M. V. The role of microglia in human disease: therapeutic tool or target? *Acta Neuropathol.* **2014**, *128*, 363–380.
(200) Colonna, M.; Butovsky, O. Microglia Function in the Central Nervous System During Health and Neurodegeneration. *Annu. Rev. Immunol.* **2017**, *35*, 441–468.

(201) Efthymiou, A. G.; Goate, A. M. Late onset Alzheimer's disease genetics implicates microglial pathways in disease risk. *Mol. Neurodegener.* **2017**, *12*, 43.
(202) Lenz, K. M.; McCarthy, M. M. A starring role for microglia in brain sex differences. *Neuroscientist* **2015**, *21*, 306–321.
(203) Li, Q.; Barres, B. A. Microglia and macrophages in brain homeostasis and disease. *Nat. Rev. Immunol.* **2018**, *18*, 225–242.
(204) Salter, M. W.; Beggs, S. Sublime microglia: expanding roles for the guardians of the CNS. *Cell* **2014**, *158*, 15–24.
(205) Chhor, V.; Le Charpentier, T.; Lebon, S.; Oré, M.-V.; Celador, I. L.; Josserand, J.; Degos, V.; Jacotot, E.; Hagberg, H.; Sävman, K.; Mallard, C.; Gressens, P.; Fleiss, B. Characterization of phenotype markers and neuronotoxic potential of polarised primary microglia in vitro. *Brain, Behav., Immun.* **2013**, *32*, 70–85.
(206) Lauro, C.; Limatola, C. Metabolic Reprograming of Microglia in the Regulation of the Innate Inflammatory Response. *Front. Immunol.* **2020**, *11*, 493.
(207) Masuda, T.; Sankowski, R.; Staszewski, O.; Prinz, M. Microglia Heterogeneity in the Single-Cell Era. *Cell Rep.* **2020**, *30*, 1271–1281.
(208) Orihuela, R.; McPherson, C. A.; Harry, G. J. Microglial M1/M2 polarization and metabolic states. *Br. J. Pharmacol.* **2016**, *173*, 649–665.
(209) Boche, D.; Perry, V. H.; Nicoll, J. A. R. Review: activation patterns of microglia and their identification in the human brain. *Neuropathol. Appl. Neurobiol.* **2013**, *39*, 3–18.
(210) Churchward, M. A.; Tchir, D. R.; Todd, K. G. Microglial Function during Glucose Deprivation: Inflammatory and Neuropsychiatric Implications. *Mol. Neurobiol.* **2018**, *55*, 1477–1487.
(211) Walther, T. C.; Farese, R. V. Lipid droplets and cellular lipid metabolism. *Annu. Rev. Biochem.* **2012**, *81*, 687–714.
(212) Cabodevilla, A. G.; Sánchez-Caballero, L.; Nintou, E.; Boiadjieva, V. G.; Picatoste, F.; Gubern, A.; Claro, E. Cell Survival during Complete Nutrient Deprivation Depends on Lipid Droplet-fueled β-Oxidation of Fatty Acids. *J. Biol. Chem.* **2013**, *288*, 27777–27788.
(213) Marschallinger, J.; Iram, T.; Zardeneta, M.; Lee, S. E.; Lehallier, B.; Haney, M. S.; Pluvinage, J. V.; Mathur, V.; Hahn, O.; Morgens, D. W.; Kim, J.; Tevini, J.; Felder, T. K.; Wolinski, H.; Bertozzi, C. R.; Bassik, M. C.; Aigner, L.; Wyss-Coray, T. Lipid-droplet-accumulating microglia represent a dysfunctional and proinflammatory state in the aging brain. *Nat. Neurosci.* **2020**, *23*, 194–208.
(214) Qiu, B.; Simon, M. C. BODIPY 493/503 Staining of Neutral Lipid Droplets for Microscopy and Quantification by Flow Cytometry. *Bio-Protoc.* **2016**, *6*, 17, e1912.
(215) Blank, M.; Enzlein, T.; Hopf, C. LPS-induced lipid alterations in microglia revealed by MALDI mass spectrometry-based cell fingerprinting in neuroinflammation studies. *Sci. Rep.* **2022**, *12*, 2908.
(216) Chausse, B.; Kakimoto, P. A.; Caldeira-da-Silva, C. C.; Chaves-Filho, A. B.; Yoshinaga, M. Y.; da Silva, R. P.; Miyamoto, S.; Kowaltowski, A. J. Distinct metabolic patterns during microglial remodeling by oleate and palmitate. *Biosci. Rep.* **2019**, *39*, 4, BSR20190072.
(217) Fitzner, D.; Bader, J. M.; Penkert, H.; Bergner, C. G.; Su, M.; Weil, M.-T.; Surma, M. A.; Mann, M.; Klose, C.; Simons, M. Cell-Type- and Brain-Region-Resolved Mouse Brain Lipidome. *Cell Rep.* **2020**, *32*, 108132.
(218) Bien, T.; Koerfer, K.; Schwenzfeier, J.; Dreisewerd, K.; Soltwisch, J. Mass spectrometry imaging to explore molecular heterogeneity in cell culture. *Proc. Natl. Acad. Sci. USA* **2022**, *119*, e2114365119.
(219) Feingold, K. R.; Shigenaga, J. K.; Kazemi, M. R.; McDonald, C. M.; Patzek, S. M.; Cross, A. S.; Moser, A.; Grunfeld, C. Mechanisms of triglyceride accumulation in activated macrophages. *J. Leukocyte Biol.* **2012**, *92*, 829–839.
(220) Funk, J. L.; Feingold, K. R.; Moser, A. H.; Grunfeld, C. Lipopolysaccharide stimulation of RAW 264.7 macrophages induces lipid accumulation and foam cell formation. *Atherosclerosis* **1993**, *98*, 67–82.

(221) Borbély, A. A. A two process model of sleep regulation. *Hum. Neurobiol.* **1982**, *1*, 195–204.
(222) Kempf, A.; Song, S. M.; Talbot, C. B.; Miesenböck, G. A potassium channel β-subunit couples mitochondrial electron transport to sleep. *Nature* **2019**, *568*, 230–234.
(223) Pimentel, D.; Donlea, J. M.; Talbot, C. B.; Song, S. M.; Thurston, A. J. F.; Miesenböck, G. Operation of a homeostatic sleep switch. *Nature* **2016**, *536*, 333–337.
(224) Donlea, J. M.; Pimentel, D.; Miesenböck, G. Neuronal machinery of sleep homeostasis in Drosophila. *Neuron* **2014**, *81*, 860–872.
(225) Donlea, J. M.; Thimgan, M. S.; Suzuki, Y.; Gottschalk, L.; Shaw, P. J. Inducing sleep by remote control facilitates memory consolidation in Drosophila. *Science* **2011**, *332*, 1571–1576.
(226) Kadesch, P.; Quack, T.; Gerbig, S.; Grevelding, C. G.; Spengler, B. Lipid Topography in Schistosoma mansoni Cryosections, Revealed by Microembedding and High-Resolution Atmospheric-Pressure Matrix-Assisted Laser Desorption/Ionization (MALDI) Mass Spectrometry Imaging. *Anal. Chem.* **2019**, *91*, 4520–4528.
(227) Hill, V. M.; O'Connor, R. M.; Sissoko, G. B.; Irobunda, I. S.; Leong, S.; Canman, J. C.; Stavropoulos, N.; Shirasu-Hiza, M. A bidirectional relationship between sleep and oxidative stress in Drosophila. *PLoS Biol.* **2018**, *16*, e2005206.
(228) Kooijman, E. E.; Chupin, V.; Fuller, N. L.; Kozlov, M. M.; Kruijff, B. de; Burger, K. N. J.; Rand, P. R. Spontaneous curvature of phosphatidic acid and lysophosphatidic acid. *Biochemistry* **2005**, *44*, 2097–2102.
(229) Kooijman, E. E.; Chupin, V.; Kruijff, B. de; Burger, K. N. J. Modulation of membrane curvature by phosphatidic acid and lysophosphatidic acid. *Traffic* **2003**, *4*, 162–174.
(230) Saha, B.; Borovskii, G.; Panda, S. K. Alternative oxidase and plant stress tolerance. *Plant Signaling Behav.* **2016**, *11*, e1256530.

Chapter II – DIUTHAME

Matrix-Free High-Resolution Atmospheric-Pressure SALDI Mass Spectrometry Imaging of Biological Samples Using Nanostructured DIUTHAME Membranes

metabolites

MDPI

Article

Matrix-Free High-Resolution Atmospheric-Pressure SALDI Mass Spectrometry Imaging of Biological Samples Using Nanostructured DIUTHAME Membranes

Max A. Müller, Dhaka R. Bhandari and Bernhard Spengler *

Institute of Inorganic and Analytical Chemistry, Justus Liebig University, 35392 Giessen, Germany; max.a.mueller@anorg.chemie.uni-giessen.de (M.A.M.); dhaka.r.bhandari@transmit.de (D.R.B.)
* Correspondence: bernhard.spengler@anorg.chemie.uni-giessen.de

Abstract: Applications of mass spectrometry imaging (MSI), especially matrix-assisted laser desorption/ionization (MALDI) in the life sciences are becoming increasingly focused on single cell analysis. With the latest instrumental developments, pixel sizes in the micrometer range can be obtained, leading to challenges in matrix application, where imperfections or inhomogeneities in the matrix layer can lead to misinterpretation of MS images. Thereby, the application of premanufactured, homogeneous ionization-assisting devices is a promising approach. Tissue sections were investigated using a matrix-free imaging technique (Desorption Ionization Using Through-Hole Alumina Membrane, DIUTHAME) based on premanufactured nanostructured membranes to be deposited on top of a tissue section, in comparison to the spray-coating of an organic matrix in a MALDI MSI approach. Atmospheric pressure MALDI MSI ion sources were coupled to orbital trapping mass spectrometers. MS signals obtained by the different ionization techniques were annotated using accurate-mass-based database research. Compared to MALDI MSI, DIUTHAME MS images captivated with higher signal homogeneities, higher contrast and reduced background signals, while signal intensities were reduced by about one order of magnitude, independent of analyte class. DIUTHAME membranes, being applicable only on tissue sections thicker than 50 µm, were successfully used for mammal, insect and plant tissue with a high lateral resolution down to 5 µm.

Keywords: mass spectrometry imaging; DIUTHAME; MALDI; SALDI; LDI; atmospheric pressure; high resolution

Citation: Müller, M.A.; Bhandari, D.R.; Spengler, B. Matrix-Free High-Resolution Atmospheric-Pressure SALDI Mass Spectrometry Imaging of Biological Samples Using Nanostructured DIUTHAME Membranes. *Metabolites* **2021**, *11*, 624. https://doi.org/10.3390/metabo11090624

Academic Editors: Peter Oefner and Zoltan Takats

Received: 15 July 2021
Accepted: 1 September 2021
Published: 15 September 2021

1. Introduction

Mass spectrometry imaging (MSI) has proven to be a valuable and versatile tool for spatially resolved chemical analysis of surfaces [1–3]. Particularly, matrix-assisted laser desorption/ionization (MALDI) MSI [4,5] under atmospheric pressure (AP) is known for its ease of sample handling, morphological authenticity and the possible combination with highly accurate, highly mass resolving Fourier-transformation-based mass spectrometers [3,6,7]. A key characteristic is the achievable lateral resolution for a detailed examination of biological structures.

With recent advancements in AP-MALDI MSI, it became possible to achieve subcellular lateral resolution down to 1.4 µm per pixel and simultaneously accomplish a mass resolution of >100,000 in less than one second using orbital trapping mass spectrometers [8]. The achievable lateral resolution is predominantly defined by the focal diameter of the laser beam on the sample surface and thereby the sample area from which analytes are desorbed and ionized. For small laser spot sizes, a high ion yield is essential, predominantly influenced by the chosen matrix material [8]. Application of the matrix, however, becomes more and more challenging with increasing lateral resolution, since inhomogeneities in the matrix layer and matrix crystals larger than the expected lateral resolution almost always have a negative impact [9]. Optimizing protocols for matrix application to achieve

homogeneous surface coverage and small matrix crystals while retaining high ion yields is crucial but time-consuming, as it relies on many parameters [10]. Introducing new matrices for high lateral resolution is therefore challenging.

A variety of organic acids and bases can be used as matrices in positive- or negative-ion mode, respectively [11,12]. Most importantly, a matrix should have optimal spectral absorption characteristics at the wavelength of the employed laser, be inert to oxidation and non-reactive with the sample, and should generate minimal background signal, a major challenge especially for low molecular mass analytes [2,10,13].

In contrast, desorption electrospray ionization (DESI) MSI is a widely used matrix-free imaging technique that uses solvents instead of laser radiation as a sample probe and thereby is reducing sample preparation time and effort compared to MALDI MSI [14,15]. Despite its versatility and ease of operation, DESI MSI cannot yet reach the high lateral resolution commonly achieved by MALDI MSI [16].

To obtain high lateral resolution without the need for a matrix to absorb the specific laser wavelength, it has been demonstrated that nanostructured surfaces can also assist in desorption and ionization (surface assisted laser desorption/ionization, SALDI) [17,18]. Despite the mechanism being not well defined, a variety of materials such as carbon [17,19,20], silicon [21,22], metals [23–26], or organic surface coatings [27] with different nanostructures have also been tested for imaging applications. Among such materials, DIUTHAME (Desorption Ionization Using Through-Hole Alumina Membrane) is showing promising features for an easy and reproducible sample preparation [28–31]. DIUTHAME consists of a 5 µm thin alumina membrane, nanostructured with 200 nm through holes. As it is manufactured in an automated process before any contact with samples, inhomogeneities are not as common as for MALDI sample preparations, where a matrix is applied directly onto the tissue. This makes DIUTHAME a promising candidate for high lateral resolution MSI [28]. It has been shown that analytes such as lipids, peptides, or small proteins can be desorbed and ionized by laser irradiation of DIUTHAME samples of standard solutions in time-of-flight (TOF) mass spectrometers under vacuum conditions with high reproducibility [28]. Under these conditions, Kuwata et al. were able to perform MSI experiments with a lateral resolution of 50 µm and a mass resolution of up to 50,000 from mouse brain tissue [30].

Here, we investigated the performance and characteristics of DIUTHAME for a higher lateral resolution of 5 µm at high mass resolution (up to 240,000) using atmospheric-pressure MSI of biomolecules from native tissues from different organisms. We evaluated the performance regarding the detectable analyte classes, sensitivity, achievable lateral resolution, and image quality in comparison to MALDI and LDI experiments.

2. Results

2.1. Desorption and Ionization Using DIUTHAME

To characterize the ionization behavior of DIUTHAME, mouse brain tissue sections were analyzed and compared to the results obtained from MALDI and LDI MSI experiments. For comparison, the ablation spot size was kept constant at 5 µm diameter, corresponding to an ablation spot size of ≈20 μm^2 (Figure S1); therefore, laser energy had to be optimized for each ionization method individually. While LDI without any tissue pretreatment had to be performed with a very high laser fluence (≈500 kJ/m^2) to yield significant signal intensities and visible ablation spots on the sample, DIUTHAME and MALDI could be performed with much lower laser pulse energies of ≈1300 J/m^2 and ≈2500 J/m^2, respectively.

Blank spectra of pure matrix or DIUTHAME membranes without applying analytes differed significantly (Figure 1). Since the MALDI matrix itself is desorbed and ionized, it produces characteristic signals in the mass spectrum. From blank (Figure 1) or incompletely attached DIUTHAME foils (Figures S2 and S3), no significant signals were observed, an observation typical for SALDI MS [18,32]. Compound identification and quantification

take advantage of background-free spectra in (partly) overlapping areas of spectra, even under high mass resolution conditions.

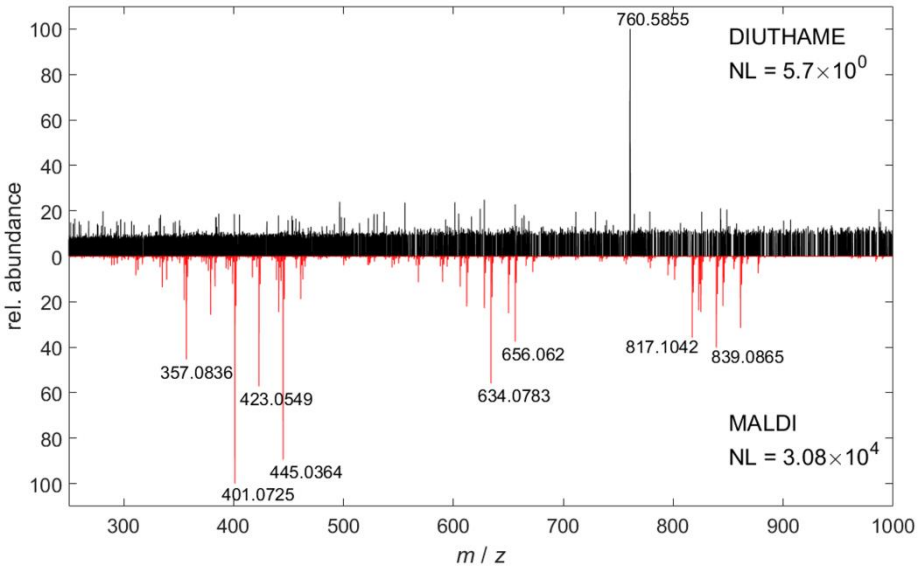

Figure 1. Comparison of 100 summed-up mass spectra in positive-ion mode acquired by DIUTHAME MS (black) from blank DIUTHAME membrane and MALDI MS (red) from pure CHCA matrix on glass, respectively.

The results show that the DIUTHAME foils during desorption and ionization work similarly efficient as the matrix in the MALDI process, leading to comparable laser energy settings, very different from LDI conditions from solid sample supports. Since the DIUTHAME material itself is not ionized, it is clear, on the other hand, that the mechanisms of energy uptake, analyte extraction, desorption and ionization are very different in nano-structured sample supports compared to matrix microcrystals.

2.2. Signal Quality and Quantity for DIUTHAME

In our MSI setup, desorption and ionization of analytes from biological tissue was possible with DIUTHAME in positive-ion mode. On mouse-brain tissue, signal intensities (normalized level NL) of the DIUTHAME measurements were lower by one order of magnitude compared to MALDI with the CHCA matrix (Figure 2).

As a result, fewer analytes reached the limit of detection, and in MSI experiments, a smaller number of images were generated from untargeted measurements. In total, 1135 versus 127 signals in the phospholipid mass range (m/z 600–1000, decimal place 0.4–0.7) were present in at least 5% of all pixels for MALDI and DIUTHAME, respectively (Figure 3A), from a mouse brain cerebellum. Similar behavior was observed for the striatum ventral region of the mouse brain. A database search resulted in phospholipid annotations for 559 (49%) and 77 (61%) of these signals for MALDI and DIUTHAME, respectively (Tables S1 and S2). The comparison revealed, that the annotations of DIUTHAME signals were mostly a subset of those found with MALDI (Figure 3B). Of all distinct phospholipid annotations, 497 (86%) were found exclusively in MALDI measurements, 15 (3%) exclusively in DIUTHAME measurements, and 62 (11%) were shared between the two.

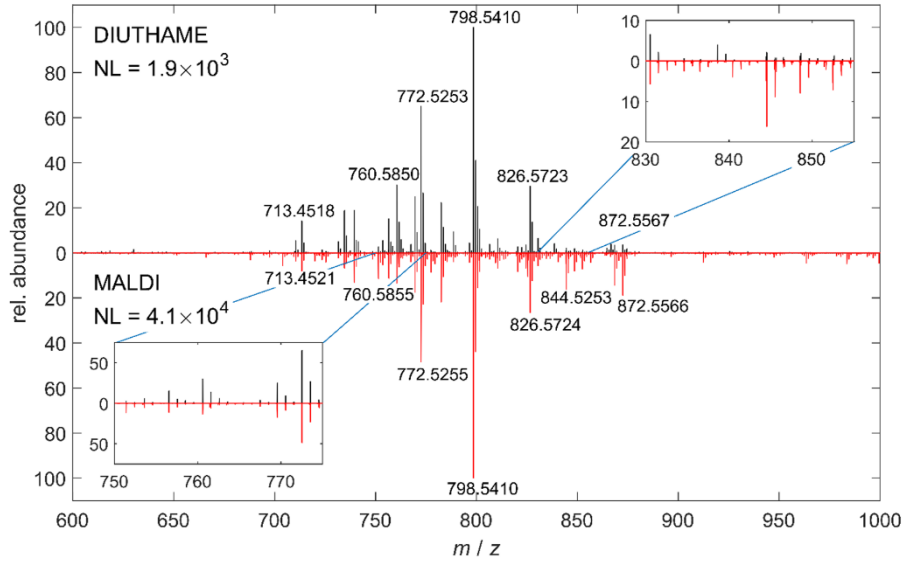

Figure 2. Comparison of 100 summed mass spectra acquired by DIUTHAME (black) and MALDI (red) MSI, respectively, from adjacent mouse brain tissue sections in the cerebellum region in positive-ion mode.

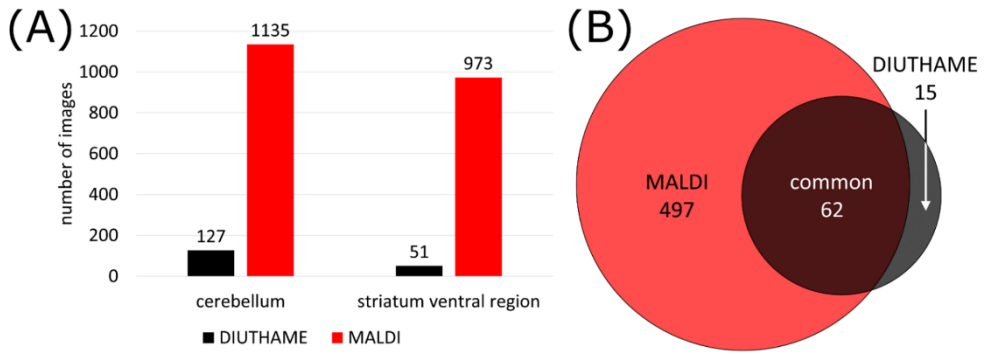

Figure 3. (**A**) Number of images available from mouse brain tissue with DIUTHAME and MALDI MSI, respectively. Only phospholipid signals in a mass range between m/z 600–1000 with a pixel coverage of >5% were considered, matrix signals were excluded. (**B**) Venn diagram of annotated phospholipids from signals detected with a MALDI or DIUTHAME MSI measurement.

Protonated signals were more prominent in the mass spectra when ionizing via DIUTHAME (30% of number of signals) compared to MALDI (25% of number of signals), whereas MALDI mass spectra had a higher percentage of $[M + K]^+$ adducts (41%) compared to DIUTHAME (35%). The fraction of $[M + Na]^+$ species was comparable between DIUTHAME (35%) and MALDI (34%) (Figure S4).

Lipid classes detected in positive-ion mode were comparable for DIUTHAME and MALDI, as both techniques preferably ionize phosphatidylcholine and phosphatidylethanolamine species (Figure S4). The percentage of phosphatidylserine,

phosphatidylglycerol, or phosphatic acid lipid species were comparable. None of the lipid classes were observed exclusively by one of the ionization techniques. Nevertheless, MALDI showed more of those lipid signals, which do not fit into standard categories, making the signals obtained by MALDI more diverse compared to DIUTHAME. This is most probably due to the overall lower signal intensities in DIUTHAME measurements, where hard-to-ionize and lower-abundant analyte species remain below the limit of detection.

In negative-ion mode, however, DIUTHAME did not generate any ion signal of analytes from mouse brain or mouse kidney tissue. The resulting mass spectra were comparable to blank DIUTHAME instead (Figure S5). In the literature, mostly positive-ion spectra were shown for DIUTHAME MSI experiments [28,30]. Negative-ion-mode experiments were only shown for time-of-flight (TOF) instruments with significantly reduced signal intensities compared to positive-ion mode [31]. The reason for this behavior might be that DIUTHAME, in contrast to MALDI matrices, does not introduce charge carriers into the rather acidic biological system but is only providing an active surface. In combination with the overall lower signal intensities from DIUTHAME compared to MALDI in our MSI setup, the number of ions generated from DIUTHAME in negative-ion mode appears to be below the detection threshold. In the lower mass range (m/z 250–500), DIUTHAME did not produce reliable signals from mouse kidney tissue (Figure S6), making it not suitable for the analysis of small metabolites. Additionally, no other biological species except lipids (such as peptides or protein fragments) could be detected (based on mass-defect calculations) from mouse brain or mouse kidney tissue.

2.3. MSI of Biological Tissues Using DIUTHAME, MALDI and LDI

As DIUTHAME is capable of retaining the spatial information of analytes within the tissue section, it can be used in MS imaging experiments. To characterize its performance, mouse brain tissue sections were analyzed using DIUTHAME, MALDI and LDI MS imaging techniques in comparison. MALDI was selected as a widely used method for MS imaging. The LDI experiments were performed to check if the DIUTHAME nanostructures improve the ionization yield over direct laser desorption/ionization from solid surfaces.

Comparable mouse brain regions in the cerebellum and the striatum ventral region from consecutive sections were investigated by DIUTHAME, MALDI and LDI for an area of 300 × 250 pixels with a pixel size and laser spot diameter of 5 µm. While the employed experimental setup is capable of focusing the laser to a smaller spot size [8], 5 µm was the smallest laser spot diameter yielding sufficient ion signal intensities for DIUTHAME imaging experiments due to its lower ionization efficiency as mentioned earlier. Signals in the phospholipid mass range of m/z 600–1000 were recorded in positive-ion mode.

The experiments clearly show, that LDI from biological tissue without the assistance of matrix or an ionizing nanostructured membrane results in very low signal intensities, poor image quality and many blank pixels below the detection threshold, clearly indicating that DIUTHAME similar to MALDI is playing an important role in the desorption and ionization process. Further, a high noise level in mass spectra and images, resulting from strong background ionization at high laser power, was observed, making it tough to find signals representing anatomical structures in the tissue investigated (Figure S7).

When comparing DIUTHAME and MALDI, it became apparent that both techniques generate similar image quality. Displaying the same m/z signals, both measurement techniques clearly show white matter, grey matter and a granular layer in the cerebellum region. Purkinje cells were spotted by the absence of the surrounding signals between the granular layer and white matter. In MALDI MSI, distinct marker signals were detected representing the Purkinje cells (Figure S8), while these were not found in DIUTHAME MSI. In the striatum ventral region, both ionization techniques precisely outlined the small spots of interlaced lateral globus pallidus. The adjacent microscopic images corresponded well, even though for the DIUTHAME application the optical images were generated with the membrane attached, leading to a rather poor quality at high magnification.

DIUTHAME, compared to MALDI, showed a slight increase in sharpness and contrast of the MS images, as well as an increased signal homogeneity in uniform tissue regions (Figure 4). This is due to the fact that sample preparation is becoming a crucial step in MALDI at small pixel sizes. Slight inhomogeneities during the application of the matrix become more apparent, and washout effects result in a minor image blur due to solvent use. Solvent-free matrix application methods such as dry sublimation usually result in a lower ion yield due to lacking co-crystallization of matrix and analyte [33]. Performing MSI with DIUTHAME also does not involve solvent use, but the moisture of the tissue itself is usually sufficient to induce analyte uptake into the membrane while preventing washout effects. More m/z images generated from the DIUTHAME MSI are shown in Figure S9.

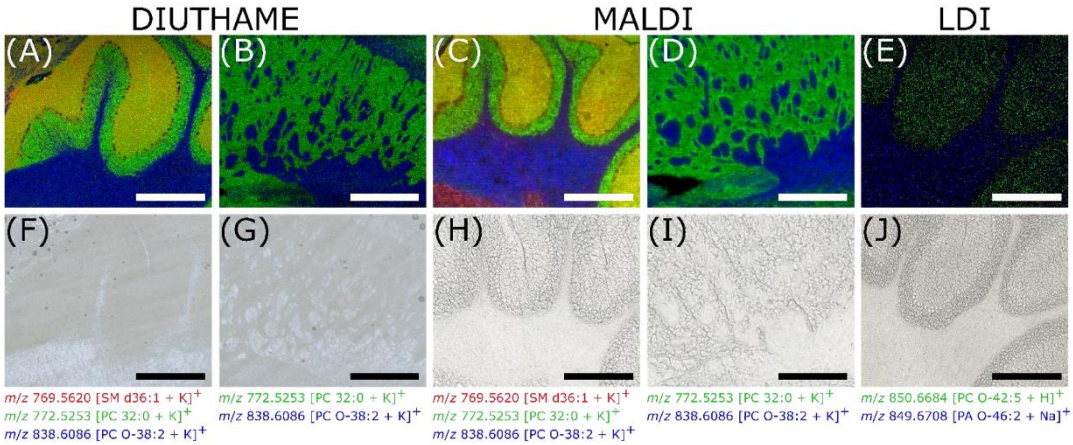

Figure 4. Comparison of DIUTHAME, MALDI and LDI MSI from adjacent mouse brain tissue sections, acquired with a pixel size of 5 µm, an image size of 300 × 250 pixels, a laser focal diameter of 5 µm, in a mass range of m/z 600–1000. (**A**), (**F**), DIUTHAME MS image of mouse brain cerebellum with corresponding microscopic image. (**B**,**G**), DIUTHAME MS image of mouse brain striatum ventral region with corresponding microscopic image. (**C**,**H**), MALDI MS image of mouse brain cerebellum with corresponding microscopic image. (**D**,**I**), MALDI MS image of mouse brain striatum ventral region with corresponding microscopic image. (**E**,**J**), LDI MS image of mouse brain cerebellum with corresponding microscopic image. Thickness of tissue sections (**A**,**B**), 50 µm, (**C**–**E**), 20 µm. Scale bars: 500 µm.

2.4. DIUTHAME MSI of Tissue Sections from Various Organisms

In addition to mouse brain tissue sections, DIUTHAME MSI was tested on a variety of sample types from different biological species and tissues such as a mouse kidney section (276 × 161 pixels, 30 µm pixel size, full-pixel mode [34]), a germinating rapeseed section (297 × 245 pixels, 20 µm pixel size) and a *Spodoptera littoralis* (caterpillar) section (300 × 250 pixels, 20 µm pixel size).

In the mouse kidney section, distinct signals of phospholipids were detected in the medulla and cortex as well as a signal deriving from the heme group in blood vessels (Figure 5A). In germinating rapeseed sections, various triglycerides [35] were detected in the endosperm as previously described for MALDI MSI [36], as well as growth-state-dependent phospholipids in the root tip (Figure 5B). However, comparing experiments from the same study, only half of the signals detected with MALDI, including phospholipids, diglycerides, triglycerides, or spermidine conjugates, were annotated in the seed sections of the rapeseed plant using DIUTHAME [36]. This is due to the overall lower intensities and sensitivity of DIUTHAME compared to MALDI, resulting in more analytes remaining below the limit of detection. For the *Spodoptera littoralis* larva section, phospholipid signals

nicely outline the caterpillar's body and the gut wall (Figure 5C). Additional MS images are shown in Figures S10–S12.

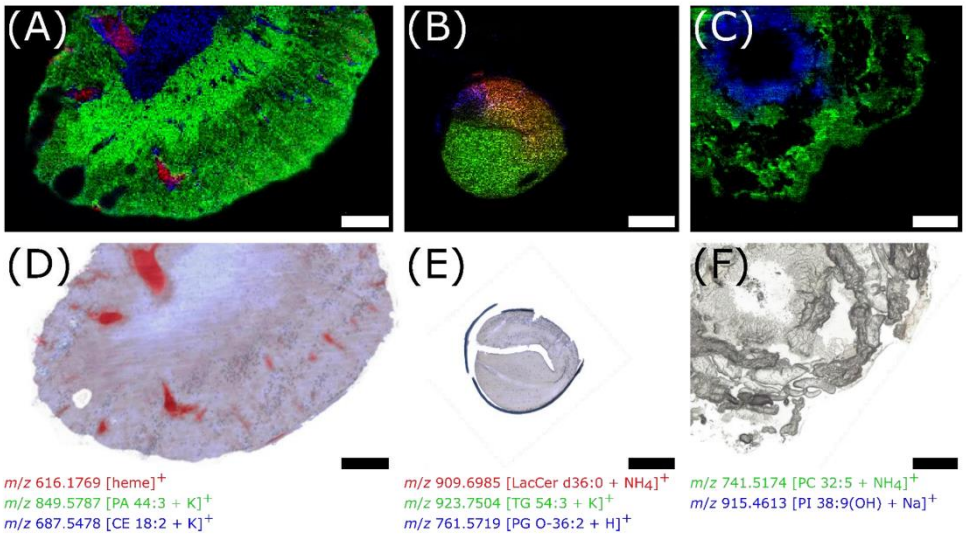

Figure 5. MS images of tissue sections from various organisms using DIUTHAME as the ionization assisting membrane (**A**–**C**) and corresponding microscopic images of the same (**E**) or an adjacent section (**D**,**F**). (**A**), 50 µm thick mouse kidney section, pixel size 30 µm, 276 × 161 pixels, m/z 400–1600. (**B**), 80 µm thick germinating rapeseed section, pixel size 20 µm, 297 × 245 pixels, m/z 500–1500. (**C**), 150 µm thick *Spodoptera littoralis* caterpillar section, pixel size 20 µm, 300 × 250 pixels, m/z 250–1000. Scale bars: 1 mm.

The experiments show the capability of DIUTHAME to produce highly resolved MS images with high contrast, expressing detailed anatomical features, independent of the biological origin of the sample. The technique has been found to be feasible on soft (mouse brain, mouse kidney), hard (rapeseed), or fragile (larva) tissue sections from mammals, plants, or insects. As shown for the mouse brain earlier, not only can tissue regions be clearly distinguished, but also fine structures and gradients can be determined as shown for the rapeseed section. Therefore, the signal intensity of m/z 909.6985 was plotted against its spatial position along the growth direction of the rapeseed (Figure S13), indicating a gradual enrichment of the compound towards the root tip.

3. Discussion

While SALDI MSI applications are an emerging field of research, little is known about the underlying mechanisms of desorption and ionization [37]. For SALDI, employing a variety of mostly inorganic materials with different shapes, sizes, or nanostructures, elucidation of these mechanisms is an ongoing matter of debate. In general, it is presumed that thermal and non-thermal processes are involved in the process of desorption and ionization [18,32,38].

One of the main roles of the nanomaterial is to absorb the energy of the ionization laser, resulting in a rapid and spatially confined increase in surface temperature, assisting analytes to desorb from the surface. In the case of DIUTHAME, this is amplified by the fact that analytes are confined into nanocapillaries. Nevertheless, recent studies using thermometer molecules revealed that not only thermal desorption is the main aspect in SALDI, but that also phase transitions play a major role. It was observed that signal intensities of analytes sharply increased when the energy input by the laser reached a phase transition

threshold [39]. Mechanistic investigations were not the main goal of our study. It was observed, however, that desorption and ionization with DIUTHAME required laser energies high enough to produce visible ablation marks on the membrane (Figures S1 and S14), which supports the idea of nanomaterial destruction and phase transitions being involved in the process. Laser energy thresholds for efficient desorption are a possible obstacle on further improving the lateral resolution of DIUTHAME MSI measurements, since high lateral resolution is usually linked to lower laser energy settings [8].

The process of ionization, being assisted by nanomaterials, is even less understood [37]. Charge carriers have to be either already present in the sample or transferred to the analyte from the nanomaterial, whereas the mechanism of the latter is highly debated. For example, one mechanism involves high-energy electrons, so-called hot electrons, being ejected by the nanomaterial upon laser irradiation and subsequent rapid heating [40]. Analytes can either use these ejected electrons or, even more efficiently, the remaining electron holes [41] in the nanomaterial for ionization in positive- or negative-ion mode, respectively. This charge accumulation in the nanomaterial would also lead to Coulomb explosion of the material [42], producing charged nanomaterial clusters, that should be detectable in the mass spectrometer [37]. Nevertheless, in our experiments with DIUTHAME, no such clusters were detected (Figure 1), presumably speaking against charge carriers to be ejected from the nanomaterial or being transferred to the analyte in significant quantities. Additionally, annotation of signals by accurate mass measurements revealed a high number of normal quasimolecular ions, such as proton, sodium or potassium adducts (Figure S4), that cannot originate from the DIUTHAME material and must have been pre-existing in the sample or produced by photochemical interactions of the laser with the water of the samples [37].

Due to the complexity and variability of nanomaterials, the underlying desorption and ionization mechanism is hard to elucidate. Further, this hinders targeted improvements regarding desorption and ionization efficiency [43], which in the case of DIUTHAME could be helpful to overcome the lower sensitivity compared to MALDI MSI and to potentially enable even higher lateral resolution measurements.

4. Materials and Methods

4.1. MSI Instrumentation

MSI measurements were carried out on an AP-SMALDI5 AF ion source (TransMIT GmbH, Giessen, Germany) coupled to a 'Q Exactive HF' orbital trapping mass spectrometer (Thermo Fisher Scientific GmbH, Bremen, Germany) and alternatively on a home-built ultra-high-resolution AP-MALDI MSI source, coupled to a 'Q Exactive' orbital trapping mass spectrometer (Thermo Fisher Scientific GmbH, Bremen, Germany). Laser fluence was adjusted by controllable dichroic filters. The highest available mass resolution of 240,000 or 140,000 was used for all experiments on the Q Exactive HF or Q Exactive, respectively. A fixed injection time of 500 ms was set on both devices and a high voltage of 4 kV was applied to the samples. Laser energy was adjusted individually for each experiment.

4.2. Sample Preparation

Thin tissue sections from fresh-frozen tissue were prepared using a microcryotome (Microm HM 525, Thermo Fisher Scientific GmbH, Bremen, Germany) at −20 °C. Tissue sections with a thickness of 20 µm were chosen for MALDI and LDI measurements, whereas for experiments with DIUTHAME, tissue sections with a thickness of 50–150 µm were used (Figure 6).

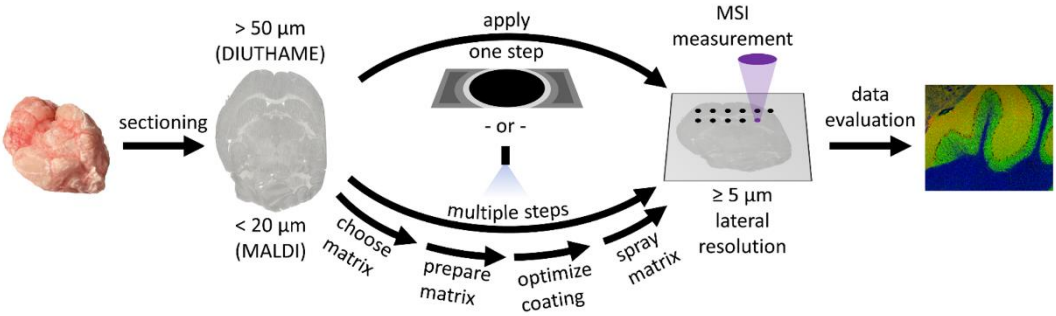

Figure 6. Illustrative overview of the workflow for a DIUTHAME and a MALDI MSI measurement, respectively. The main difference in the workflow is the preparation step between sectioning and MSI measurement.

DIUTHAME-ionizing membranes (Hamamatsu Photonics, Hamamatsu, Japan) have a circular effective area of up to 18 mm in diameter, fixed in a metal frame with a self-adhesive backside (Figure S14). After exposing the adhesive area, the effective area of the membrane has to be placed on top of a frozen tissue section without application of pressure (Figure 6). Due to the low mechanical strength of the 5 µm thin membrane, even weak forces applied can break the membrane and therefore render it useless for further experiments. During thawing of the sample, the membrane attaches itself to the tissue in a process similar to thaw-mounting. As a result of the geometry of the frame-membrane arrangement of the first-generation DIUTHAME units, tissue sections had to be at least 50 µm thick (Figure S2) to ensure a firm and complete attachment of the membrane without causing air bubbles, which would lead to a loss of signal and blind spots in MSI experiments (Figure S3). For dry tissue sections such as germinated seeds from a rapeseed plant, this process was facilitated by applying 2 µL of ethanol on top of the already attached membrane.

For MALDI measurements, matrix was applied using a SMALDIPrep (TransMIT GmbH, Giessen, Germany) pneumatic spraying system. A total of 14 mg of α-Cyano-4-hydroxycinnamic acid (CHCA, Sigma Aldrich, Munich, Germany) were dissolved in 1998 µL of a mixture of 1:1 acetone-water and acidified with 2 µL of pure trifluoroacetic acid (Merck KGaA, Darmstadt, Germany) to produce 2 mL of a solution with a matrix concentration of 7 mg/mL. A volume of 80 µL of the solution was applied to the sample by pneumatic spraying at a flow rate of 10 µL/min (Figure 6).

4.3. Histology

Microscopic images were acquired with a digital microscope (VHX-5000, Keyence GmbH, Neu Isenburg, Germany) before the MSI experiment under epi-illumination for MALDI and LDI samples. Precedent to DIUTHAME experiments, the microscopic images were acquired with transmitted light with the membrane attached, since it has to be applied prior to thawing (Figure S15).

After MALDI MSI experiments, the matrix was removed with ethanol and the tissue was stained with hematoxylin and eosin (Figure S16) following an established protocol (Table S3). Histological staining is not possible after a DIUTHAME experiment since the membrane cannot be removed from the tissue.

4.4. Data Analysis

Mass spectra from mouse brain tissue were recalibrated to m/z 798.5410, which is known to be $[PC\ 34{:}1 + K]^+$. MALDI images were created using Mirion [44] software with a bin width $\Delta(m/z)$ of $\pm$ 0.005, and signal intensities were normalized to total ion charge [34] in each single pixel. Signals were evaluated if they were detected in at least 5% of the pixels of an image. The signal assignment was carried out via a database search

in LIPID MAPS [45] using compiled data from up to 75,000 mass spectra per experiment. Potential lipid groups and ion species were assigned based on the smallest deviations from calculated m/z values and allowing for a maximal mass error of 3 ppm without cross-validating for isotopologues or different ion adducts being present and showing the same lateral distribution. Thereby, annotations remain putative. All data from imaging experiments were uploaded to metaspace [46], a platform for metabolite annotation of MSI data. The results from the platform are publicly available.

5. Conclusions

We demonstrated the applicability of DIUTHAME membranes for MSI at a high lateral resolution of 5 µm pixel size under atmospheric-pressure conditions. Due to DIUTHAME assisting desorption and ionization via a SALDI-like mechanism, background signals are reduced compared to MALDI or LDI experiments. MS images produced with DIUTHAME benefit from a higher signal homogeneity and a higher contrast than those produced by MALDI experiments under otherwise same conditions. Tissue sections for DIUTHAME experiments have to be significantly thicker ($\geq$50 µm) than for MALDI ($\leq$20 µm) for geometrical reasons. Tissue sections from different organisms including mammals, insects and plants were successfully investigated, and various analyte classes such as metabolites ($m/z > 500$), triglycerides, phospholipids, or enzymatic co-factors were detected. However, the ionization efficiency of DIUTHAME is significantly lower than that of MALDI, resulting in signal intensities being reduced by roughly one order of magnitude for DIUTHAME, thus hindering the detection of lowly abundant or hard-to-ionize analytes (e.g., metabolites ($m/z < 500$), drugs, peptides) which are nicely detectable by MALDI MSI. Thereby, DIUTHAME cannot always be used to improve MSI at higher lateral resolution yet, but might be improved in the future in terms of thinner tissue sections and higher ionization efficiencies.

Supplementary Materials: The following are available online at https://www.mdpi.com/article/10.3390/metabo11090624/s1, Figure S1: Microscopic image of ablation spots in MALDI, DIUTHAME and LDI mode, Figure S2: Scheme of incomplete or complete DIUTHAME attachment, Figure S3: MS image from incompletely attached DIUTHAME on mouse brain tissue, Figure S4: Pie chart of ion adducts and lipid class annotations for MS measurements with MALDI or DIUTHAME on mouse brain tissue, Figure S5: Mass spectra from blank DIUTHAME and DIUTHAME attached to mouse kidney tissue in negative-ion mode, Figure S6: Mass spectrum of DIUTHAME measurement on mouse kidney tissue with a mass range from m/z 250–1000, Figure S7: Mass spectrum of LDI measurement on mouse brain tissue, Figure S8: MALDI MS image from mouse brain cerebellum showing Purkinje cells, Figure S9: MS images from mouse brain tissue with DIUTHAME membrane attached, Figure S10: MS images from mouse kidney tissue with DIUTHAME membrane attached, Figure S11: MS images from germinated rapeseed with DIUTHAME membrane attached, Figure S12: MS images from *Spodoptera littoralis* tissue with DIUTHAME membrane attached, Figure S13: Evaluation of intensity gradient from rapeseed DIUTHAME MSI measurement, Figure S14: Optical image of a DIUTHAME membrane, Figure S15: Microscopic image of mouse brain tissue with a DIUTHAME foil attached, Figure S16: Microscopic image of mouse brain tissue stained with hematoxylin and eosin, Table S1: List of lipid annotations to mass signals for DIUTHAME MSI on mouse brain tissue, Table S2: List of lipid annotations to mass signals for MALDI MSI on mouse brain tissue, Table S3: Protocol for hematoxylin and eosin staining.

Author Contributions: Conceptualization, B.S. and D.R.B.; methodology, M.A.M.; software, M.A.M.; validation, M.A.M. and D.R.B.; formal analysis, M.A.M.; investigation, M.A.M.; resources, B.S.; data curation, M.A.M.; writing—original draft preparation, M.A.M.; writing—review and editing, M.A.M., D.R.B. and B.S.; visualization, M.A.M.; supervision, B.S.; project administration, B.S.; funding acquisition, B.S. All authors have read and agreed to the published version of the manuscript.

Funding: Financial support by the German Science Foundation (DFG) under Grant Sp314/23-1 and INST 162/500-1 FUGG are gratefully acknowledged. M.A.M. thanks the Fonds der Chemischen Industrie for providing a Ph.D. scholarship.

Institutional Review Board Statement: Animal parts used for this study were obtained by veterinary experts under ethical approval by Justus Liebig University (Approval code: 639_M, Approval date: 21 February 2017).

Informed Consent Statement: Not applicable.

Data Availability Statement: Data are publicly available on metaspace, an annotation platform for mass spectrometry imaging under the following link: https://metaspace2020.eu/project/diuthame_mueller (accessed on 1 September 2021).

Acknowledgments: The authors want to thank Hamamatsu Photonics for providing DIUTHAME membranes, Prayan Pokharel and G. Petschenka (Institute of Insect Biotechnology, Justus Liebig University Giessen, Germany) for providing *Spodoptera littoralis* samples and W. Kummer (Institute of Anatomy and Cell Biology, Justus Liebig University Giessen, Germany) for providing mouse brain and mouse kidney samples. Technical support by TransMIT GmbH (Giessen, Germany) is gratefully acknowledged.

Conflicts of Interest: B.S. is a consultant for TransMIT GmbH, Giessen, Germany. M.A.M and D.R.B. are or were part-time employees of TransMIT GmbH, Giessen, Germany.

References

1. Liebl, H. Ion Microprobe Mass Analyzer. *J. Appl. Phys.* **1967**, *38*, 5277–5283. [CrossRef]
2. Gilmore, I.S.; Heiles, S.; Pieterse, C.L. Metabolic Imaging at the Single-Cell Scale: Recent Advances in Mass Spectrometry Imaging. *Annu. Rev. Anal. Chem.* **2019**, *12*, 201–224. [CrossRef] [PubMed]
3. Spengler, B. Mass spectrometry imaging of biomolecular information. *Anal. Chem.* **2015**, *87*, 64–82. [CrossRef]
4. Hillenkamp, F.; Karas, M.; Beavis, R.C.; Chait, B.T. Matrix-Assisted Laser Desorption/Ionization Mass Spectrometry of Biopolymers. *Anal. Chem.* **1991**, *63*, 1193A–1203A. [CrossRef]
5. Spengler, B.; Hubert, M.; Kaufmann, R. MALDI ion imaging and biological ion imaging with a new scanning UV-laser microprobe. In Proceedings of the 42nd ASMS Conference on Mass Spectrometry and Allied Topics, Chicago, IL, USA, 29 May–3 June 1994; p. 1041. Available online: https://www.uni-giessen.de/fbz/fb08/Inst/iaac/spengler/forschung/dateien/poster_maldi_anwendung (accessed on 1 September 2021).
6. Römpp, A.; Spengler, B. Mass spectrometry imaging with high resolution in mass and space. *Histochem. Cell Biol.* **2013**, *139*, 759–783. [CrossRef] [PubMed]
7. Sturtevant, D.; Lee, Y.-J.; Chapman, K.D. Matrix assisted laser desorption/ionization-mass spectrometry imaging (MALDI-MSI) for direct visualization of plant metabolites in situ. *Curr. Opin. Biotechnol.* **2016**, *37*, 53–60. [CrossRef] [PubMed]
8. Kompauer, M.; Heiles, S.; Spengler, B. Atmospheric pressure MALDI mass spectrometry imaging of tissues and cells at 1.4-μm lateral resolution. *Nat. Methods* **2017**, *14*, 90–96. [CrossRef]
9. Goodwin, R.J.A. Sample preparation for mass spectrometry imaging: Small mistakes can lead to big consequences. *J. Proteomics* **2012**, *75*, 4893–4911. [CrossRef]
10. Calvano, C.D.; Monopoli, A.; Cataldi, T.R.I.; Palmisano, F. MALDI matrices for low molecular weight compounds: An endless story? *Anal. Bioanal. Chem.* **2018**, *410*, 4015–4038. [CrossRef]
11. Beavis, R.C.; Chait, B.T. Cinnamic acid derivatives as matrices for ultraviolet laser desorption mass spectrometry of proteins. *Rapid Commun. Mass Spectrom.* **1989**, *3*, 432–435. [CrossRef]
12. Thomas, A.; Charbonneau, J.L.; Fournaise, E.; Chaurand, P. Sublimation of new matrix candidates for high spatial resolution imaging mass spectrometry of lipids: Enhanced information in both positive and negative polarities after 1,5-diaminonapthalene deposition. *Anal. Chem.* **2012**, *84*, 2048–2054. [CrossRef]
13. Soltwisch, J.; Jaskolla, T.W.; Hillenkamp, F.; Karas, M.; Dreisewerd, K. Ion yields in UV-MALDI mass spectrometry as a function of excitation laser wavelength and optical and physico-chemical properties of classical and halogen-substituted MALDI matrixes. *Anal. Chem.* **2012**, *84*, 6567–6576. [CrossRef] [PubMed]
14. Takáts, Z.; Wiseman, J.M.; Gologan, B.; Cooks, R.G. Mass spectrometry sampling under ambient conditions with desorption electrospray ionization. *Science* **2004**, *306*, 471–473. [CrossRef]
15. Wiseman, J.M.; Ifa, D.R.; Song, Q.; Cooks, R.G. Tissue imaging at atmospheric pressure using desorption electrospray ionization (DESI) mass spectrometry. *Angew. Chem. Int. Ed. Engl.* **2006**, *45*, 7188–7192. [CrossRef] [PubMed]
16. Goodwin, R.J.A.; Takats, Z.; Bunch, J. A Critical and Concise Review of Mass Spectrometry Applied to Imaging in Drug Discovery. *SLAS DISCOV. Adv. Sci. Drug Discov.* **2020**, *25*, 963–976. [CrossRef]
17. Sunner, J.; Dratz, E.; Chen, Y.C. Graphite surface-assisted laser desorption/ionization time-of-flight mass spectrometry of peptides and proteins from liquid solutions. *Anal. Chem.* **1995**, *67*, 4335–4342. [CrossRef]
18. Picca, R.A.; Calvano, C.D.; Cioffi, N.; Palmisano, F. Mechanisms of Nanophase-Induced Desorption in LDI-MS. A Short Review. *Nanomaterials* **2017**, *7*, 75. [CrossRef]
19. Chen, Y.-C.; Shiea, J.; Sunner, J. Thin-layer chromatography–mass spectrometry using activated carbon, surface-assisted laser desorption/ionization. *J. Chromatogr. A* **1998**, *826*, 77–86. [CrossRef]

20. Lo, C.-Y.; Lin, J.-Y.; Chen, W.-Y.; Chen, C.-T.; Chen, Y.-C. Surface-assisted laser desorption/ionization mass spectrometry on titania nanotube arrays. *J. Am. Soc. Mass Spectrom.* **2008**, *19*, 1014–1020. [CrossRef] [PubMed]
21. Go, E.P.; Apon, J.V.; Luo, G.; Saghatelian, A.; Daniels, R.H.; Sahi, V.; Dubrow, R.; Cravatt, B.F.; Vertes, A.; Siuzdak, G. Desorption/ionization on silicon nanowires. *Anal. Chem.* **2005**, *77*, 1641–1646. [CrossRef]
22. Chen, Y.; Vertes, A. Adjustable fragmentation in laser desorption/ionization from laser-induced silicon microcolumn arrays. *Anal. Chem.* **2006**, *78*, 5835–5844. [CrossRef] [PubMed]
23. McLean, J.A.; Stumpo, K.A.; Russell, D.H. Size-selected (2–10 nm) gold nanoparticles for matrix assisted laser desorption ionization of peptides. *J. Am. Chem. Soc.* **2005**, *127*, 5304–5305. [CrossRef]
24. Kawasaki, H.; Yonezawa, T.; Watanabe, T.; Arakawa, R. Platinum Nanoflowers for Surface-Assisted Laser Desorption/Ionization Mass Spectrometry of Biomolecules. *J. Phys. Chem. C* **2007**, *111*, 16278–16283. [CrossRef]
25. Lee, K.-H.; Chiang, C.-K.; Lin, Z.-H.; Chang, H.-T. Determining enediol compounds in tea using surface-assisted laser desorption/ionization mass spectrometry with titanium dioxide nanoparticle matrices. *Rapid Commun. Mass Spectrom.* **2007**, *21*, 2023–2030. [CrossRef] [PubMed]
26. Watanabe, T.; Kawasaki, H.; Yonezawa, T.; Arakawa, R. Surface-assisted laser desorption/ionization mass spectrometry (SALDI-MS) of low molecular weight organic compounds and synthetic polymers using zinc oxide (ZnO) nanoparticles. *J. Mass Spectrom.* **2008**, *43*, 1063–1071. [CrossRef] [PubMed]
27. Yang, J.; Zhang, W.; Zhang, H.; Zhong, M.; Cao, W.; Li, Z.; Huang, X.; Nie, Z.; Liu, J.; Li, P.; et al. Polydopamine-Modified Substrates for High-Sensitivity Laser Desorption Ionization Mass Spectrometry Imaging. *ACS Appl. Mater. Interfaces* **2019**, *11*, 46140–46148. [CrossRef]
28. Naito, Y.; Kotani, M.; Ohmura, T. A novel laser desorption/ionization method using through hole porous alumina membranes. *Rapid Commun. Mass Spectrom.* **2018**, *32*, 1851–1858. [CrossRef] [PubMed]
29. Sato, H.; Nakamura, S.; Fouquet, T.N.J.; Ohmura, T.; Kotani, M.; Naito, Y. Simple Pretreatment for the Analysis of Additives and Polymers by Surface-Assisted Laser Desorption/Ionization Mass Spectrometry Using a Through-Hole Alumina Membrane as a Functional Substrate. *J. Am. Soc. Mass Spectrom.* **2020**, *31*, 298–307. [CrossRef]
30. Kuwata, K.; Itou, K.; Kotani, M.; Ohmura, T.; Naito, Y. DIUTHAME enables matrix-free mass spectrometry imaging of frozen tissue sections. *Rapid Commun. Mass Spectrom.* **2020**, *34*, e8729. [CrossRef] [PubMed]
31. Enomoto, H.; Kotani, M.; Ohmura, T. Novel Blotting Method for Mass Spectrometry Imaging of Metabolites in Strawberry Fruit by Desorption/Ionization Using Through Hole Alumina Membrane. *Foods* **2020**, *9*, 408. [CrossRef]
32. Law, K.P.; Larkin, J.R. Recent advances in SALDI-MS techniques and their chemical and bioanalytical applications. *Anal. Bioanal. Chem.* **2011**, *399*, 2597–2622. [CrossRef]
33. Kompauer, M.; Heiles, S.; Spengler, B. AP-MALDI MSI of Lipids in Mouse Brain Tissue Sections. 2017. Available online: https://protocolexchange.researchsquare.com/article/nprot-5227/v1 (accessed on 1 September 2021).
34. Müller, M.A.; Kompauer, M.; Strupat, K.; Heiles, S.; Spengler, B. Implementation of a High-Repetition-Rate Laser in an AP-SMALDI MSI System for Enhanced Measurement Performance. *J. Am. Soc. Mass Spectrom.* **2021**, *32*, 465–472. [CrossRef]
35. Small, D.M. The Effects of Glyceride Structure on Absorption and Metabolism. *Annu. Rev. Nutr.* **1991**, *11*, 413–434. [CrossRef] [PubMed]
36. Bhandari, D.R.; Wang, Q.; Friedt, W.; Spengler, B.; Gottwald, S.; Römpp, A. High resolution mass spectrometry imaging of plant tissues: Towards a plant metabolite atlas. *Analyst* **2015**, *140*, 7696–7709. [CrossRef] [PubMed]
37. Müller, W.H.; Verdin, A.; de Pauw, E.; Malherbe, C.; Eppe, G. Surface-assisted laser desorption/ionization mass spectrometry imaging: A review. *Mass Spectrom. Rev.* **2020**, 1–48. [CrossRef]
38. Song, K.; Cheng, Q. Desorption and ionization mechanisms and signal enhancement in surface assisted laser desorption ionization mass spectrometry (SALDI-MS). *Appl. Spectrosc. Rev.* **2020**, *55*, 220–242. [CrossRef]
39. Lai, S.K.-M.; Tang, H.-W.; Lau, K.-C.; Ng, K.-M. Nanosecond UV Laser Ablation of Gold Nanoparticles: Enhancement of Ion Desorption by Thermal-Driven Desorption, Vaporization, or Phase Explosion. *J. Phys. Chem. C* **2016**, *120*, 20368–20377. [CrossRef]
40. Li, Y.; Cao, X.; Zhan, L.; Xue, J.; Wang, J.; Xiong, C.; Nie, Z. Hot electron transfer promotes ion production in plasmonic metal nanostructure assisted laser desorption ionization mass spectrometry. *Chem. Commun.* **2018**, *54*, 10905–10908. [CrossRef] [PubMed]
41. Cheng, Y.-H.; Ng, K.-M. The Hidden Heroes: Holes in Charge-Driven Desorption Mass Spectrometry. *Anal. Chem.* **2020**, *92*, 5645–5649. [CrossRef]
42. Yamada, K.; Miyajima, K.; Mafuné, F. Thermionic Emission of Electrons from Gold Nanoparticles by Nanosecond Pulse-Laser Excitation of Interband. *J. Phys. Chem. C* **2007**, *111*, 11246–11251. [CrossRef]
43. Zhu, Q.; Wang, Z.; Wang, Y.; Teng, F.; Du, J.; Dou, S.; Lu, N. Investigation of Surface Morphology on Ion Desorption in SALDI-MS on Tailored Silicon Nanopillar Arrays. *J. Phys. Chem. C* **2020**, *124*, 2450–2457. [CrossRef]
44. Paschke, C.; Leisner, A.; Hester, A.; Maass, K.; Guenther, S.; Bouschen, W.; Spengler, B. Mirion—A software package for automatic processing of mass spectrometric images. *J. Am. Soc. Mass Spectrom.* **2013**, *24*, 1296–1306. [CrossRef] [PubMed]
45. Sud, M.; Fahy, E.; Cotter, D.; Brown, A.; Dennis, E.A.; Glass, C.K.; Merrill, A.H.; Murphy, R.C.; Raetz, C.R.H.; Russell, D.W.; et al. LMSD: LIPID MAPS structure database. *Nucleic Acids Res.* **2006**, *35*, D527–D532. [CrossRef] [PubMed]
46. Palmer, A.; Phapale, P.; Chernyavsky, I.; Lavigne, R.; Fay, D.; Tarasov, A.; Kovalev, V.; Fuchser, J.; Nikolenko, S.; Pineau, C.; et al. FDR-controlled metabolite annotation for high-resolution imaging mass spectrometry. *Nat. Methods* **2017**, *14*, 57–60. [CrossRef] [PubMed]

Supporting Information

Matrix-free high-resolution atmospheric-pressure SALDI mass spectrometry imaging of biological samples using DIUTHAME membranes

Max A. Müller, Dhaka R. Bhandari, Bernhard Spengler

Institute of Inorganic and Analytical Chemistry, Justus Liebig University, Giessen, Germany

Supporting Information

*Address correspondence to:
Institute of Inorganic and Analytical Chemistry
Justus Liebig University Giessen
Heinrich Buff Ring 17
35392 Giessen, Germany
Phone: +49 641 99 34801
e-mail: bernhard.spengler@anorg.chemie.uni-giessen.de

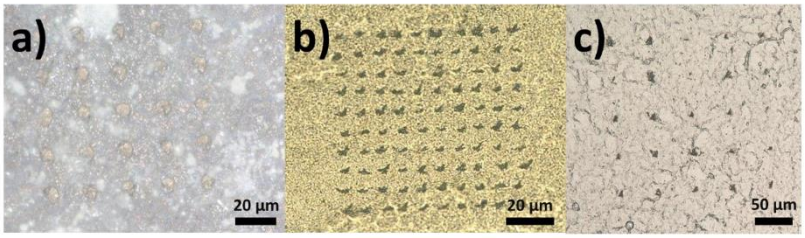

Supporting Figure 1: Microscopic images of ablation spots produced by MALD MSI with 20 µm step size (a), DIUTHAME with 10 µm step size (b) and LDI with 50 µm step size (c), respectively. Laser intensity was the same as for the imaging experiments shown in Figure 2.

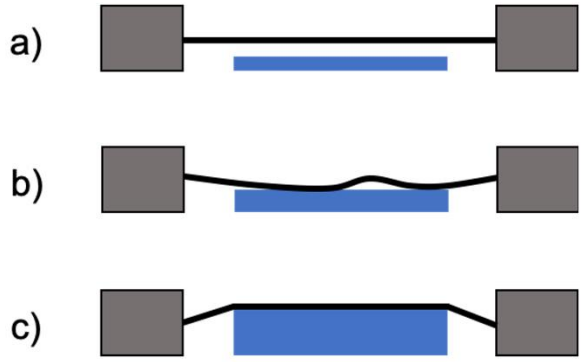

Supporting Figure 2: Scheme of DIUTHAME effective area (black) attachment to a sample (blue). a) No connection between DIUTHAME and the sample when the sample is too thin. Thereby, no ion signal is generated. b) Incomplete attachment of DIUTHAME to a medium thick sample, leaving room for air bubbles, causing intermediate signal loss. c) Complete and firm attachment of DIUTHAME to a thicker sample, ensuring a homogeneous and distortion-free desorption and ionization of analytes.

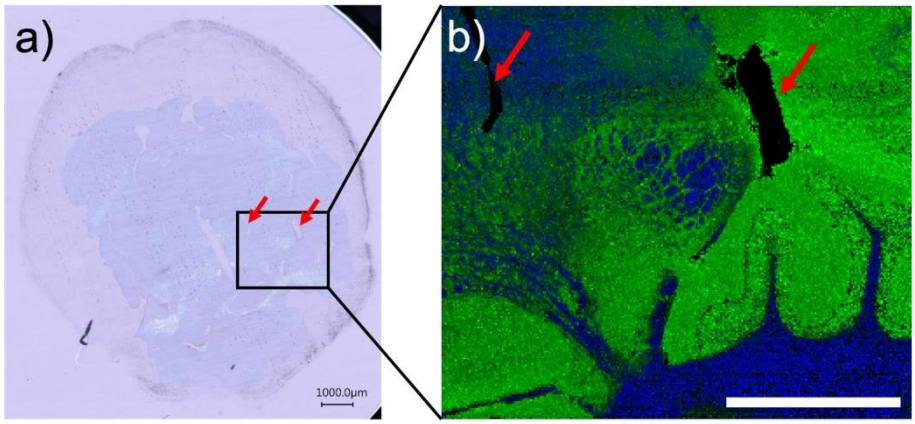

Supporting Figure 3: a) Microscopic image of mouse brain tissue with incomplete DIUTHAME membrane attachment. Air bubbles are highlighted with red arrows. b) DIUTHAME MSI image of a region in mouse brain cerebellum in positive-ion mode. Pixel size 10 µm, 270x270 pixels, m/z 600 – 1000. Color coding: green: m/z 772.5279 $[PC\ 32:0 + K]^+$, blue: m/z 848.6405 $[PS\ 40:0 + H]^+$. Red arrows indicate the position of the air bubbles visible from (a), producing blind spots in the MSI results. Scale bars: 1 mm.

2

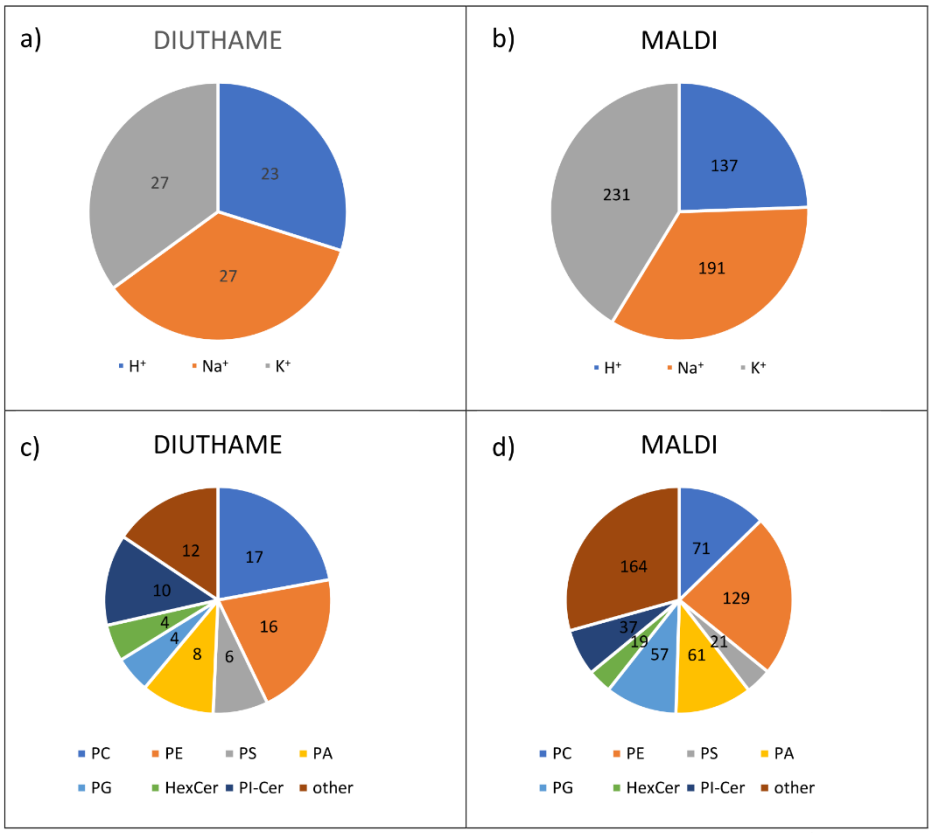

Supporting Figure 4: Pie chart of the ion adducts and lipid classes found through annotation by LIPIDMAPS. a) DIUTHAME ion adducts. b) MALDI ion adducts. c) DIUTHAME lipid classes. d) MALDI lipid classes. PC = phosphatidylcholine, PE = phosphatidylethanolamine, PS = phosphatidylserine, PA = Phosphatidic acid, PG = Phosphatidylglycerol, HexCer = Hexosylceramide, PI-Cer = ceramide phosphoinositol, other = belonging to any other lipid class than the ones listed.

3

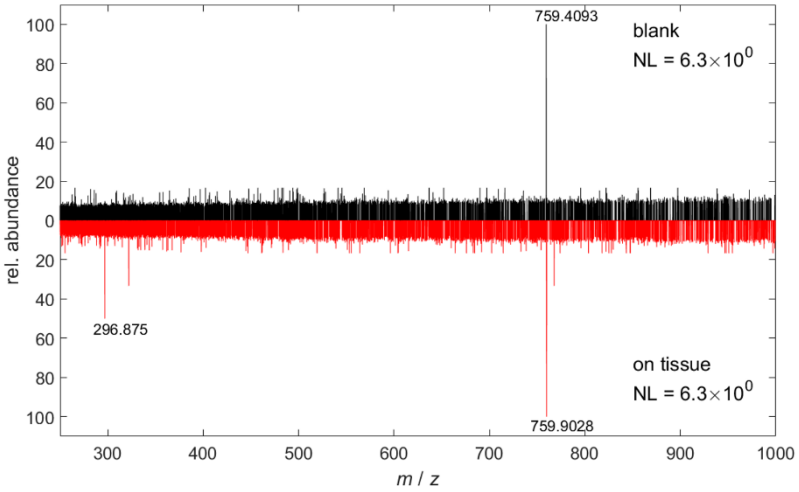

Supporting Figure 5: Comparison of 100 summed-up mass spectra in negative-ion mode acquired using a blank DIUTHAME membrane (black) and a DIUTHAME membrane attached to mouse kidney tissue (red).

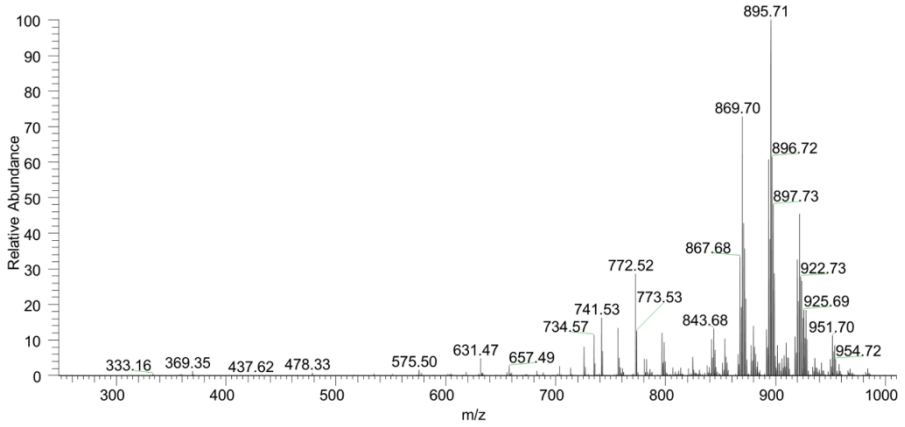

Supporting Figure 6: 100 summed-up mass spectra from mouse kidney tissue investigated by DIUTHAME MSI in positive ion mode showing no significant signal in the lower mass range below m/z 500. Normalized level: 1.37·10³.

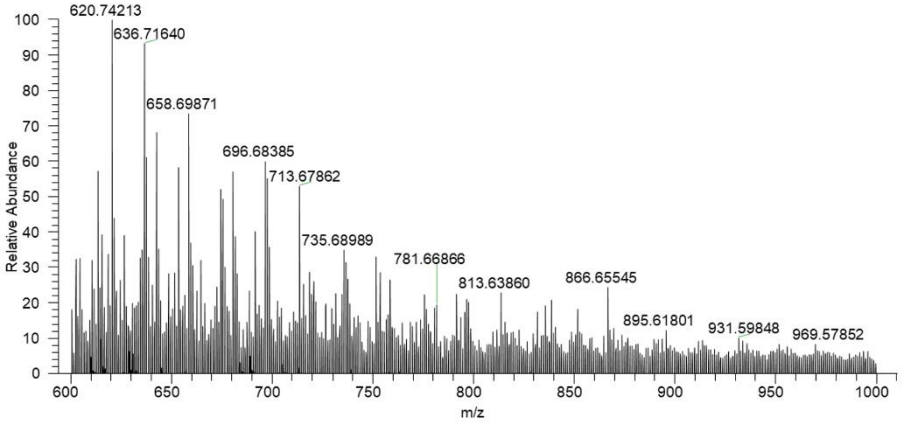

Supporting Figure 7: Single LDI mass spectrum from mouse brain cerebellum. All parameters were the same as for the imaging experiment shown in Figure 2e.

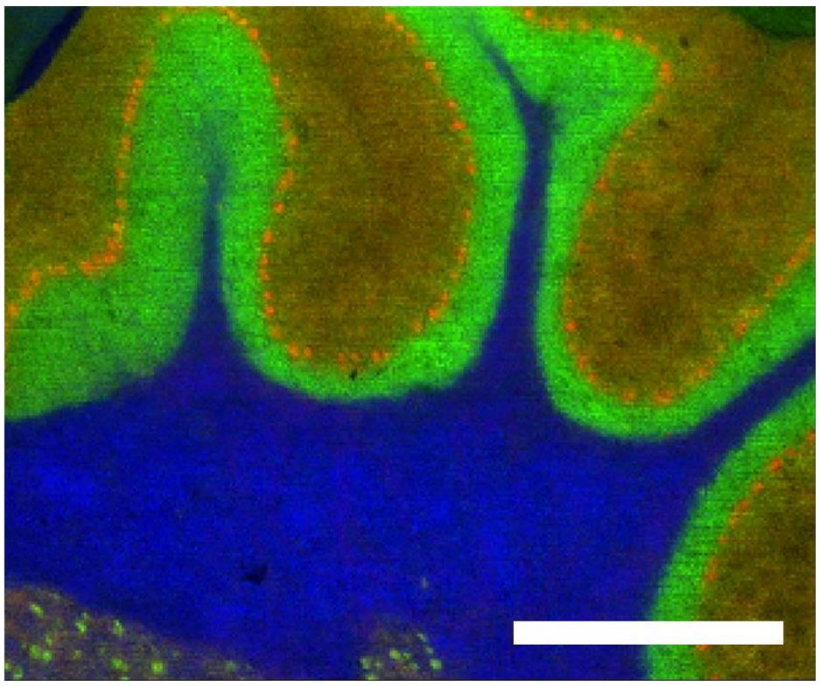

Supporting Figure 8: MALDI MS image of mouse brain cerebellum with 300x250 pixels and 5 µm pixel size. Color coding: red: m/z 872.5525 [SHexCer t38:2 + Na]⁺, green: m/z 844.5212 [SHexCer t36:2 + Na]⁺, blue: m/z 848.6329 [PS 40:0 + H]⁺. Markers of the Purkinje cells (red) where observed in the MALDI experiment, while being absent in the DIUTHAME measurements. Scale bar: 500 µm.

5

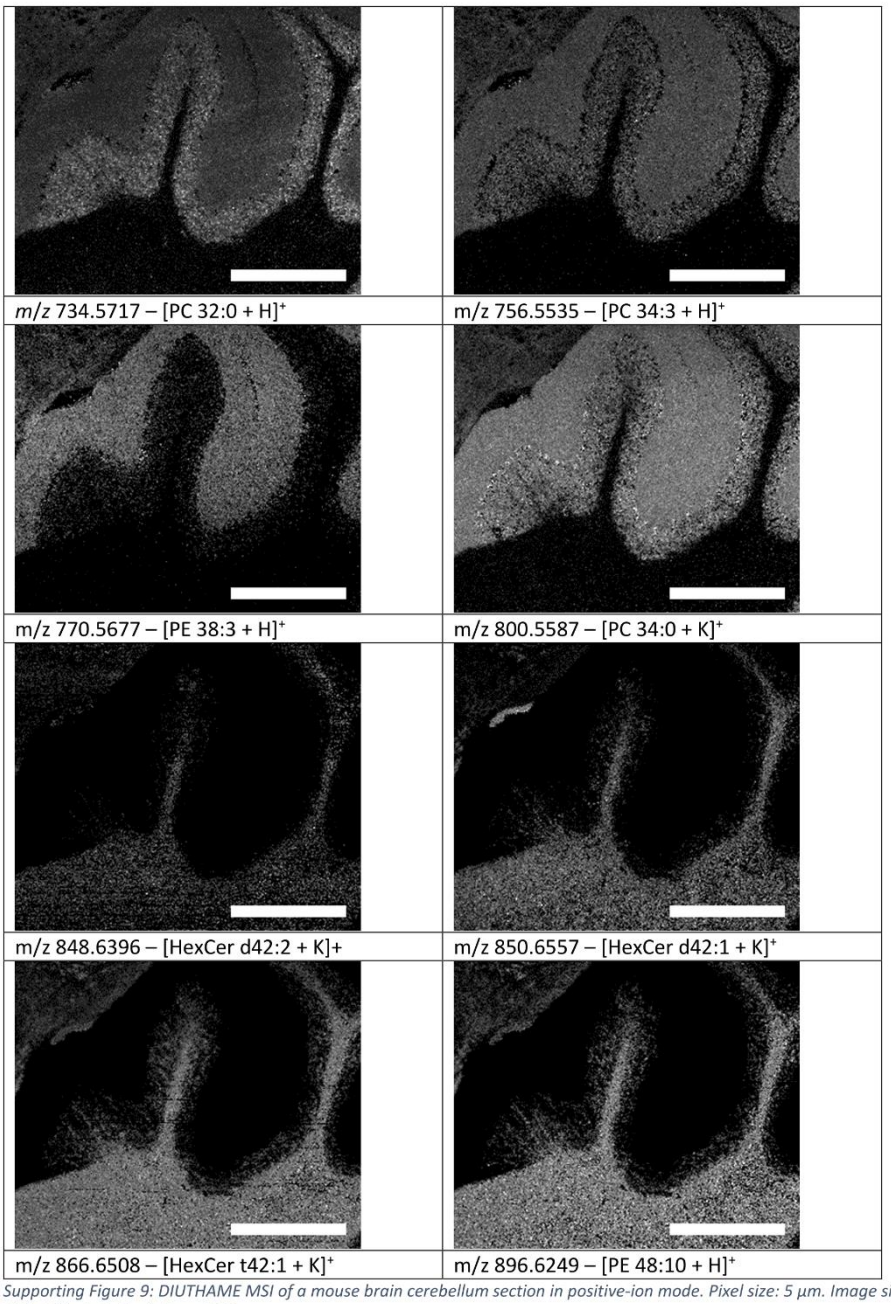

Supporting Figure 9: DIUTHAME MSI of a mouse brain cerebellum section in positive-ion mode. Pixel size: 5 µm. Image size: 300x250 pixels. Scale bars: 500 µm.

6

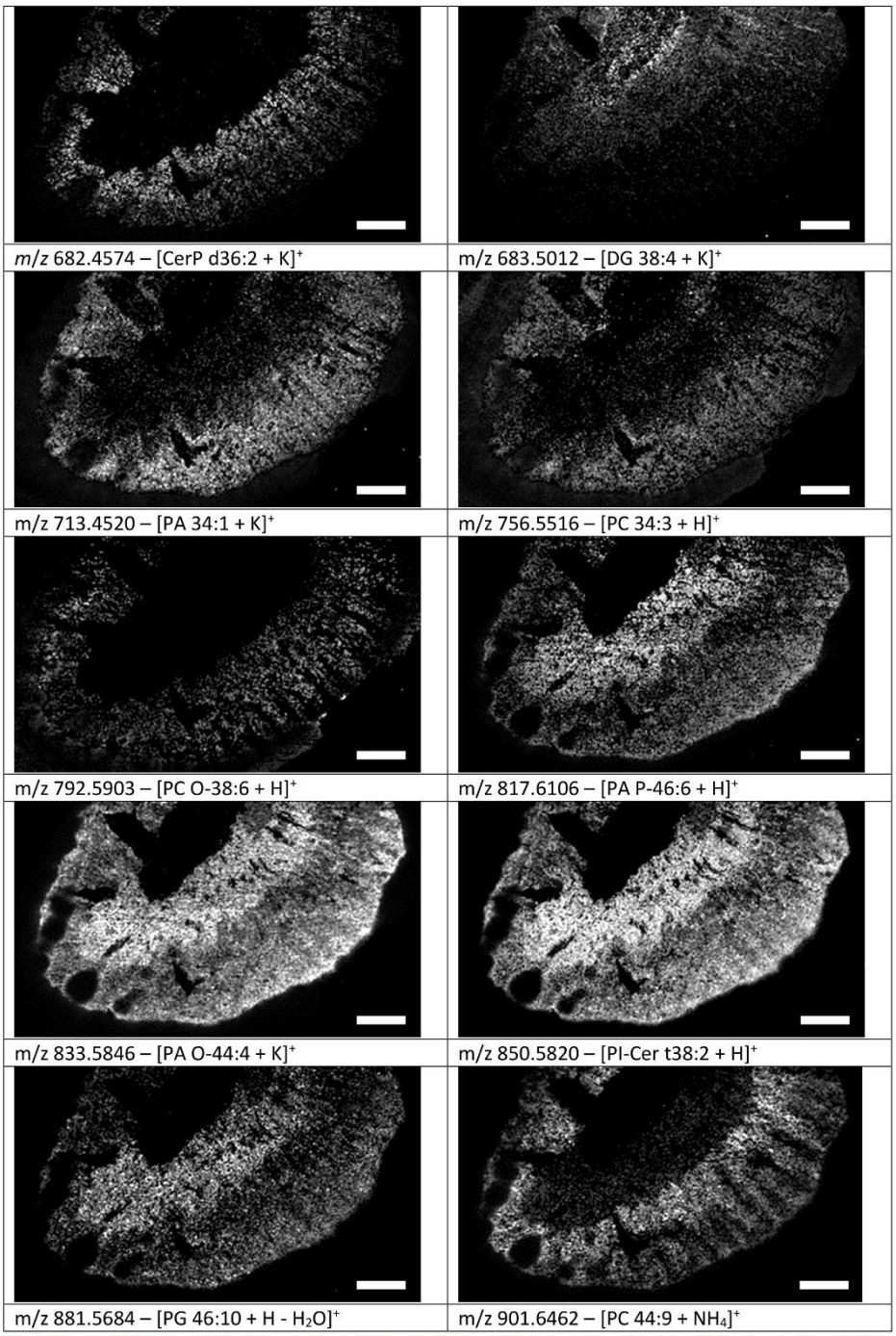

Supporting Figure 10: DIUTHAME MSI of a mouse kidney section in positive-ion mode. Pixel size: 30 µm. Image size: 276x161 pixels. Scale bar: 1 mm.

7

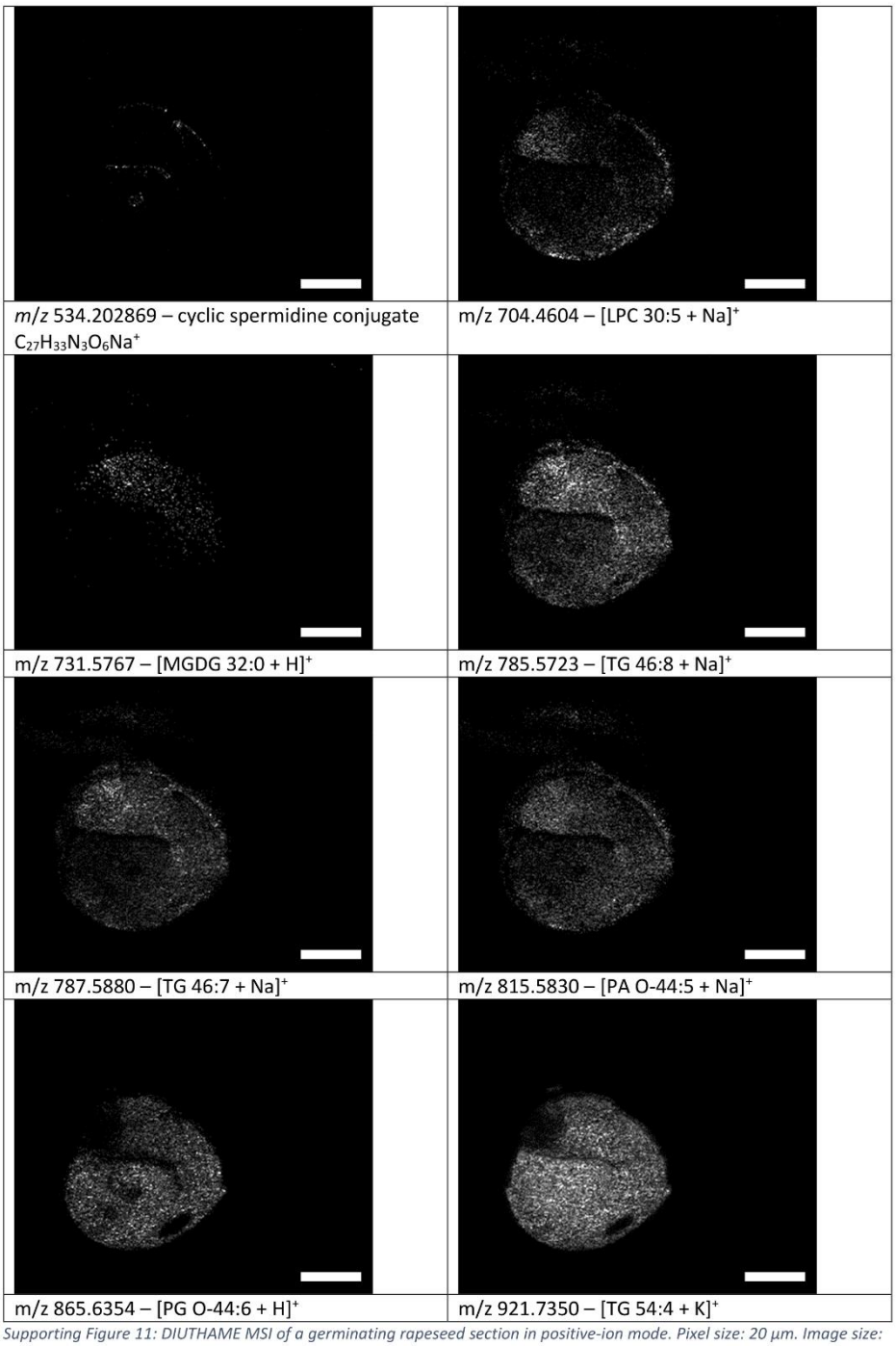

Supporting Figure 11: DIUTHAME MSI of a germinating rapeseed section in positive-ion mode. Pixel size: 20 µm. Image size: 297x245 pixels. Scale bar: 1 mm.

8

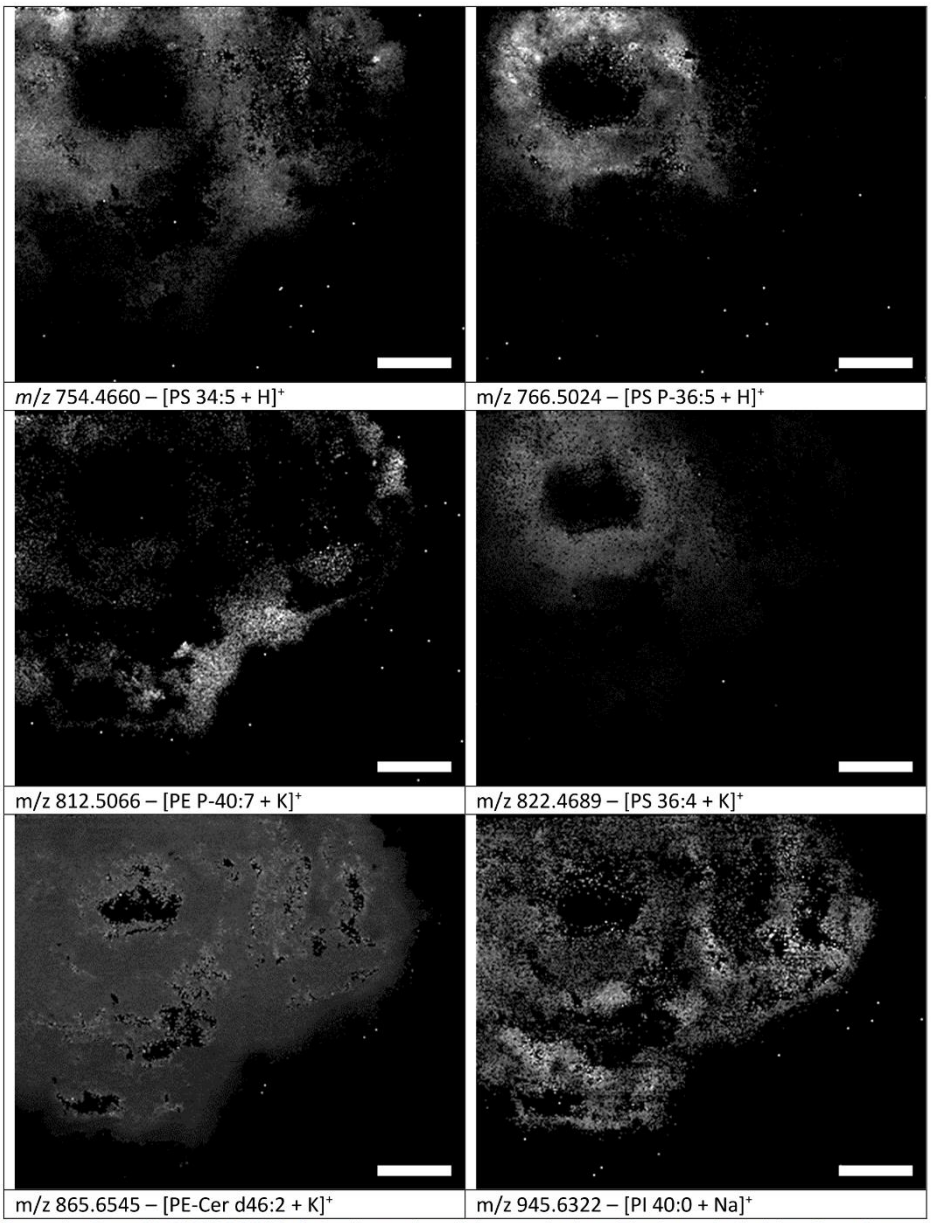

Supporting Figure 12: DIUTHAME MSI of a Spodoptera littoralis larva section in positive-ion mode. Pixel size: 20 µm. Image size: 300x250 pixels. Scale bar: 1mm.

9

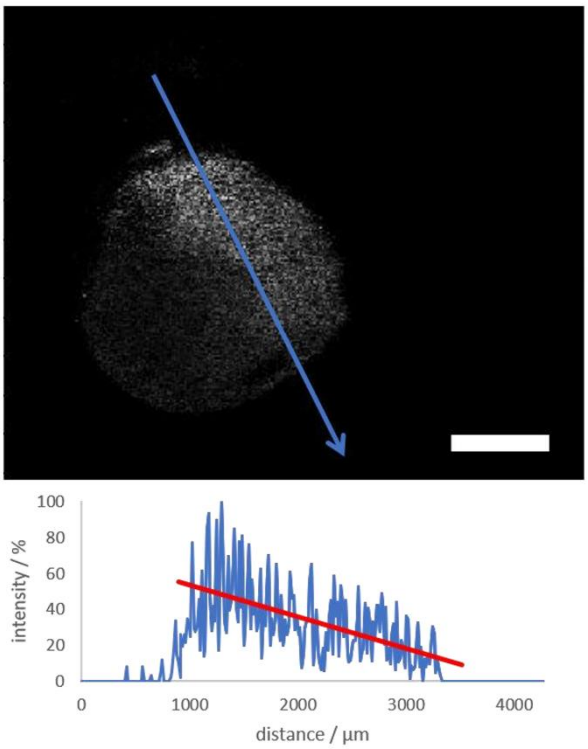

Supporting Figure 13: Line scan through a part of the rapeseed sample measured by DIUTHAME and shown in Figure 3 for m/z 909.6985 [LacCer d36:0 + NH_4]$^+$, indicating a decrease of the compound from the root tip towards the endosperm. Linear regression for the linear part from 1100 µm – 3320 µm is overlaid. Direction and position of the line scan indicated by blue arrow. Scale bar: 1 mm.

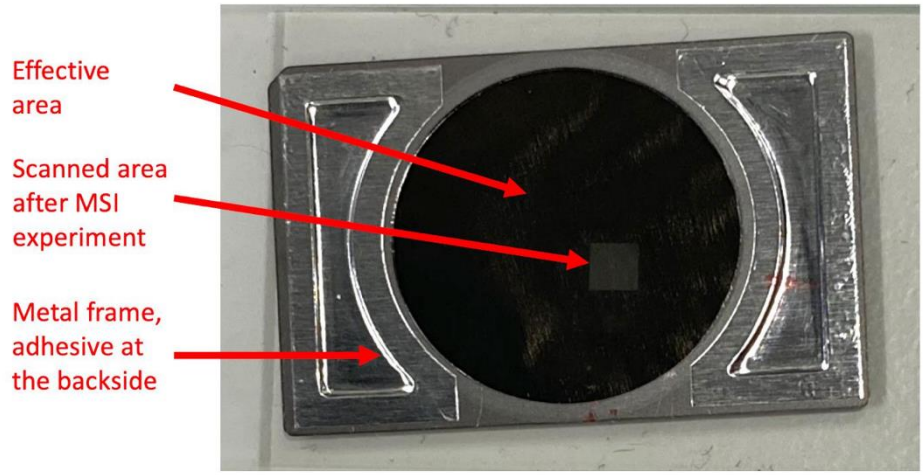

Supporting Figure 14: Optical image of the DIUTHAME membrane attached to a sample on a glass slide. The sample cannot be seen by eye, only under a microscope with transmitted light setting.

10

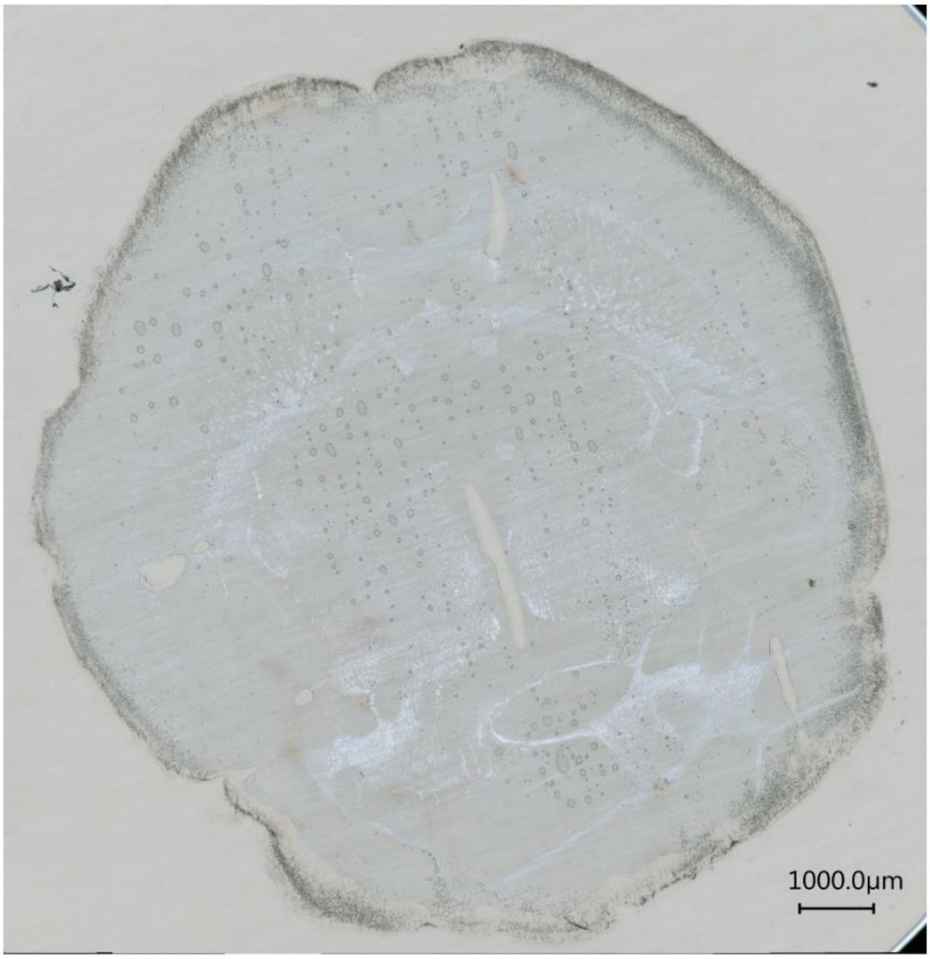

Supporting Figure 15: Transmission light optical microscopy image of a horizontal mouse brain section with DIUTHAME membrane completely attached on top of the sample.

11

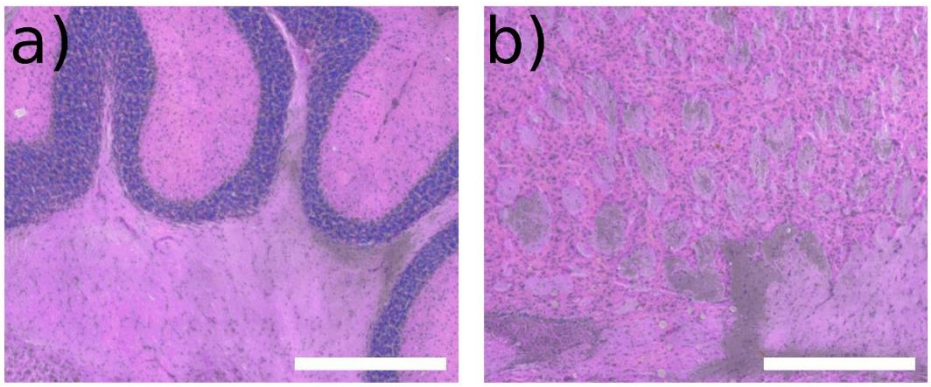

Supporting Figure 16: Optical microscopy image of regions of a mouse brain section stained with hematoxylin and eosin after the MALDI MSI experiment shown in Figure 2. a) Region in cerebellum. b) Striatum ventral region. Scale bars: 500 µm.

12

Supporting Table 1: List of mass signals detected by DIUTHAME MS from mouse brain cerebellum and annotated by LIPIDMAPS in shorthand notation [1,2].

Number	m/z measured	m/z literature	$\Delta_{m/z}$ / *ppm*	annotated lipid	ion adduct
1	620.4278	620.4286	1.3	PC(24:1)	$[M+H]^+$
2	650.4385	650.4391	0.9	PE(28:1(OH))	$[M+H]^+$
3	660.3995	660.4000	0.8	LPE(30:6)	$[M+Na]^+$
4	672.4205	672.4211	0.9	PE(28:1(OH))	$[M+Na]^+$
5	678.4698	678.4704	0.9	PE(30:1(OH))	$[M+H]^+$
6	686.4152	686.4158	0.9	PC(26:1)	$[M+K]^+$
7	687.4356	687.4362	0.9	PA(32:0)	$[M+K]^+$
8	688.4308	688.4313	0.7	LPE(32:6)	$[M+Na]^+$
9	697.4773	697.4779	0.9	PA(34:1)	$[M+Na]^+$
10	700.4518	700.4524	0.9	PE(30:1(OH))	$[M+Na]^+$
11	702.4101	702.4105	0.6	PE(32:6)	$[M+Na]^+$
12	710.4881	710.4885	0.6	CerP(d38:2)	$[M+K]^+$
13	711.4357	711.4362	0.7	PA(34:2)	$[M+K]^+$
14	713.4515	713.4518	0.4	PA(34:1)	$[M+K]^+$
15	714.4548	714.4552	0.6	PI-Cer(t28:0)	$[M+H]^+$
16	716.4258	716.4263	0.7	PE(30:1(OH))	$[M+K]^+$
17	731.6058	731.6061	0.4	SM(d36:1)	$[M+H]^+$
18	732.4208	732.4211	0.4	LPS(32:6)	$[M+Na]^+$
19	733.4242	733.4262	2.7	LPI(26:1)	$[M+Na]^+$
20	734.5692	734.5694	0.3	PC(32:0)	$[M+H]^+$
21	739.4673	739.4675	0.3	PA(36:2)	$[M+K]^+$
22	740.4706	740.4708	0.3	PI-Cer(t30:1)	$[M+H]^+$
23	741.4828	741.4831	0.4	PA(36:1)	$[M+K]^+$
24	742.4862	742.4865	0.4	PI-Cer(t30:0)	$[M+H]^+$
25	744.4572	744.4575	0.4	PC(32:6)	$[M+Na]^+$
26	748.5846	748.5851	0.7	PE(36:0)	$[M+H]^+$
27	753.5877	753.5881	0.5	SM(d36:1)	$[M+Na]^+$
28	756.4937	756.494	0.4	PE(34:1)	$[M+K]^+$
29	756.5510	756.5514	0.5	PC(32:0)	$[M+Na]^+$
30	758.5093	758.5095	0.3	LPC(34:6)	$[M+Na]^+$
31	760.5849	760.5851	0.3	PC(34:1)	$[M+H]^+$
32	762.6003	762.6007	0.5	PC(34:0)	$[M+H]^+$
33	766.5590	766.5593	0.4	PS(O-34:0(OH))	$[M+H]^+$
34	767.4985	767.4988	0.4	PA(38:2)	$[M+K]^+$
35	769.5619	769.5620	0.1	SM(d36:1)	$[M+K]^+$
36	770.5094	770.5095	0.1	PE(P-38:6)	$[M+Na]^+$
37	770.5652	770.5670	2.3	PE(36:0)	$[M+Na]^+$
38	772.5251	772.5252	0.1	PE(O-38:6)	$[M+Na]^+$
39	773.5285	773.5303	2.3	PG(34:0)	$[M+Na]^+$
40	775.5265	775.5272	0.9	PA(42:7)	$[M+H]^+$
41	782.5095	782.5097	0.3	PE(36:2)	$[M+K]^+$
42	782.5541	782.5542	0.1	PI-Cer(d34:0)	$[M+H]^+$

43	782.5670	782.5670	< 0.1	PC(34:1)	$[M+Na]^+$
44	784.5251	784.5253	0.3	PE(36:1)	$[M+K]^+$
45	784.5824	784.5827	0.4	PC(34:0)	$[M+Na]^+$
46	786.5407	786.5408	0.1	PC(P-36:5)	$[M+Na]^+$
47	788.6163	788.6164	0.1	PC(36:1)	$[M+H]^+$
48	796.5252	796.5252	< 0.1	PE(P-40:7)	$[M+Na]^+$
49	797.5932	797.5933	0.1	SM(d38:1)	$[M+K]^+$
50	798.5410	798.5410	< 0.1	PC(34:1)	$[M+K]^+$
51	799.5444	799.5460	2.0	PG(36:1)	$[M+Na]^+$
52	800.5566	800.5566	< 0.1	PC(34:0)	$[M+K]^+$
53	801.5599	801.5616	2.1	PG(36:0)	$[M+Na]^+$
54	806.5090	806.5097	0.9	PE(38:4)	$[M+K]^+$
55	808.5696	808.5698	0.2	PI-Cer(d36:1)	$[M+H]^+$
56	810.5855	810.5855	< 0.1	PI-Cer(d36:0)	$[M+H]^+$
57	810.5985	810.5983	0.2	PC(36:1)	$[M+Na]^+$
58	814.5358	814.5359	0.1	PC(34:1(OH))	$[M+K]^+$
59	822.6218	822.6219	0.1	PS(O-38:0(OH))	$[M+H]^+$
60	822.6427	822.6429	0.2	HexCer(t40:1)	$[M+Na]^+$
61	824.5566	824.5566	< 0.1	PC(36:2)	$[M+K]^+$
62	826.5724	826.5723	0.1	PC(36:1)	$[M+K]^+$
63	827.5757	827.5773	1.9	PG(38:1)	$[M+Na]^+$
64	828.5151	828.5151	< 0.1	PS(36:1)	$[M+K]^+$
65	830.5097	830.5097	< 0.1	PE(40:6)	$[M+K]^+$
66	832.5100	832.5099	0.1	PS(38:5)	$[M+Na]^+$
67	836.6009	836.6011	0.2	PI-Cer(d38:1)	$[M+H]^+$
68	838.6168	838.6168	< 0.1	PI-Cer(d38:0)	$[M+H]^+$
69	840.6230	840.6243	1.5	CerP(t46:1)	$[M+K]^+$
70	840.6325	840.6325	< 0.1	HexCer(t40:0)	$[M+K]^+$
71	846.5254	846.5257	0.4	PI-Cer(d36:1)	$[M+K]^+$
72	848.6375	848.6375	< 0.1	PS(40:0)	$[M+H]^+$
73	850.6532	850.6532	< 0.1	PS(O-40:0(OH))	$[M+H]^+$
74	850.6739	850.6742	0.4	HexCer(t42:1)	$[M+Na]^+$
75	864.6324	864.6324	< 0.1	PI-Cer(d40:1)	$[M+H]^+$
76	866.6483	866.6482	0.1	HexCer(t42:1)	$[M+K]^+$
77	868.6546	868.6556	1.2	CerP(t48:1)	$[M+K]^+$

14

Supporting Table 2: List of mass signals detected by MALDI MS from mouse brain cerebellum and annotated by LIPIDMAPS in shorthand notation [1,2].

Number	m/z measured	m/z literature	$\Delta_{m/z}$ / ppm	annotated lipid	ion adduct
1	606.4141	606.4129	2.0	PE(26:1)	$[M+H]^+$
2	620.4295	620.4286	1.5	PC(24:1)	$[M+H]^+$
3	622.4451	622.4442	1.4	PC(24:0)	$[M+H]^+$
4	633.4868	633.4855	2.1	DG(34:1)	$[M+K]^+$
5	634.4451	634.4442	1.4	PE(28:1)	$[M+H]^+$
6	642.4113	642.4105	1.2	PC(24:1)	$[M+Na]^+$
7	644.4271	644.4262	1.4	PC(24:0)	$[M+Na]^+$
8	648.4607	648.4599	1.2	PC(26:1)	$[M+H]^+$
9	650.4399	650.4391	1.2	PE(28:1(OH))	$[M+H]^+$
10	650.4762	650.4755	1.1	PC(26:0)	$[M+H]^+$
11	652.4192	652.4185	1.1	HexCer(d28:2)	$[M+K]^+$
12	656.4269	656.4262	1.1	PE(28:1)	$[M+Na]^+$
13	661.4042	661.4051	1.4	PG(26:0)	$[M+Na]^+$
14	661.5176	661.5168	1.2	DG(36:1)	$[M+K]^+$
15	664.4555	664.4548	1.1	LPS(28:1)	$[M+H]^+$
16	667.4381	667.4392	1.6	MGDG(26:1)	$[M+Na]^+$
17	668.4140	668.4133	1.0	PI-Cer(d26:1)	$[M+H]^+$
18	670.4425	670.4418	1.0	PC(26:1)	$[M+Na]^+$
19	672.4218	672.4211	1.0	PE(28:1(OH))	$[M+Na]^+$
20	672.4582	672.4575	1.0	PC(26:0)	$[M+Na]^+$
21	674.4160	674.4158	0.3	PE(28:0)	$[M+K]^+$
22	678.4708	678.4704	0.6	PE(30:1(OH))	$[M+H]^+$
23	680.4502	680.4498	0.6	HexCer(d30:2)	$[M+K]^+$
24	682.4580	682.4572	1.2	CerP(d36:2)	$[M+K]^+$
25	683.5022	683.5011	1.6	DG(38:4)	$[M+K]^+$
26	684.4738	684.4729	1.3	CerP(d36:1)	$[M+K]^+$
27	685.4048	685.4051	0.4	PG(28:2)	$[M+Na]^+$
28	685.4215	685.4205	1.5	PA(32:1)	$[M+K]^+$
29	686.4161	686.4158	0.4	PC(26:1)	$[M+K]^+$
30	687.4200	687.4208	1.2	PG(28:1)	$[M+Na]^+$
31	687.4371	687.4362	1.3	PA(32:0)	$[M+K]^+$
32	688.4314	688.4314	< 0.1	PC(26:0)	$[M+K]^+$
33	689.4197	689.4177	2.9	PA(36:8)	$[M+H]^+$
34	689.4349	689.4364	2.2	PG(28:0)	$[M+Na]^+$
35	692.4864	692.4861	0.4	LPS(30:1)	$[M+H]^+$
36	693.4456	693.4466	1.4	PA(34:3)	$[M+Na]^+$
37	694.5155	694.5146	1.3	CerP(d38:2)	$[M+Na]^+$
38	695.4422	695.4412	1.4	PA(O-34:3)	$[M+K]^+$
39	695.4687	695.4705	2.6	MGDG(28:1)	$[M+Na]^+$
40	696.4449	696.4447	0.3	HexCer(t30:2)	$[M+K]^+$
41	697.4789	697.4779	1.4	PA(34:1)	$[M+Na]^+$
42	698.4163	698.4158	0.7	PE(30:2)	$[M+K]^+$

15

43	699.4853	699.4838	2.1	PE-Cer(d34:1)	$[M+K]^+$
44	700.4319	700.4314	0.7	PE(30:1)	$[M+K]^+$
45	700.4529	700.4524	0.7	PE(30:1(OH))	$[M+Na]^+$
46	701.4549	701.4542	1.0	DG(40:9)	$[M+K]^+$
47	702.4110	702.4107	0.4	LPS(28:1)	$[M+K]^+$
48	703.4144	703.4157	1.8	PG(28:1(OH))	$[M+Na]^+$
49	706.5386	706.5381	0.7	PC(30:0)	$[M+H]^+$
50	707.5021	707.5011	1.4	DG(40:6)	$[M+K]^+$
51	708.4813	708.4811	0.3	HexCer(d32:2)	$[M+K]^+$
52	709.4192	709.4191	0.1	SQDG(26:1)	$[M+H]^+$
53	710.4744	710.4755	1.5	PE(34:5)	$[M+H]^+$
54	710.4892	710.4885	1.0	CerP(d38:2)	$[M+K]^+$
55	711.4197	711.4208	1.5	PG(30:3)	$[M+Na]^+$
56	711.4372	711.4362	1.4	PA(34:2)	$[M+K]^+$
57	712.4317	712.4314	0.4	PC(28:2)	$[M+K]^+$
58	712.4410	712.4395	2.1	PI-Cer(t28:1)	$[M+H]^+$
59	712.4877	712.4888	1.5	PE(32:1)	$[M+Na]^+$
60	713.4367	713.4364	0.4	PG(30:2)	$[M+Na]^+$
61	713.4525	713.4518	1.0	PA(34:1)	$[M+K]^+$
62	714.4111	714.4107	0.6	PE(30:2(OH))	$[M+K]^+$
63	714.4563	714.4552	1.5	PI-Cer(t28:0)	$[M+H]^+$
64	715.4505	715.4521	2.2	PG(30:1)	$[M+Na]^+$
65	716.4267	716.4263	0.6	PE(30:1(OH))	$[M+K]^+$
66	716.4622	716.4626	0.6	LPE(34:6)	$[M+Na]^+$
67	717.4505	717.4490	2.1	PA(38:8)	$[M+H]^+$
68	718.4061	718.4056	0.7	PS(28:0)	$[M+K]^+$
69	718.4245	718.4266	2.9	PI-Cer(d28:1)	$[M+Na]^+$
70	719.4609	719.4622	1.8	PA(36:4)	$[M+Na]^+$
71	720.5546	720.5538	1.1	PE(34:0)	$[M+H]^+$
72	721.4781	721.4779	0.3	PA(36:3)	$[M+Na]^+$
73	723.4744	723.4725	2.6	PA(O-36:3)	$[M+K]^+$
74	723.4942	723.4935	1.0	PA(36:2)	$[M+Na]^+$
75	724.4762	724.4760	0.3	HexCer(t32:2)	$[M+K]^+$
76	725.4884	725.4882	0.3	PA(O-36:2)	$[M+K]^+$
77	725.5105	725.5116	1.5	PA(38:4)	$[M+H]^+$
78	725.5577	725.5568	1.2	SM(d34:1)	$[M+Na]^+$
79	726.4110	726.4107	0.4	LPS(30:3)	$[M+K]^+$
80	726.4476	726.4471	0.7	PE(32:2)	$[M+K]^+$
81	726.4916	726.4916	< 0.1	PI-Cer(d30:0)	$[M+H]^+$
82	727.4683	727.4673	1.4	PA(P-38:6)	$[M+Na]^+$
83	728.4266	728.4263	0.4	LPS(30:2)	$[M+K]^+$
84	728.4629	728.4627	0.3	PE(32:1)	$[M+K]^+$
85	728.4844	728.4837	1.0	PE(32:1(OH))	$[M+Na]^+$
86	728.5207	728.5201	0.8	PC(30:0)	$[M+Na]^+$
87	730.5749	730.5745	0.5	PE(O-36:2)	$[M+H]^+$

16

88	731.6068	731.6061	1.0	SM(d36:1)	$[M+H]^+$
89	732.4215	732.4211	0.5	LPS(32:6)	$[M+Na]^+$
90	732.5545	732.5538	1.0	PC(32:1)	$[M+H]^+$
91	733.4245	733.4262	2.3	LPI(26:1)	$[M+Na]^+$
92	734.4199	734.4215	2.2	PI-Cer(t28:1)	$[M+Na]^+$
93	734.5701	734.5694	1.0	PC(32:0)	$[M+H]^+$
94	735.4345	735.4348	0.4	SQDG(28:2)	$[M+H]^+$
95	736.4377	736.4371	0.8	PI-Cer(t28:0)	$[M+Na]^+$
96	737.4521	737.4518	0.4	PA(36:3)	$[M+K]^+$
97	738.4114	738.4107	0.9	PE(32:4(OH))	$[M+K]^+$
98	738.4551	738.4552	0.1	PI-Cer(t30:2)	$[M+H]^+$
99	738.5205	738.5198	0.9	CerP(d40:2)	$[M+K]^+$
100	739.4510	739.4521	1.5	PG(32:3)	$[M+Na]^+$
101	739.4680	739.4675	0.7	PA(36:2)	$[M+K]^+$
102	740.4119	740.4109	1.4	PS(30:3(OH))	$[M+Na]^+$
103	740.4717	740.4708	1.2	PI-Cer(t30:1)	$[M+H]^+$
104	740.4986	740.4991	0.7	PE(O-34:2)	$[M+K]^+$
105	740.5203	740.5201	0.3	PE(34:1)	$[M+Na]^+$
106	741.4487	741.4490	0.4	PA(40:10)	$[M+H]^+$
107	741.4676	741.4677	0.1	PG(32:2)	$[M+Na]^+$
108	741.4846	741.4831	2.0	PA(36:1)	$[M+K]^+$
109	741.5311	741.5307	0.5	SM(d34:1)	$[M+K]^+$
110	742.4065	742.4056	1.2	PS(30:2)	$[M+K]^+$
111	742.4424	742.4420	0.5	PE(32:2(OH))	$[M+K]^+$
112	742.4875	742.4865	1.3	PI-Cer(t30:0)	$[M+H]^+$
113	742.5155	742.5147	1.1	PE(O-34:1)	$[M+K]^+$
114	742.5351	742.5357	0.8	PE(34:0)	$[M+Na]^+$
115	743.4818	743.4834	2.2	PG(32:1)	$[M+Na]^+$
116	744.4578	744.4576	0.3	PE(32:1(OH))	$[M+K]^+$
117	744.4946	744.4940	0.8	PC(30:0)	$[M+K]^+$
118	744.5540	744.5538	0.3	PE(36:2)	$[M+H]^+$
119	745.4778	745.4779	0.1	PA(38:5)	$[M+Na]^+$
120	745.4978	745.4990	1.6	PG(32:0)	$[M+Na]^+$
121	745.6227	745.6218	1.2	PE-Cer(d40:1)	$[M+H]^+$
122	746.5701	746.5694	0.9	PE(36:1)	$[M+H]^+$
123	746.6061	746.6058	0.4	CerP(t42:1)	$[M+H]^+$
124	747.4714	747.4725	1.5	PA(O-38:5)	$[M+K]^+$
125	747.4929	747.4935	0.8	PA(38:4)	$[M+Na]^+$
126	748.5858	748.5851	0.9	PE(36:0)	$[M+H]^+$
127	749.5100	749.5092	1.1	PA(38:3)	$[M+Na]^+$
128	750.5421	750.5432	1.5	PE(O-38:6)	$[M+H]^+$
129	750.5856	750.5854	0.3	DGCC(32:0)	$[M+Na]^+$
130	751.5252	751.5248	0.5	PA(38:2)	$[M+Na]^+$
131	751.5731	751.5724	0.9	SM(d36:2)	$[M+Na]^+$
132	752.4116	752.4111	0.7	PI-Cer(t28:0)	$[M+K]^+$

17

133	752.4271	752.4263	1.1	LPS(32:4)	$[M+K]^+$
134	752.5074	752.5073	0.1	HexCer(t34:2)	$[M+K]^+$
135	752.5571	752.5565	0.8	PE(O-36:2)	$[M+Na]^+$
136	753.4835	753.4855	2.7	DG(44:11)	$[M+K]^+$
137	753.5886	753.5881	0.7	SM(d36:1)	$[M+Na]^+$
138	754.4788	754.4784	0.5	PE(34:2)	$[M+K]^+$
139	754.5364	754.5357	0.9	PC(32:1)	$[M+Na]^+$
140	755.4070	755.4049	2.8	PA(38:8)	$[M+K]^+$
141	755.4630	755.4624	0.8	PA(36:2(OH))	$[M+K]^+$
142	755.4996	755.4986	1.3	PA(P-40:6)	$[M+Na]^+$
143	755.5446	755.5464	2.4	PE-Cer(d38:1)	$[M+K]^+$
144	756.4944	756.4940	0.5	PE(34:1)	$[M+K]^+$
145	756.5519	756.5514	0.7	PC(32:0)	$[M+Na]^+$
146	757.4192	757.4191	0.1	SQDG(30:5)	$[M+H]^+$
147	758.4929	758.4943	1.8	PS(32:0)	$[M+Na]^+$
148	758.5104	758.5097	0.9	PE(34:0)	$[M+K]^+$
149	758.5711	758.5694	2.2	PC(34:2)	$[M+H]^+$
150	759.4360	759.4362	0.3	PA(38:6)	$[M+K]^+$
151	759.6383	759.6374	1.2	SM(d38:1)	$[M+H]^+$
152	760.4389	760.4371	2.4	PI-Cer(t30:2)	$[M+Na]^+$
153	760.4526	760.4524	0.3	LPS(34:6)	$[M+Na]^+$
154	760.5854	760.5851	0.4	PC(34:1)	$[M+H]^+$
155	761.4507	761.4504	0.4	SQDG(30:3)	$[M+H]^+$
156	762.4541	762.4528	1.7	PI-Cer(t30:1)	$[M+Na]^+$
157	762.4817	762.4834	2.2	PE(O-36:5)	$[M+K]^+$
158	762.6026	762.6007	2.5	PC(34:0)	$[M+H]^+$
159	763.4663	763.4661	0.3	SQDG(30:2)	$[M+H]^+$
160	764.4695	764.4684	1.4	PI-Cer(t30:0)	$[M+Na]^+$
161	764.4986	764.4991	0.7	PE(O-36:4)	$[M+K]^+$
162	765.4661	765.4677	2.1	PG(34:4)	$[M+Na]^+$
163	765.4840	765.4831	1.2	PA(38:3)	$[M+K]^+$
164	766.4274	766.4266	1.0	PS(32:4(OH))	$[M+Na]^+$
165	766.4870	766.4865	0.7	PI-Cer(t32:2)	$[M+H]^+$
166	766.5147	766.5147	< 0.1	PE(O-36:3)	$[M+K]^+$
167	766.5359	766.5357	0.3	PE(36:2)	$[M+Na]^+$
168	766.5592	766.5593	0.1	PS(O-34:0(OH))	$[M+H]^+$
169	766.5786	766.5803	2.2	HexCer(t36:1)	$[M+Na]^+$
170	767.4820	767.4834	1.8	PG(34:3)	$[M+Na]^+$
171	767.4993	767.4988	0.7	PA(38:2)	$[M+K]^+$
172	767.5178	767.5197	2.5	PA(38:2(OH))	$[M+Na]^+$
173	767.5468	767.5464	0.5	SM(d36:2)	$[M+K]^+$
174	768.5030	768.5021	1.2	PI-Cer(t32:1)	$[M+H]^+$
175	768.5306	768.5304	0.3	PE(O-36:2)	$[M+K]^+$
176	768.5515	768.5514	0.1	PE(36:1)	$[M+Na]^+$
177	768.5883	768.5878	0.7	CerP(t42:1)	$[M+Na]^+$

18

178	769.4784	769.4780	0.5	PG(O-34:3)	$[M+K]^+$
179	769.4985	769.4990	0.6	LBPA(34:2)	$[M+Na]^+$
180	769.5159	769.5144	1.9	PA(38:1)	$[M+K]^+$
181	769.5344	769.5354	1.3	PA(38:1(OH))	$[M+Na]^+$
182	769.5625	769.5620	0.6	SM(d36:1)	$[M+K]^+$
183	770.5103	770.5097	0.8	PC(32:1)	$[M+K]^+$
184	770.5659	770.5670	1.4	PE(36:0)	$[M+Na]^+$
185	771.4951	771.4959	1.0	PA(42:9)	$[M+H]^+$
186	771.5134	771.5147	1.7	LBPA(34:1)	$[M+Na]^+$
187	772.5257	772.5253	0.5	PC(32:0)	$[M+K]^+$
188	772.5634	772.5617	2.2	PE(O-36:0)	$[M+K]^+$
189	772.5840	772.5851	1.4	PE(38:2)	$[M+H]^+$
190	773.5290	773.5303	1.7	PG(34:0)	$[M+Na]^+$
191	774.6010	774.6007	0.4	PE(38:1)	$[M+H]^+$
192	775.4079	775.4063	2.1	SQDG(28:1)	$[M+K]^+$
193	775.5271	775.5272	0.1	PA(42:7)	$[M+H]^+$
194	775.5345	775.5355	1.3	MGDG(36:6)	$[M+H]^+$
195	776.4113	776.4111	0.3	PI-Cer(t30:2)	$[M+K]^+$
196	776.4624	776.4627	0.4	PE(36:5)	$[M+K]^+$
197	776.5596	776.5589	0.9	PE(P-40:6)	$[M+H]^+$
198	776.5927	776.5928	0.1	CerP(d44:3)	$[M+Na]^+$
199	776.6179	776.6164	1.9	PE(38:0)	$[M+H]^+$
200	777.4236	777.4220	2.1	SQDG(28:0)	$[M+K]^+$
201	778.4272	778.4267	0.6	PI-Cer(t30:1)	$[M+K]^+$
202	778.4768	778.4784	2.1	PE(36:4)	$[M+K]^+$
203	779.4799	779.4787	1.5	DGDG(24:1)	$[M+H]^+$
204	780.4424	780.4424	< 0.1	PI-Cer(t30:0)	$[M+K]^+$
205	780.4926	780.4940	1.8	PE(36:3)	$[M+K]^+$
206	780.5521	780.5514	0.9	PC(34:2)	$[M+Na]^+$
207	781.4189	781.4191	0.3	SQDG(32:7)	$[M+H]^+$
208	781.4762	781.4779	2.2	PPA(36:2)	$[M+H]^+$
209	781.4961	781.4944	2.2	DGDG(24:0)	$[M+H]^+$
210	781.6201	781.6194	0.9	SM(d38:1)	$[M+Na]^+$
211	782.5099	782.5097	0.3	PE(36:2)	$[M+K]^+$
212	782.5675	782.5670	0.6	PC(34:1)	$[M+Na]^+$
213	783.4349	783.4348	0.1	SQDG(32:6)	$[M+H]^+$
214	783.5544	783.5534	1.3	PG(O-38:5)	$[M+H]^+$
215	784.5257	784.5253	0.5	PE(36:1)	$[M+K]^+$
216	784.5602	784.5617	1.9	CerP(t42:1)	$[M+K]^+$
217	784.5841	784.5851	1.3	PC(36:3)	$[M+H]^+$
218	785.4516	785.4518	0.3	PA(40:7)	$[M+K]^+$
219	785.5647	785.5667	2.5	PG(O-36:1)	$[M+Na]^+$
220	786.4840	786.4834	0.8	PE(P-38:6)	$[M+K]^+$
221	786.5046	786.5046	< 0.1	PC(32:1(OH))	$[M+K]^+$
222	786.5416	786.5410	0.8	PE(36:0)	$[M+K]^+$

19

223	786.6014	786.6007	0.9	PC(36:2)	$[M+H]^+$
224	787.4508	787.4521	1.7	PG(36:7)	$[M+Na]^+$
225	787.4680	787.4675	0.6	PA(40:6)	$[M+K]^+$
226	787.4875	787.4884	1.1	PA(40:6(OH))	$[M+Na]^+$
227	787.5077	787.5096	2.4	PG(34:1(OH))	$[M+Na]^+$
228	787.6688	787.6687	0.1	SM(d40:1)	$[M+H]^+$
229	788.4978	788.4991	1.6	PE(O-38:6)	$[M+K]^+$
230	788.5190	788.5201	1.4	PE(38:5)	$[M+Na]^+$
231	788.6165	788.6164	0.1	PC(36:1)	$[M+H]^+$
232	789.4828	789.4831	0.4	PA(40:5)	$[M+K]^+$
233	790.4863	790.4841	2.8	PI-Cer(t32:1)	$[M+Na]^+$
234	790.5139	790.5147	1.0	PE(O-38:5)	$[M+K]^+$
235	790.5356	790.5357	0.1	PE(38:4)	$[M+Na]^+$
236	791.4973	791.4974	0.1	SQDG(32:2)	$[M+H]^+$
237	792.4982	792.4997	1.9	PI-Cer(t32:0)	$[M+Na]^+$
238	792.5298	792.5304	0.8	PE(O-38:4)	$[M+K]^+$
239	792.5540	792.5538	0.3	PE(40:6)	$[M+H]^+$
240	792.5667	792.5668	0.1	CerP(d44:3)	$[M+K]^+$
241	793.4187	793.4181	0.8	PPA(34:1)	$[M+K]^+$
242	793.4762	793.4779	2.1	PA(42:9)	$[M+Na]^+$
243	793.5019	793.5014	0.6	PG(38:7)	$[M+H]^+$
244	793.5144	793.5144	< 0.1	PA(40:3)	$[M+K]^+$
245	793.5575	793.5589	1.8	PG(36:1(OH))	$[M+H]^+$
246	794.5078	794.5083	0.6	SHexCer(t34:2)	$[M+H]^+$
247	794.5174	794.5178	0.5	PI-Cer(t34:2)	$[M+H]^+$
248	794.5458	794.5460	0.3	PE(O-38:3)	$[M+K]^+$
249	794.5835	794.5824	1.4	CerP(d44:2)	$[M+K]^+$
250	794.6106	794.6116	1.3	HexCer(t38:1)	$[M+Na]^+$
251	795.4943	795.4937	0.8	PG(O-36:4)	$[M+K]^+$
252	795.5305	795.5301	0.5	PA(40:2)	$[M+K]^+$
253	795.5497	795.5510	1.6	PA(40:2(OH))	$[M+Na]^+$
254	796.5255	796.5253	0.3	PC(34:2)	$[M+K]^+$
255	796.5617	796.5617	< 0.1	PE(O-38:2)	$[M+K]^+$
256	796.5846	796.5851	0.6	PE(40:4)	$[M+H]^+$
257	797.5099	797.5093	0.8	PG(O-36:3)	$[M+K]^+$
258	797.5291	797.5303	1.5	LBPA(36:2)	$[M+Na]^+$
259	797.5655	797.5667	1.5	PA(40:1(OH))	$[M+Na]^+$
260	797.5932	797.5933	0.1	SM(d38:1)	$[M+K]^+$
261	798.5410	798.5410	< 0.1	PC(34:1)	$[M+K]^+$
262	798.5965	798.5983	2.3	PE(38:0)	$[M+Na]^+$
263	799.4085	799.4063	2.8	SQDG(30:3)	$[M+K]^+$
264	799.5444	799.5460	2.0	PG(36:1)	$[M+Na]^+$
265	800.4617	800.4627	1.2	PE(38:7)	$[M+K]^+$
266	800.5576	800.5566	1.2	PC(34:0)	$[M+K]^+$
267	800.6162	800.6164	0.2	PE(40:2)	$[M+H]^+$

20

268	801.4236	801.4220	2.0	SQDG(30:2)	$[M+K]^+$
269	801.5432	801.5430	0.2	TG(46:8)	$[M+K]^+$
270	801.5606	801.5616	1.2	PG(36:0)	$[M+Na]^+$
271	802.4784	802.4784	< 0.1	PE(38:6)	$[M+K]^+$
272	802.6321	802.6320	0.1	PE(40:1)	$[M+H]^+$
273	803.4385	803.4376	1.1	SQDG(30:1)	$[M+K]^+$
274	803.4593	803.4599	0.7	PPA(36:2)	$[M+Na]^+$
275	803.4818	803.4835	2.1	PG(34:1(OH))	$[M+K]^+$
276	803.5594	803.5586	1.0	TG(46:7)	$[M+K]^+$
277	803.5658	803.5668	1.2	MGDG(38:6)	$[M+H]^+$
278	804.4417	804.4424	0.9	PI-Cer(t32:2)	$[M+K]^+$
279	804.4923	804.4940	2.1	PE(38:5)	$[M+K]^+$
280	804.5512	804.5514	0.2	PC(36:4)	$[M+Na]^+$
281	804.6111	804.6113	0.2	PC(36:1(OH))	$[M+H]^+$
282	805.4547	805.4533	1.7	SQDG(30:0)	$[M+K]^+$
283	805.4957	805.4944	1.6	DGDG(26:2)	$[M+H]^+$
284	806.4573	806.4580	0.9	PI-Cer(t32:1)	$[M+K]^+$
285	806.5089	806.5097	1.0	PE(38:4)	$[M+K]^+$
286	806.5697	806.5694	0.4	PC(38:6)	$[M+H]^+$
287	806.6474	806.6480	0.7	HexCer(d40:1)	$[M+Na]^+$
288	807.4343	807.4348	0.6	SQDG(34:8)	$[M+H]^+$
289	807.5122	807.5100	2.7	DGDG(26:1)	$[M+H]^+$
290	808.4730	808.4737	0.9	PI-Cer(t32:0)	$[M+K]^+$
291	808.4869	808.4888	2.4	PE(40:9)	$[M+Na]^+$
292	808.5677	808.5698	2.6	PI-Cer(d36:1)	$[M+H]^+$
293	808.5839	808.5851	1.5	PC(38:5)	$[M+H]^+$
294	809.4498	809.4504	0.7	SQDG(34:7)	$[M+H]^+$
295	809.5713	809.5691	2.7	PG(O-40:6)	$[M+H]^+$
296	809.6506	809.6507	0.1	SM(d40:1)	$[M+Na]^+$
297	810.4334	810.4318	2.0	PS(34:4(OH))	$[M+K]^+$
298	810.5409	810.5410	0.1	PE(38:2)	$[M+K]^+$
299	810.5990	810.5983	0.9	PC(36:1)	$[M+Na]^+$
300	810.6813	810.6817	0.5	HexCer(d42:2)	$[M+H]^+$
301	811.4507	811.4521	1.7	PG(38:9)	$[M+Na]^+$
302	811.4677	811.4675	0.2	PA(42:8)	$[M+K]^+$
303	811.5850	811.5847	0.4	PG(O-40:5)	$[M+H]^+$
304	812.4981	812.4991	1.2	PE(P-40:7)	$[M+K]^+$
305	812.5195	812.5201	0.7	PE(40:7)	$[M+Na]^+$
306	812.5399	812.5412	1.6	PS(36:1)	$[M+Na]^+$
307	812.5568	812.5566	0.2	PE(38:1)	$[M+K]^+$
308	812.5908	812.5930	2.7	CerP(t44:1)	$[M+K]^+$
309	813.4834	813.4831	0.4	PA(42:7)	$[M+K]^+$
310	813.5017	813.5041	3.0	PA(42:7(OH))	$[M+Na]^+$
311	813.5229	813.5252	2.8	PG(36:2(OH))	$[M+Na]^+$
312	813.6841	813.6844	0.4	SM(d42:2)	$[M+H]^+$

21

313	814.5151	814.5147	0.5	PE(P-40:6)	$[M+K]^+$
314	814.5358	814.5359	0.1	PC(34:1(OH))	$[M+K]^+$
315	814.5556	814.5569	1.6	PS(36:0)	$[M+Na]^+$
316	814.6318	814.6320	0.2	PC(38:2)	$[M+H]^+$
317	815.5186	815.5197	1.3	PA(42:6(OH))	$[M+Na]^+$
318	815.5393	815.5409	2.0	PG(36:1(OH))	$[M+Na]^+$
319	815.6998	815.7000	0.2	SM(d42:1)	$[M+H]^+$
320	816.4941	816.4940	0.1	PC(36:6)	$[M+K]^+$
321	816.5290	816.5304	1.7	PE(O-40:6)	$[M+K]^+$
322	816.6476	816.6477	0.1	PC(38:1)	$[M+H]^+$
323	817.5142	817.5144	0.2	PA(42:5)	$[M+K]^+$
324	818.5101	818.5097	0.5	PC(36:5)	$[M+K]^+$
325	818.5448	818.5460	1.5	PE(O-40:5)	$[M+K]^+$
326	820.5255	820.5253	0.2	PC(36:4)	$[M+K]^+$
327	820.5853	820.5851	0.2	PE(42:6)	$[M+H]^+$
328	820.6057	820.6062	0.6	PS(38:0)	$[M+H]^+$
329	821.5289	821.5303	1.7	PG(38:4)	$[M+Na]^+$
330	821.5888	821.5902	1.7	PG(38:1(OH))	$[M+H]^+$
331	822.5410	822.5410	< 0.1	PC(36:3)	$[M+K]^+$
332	822.6215	822.6219	0.5	PS(O-38:0(OH))	$[M+H]^+$
333	822.6425	822.6429	0.5	HexCer(t40:1)	$[M+Na]^+$
334	823.4081	823.4063	2.2	SQDG(32:5)	$[M+K]^+$
335	823.5272	823.5272	< 0.1	PA(46:11)	$[M+H]^+$
336	823.5448	823.5460	1.5	PG(38:3)	$[M+Na]^+$
337	823.5622	823.5614	1.0	PA(42:2)	$[M+K]^+$
338	823.6080	823.6090	1.2	SM(d40:2)	$[M+K]^+$
339	824.4608	824.4627	2.3	PE(40:9)	$[M+K]^+$
340	824.5566	824.5566	< 0.1	PC(36:2)	$[M+K]^+$
341	824.6159	824.6164	0.6	PE(42:4)	$[M+H]^+$
342	824.6363	824.6376	1.6	HexCer(d40:0)	$[M+K]^+$
343	824.6570	824.6586	1.9	HexCer(t40:0)	$[M+Na]^+$
344	825.4238	825.4220	2.2	SQDG(32:4)	$[M+K]^+$
345	825.4640	825.4631	1.1	DGDG(28:6)	$[M+H]^+$
346	825.5599	825.5616	2.1	PG(38:2)	$[M+Na]^+$
347	825.6237	825.6246	1.1	SM(d40:1)	$[M+K]^+$
348	826.4766	826.4784	2.2	PE(40:8)	$[M+K]^+$
349	826.4995	826.4995	< 0.1	PS(36:2)	$[M+K]^+$
350	826.5721	826.5721	< 0.1	PE(P-42:6)	$[M+Na]^+$
351	827.4396	827.4376	2.4	SQDG(32:3)	$[M+K]^+$
352	827.4800	827.4787	1.6	DGDG(28:5)	$[M+H]^+$
353	827.5755	827.5773	2.2	PG(38:1)	$[M+Na]^+$
354	827.6401	827.6403	0.2	SM(d40:0)	$[M+K]^+$
355	828.4925	828.4940	1.8	PE(40:7)	$[M+K]^+$
356	828.5145	828.5150	0.6	PE(40:7(OH))	$[M+Na]^+$
357	828.5520	828.5515	0.6	PE(38:1(OH))	$[M+K]^+$

22

358	828.6453	828.6453	< 0.1	PE(O-40:0(OH))	$[M+Na]^+$
359	829.4547	829.4533	1.7	SQDG(32:2)	$[M+K]^+$
360	829.4960	829.4944	1.9	DGDG(28:4)	$[M+H]^+$
361	829.5750	829.5743	0.8	TG(48:8)	$[M+K]^+$
362	830.5099	830.5097	0.2	PE(40:6)	$[M+K]^+$
363	830.5286	830.5306	2.4	PE(40:6(OH))	$[M+Na]^+$
364	830.5578	830.5600	2.6	LacCer(d30:0)	$[M+Na]^+$
365	830.5672	830.5672	< 0.1	PE(38:0(OH))	$[M+K]^+$
366	830.6266	830.6269	0.4	PC(38:2(OH))	$[M+H]^+$
367	830.6634	830.6633	0.1	PE(42:1)	$[M+H]^+$
368	831.4342	831.4348	0.7	SQDG(36:10)	$[M+H]^+$
369	831.4695	831.4689	0.7	SQDG(32:1)	$[M+K]^+$
370	831.4918	831.4937	2.3	PA(42:6(OH))	$[M+K]^+$
371	831.5132	831.5148	1.9	PG(36:1(OH))	$[M+K]^+$
372	832.4718	832.4737	2.3	PI-Cer(t34:2)	$[M+K]^+$
373	832.5101	832.5099	0.2	PS(38:5)	$[M+Na]^+$
374	832.5833	832.5827	0.7	PC(38:4)	$[M+Na]^+$
375	832.6430	832.6426	0.5	PC(38:1(OH))	$[M+H]^+$
376	832.6628	832.6637	1.1	HexCer(d42:2)	$[M+Na]^+$
377	833.4502	833.4504	0.2	SQDG(36:9)	$[M+H]^+$
378	833.4855	833.4846	1.1	SQDG(32:0)	$[M+K]^+$
379	833.5259	833.5257	0.2	DGDG(28:2)	$[M+H]^+$
380	833.6485	833.6507	2.6	SM(d42:3)	$[M+Na]^+$
381	834.5400	834.5410	1.2	PE(40:4)	$[M+K]^+$
382	834.6012	834.6007	0.6	PC(40:6)	$[M+H]^+$
383	834.6788	834.6793	0.6	HexCer(d42:1)	$[M+Na]^+$
384	835.4658	835.4661	0.4	SQDG(36:8)	$[M+H]^+$
385	835.5434	835.5413	2.5	DGDG(28:1)	$[M+H]^+$
386	835.6656	835.6663	0.8	SM(d42:2)	$[M+Na]^+$
387	836.4970	836.4955	1.8	SHexCer(t34:0)	$[M+K]^+$
388	836.5180	836.5201	2.5	PE(42:9)	$[M+Na]^+$
389	836.5996	836.6011	1.8	PI-Cer(d38:1)	$[M+H]^+$
390	836.6125	836.6140	1.8	PC(38:2)	$[M+Na]^+$
391	836.6370	836.6375	0.6	DGTA(40:5)	$[M+Na]^+$
392	837.6407	837.6426	2.3	MGDG(38:0)	$[M+Na]^+$
393	837.6825	837.6820	0.6	SM(d42:1)	$[M+Na]^+$
394	838.4398	838.4420	2.6	PE(40:10(OH))	$[M+K]^+$
395	838.5727	838.5723	0.5	PE(40:2)	$[M+K]^+$
396	838.6157	838.6168	1.3	PI-Cer(d38:0)	$[M+H]^+$
397	838.6304	838.6296	1.0	PC(38:1)	$[M+Na]^+$
398	839.4988	839.4988	< 0.1	PA(44:8)	$[M+K]^+$
399	840.5511	840.5514	0.4	PE(42:7)	$[M+Na]^+$
400	840.5878	840.5878	< 0.1	PC(P-40:6)	$[M+Na]^+$
401	840.6227	840.6243	1.9	CerP(t46:1)	$[M+K]^+$
402	840.6328	840.6325	0.4	HexCer(t40:0)	$[M+K]^+$

23

403	841.5544	841.5565	2.5	PG(38:2(OH))	$[M+Na]^+$
404	841.6177	841.6195	2.1	SM(t40:1)	$[M+K]^+$
405	842.5100	842.5097	0.4	PC(38:7)	$[M+K]^+$
406	842.5669	842.5670	0.1	PE(42:6)	$[M+Na]^+$
407	842.6381	842.6399	2.1	CerP(t46:0)	$[M+K]^+$
408	842.6623	842.6633	1.2	PC(40:2)	$[M+H]^+$
409	843.5134	843.5147	1.5	PG(40:7)	$[M+Na]^+$
410	843.5702	843.5722	2.4	PG(38:1(OH))	$[M+Na]^+$
411	843.6352	843.6352	< 0.1	SM(t40:0)	$[M+K]^+$
412	844.5076	844.5101	3.0	PI-Cer(d36:2)	$[M+K]^+$
413	844.5253	844.5253	< 0.1	PC(38:6)	$[M+K]^+$
414	844.6783	844.6790	0.8	PC(40:1)	$[M+H]^+$
415	845.5287	845.5303	1.9	PG(40:6)	$[M+Na]^+$
416	846.4659	846.4682	2.7	PS(38:6)	$[M+K]^+$
417	846.5255	846.5257	0.2	PI-Cer(d36:1)	$[M+K]^+$
418	846.5409	846.5410	0.1	PC(38:5)	$[M+K]^+$
419	846.6008	846.6007	0.1	PE(44:7)	$[M+H]^+$
420	846.6213	846.6219	0.7	PS(40:1)	$[M+H]^+$
421	847.4061	847.4063	0.2	SQDG(34:7)	$[M+K]^+$
422	847.5456	847.5460	0.5	PG(40:5)	$[M+Na]^+$
423	847.6639	847.6663	2.8	PE-Cer(d46:3)	$[M+Na]^+$
424	848.4815	848.4837	2.6	PE(42:11(OH))	$[M+Na]^+$
425	848.5567	848.5566	0.1	PC(38:4)	$[M+K]^+$
426	848.6163	848.6164	0.1	PE(44:6)	$[M+H]^+$
427	848.6370	848.6375	0.6	PS(40:0)	$[M+H]^+$
428	848.6576	848.6586	1.2	HexCer(t42:2)	$[M+Na]^+$
429	849.4240	849.4220	2.4	SQDG(34:6)	$[M+K]^+$
430	849.5600	849.5616	1.9	PG(40:4)	$[M+Na]^+$
431	849.6214	849.6215	0.1	PG(40:1(OH))	$[M+H]^+$
432	850.4764	850.4784	2.4	PE(42:10)	$[M+K]^+$
433	850.5710	850.5709	0.1	SHexCer(t38:2)	$[M+H]^+$
434	850.6520	850.6532	1.4	PS(O-40:0(OH))	$[M+H]^+$
435	850.6736	850.6742	0.7	HexCer(t42:1)	$[M+Na]^+$
436	851.4392	851.4376	1.9	SQDG(34:5)	$[M+K]^+$
437	851.4800	851.4810	1.2	PGP(34:1)	$[M+Na]^+$
438	851.5587	851.5585	0.2	PA(48:11)	$[M+H]^+$
439	851.5758	851.5773	1.8	PG(40:3)	$[M+Na]^+$
440	851.6392	851.6403	1.3	SM(d42:2)	$[M+K]^+$
441	852.4918	852.4940	2.6	PE(42:9)	$[M+K]^+$
442	852.5130	852.5150	2.3	PE(42:9(OH))	$[M+Na]^+$
443	852.5876	852.5879	0.4	PC(38:2)	$[M+K]^+$
444	852.6448	852.6453	0.6	PE(42:1)	$[M+Na]^+$
445	852.6825	852.6817	0.9	CerP(t48:1)	$[M+Na]^+$
446	853.4185	853.4167	2.1	SQDG(36:10)	$[M+Na]^+$
447	853.4952	853.4944	0.9	DGDG(30:6)	$[M+H]^+$

24

448	853.5909	853.5929	2.3	PG(40:2)	$[M+Na]^+$
449	853.6558	853.6559	0.1	SM(d42:1)	$[M+K]^+$
450	854.4977	854.4967	1.2	PS(42:11)	$[M+H]^+$
451	854.5303	854.5306	0.4	PE(42:8(OH))	$[M+Na]^+$
452	854.5675	854.5672	0.4	PE(40:2(OH))	$[M+K]^+$
453	854.6035	854.6036	0.1	PC(38:1)	$[M+K]^+$
454	854.6389	854.6399	1.2	PE(O-42:1)	$[M+K]^+$
455	854.6594	854.6609	1.8	PE(42:0)	$[M+Na]^+$
456	855.4913	855.4937	2.8	PA(44:8(OH))	$[M+K]^+$
457	855.6067	855.6086	2.2	PG(40:1)	$[M+Na]^+$
458	856.5241	856.5253	1.4	PE(42:7)	$[M+K]^+$
459	856.5457	856.5463	0.7	PE(42:7(OH))	$[M+Na]^+$
460	856.5828	856.5828	< 0.1	PE(40:1(OH))	$[M+K]^+$
461	857.4505	857.4480	2.9	SQDG(36:8)	$[M+Na]^+$
462	858.5044	858.5044	< 0.1	PE(44:12)	$[M+Na]^+$
463	858.5248	858.5256	0.9	PS(40:6)	$[M+Na]^+$
464	858.5416	858.5410	0.7	PE(42:6)	$[M+K]^+$
465	858.5609	858.5619	1.2	PE(42:6(OH))	$[M+Na]^+$
466	858.5891	858.5913	2.6	LacCer(d32:0)	$[M+Na]^+$
467	859.5450	859.5461	1.3	PG(38:1(OH))	$[M+K]^+$
468	860.5198	860.5201	0.3	PE(44:11)	$[M+Na]^+$
469	860.6148	860.6140	0.9	PC(40:4)	$[M+Na]^+$
470	861.5175	861.5159	1.9	SQDG(34:0)	$[M+K]^+$
471	862.5338	862.5357	2.2	PE(44:10)	$[M+Na]^+$
472	862.6160	862.6168	0.9	PI-Cer(d40:2)	$[M+H]^+$
473	864.4552	864.4576	2.8	PE(42:11(OH))	$[M+K]^+$
474	864.6315	864.6324	1.0	PI-Cer(d40:1)	$[M+H]^+$
475	866.6474	866.6481	0.8	PI-Cer(d40:0)	$[M+H]^+$
476	867.4537	867.4549	1.4	PGP(34:1)	$[M+K]^+$
477	867.6585	867.6603	2.1	PA(O-46:1)	$[M+K]^+$
478	868.5253	868.5253	< 0.1	PC(40:8)	$[M+K]^+$
479	868.6190	868.6191	0.1	PC(P-42:6)	$[M+Na]^+$
480	868.6531	868.6556	2.9	CerP(t48:1)	$[M+K]^+$
481	868.6623	868.6638	1.7	HexCer(t42:0)	$[M+K]^+$
482	869.6496	869.6508	1.4	SM(t42:1)	$[M+K]^+$
483	870.4661	870.4682	2.4	PS(40:8)	$[M+K]^+$
484	870.5409	870.5410	0.1	PC(40:7)	$[M+K]^+$
485	870.6938	870.6946	0.9	PC(42:2)	$[M+H]^+$
486	871.5443	871.5460	2.0	PG(42:7)	$[M+Na]^+$
487	872.5566	872.5566	< 0.1	PC(40:6)	$[M+K]^+$
488	873.4235	873.4220	1.7	SQDG(36:8)	$[M+K]^+$
489	873.5600	873.5616	1.8	PG(42:6)	$[M+Na]^+$
490	874.4775	874.4784	1.0	PE(44:12)	$[M+K]^+$
491	874.4993	874.4993	< 0.1	PE(44:12(OH))	$[M+Na]^+$
492	874.5550	874.5570	2.3	PI-Cer(d38:1)	$[M+K]^+$

25

493	875.5028	875.5045	1.9	LPIP(32:1)	$[M+H]^+$
494	876.5129	876.5150	2.4	PE(44:11(OH))	$[M+Na]^+$
495	876.5636	876.5631	0.6	SHexCer(d38:0)	$[M+K]^+$
496	876.5878	876.5879	0.1	PC(40:4)	$[M+K]^+$
497	877.5912	877.5929	1.9	PG(42:4)	$[M+Na]^+$
498	878.5073	878.5097	2.7	PE(44:10)	$[M+K]^+$
499	878.5280	878.5306	3.0	PE(44:10(OH))	$[M+Na]^+$
500	879.5107	879.5100	0.8	DGDG(32:7)	$[M+H]^+$
501	880.5233	880.5253	2.3	PE(44:9)	$[M+K]^+$
502	880.5449	880.5463	1.6	PE(44:9(OH))	$[M+Na]^+$
503	880.6184	880.6178	0.7	SHexCer(t40:1)	$[M+H]^+$
504	881.6219	881.6242	2.6	PG(42:2)	$[M+Na]^+$
505	882.6344	882.6347	0.3	PE(P-46:6)	$[M+Na]^+$
506	883.6376	883.6399	2.6	PG(42:1)	$[M+Na]^+$
507	888.5509	888.5514	0.6	PE(46:11)	$[M+Na]^+$
508	892.5255	892.5253	0.2	PC(42:10)	$[M+K]^+$
509	892.6612	892.6637	2.8	PI-Cer(d42:1)	$[M+H]^+$
510	895.6905	895.6916	1.2	PA(O-48:1)	$[M+K]^+$
511	896.6498	896.6504	0.7	PC(P-44:6)	$[M+Na]^+$
512	897.4846	897.4865	2.1	LPIP(32:1)	$[M+Na]^+$
513	898.4893	898.4900	0.8	MIPC(t28:0)	$[M+Na]^+$
514	898.5723	898.5723	< 0.1	PC(42:7)	$[M+K]^+$
515	899.5759	899.5773	1.6	PG(44:7)	$[M+Na]^+$
516	904.5228	904.5253	2.8	PE(46:11)	$[M+K]^+$
517	904.5456	904.5463	0.8	PE(46:11(OH))	$[M+Na]^+$
518	905.4944	905.4941	0.3	PI(P-38:6)	$[M+K]^+$
519	907.5414	907.5413	0.1	DGDG(34:7)	$[M+H]^+$
520	908.6496	908.6491	0.6	SHexCer(t42:1)	$[M+H]^+$
521	909.5461	909.5463	0.2	Glc-GP(38:4)	$[M+Na]^+$
522	909.6529	909.6555	2.9	PG(44:2)	$[M+Na]^+$
523	909.6696	909.6709	1.4	PA(48:1)	$[M+K]^+$
524	910.6657	910.6660	0.3	PE(P-48:6)	$[M+Na]^+$
525	911.6688	911.6712	2.6	PG(44:1)	$[M+Na]^+$
526	913.4586	913.4604	2.0	LPIP(32:1)	$[M+K]^+$
527	915.5989	915.6015	2.8	DGDG(32:0)	$[M+Na]^+$
528	916.5252	916.5253	0.1	PC(44:12)	$[M+K]^+$
529	917.4674	917.4659	1.6	DGDG(32:7)	$[M+K]^+$
530	919.4706	919.4708	0.2	LPIP(34:4)	$[M+Na]^+$
531	919.6894	919.6916	2.4	PA(O-50:3)	$[M+K]^+$
532	920.5180	920.5202	2.4	PE(46:11(OH))	$[M+K]^+$
533	920.6930	920.6950	2.2	PI-Cer(d44:1)	$[M+H]^+$
534	921.5143	921.5124	2.1	PI(40:9(OH))	$[M+H]^+$
535	923.5043	923.5045	0.2	PIP(O-36:5)	$[M+H]^+$
536	925.5199	925.5202	0.3	CL(36:4)	$[M+H]^+$
537	926.5237	926.5213	2.6	MIPC(t30:0)	$[M+Na]^+$

26

538	931.5286	931.5307	2.3	PI(40:7)	$[M+Na]^+$
539	935.4442	935.4448	0.6	LPIP(34:4)	$[M+K]^+$
540	935.4967	935.4950	1.8	SQDG(42:11)	$[M+Na]^+$
541	936.6810	936.6804	0.6	SHexCer(t44:1)	$[M+H]^+$
542	937.7005	937.7022	1.8	PA(50:1)	$[M+K]^+$
543	941.4915	941.4917	0.2	PIP(O-34:1)	$[M+K]^+$
544	945.4870	945.4865	0.5	PIP(O-36:5)	$[M+Na]^+$
545	947.5024	947.5021	0.3	CL(36:4)	$[M+Na]^+$
546	959.4448	959.4448	< 0.1	PIP(P-36:5)	$[M+K]^+$
547	961.4604	961.4604	< 0.1	PIP(O-36:5)	$[M+K]^+$
548	961.5119	961.5106	1.4	SQDG(44:12)	$[M+Na]^+$
549	963.4762	963.4761	0.1	CL(36:4)	$[M+K]^+$
550	965.6161	965.6172	1.1	DGDG(36:3)	$[M+Na]^+$
551	969.4850	969.4865	1.5	PIP(P-38:6)	$[M+Na]^+$
552	969.5489	969.5465	2.5	PI(40:4(OH))	$[M+K]^+$
553	978.5228	978.5216	1.2	CDP-DG(34:2)	$[M+H]^+$
554	981.5897	981.5911	1.4	DGDG(36:3)	$[M+K]^+$
555	982.5922	982.5934	1.2	PS(48:8)	$[M+K]^+$
556	987.4758	987.4761	0.3	PIP(O-38:6)	$[M+K]^+$
557	987.5614	987.5628	1.4	SQDG(44:7)	$[M+K]^+$
558	989.5426	989.5419	0.7	SQDG(46:12)	$[M+Na]^+$
559	992.4220	992.4227	0.7	M(IP)2C(t20:0)	$[M+H]^+$

Supporting Table 3: Established protocol for hematoxylin and eosin staining. Tissue sections were submerged in solvents for the dedicated time.

Solvent	**Duration**
100 % ethanol	2 min
70 % ethanol	2 min
40 % ethanol	2 min
Aqua dest.	2 min
Hematoxylin	12 min
Tap water	10 min
1 % eosin Y	1 min
Aqua dest.	2 min
40 % ethanol	2 min
70 % ethanol	2 min
100 % ethanol	2 min
Xylene	2 min

References

1. Liebisch, G.; Vizcaíno, J.A.; Köfeler, H.; Trötzmüller, M.; Griffiths, W.J.; Schmitz, G.; Spener, F.; Wakelam, M.J.O. Shorthand notation for lipid structures derived from mass spectrometry. *Journal of Lipid Research* **2013**, *54*, 1523–1530, doi:10.1194/jlr.M033506.
2. Liebisch, G.; Fahy, E.; Aoki, J.; Dennis, E.A.; Durand, T.; Ejsing, C.S.; Fedorova, M.; Feussner, I.; Griffiths, W.J.; Köfeler, H.; et al. Update on LIPID MAPS classification, nomenclature, and shorthand notation for MS-derived lipid structures. *Journal of Lipid Research* **2020**, *61*, 1539–1555, doi:10.1194/jlr.S120001025.

Chapter III – Microglia

Lipid Signatures and Inter-Cellular Heterogeneity of Naïve and Lipopolysaccharide-Stimulated Human Microglia-like Cells

analytical chemistry

pubs.acs.org/ac Article

Lipid Signatures and Inter-Cellular Heterogeneity of Naïve and Lipopolysaccharide-Stimulated Human Microglia-like Cells

Max A. Müller, Norman Zweig, Bernhard Spengler, Maria Weinert, and Sven Heiles*

Cite This: *Anal. Chem.* 2023, 95, 11672–11679 Read Online

ACCESS | Metrics & More | Article Recommendations | Supporting Information

ABSTRACT: Microglia are non-neuronal cells, which reside in the central nervous system and are known to play an important role in health and disease. We investigated the lipidomic phenotypes of human naïve and stimulated microglia-like cells by atmospheric-pressure scanning microprobe matrix-assisted laser desorption/ionization mass spectrometry imaging (AP-SMALDI MSI). With lateral resolutions between 5 and 1.5 μm pixel size, we were able to chart lipid compositions of individual cells, enabling differentiation of cell lines and stimulation conditions. This allowed us to reveal local lipid heterogeneities in naïve and lipopolysaccharide (LPS)-stimulated cells. We were able to identify individual cells with elevated triglyceride (TG) levels and could show that the number of these TG-enriched cells increased with LPS stimulation as a hallmark for a proinflammatory phenotype. Additionally, the observed local abundance alterations of specific phosphatidylinositols (PIs) indicate a cell specific regulation of the PI metabolism.

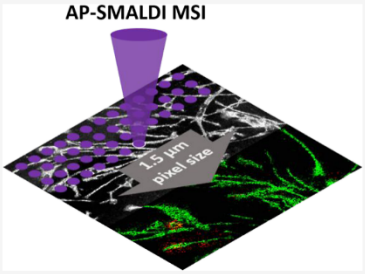

INTRODUCTION

Microglia are non-neuronal cells of the central nervous system[1] that play important roles in brain development, cellular maintenance,[2] and homeostasis.[3,4] They are the immune cells of the brain[5] and have been implicated in several neurodegenerative diseases, including Alzheimer's disease, Parkinson's disease, and multiple sclerosis.[6−10] Microglia respond to a changing micro-environment morphologically and through their protein expression pattern.[11−14] Both characteristics have been used historically to crudely define microglia phenotypes. It is still a matter of debate, however, how these different subsets of microglia contribute to homeostasis and disease.

Another access to cell function is to directly probe downstream products such as metabolites and their makeup by mass spectrometry, for which lipids are particularly attractive bioanalytes. Besides making up most of the cell membrane, lipids fulfill bioactive functions such as signaling[15] and energy storage[16] and are both directly affected by and are themselves affecting cell states.[17−19] In recent years, mass spectrometry imaging (MSI), especially matrix-assisted laser desorption/ionization (MALDI) MSI,[20,21] has been increasingly used for single-cell analysis in tissue or on cell cultures.[22] For example, a multimodal approach applying optical or fluorescence microscopy can be used to first identify single cells and then direct MS analysis toward the selected cells for sampling. Subsequently, the microscopy results can be used to yield a spatial distribution of the detected analytes.[23,24] If multiple measurements per cell are feasible, previously developed computational methods can be used to merge low-lateral-resolution MSI data into high-lateral-resolution images based on microscopy results.[25] In another approach, lateral resolution and sensitivity were improved to achieve sub-cellular lateral resolution on the low micrometer scale using MALDI MSI, applying specialized laser optics or boosting ion signal using post-ionization techniques.[26−28] For visualizing these cellular features, optimized sample preparation is key to preserve cellular morphology and bioanalytical composition as demonstrated by Bien and co-workers.[29] These MSI methods enable the spatial discrimination of cellular phenotypes and heterogeneity on a sub-cellular level, both in tissue and in vitro, based on lipid signatures.[17,30,31] Although lipidomic analyses of microglia cell lines have already been performed,[32,33] the approach or lateral resolution in previous studies did not allow for interrogation of single-cell heterogeneity.

Here, we used human-induced pluripotent stem cell (iPSC)-derived microglia-like cells (MGLCs) to investigate the heterogeneity between and within the cell lines by applying atmospheric-pressure scanning microprobe matrix-assisted laser desorption/ionization (AP-SMALDI) MSI.[20,21] Technical and preparative methods were optimized to achieve a pixel size of 1.5 μm, allowing for single-cell analysis. This enabled us to distinguish between otherwise isogenic cell lines, indicating a

Received: April 8, 2023
Accepted: July 19, 2023
Published: July 28, 2023

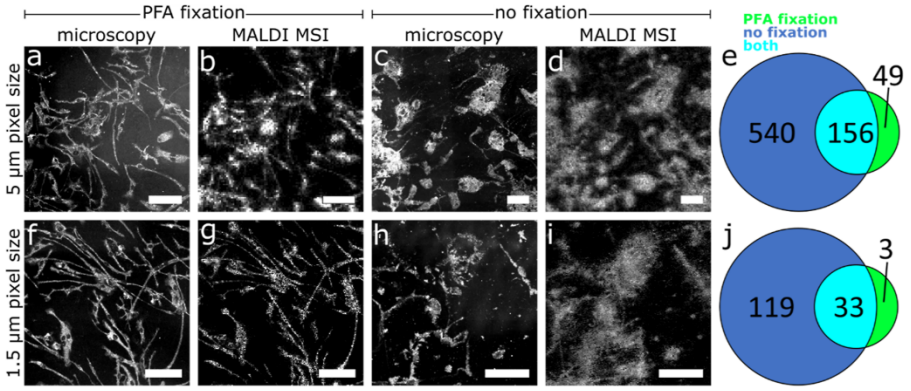

Figure 1. Effect of sample preparation and pixel size on the detection of lipids from iPSC-derived MGLCs. (a,c,f,h) Microscopic images. (b,d,g,i) AP-SMALDI MS images of PC 34:1 (m/z 896.6012, $[M + DHB-H_2O + H]^+$) at 5 or 1.5 μm pixel size. (b) LPS-stimulated MGLCs from the B8 cell line, 100 × 100 pixels, 5 μm pixel size (PFA fixation). (d) LPS-stimulated MGLCs from the D9 cell line, 150 × 150 pixels, 5 μm pixel size (no fixation). (g) Naïve MGLCs from the B8 cell line, 300 × 300 pixels, 1.5 μm pixel size (PFA fixation). (i) Naïve MGLCs from the E2 cell line, 250 × 250 pixels, 1.5 μm pixel size (no fixation). (e,j) Venn diagrams of individual lipid signals annotated to cells shown in (b,d,g,i), respectively, with fixation (green), without fixation (blue), or with both methods (cyan) for 5 μm (e) and 1.5 μm (j) measurements. Numbers represent unique lipid annotations with a mass deviation of <5 ppm, counting multiple adducts of the same lipid as only one lipid. Scale bars: 100 μm.

high sensitivity for detecting different subpopulations. We used AP-SMALDI MSI to identify individual molecular species involved in the well-established upregulation of triglycerides in MGLCs and classically activated with the proinflammatory stimulus lipopolysaccharide (LPS). Finally, our single-cell analysis revealed, for the first time, MGLC heterogeneity based on lipid classes and individual lipid species, despite a homogeneous microglia marker expression profile.

EXPERIMENTAL SECTION

Cell Cultures. MGLCs were differentiated from human iPSCs and cultured on glass slides. A detailed protocol on cell culture can be found in the Supporting Information. The cells were either fixed using paraformaldehyde (PFA) and stored in phosphate-buffered saline (PBS) at 4 °C or snap-frozen without PBS and stored at −80 °C.

Microscopy. Light microscopic images of samples investigated by AP-SMALDI MSI were obtained with a digital microscope (VHX 5000, Keyence GmbH, Neu Isenburg, Germany) after washing and prior to matrix application.

AP-SMALDI MSI. Matrix was applied using an ultra-fine pneumatic spraying system (SMALDIPrep, TransMIT GmbH). For measurements in positive-ion mode, 80 μL of a solution of 60 mg of 2,5-dihydroxybenzoic acid (DHB; Merck, Darmstadt, Germany) in a mixture of 999 μL of deionized water, 999 μL of acetone and 2 μL of pure trifluoroacetic acid (TFA; Merck) was applied to the samples. For measurements in negative-ion mode, 9-aminoacridine (9-AA; TCI Deutschland GmbH, Eschborn, Germany) was used. Samples for statistical analysis were covered with 300 μL of a solution of 10 mg/mL 9-AA in 70:30 ethanol/water. Samples intended for high-resolution AP-SMALDI MSI experiments were spray-coated with an optimized protocol using 160 μL of a solution of 7 mg/mL 9-AA in 60:40 acetone/water (Figure S1). AP-SMALDI MSI was performed with a custom-built ion source based on an AP-SMALDI5 AF system (TransMIT GmbH, Giessen, Germany). The ion source is equipped with a specialized focusing objective lens capable of producing ablation spots with an average diameter of <1 μm (Figure S2) in reflective geometry while retaining sufficient ion signal. The ablation spot diameter on a sample (i.e., the size of the area on which desorption and ionization were induced) is an important measure for achievable pixel size (i.e., the set distance between neighboring ablation spots) because the ablation spot diameter needs to be smaller than the pixel size to avoid oversampling. At the same time, the maximum intensity for a given pixel size setting requires maximizing the ablation spot diameter. In our setup, laser energy was adjusted to control the ablation spot diameter and at the same time maximize ion signals (Figure S3). Laser energy settings were kept constant for a given set of parameters, such as matrix material and pixel size, to allow for comparison of measurements with identical parameters. The distance between the end of the MS-inlet capillary and laser focal point was carefully optimized to yield a Gaussian ablation profile and maximize ion transmission. A distance of 4 mm was found to be optimal to have a preferably short distance for ions to cover while minimizing the reflection and cutoff of the laser beam by the inlet capillary, which would result in greatly reduced beam quality. The ion source was coupled to a Q Exactive (Thermo Fisher Scientific, Bremen, Germany) orbital trapping mass spectrometer. All measurements were performed with a mass resolution of 140,000 at m/z 200, and a high voltage of 2.5 kV in positive-ion mode or −3 kV in negative-ion mode was applied between the sample stage and inlet capillary, respectively, and automated gain control (AGC) was disabled.

Data Analysis. Data evaluation was performed using the Mirion[34] software to create MS images normalized to total ion charge[35] and to export data for statistical analysis. The latter was performed using Perseus software package.[36] The results of mass spectrometric data acquisition, based on signals averaged over the corresponding measurement area, were filtered for differences between the cell lines in naïve or LPS-stimulated state by an analysis of variance (ANOVA)-based

https://doi.org/10.1021/acs.analchem.3c01533
Anal. Chem. 2023, 95, 11672−11679

multiple-sample test followed by a principal component analysis (PCA). Additionally, cell line-specific differences between naïve and LPS-stimulated cells were investigated following the same workflow. Cluster analysis was performed using t-SNE, PCA, and k-means algorithms in Matlab (The Mathworks Inc., Natick, Massachusetts, USA). Violin plots were created using a Matlab script by Bechtold.[37] Automated signal annotations were performed using LIPID MAPS, allowing for $[M + H]^+$, $[M + Na]^+$, and $[M + K]^+$ ions in positive-ion mode and $[M - H]^-$ ions in negative-ion mode. Maximal mass deviation was selected to be <5 ppm (Table S1). $[M + DHB - H_2O + X]^+$ (X = H, Na, K) adducts were manually calculated for each signal and only considered if the corresponding signal without DHB adduction of a putative DHB adduct was also detected (Table S2). Metaspace,[38] applying the LIPID MAPS[39] or SwissLipids[40] databases, was used to pre-filter triglyceride annotations for further analysis or to evaluate salt content during optimization of sample pretreatment. Further, triglyceride species were manually evaluated as an additional criterion for quality control.

RESULTS AND DISCUSSION

High-Lateral-Resolution AP-SMALDI MSI Experiments of Microglia Cells. We commenced by studying the impact of sample preparation on lipidome coverage, lipid distributions, and cell morphology. For this purpose, different washing and fixation workflows were tested as summarized in Figures S4 and S5 and detailed in the methods section of the Supporting Information. While fixation of the cells with PFA best preserved the morphology (Figure 1a,b,f,g), signal intensities and thereby the number of unique lipid annotations were higher for snap-frozen cells (Figure 1c,d,h,i). A large fraction of the most intense lipid-associated signals was not affected by sample fixation, indicating that PFA does not induce major changes of the lipidome (Figure 1e,j). Further, the lipids annotated in the fixed samples were primarily a subset of those detected in the snap-frozen samples. The lipids found uniquely in one group might stem from cell-specific signals. The choice of solvents for matrix deposition also impacted lipid distribution patterns. Use of ethanol in solvent mixtures for 9-AA, for example, resulted in significant lipid delocalization (Figure S6), whereas DHB and 9-AA matrices sprayed with acetone-water solutions yielded lipid distributions coinciding with cell locations, as determined by optical microscopy (Figures S7–S9). For fixed and snap-frozen MGLCs, the number of annotations based on accurate mass measurements are reported in Figure 1e,j, and selected MS images are shown in Figure 1b,d,g,i. Mainly, phosphatidylcholine (PC), phosphatidylethanolamine (PE), phosphatidic acid (PA), phosphatidylserine (PS), and di- or triacylglyceride (DG or TG) lipids were detected in positive-ion mode as $[M + H]^+$, $[M + Na]^+$, $[M + K]^+$, or matrix adducts, e.g., $[M + DHB-H_2O + H]^+$ ions. In negative-ion mode, $[M - H]^-$ ions of phosphatidylinositols (PIs) dominated the spectra. The identity of the ion types was influenced by the fixation step when investigating the most likely lipid annotations for the measurements shown in Figure 1. In 5 μm pixel size measurements, the relative abundance of $[M + K]^+$ adducts was reduced (29–16%) after PFA fixation, whereas both $[M + H]^+$ (26–35%) and $[M + Na]^+$ (44–48%) adducts increased upon fixation. A similar trend and relative abundance were observed at 1.5 μm pixel size, indicating that pixel size does not alter preferred adduct formation. We further tested the effect of the ablation spot size, which was adjusted to match the chosen pixel size, on lipid class detection of MGLCs. Among the most intense signals, no major change of detected species with pixel size was observed in the mass spectra (Figure S10). However, less intense signals gradually fell under the detection threshold with decreasing pixel size due to the reduced ablation spot size. For example, at 5 μm pixel size, 696 unique lipid-associated signals were observed in at least 1% of all pixels, whereas at 1.5 μm pixel size, only 152 unique lipid-associated signals were detected under otherwise same conditions for the snap-frozen cells. When comparing lipid annotations at 5 or 1.5 μm pixel size, all major lipid classes were found to have reduced signal intensity to similar extents. On the other hand, fixation reduced the relative number of PS annotations while having no such effect on other lipid classes. This might be due to the amine group in the PS headgroup being especially prone to reactions with the PFA fixation reagent.[41] Most of our lipid annotations at 5 and 1.5 μm pixel size are in line with reports by Fitzner and co-workers on lipid extracts of mouse microglia using nano-electrospray ionization following liquid chromatographic separation, one of the most commonly used methods for high coverage lipid identification, yielding the most comprehensive database on the microglia lipidome in literature.[42]

In our 5 and 1.5 μm measurements, we were able to detect signals that correspond to 94 and 92% of the annotations presented in the work of Fitzner and co-workers, respectively, accepting a mass deviation of <0.05 m/z. The 6 and 8% of signals that could not be reproduced primarily corresponded to lysophospholipids. When only accepting a stricter mass deviation of <5 ppm, 47 and 37% could still be reproduced (Table S1). Similarly, we also detected additional lipid-associated signals from all lipid classes that were not covered by Fitzner and co-workers.

This indicates that our AP-SMALDI MSI workflow is able to sample a large fraction of all glycerol-, sphingo-, and glycerophospholipids. Annotation numbers are reduced at a higher lateral resolution of 1.5 μm pixel size, but individual and overlapping cells are better resolved. This is the first time single cells are resolved at such high lateral resolution without applying post-ionization techniques.[28] Especially, acquisition of the fine branched cell protrusions benefits from high lateral resolution and PFA-fixation (Figures 1 and S11). At the same time, the ion intensity remained high enough in our measurements to facilitate a high pixel coverage of up to 96, 91, or 75% (Figure S12) on MGLCs at 5, 2, or 1.5 μm pixel size, respectively, minimizing the occurrence of blank pixels. This is in line with previous results, which showed that a short fixation is beneficial for preserving cell morphology while limiting the loss in ion signal through fixation and chemical modification.[29] Therefore, we employed 5 μm pixel size to compare lipid signatures between samples and switched to higher lateral resolution to study the spatial distribution of selected lipid classes or individual lipid ion signals within the samples.

Differentiation between Cell Lines and Activation Profile. Next, we investigated the ability to discern inter-cell-line heterogeneity of naïve and LPS-stimulated MGLCs based on lipid signatures recorded in positive- and negative-ion modes at 5 μm pixel size. Three biological replicates cultured in separate wells on the same glass slide, each containing a multitude of individual cells, were investigated per cell line and stimulation status.

https://doi.org/10.1021/acs.analchem.3c01533
Anal. Chem. 2023, 95, 11672–11679

When comparing AP-SMALDI MSI results of different cell lines or of naïve and LPS-stimulated cells of the same cell line, some signals were only detected in one group, while others had a similar abundance in all observed groups (Figures 2e,f and S13). Data is averaged over all the cells measured per sample, and biological triplicates were investigated. PCA groups data of biological triplicates of identical cell lines (Figures 2a,b and S14) and separates them from the other cell lines based on the first and second principal components. Naïve and LPS-stimulated states of the same cell line (Figures 2c and S14) are also separated from each other, while biological triplicates group together. This allows distinguishing cell lines or activation status based on AP-SMALDI MSI results. Especially, LPS stimulation influences the lipidomic profiles of cells (Figures 2c and S14). In the PCA plot, the separation along the first principal component alone (making up between 78.2 and 91.4% of total variance in positive-ion mode and 91.0–95.4% of total variance in negative-ion mode) allows for differentiation of the stimulation status. A major contribution to this separation relates to TG species.

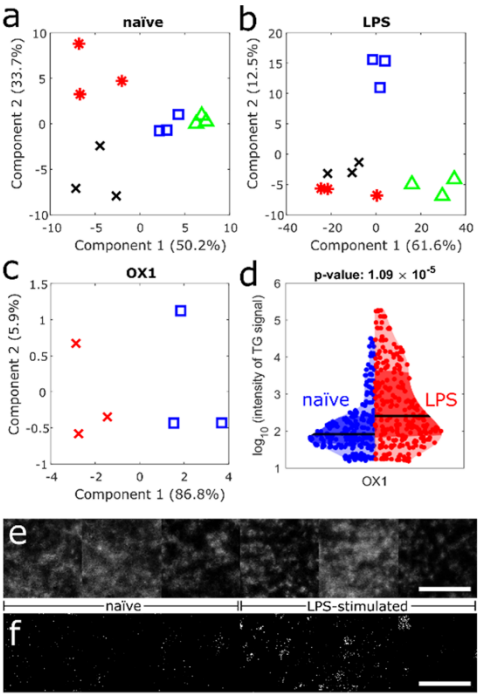

Figure 2. Cell-line heterogeneity assessed by AP-SMALDI MSI. (a–c) PCA of AP-SMALDI MSI results in positive-ion mode using an ANOVA-based multiple sample test. Significance of the signals was evaluated using p-values of <0.01. (a) Cell lines OX1 (red, star), D9 (green, triangle), C12 (blue, square), and E2 (black, ×) in naïve state. (b) Cell lines OX1 (red, star), D9 (green, triangle), C12 (blue, square), and E2 (black, ×) in LPS-stimulated state. (c) Naïve (blue, square) and LPS-stimulated (red, ×) cells of the OX1 cell line. (d) Violin plot of 252 TG-associated signal intensities at 5 μm pixel size for naïve (blue) and LPS-stimulated (red) OX1 cells averaged over all cells of the three biological replicates of the cell line. Black line indicates median. p-Value is calculated by the double-sided t-test. (e,f) AP-SMALDI MS image of PC 34:1 [(e) m/z 896.6140, $[M + DHB - H_2O + H]^+$], or DG O-38:8 [(f) m/z 661.4593, $[M + K]^+$] of biological triplicates of the OX1 cell line, each in naïve and LPS-stimulated state at 5 μm pixel size, showing homogeneous or heterogeneous distributions. Scale bars: 500 μm.

When comparing the averaged intensity per cell line and stimulation status of all signals annotated as TGs by Metaspace[38] using the LIPIDMAPS database,[39] TG intensities in LPS-stimulated MGLCs are significantly increased (p-values of 1.09×10^{-5}, 6.95×10^{-6}, and 6.73×10^{-4} for OX1, C12, and E2 cell lines, respectively) over naïve cells (Figures 2d and S15), consistent with earlier reports regarding macrophage cell lines.[43,44] Further, LPS-stimulated cells showed a higher number of individual TG-associated signals (Figures S16 and S17), with an average increase of 8.4-, 2.4-, and 4.4-fold relative to naïve cells in OX1, C12, and E2 lines, respectively. Only the D9 cell line showed an opposing behavior with the number of TGs, and the mean intensity of TG signals remained virtually unchanged in naïve compared to that in LPS-stimulated cells (Figures S15–S17), which is driven by an increased number of TG signals in the naïve state, rather than a missing reaction to LPS stimulation (Figure S15). Although the MGLCs of D9 expressed the conventional myeloid markers CD14 and CD11b, indicating successful differentiation, the cell yield and time of productivity of the D9 cell factories were consistently lower compared to those of all other cell lines (Figure S18). The lack of MGLC precursor proliferation and increased TG signal intensities are consistent with a premature senescence of D9 mesodermal factories.[45] TGs are known to be the main component of lipid droplets (LDs) in cells.[46] In microglia, reports indicate that lipid droplets play a major role during metabolic changes such as glucose deprivation[47] and that their accumulation is associated with a pro-inflammatory phenotype[18] and inflammatory response mechanisms, such as those elicited by LPS.[48,49] AP-SMALDI MSI allows elucidation of the composition of these TG accumulations, and a list of TG annotations is given in Figure S16.

Lipid Droplet Distribution Differs Locally between Individual Cells. We investigated the capability of AP-SMALDI MSI to identify heterogeneous compound distributions within the cell cultures of the same line. Representative results with 5, 2, and 1.5 μm pixel size of PFA-fixed B8 cells are shown in Figure 3a,c,e and compared to corresponding microscopic results in Figure 3b,d,f. With increasingly smaller pixel sizes, cellular features such as cell bodies and especially protrusions were readily resolved by visualizing major cell membrane components such as PC 34:1 (in Figure 3, green). The diameter of the protrusions imaged by AP-SMALDI MSI with 1.5 μm pixel size was ≈5 μm, consistent with the diameter of the same features in the optical images (Figure S11). This indicates that lipids do not disperse in the matrix upon sample preparation. This stands in contrast to publications of other research groups, where spray-coating was found to introduce noticeable wash-out effects, even on fixed cells.[29]

We therefore conclude that careful optimization of the spray-coating protocol is crucial to prevent analyte delocalization from single cells. In addition to signals that colocalize with all cells, many signals were confined to individual cells and were either absent or decreased in intensity in other cells of the same culture (blue color representing TG 52:2-associated ions in Figures 3, S19, and S20). This was observed in all cell lines

https://doi.org/10.1021/acs.analchem.3c01533
Anal. Chem. 2023, 95, 11672–11679

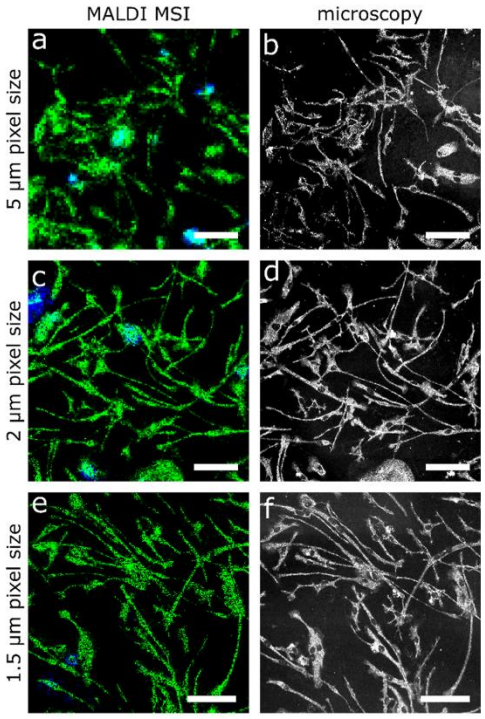

Figure 3. Increasing lateral resolution enables the localization of discrete subcellular features by AP-SMALDI MSI. (a) LPS-stimulated MGLCs of the B8 cell line, 100 × 100 pixels, 5 μm pixel size. (c) Naïve MGLCs of the B8 cell line, 250 × 250 pixels, 2 μm pixel size. (e) Naïve MGLCs from the B8 cell line, 300 × 300 pixels, 1.5 μm pixel size. (b,d,f) Corresponding microscopic images of the measured sample regions. (a,c,e) Color coding: blue: TG 52:2 (m/z 881.7568, $[M + Na]^+$) and green: PC 34:1 (m/z 896.6140, $[M + DHB-H_2O + H]^+$). Scale bars: 100 μm.

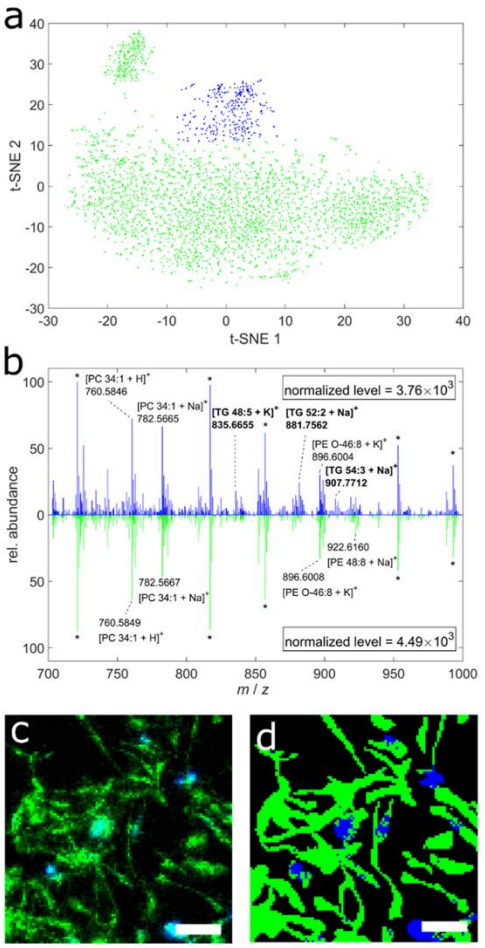

Figure 4. AP-SMALDI MSI and statistical analysis for the identification of LPS-stimulated B8 cells with increased TG production. (a) Pixel-wise t-SNE analysis of mass spectrometric data (m/z 800−1000), where each of the 6511 datapoints relates to an individual mass spectrum. Off-cell signals were excluded from analysis. (b) Example of single-pixel mass spectra corresponding to the blue and green cluster as identified by pixel-based t-SNE analysis in (a). Stars indicate matrix-related signals, which are increased upon fixation. (c) AP-SMALDI MSI image with 100 × 100 pixels at 5 μm pixel size of LPS-stimulated PFA-fixed B8 cells. Color-coding: blue: TG 52:2 (m/z 881.7568, $[M + Na]^+$) and green: PC 36:2 (m/z 808.5826, $[M + Na]^+$). (d) Pixel-wise classification based on t-SNE analysis of the mass spectrometric data with automated color-coding referring to clusters identified in (a). Additional information in Figure S21. Scale bars: 100 μm.

for all lateral resolutions down to 1.5 μm pixel size, including LPS-stimulated B8 cells shown in Figure 4. When employing t-distributed stochastic neighbor embedding (t-SNE) on mass spectrometric data from all on-cell pixels of a measurement, two clusters were identified, colored in green and blue in Figure 4a. A third cluster was identified, but corresponding mass spectra were virtually identical with those of the main cluster (green), showing >95% congruence for all signals with an intensity >2%, and corresponding pixels seem to be randomly distributed (Figure S21, red pixels). These data points were thus included in the main cluster (green, Figure 4a).

Differences between mass spectra of pixels of the two identified groups (blue and green cluster, Figure 4a) were found especially in the mass range above m/z 800, contributed by high-intensity signals, while spectra were rather similar in the lower mass range where only low-intensity signals were dissimilar (Figure 4b). The majority of signals in the range m/z 800−1000 were assigned to TGs (Figure S17), with some being elevated in signal intensities for the blue cluster while being reduced or absent for the green cluster. When visualizing the spatial distributions of the two clusters, pixels of the less abundant blue cluster were highly localized to individual cells (Figure 4d). Comparison of the spatial distribution of the blue

https://doi.org/10.1021/acs.analchem.3c01533
Anal. Chem. 2023, 95, 11672−11679

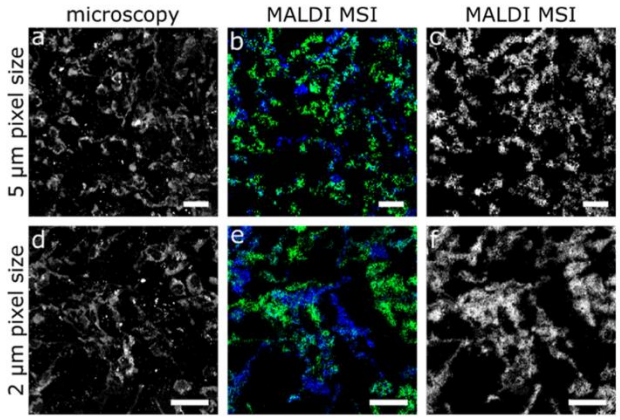

Figure 5. Degree of FA saturation differs between MGLCs. (a,d) Microscopic image of the region investigated by AP-SMALDI MSI of naïve B8 MGLCs. (b–e) AP-SMALDI MSI images acquired with 150 × 150 pixels at 5 μm pixel size (b,c) or 250 × 250 pixels at 2 μm pixel size (e,f) in negative-ion mode, showing (b,e) the heterogeneity of PI 38:3 (m/z 887.5655, $[M - H]^-$, blue) and PI 38:5 (m/z 883.5342, $[M - H]^-$, green) and (c,f) the homogeneous distribution of PI 38:4 (m/z 885.5499, $[M - H]^-$, grayscale). Scale bars: 100 μm.

cluster (Figure 4d) with that of the highly variable signal corresponding to TG 52:2 (Figure 4c) revealed that both images virtually overlap. Analysis of other MS images yielded similar results (Figure S22). This demonstrates that our methodology is able to locally resolve regions with elevated TG content, most likely areas of lipid droplet accumulation. They further serve as a proof of concept that our approach is suitable to study the subtype heterogeneity among cells. When comparing MS images of naïve and LPS-stimulated MGLCs, we observed that the number of cells with elevated TG levels increased with activation (Figures S19 and S20), consistent with the finding that LPS stimulation augmented triglyceride levels (Figure S15).

However, data also revealed that not all cells responded with TG accumulation, suggesting a heterogeneous phenotype even when activated with the strong stimulant LPS. We confirmed the heterogeneous nature of LD formation with fluorescence microscopy as shown in Figure S23. Lipid droplets were found to be heterogeneously distributed in the cell culture, consistent with our AP-SMALDI MSI findings. Our results are also in line with the reports on microglia in human and mouse brains that exhibited highly heterogeneous LD distributions with more cells containing increased LD levels upon LPS stimulation.[18,48] Unlike in previous studies, our untargeted methodology identified heterogeneous lipid distributions between individual cells, most likely associated with LDs. In addition, AP-SMALDI MSI provided molecular information about the TG composition, a feature that cannot be achieved with fluorescence microscopy.

Fatty Acid Composition of PI Lipids Differentiates MGLC Phenotypes. Other signals besides TGs were found to be heterogeneously distributed between cells. In negative-ion mode, several PIs showed locally varying intensities. A reproducible pattern of locally different degrees of fatty acid (FA) saturation was found for PI 38:X species when measured with AP-SMALDI MSI (Figures 5 and S8). While PI 38:4 (m/z 885.5498, $[M - H]^-$) was detected in all cells (Figure 5c,f), indicating no technical cell-to-cell variations during measurement, PI 38:3 (m/z 887.5655, $[M - H]^-$) and PI 38:5 (m/z 883.5342, $[M - H]^-$) were found to be enriched in different subpopulations (Figures 5b,e and S24). This heterogeneity might be linked to differential desaturase enzyme activity, which is known to occur for different microglia phenotypes.[50−52] Interestingly, this variance was found in both naïve and LPS-stimulated cells (Figure S8) and can be used to classify cells based on hierarchical clustering of mass spectrometric data (Figure S25).

This heterogeneity was found to be exclusive for PI 38:X species in our measurements. Other phospholipid classes such as PC 38:X or PE 38:X were found to be evenly distributed across all cells, making heterogeneity that is caused by selective FA production or FA uptake unlikely. However, not all phospholipid classes are synthesized from FAs via the same pathways.[53] While in mammalian cells PC and PE are synthesized via the Kennedy pathway,[54] PI is synthesized via a cytidinediphosphate diacylglycerol (CDP-DG) intermediate.[55] A selectivity for the synthesis of PI 38:4 over other fatty acid derivates was described earlier[56] and is supported by the homogeneous expression in all the cells in our experiments. Kim et al. have recently demonstrated that considerable FA remodeling of PIs takes place, even though the FA composition of PA precursors is not affacted to a similar extent.[57] This remodeling is most likely associated with lysophosphatidylinositol acetyltransferase (LPIAT) enzymes that could also be the cause for cell-specific PI expression. Also, PIs were recently found to be directly involved in cellular stress regulation.[58] Combined with the heterogeneous stress-related lipid-droplet formation observed in our study, we hypothesize that cell-specific regulatory switches linked to LPIAT for PI metabolism exist, similar to findings in recent reports on glycosphingolipids,[17] leading to spontaneous formation of two distinct phenotypes. However, further research is needed to resolve the cause for the observation that MGLCs in culture exhibit heterogeneous PI distributions.

https://doi.org/10.1021/acs.analchem.3c01533
Anal. Chem. 2023, 95, 11672−11679

CONCLUSIONS

We were able to visualize population-based and single-cell-based heterogeneities in fixed or snap-frozen human MGLCs, cultured on glass slides, using AP-SMALDI MSI with lateral resolutions of down to 1.5 μm pixel size without oversampling. At the same time, we were able to maintain sufficiently high signal intensity to simultaneously detect >100 unique lipid species per pixel. We were able to differentiate multiple cell lines from each other in positive- and negative-ion modes using high-mass-resolution data and statistical analysis on biological triplicates. Further, our method was able to identify and visualize inter- (e.g., LD) or intra-cellular (e.g., PI species) heterogeneity between individual cells of the same cell culture, indicating the differentiation of MGLCs into different phenotypes, which is consistent with previous findings.[11−14,59] On the one hand, we observed sub-cellular inflammation-induced heterogeneity expressed through lipid-droplet formation.[48] To the best of our knowledge, this is the first reported visualization of intact biomolecules within sub-cellular features, i.e., LDs, by MSI. LDs were localized at specific positions in some cells, whereas the rest of the cells remained unaffected, consistent with fluorescence microscopy and literature reports. This kind of heterogeneity was more pronounced in LPS-stimulated samples due to LPS triggering the inflammatory response mechanism of microglia. On the other hand, single-cell heterogeneity affecting a complete cell body was found irrespective of the cell line and stimulation in positive- and negative-ion modes, which was particularly prominent in negative-ion mode detecting PI lipid species. These findings together with recent reports of fibroblasts[17] and multiple cell lines[26] reveal that state-of-the-art MSI technologies allow differentiation of lipidomic phenotypes of single cells in culture and call for large-scale studies to chart the heterogeneity of the cellular lipidome or even sub-cellular compositions within the context of the results of other single-cell methods. However, the analysis of cells cultured on glass slides, as investigated here, may not completely reflect the behavior and biochemical composition of cells *in vivo* and their extracellular interactions with other cell types in the complex environment of living organisms. In the future, our AP-SMALDI MSI approach with high lateral resolution and the findings presented in this work can be used to further investigate MGLCs directly in tissues. This will facilitate further insights into biochemical switches of cell-specific lipid metabolism and plasticity. In the future, this could be facilitated by technical improvements of mass analyzers or an adjustable intensity cutoff limit in order to visualize low-abundant ion signals.

ASSOCIATED CONTENT

Supporting Information

The Supporting Information is available free of charge at https://pubs.acs.org/doi/10.1021/acs.analchem.3c01533.

Additional experimental methods, microscopic images of ablation spots or samples, additional AP-SMALDI MS images, list of annotated lipid species, and statistics of MSI results (PDF)

AUTHOR INFORMATION

Corresponding Author

Sven Heiles − *Institute of Inorganic and Analytical Chemistry, Analytical Chemistry, Justus Liebig University Giessen, 35392 Giessen, Germany; Leibniz-Institut für Analytische Wissenschaften—ISAS—e.V., 44139 Dortmund, Germany; Faculty of Chemistry, University of Duisburg-Essen, 45141 Essen, Germany;* orcid.org/0000-0003-3779-8071; Phone: +49 2 31.13 92-4202; Email: sven.heiles@isas.de

Authors

Max A. Müller − *Institute of Inorganic and Analytical Chemistry, Analytical Chemistry, Justus Liebig University Giessen, 35392 Giessen, Germany;* orcid.org/0000-0002-9960-5020

Norman Zweig − *Institute of Inorganic and Analytical Chemistry, Analytical Chemistry, Justus Liebig University Giessen, 35392 Giessen, Germany*

Bernhard Spengler − *Institute of Inorganic and Analytical Chemistry, Analytical Chemistry, Justus Liebig University Giessen, 35392 Giessen, Germany;* orcid.org/0000-0003-0179-5653

Maria Weinert − *Department of Brain Sciences, Imperial College London, Hammersmith Hospital, W12 0NN London, U.K.*

Complete contact information is available at: https://pubs.acs.org/10.1021/acs.analchem.3c01533

Author Contributions

Original manuscript draft and figures: M.A.M.; manuscript review: M.A.M., S.H., M.W., B.S., and N.Z.; cell growth: M.W.; sample preparation: M.A.M., and N.Z.; AP-SMALDI MSI instrumentation and experiments: M.A.M., S.H., and N.Z.; light microscopy: M.A.M. and S.H.; fluorescence microscopy: M.W.; flow cytometry: M.W.; statistical evaluation: M.A.M.; software code: M.A.M.; review of data and planning of experiments: M.A.M., S.H., and M.W.; concept and design of project: S.H. and M.W.; supervision: S.H. and B.S. All the authors have given approval to the final version of the manuscript.

Notes

The authors declare the following competing financial interest(s): M. A. M. is part-time employee and B. S. is consultant of TransMIT GmbH, Germany. All other authors declare no competing financial interest.

ACKNOWLEDGMENTS

We gratefully acknowledge the financial support by the German Science Foundation (DFG) under the grants Sp314/23-1 and INST 162/500-1 FUGG. M.A.M. thanks the Fonds der Chemischen Industrie for granting a Kekulé fellowship. S.H. thanks the Fonds der Chemischen Industrie for granting a Liebig fellowship, and financial support by the Deutsche Forschungsgemeinschaft (HE 8521/1-1) is gratefully acknowledged. S.H. acknowledges the support by the "Ministerium für Kultur und Wissenschaft des Landes Nordrhein-Westfalen" and the German Ministry of Research and Education (BMBF) and is grateful for financial support by the Justus Liebig University via the JLU price 2022.

REFERENCES

(1) Lawson, L. J.; Perry, V. H.; Dri, P.; Gordon, S. *Neuroscience* **1990**, *39*, 151−170.
(2) Lenz, K. M.; McCarthy, M. M. *Neuroscientist* **2015**, *21*, 306−321.
(3) Butovsky, O.; Weiner, H. L. *Nat. Rev. Neurosci.* **2018**, *19*, 622−635.
(4) Li, Q.; Barres, B. A. *Nat. Rev. Immunol.* **2018**, *18*, 225−242.

(5) Salter, M. W.; Beggs, S. *Cell* **2014**, *158*, 15−24.
(6) Block, M. L.; Hong, J.-S. *Prog. Neurobiol.* **2005**, *76*, 77−98.
(7) Cartier, N.; Lewis, C.-A.; Zhang, R.; Rossi, F. M. V. *Acta Neuropathol.* **2014**, *128*, 363−380.
(8) Colonna, M.; Butovsky, O. *Annu. Rev. Immunol.* **2017**, *35*, 441−468.
(9) Efthymiou, A. G.; Goate, A. M. *Mol. Neurodegener.* **2017**, *12*, 43.
(10) Loving, B. A.; Bruce, K. D. *Front. Physiol.* **2020**, *11*, 393.
(11) Chhor, V.; Le Charpentier, T.; Lebon, S.; Oré, M.-V.; Celador, I. L.; Josserand, J.; Degos, V.; Jacotot, E.; Hagberg, H.; Sävman, K.; Mallard, C.; Gressens, P.; Fleiss, B. *Brain Behav. Immun.* **2013**, *32*, 70−85.
(12) Lauro, C.; Limatola, C. *Front. Immunol.* **2020**, *11*, 493.
(13) Masuda, T.; Sankowski, R.; Staszewski, O.; Prinz, M. *Cell Rep.* **2020**, *30*, 1271−1281.
(14) Orihuela, R.; McPherson, C. A.; Harry, G. J. *Br. J. Pharmacol.* **2016**, *173*, 649−665.
(15) Hannun, Y. A.; Obeid, L. M. *Nat. Rev. Mol. Cell Biol.* **2008**, *9*, 139−150.
(16) Hu, T.; Zhang, J.-L. *J. Sep. Sci.* **2018**, *41*, 351−372.
(17) Capolupo, L.; Khven, I.; Lederer, A. R.; Mazzeo, L.; Glousker, G.; Ho, S.; Russo, F.; Montoya, J. P.; Bhandari, D. R.; Bowman, A. P.; Ellis, S. R.; Guiet, R.; Burri, O.; Detzner, J.; Muthing, J.; Homicsko, K.; Kuonen, F.; Gilliet, M.; Spengler, B.; Heeren, R. M. A.; Dotto, G. P.; La Manno, G.; D'Angelo, G. *Science* **2022**, *376*, No. eabh1623.
(18) Marschallinger, J.; Iram, T.; Zardeneta, M.; Lee, S. E.; Lehallier, B.; Haney, M. S.; Pluvinage, J. V.; Mathur, V.; Hahn, O.; Morgens, D. W.; Kim, J.; Tevini, J.; Felder, T. K.; Wolinski, H.; Bertozzi, C. R.; Bassik, M. C.; Aigner, L.; Wyss-Coray, T. *Nat. Neurosci.* **2020**, *23*, 194−208.
(19) Riera-Borrull, M.; Cuevas, V. D.; Alonso, B.; Vega, M. A.; Joven, J.; Izquierdo, E.; Corbí, Á. L. *J. Immunol.* **2017**, *199*, 3858−3869.
(20) Römpp, A.; Spengler, B. *Histochem. Cell Biol.* **2013**, *139*, 759−783.
(21) Spengler, B. *Anal. Chem.* **2015**, *87*, 64−82.
(22) Zhu, X.; Xu, T.; Peng, C.; Wu, S. *Front. Chem.* **2022**, *9*, 782432.
(23) Neumann, E. K.; Comi, T. J.; Rubakhin, S. S.; Sweedler, J. V. *Angew. Chem., Int. Ed.* **2019**, *58*, 5910−5914.
(24) Stopka, S. A.; Wood, E. A.; Khattar, R.; Agtuca, B. J.; Abdelmoula, W. M.; Agar, N. Y. R.; Stacey, G.; Vertes, A. *Anal. Chem.* **2021**, *93*, 9677−9687.
(25) Rappez, L.; Stadler, M.; Triana, S.; Gathungu, R. M.; Ovchinnikova, K.; Phapale, P.; Heikenwalder, M.; Alexandrov, T. *Nat. Methods* **2021**, *18*, 799−805.
(26) Bien, T.; Koerfer, K.; Schwenzfeier, J.; Dreisewerd, K.; Soltwisch, J. *Proc. Natl. Sci.* **2022**, *119*, No. e2114365119.
(27) Kompauer, M.; Heiles, S.; Spengler, B. *Nat. Methods* **2017**, *14*, 90−96.
(28) Niehaus, M.; Soltwisch, J.; Belov, M. E.; Dreisewerd, K. *Nat. Methods* **2019**, *16*, 925−931.
(29) Bien, T.; Bessler, S.; Dreisewerd, K.; Soltwisch, J. *Anal. Chem.* **2021**, *93*, 4513−4520.
(30) Bandu, R.; Mok, H. J.; Kim, K. P. *Mass Spectrom. Rev.* **2018**, *37*, 107−138.
(31) Tian, H.; Sparvero, L. J.; Anthonymuthu, T. S.; Sun, W.-Y.; Amoscato, A. A.; He, R.-R.; Bayır, H.; Kagan, V. E.; Winograd, N. *Anal. Chem.* **2021**, *93*, 8143−8151.
(32) Blank, M.; Enzlein, T.; Hopf, C. *Sci. Rep.* **2022**, *12*, 2908.
(33) Chausse, B.; Kakimoto, P. A.; Caldeira-da-Silva, C. C.; Chaves-Filho, A. B.; Yoshinaga, M. Y.; da Silva, R. P.; Miyamoto, S.; Kowaltowski, A. J. *Biosci. Rep.* **2019**, *39*, BSR20190072.
(34) Paschke, C.; Leisner, A.; Hester, A.; Maass, K.; Guenther, S.; Bouschen, W.; Spengler, B. *J. Am. Soc. Mass Spectrom.* **2013**, *24*, 1296−1306.
(35) Müller, M. A.; Kompauer, M.; Strupat, K.; Heiles, S.; Spengler, B. *J. Am. Soc. Mass Spectrom.* **2021**, *32*, 465−472.
(36) Tyanova, S.; Temu, T.; Sinitcyn, P.; Carlson, A.; Hein, M. Y.; Geiger, T.; Mann, M.; Cox, J. *Nat. Methods* **2016**, *13*, 731−740.
(37) Bechtold, B. Violin Plots for Matlab. https://github.com/bastibe/Violinplot-Matlab accessed June 14, 2022.
(38) Palmer, A.; Phapale, P.; Chernyavsky, I.; Lavigne, R.; Fay, D.; Tarasov, A.; Kovalev, V.; Fuchser, J.; Nikolenko, S.; Pineau, C.; Becker, M.; Alexandrov, T. *Nat. Methods* **2017**, *14*, 57−60.
(39) Sud, M.; Fahy, E.; Cotter, D.; Brown, A.; Dennis, E. A.; Glass, C. K.; Merrill, A. H.; Murphy, R. C.; Raetz, C. R. H.; Russell, D. W.; Subramaniam, S. *Nucleic Acids Res.* **2007**, *35*, D527−D532.
(40) Aimo, L.; Liechti, R.; Hyka-Nouspikel, N.; Niknejad, A.; Gleizes, A.; Götz, L.; Kuznetsov, D.; David, F. P. A.; van der Goot, F. G.; Riezman, H.; Bougueleret, L.; Xenarios, I.; Bridge, A. *Bioinformatics* **2015**, *31*, 2860−2866.
(41) Meade, A. D.; Clarke, C.; Draux, F.; Sockalingum, G. D.; Manfait, M.; Lyng, F. M.; Byrne, H. J. *Anal. Bioanal. Chem.* **2010**, *396*, 1781−1791.
(42) Fitzner, D.; Bader, J. M.; Penkert, H.; Bergner, C. G.; Su, M.; Weil, M.-T.; Surma, M. A.; Mann, M.; Klose, C.; Simons, M. *Cell Rep.* **2020**, *32*, 108132.
(43) Feingold, K. R.; Shigenaga, J. K.; Kazemi, M. R.; McDonald, C. M.; Patzek, S. M.; Cross, A. S.; Moser, A.; Grunfeld, C. *J. Leukocyte Biol.* **2012**, *92*, 829−839.
(44) Funk, J. L.; Feingold, K. R.; Moser, A. H.; Grunfeld, C. *Atherosclerosis* **1993**, *98*, 67−82.
(45) Hamsanathan, S.; Gurkar, A. U. *Front. Physiol.* **2022**, *13*, 796850.
(46) Olzmann, J. A.; Carvalho, P. *Nat. Rev. Mol. Cell Biol.* **2019**, *20*, 137−155.
(47) Churchward, M. A.; Tchir, D. R.; Todd, K. G. *Mol. Neurobiol.* **2018**, *55*, 1477−1487.
(48) Khatchadourian, A.; Bourque, S. D.; Richard, V. R.; Titorenko, V. I.; Maysinger, D. *Biochim. Biophys. Acta* **2012**, *1821*, 607−617.
(49) Lund, S.; Christensen, K. V.; Hedtjärn, M.; Mortensen, A. L.; Hagberg, H.; Falsig, J.; Hasseldam, H.; Schrattenholz, A.; Pörzgen, P.; Leist, M. *J. Neuroimmunol.* **2006**, *180*, 71−87.
(50) Bogie, J. F. J.; Grajchen, E.; Wouters, E.; Corrales, A. G.; Dierckx, T.; Vanherle, S.; Mailleux, J.; Gervois, P.; Wolfs, E.; Dehairs, J.; van Broeckhoven, J.; Bowman, A. P.; Lambrichts, I.; Gustafsson, J.-Å.; Remaley, A. T.; Mulder, M.; Swinnen, J. V.; Haidar, M.; Ellis, S. R.; Ntambi, J. M.; Zelcer, N.; Hendriks, J. J. A. *J. Exp. Med.* **2020**, *217*, 217.
(51) Garcia Corrales, A. V.; Haidar, M.; Bogie, J. F. J.; Hendriks, J. J. A. *Int. J. Mol. Sci.* **2021**, *22*, 8159.
(52) Guillou, H.; Zadravec, D.; Martin, P. G. P.; Jacobsson, A. *Prog. Lipid Res.* **2010**, *49*, 186−199.
(53) Harayama, T.; Shimizu, T. *J. Lipid Res.* **2020**, *61*, 1150−1160.
(54) Kennedy, E. P.; Weiss, S. B. *J. Biol. Chem.* **1956**, *222*, 193−214.
(55) Blunsom, N. J.; Cockcroft, S. *Front. Cell Dev. Biol.* **2020**, *8*, 63.
(56) Barneda, D.; Janardan, V.; Niewczas, I.; Collins, D. M.; Cosulich, S.; Clark, J.; Stephens, L. R.; Hawkins, P. T. *EMBO J.* **2022**, *41*, No. e110038.
(57) Kim, Y. J.; Sengupta, N.; Sohn, M.; Mandal, A.; Pemberton, J. G.; Choi, U.; Balla, T. *EMBO Rep.* **2022**, *23*, No. e54532.
(58) Thürmer, M.; Gollowitzer, A.; Pein, H.; Neukirch, K.; Gelmez, E.; Waltl, L.; Wielsch, N.; Winkler, R.; Löser, K.; Grander, J.; Hotze, M.; Harder, S.; Döding, A.; Meßner, M.; Troisi, F.; Ardelt, M.; Schlüter, H.; Pachmayr, J.; Gutiérrez-Gutiérrez, Ó.; Rudolph, K. L.; Thedieck, K.; Schulze-Späte, U.; González-Estévez, C.; Kosan, C.; Svatoš, A.; Kwiatkowski, M.; Koeberle, A. *Nat. Commun.* **2022**, *13*, 2982.
(59) Boche, D.; Perry, V. H.; Nicoll, J. A. R. *Neuropathol. Appl. Neurobiol.* **2013**, *39*, 3−18.

https://doi.org/10.1021/acs.analchem.3c01533
Anal. Chem. 2023, 95, 11672−11679

Supporting Information

Supporting Information

Lipid signatures and inter-cellular heterogeneity of naïve and lipopolysaccharide-stimulated human microglia-like cells

Max A. Müller[1], Norman Zweig[1], Bernhard Spengler[1], Maria Weinert[2], Sven Heiles[1,3,4*]

[1]Institute of Inorganic and Analytical Chemistry, Analytical Chemistry, Justus Liebig University Giessen, 35392 Giessen, Germany

[2]Department of Brain Sciences, Imperial College London, Hammersmith Hospital, London, W12 0NN, United Kingdom

[3]Leibniz-Institut für Analytische Wissenschaften - ISAS - e.V., 44139 Dortmund, Germany

[4]Faculty of Chemistry, University of Duisburg-Essen, 45141 Essen, Germany

*Address correspondence to:
Sven Heiles
Leibniz-Institut für Analytische Wissenschaften - ISAS - e.V.
Otto-Hahn-Straße 6b
44227 Dortmund, Germany
Phone: +49 231 1392-4202
e-mail: sven.heiles@isas.de

Table of content

Cell pretreatment for AP-SMALDI MSI

Microscopic images of the samples upon warming to room temperature and drying revealed an irregular coverage with salt residues potentially affecting lipid ion yields in AP-SMALDI MSI experiments (Figure S5 A,C). For example, lipid annotations of unfixed LPS-stimulated microglia cells from the OX1 cell line using Metaspace[1] (false discovery rate 10%) based on the SwissLipids[2] database reveal a high number of sodium adducts (116) being detected, whereas protonated signals (33) were suppressed. An additional washing step with 250 µL of deionized water flowing over individual cell-compartments with the sample tilted to facilitate rinsing, followed by drying at room temperature in an evacuated desiccator (50 mbar) for 10 minutes removed salt residues efficiently. Washed samples showed a more even ratio of protonated (156) and sodiated (78) adducts under otherwise same conditions. Sample morphology was unaffected by the washing process (Figure S5 B,D), but snap-frozen cells seemed to be already damaged by the freezing process. However, cell morphology was best preserved during washing and drying for cells after PFA fixation, which is in line with literature results.[3]

Matrix optimization and application protocols

The choice of the matrix substance and its preparation protocol play a major role for ionization in AP-SMALDI MSI. In positive-ion mode, the above-described sample pretreatment for flash-frozen cells led to 150 annotations with Metaspace using 2,5-dihydroxybenzoic acid (DHB), an approximately 3-fold increase compared to annotations using the α-Cyano-4-hydroxycinnamic acid (CHCA) matrix (55). In negative-ion mode, matrix application of 9-AA was optimized by varying solvent composition, matrix concentration and application volume, since recently reported approaches[4,5] did result in intense washout effects. The spatial distribution of analytes was not preserved but dispersed all over the measurement area, resulting in a highly blurred representation of cellular features (Figure S6). With the newly developed preparation method, the sample was covered homogeneously with small crystals (< 1 µm, Figure S1) and minimal thickness variations, which are favorable characteristics for high-resolution AP-SMALDI MSI.[6]

Cell cultures

Microglia-like cells (MGL) were differentiated from human induced pluripotent stem cells (iPSCs) via primitive macrophage precursors (pMacPre) according to Haenseler *et al.*[7] with small modifications. Of note, in this protocol microglia-like identity is induced through the use of brain-specific microglia growth factor IL-34 as opposed to peripherally expressed macrophage growth factor M-CSF during final differentiation. In brief, iPSC were grown in OXE8 medium[8] on Geltrex (Gibco, Thermo Fisher Scientific, Altrincham, UK) with daily medium change and EDTA lifting at approximately 80% confluence for standard culture. For embryoid body production, $3 \cdot 10^6$ iPSC were lifted with TrypLE Express (Gibco) and plated in one well of a 24-well Aggrewell 800 plate (STEMCELL Technologies, Cambridge, UK) in 2 ml EB medium (OXE8 supplemented with 20 ng/mL SCF (Miltenyi Biotec, Woking, UK), 50 ng/mL BMP4 (Gibco) and 50 ng/mL VEGF (PeproTech, London, UK)) for induction of mesoderm. Embryoid bodies were incubated for one week in EB medium with daily exchange of 75% medium and then transferred into 2x T175 flasks containing FM7a factory medium[8] for factory maturation. For 4 weeks, factories were fed weekly with addition of 10-15 mL FM7a. From week 4 to 6, the presence of pMacPre cells in the supernatant was assessed by flow cytometry using antibodies against CD45, CD14 (both Immunotools, Friesoythe, Germany) and CD11b (Biolegend, London, UK). Flasks that produced >95% triple-positive cells were subsequently used for weekly cell harvest. pMacPre were harvested from the factory supernatant, plated directly at 25000 cells/cm2 on glass slides and finally differentiated into

MGL for 7 days in MIC10 medium (SILAC Advanced DMEM/F12, 2mM GlutaMax (both Gibco), 10 mM glucose, 0.5 mM L-lysine, 0.7 mM L-arginine, 0.00075% phenol red (all Sigma Aldrich, Gillingham, UK), 100 ng/mL IL-34 (PeproTech), 10 ng/mL GM-CSF (Gibco)). An equal volume of MIC10 was added after 3 days in culture. The five cell lines used for this study (OX1, B8, D9, C12, E2) are clonal expansions of the parental line SFC841-03-01 (OX1; StemBANCC). For proinflammatory activation, MGL were exposed to 100 ng/mL lipopolysaccharide (LPS; Sigma Aldrich)[9] in MIC10 for 24h. For MSI sample preparation, medium was removed, cells were washed once in phosphate-buffered saline (PBS; Sigma Aldrich) and either snap-frozen in liquid nitrogen for storage at -80°C or fixed in 4% paraformaldehyde (PFA; Thermo Fisher Scientific) for 5 min at room temperature before washing and storage in PBS at 4°C.

Fluorescence microscopy

For fluorescence microscopy, MGL were grown in 96-well glass bottom imaging plates, fixed for 10 min with 4% PFA (Alfa Aesar, Heysham, UK) and washed 3x with PBS (Sigma, Gillingham, UK). For visualisation of lipid droplets, cells were stained with 0.5 µg/mL Bodipy™ 493/503 and 1 µg/mL DAPI (both Thermo Fisher Scientific, Paisley, UK) diluted in PBS for 30 min at room temperature and washed 3x with PBS. For immune fluorescence, cells were incubated over night with primary antibody Iba-1 (Abcam, ab5076, 1:250) or PU.1 (Cell Signaling, 2258, 1:250) in staining buffer (5% bovine serum albumin, 0.2% TritonX-100 in PBS), washed 3x with wash buffer (PBS/0.1% TritonX-100), incubated for 2 h with secondary antibody anti-goat-AF488 (Thermo Fisher, A-11055, 1:1000) or anti-rabbit-AF488 (Thermo Fisher, A-21206, 1:1000) and 1 µg/mL DAPI in wash buffer. MGL were washed 3x with PBS and images were acquired on a Leica SP8 confocal microscope (Leica Microsystems, Wetzlar, Germany). In our experiments, staining was only possible on samples not measured by AP-SMALDI MSI, due to the destructive nature of the method at high lateral resolution.

Flow cytometry

Freshly harvested $5x10^5$ pMacPre were incubated for 30 min at 4°C with primary antibodies CD45-FITC (Immunotools, 21270453, 1:20), CD14-PE (Immunotools, 21620144, 1:20) and CD11b-APC (Biolegend, 301309, 1:20) or CD11c-FITC (Immunotools, 21487113, 1:20) in 50 µl FACS buffer (1% FBS, 10 µg/ml human IgG in PBS), spun at 500xg for 5 min and washed 3x with PBS. Fluorescence was acquired on a FACSCalibur (BD Biosciences).

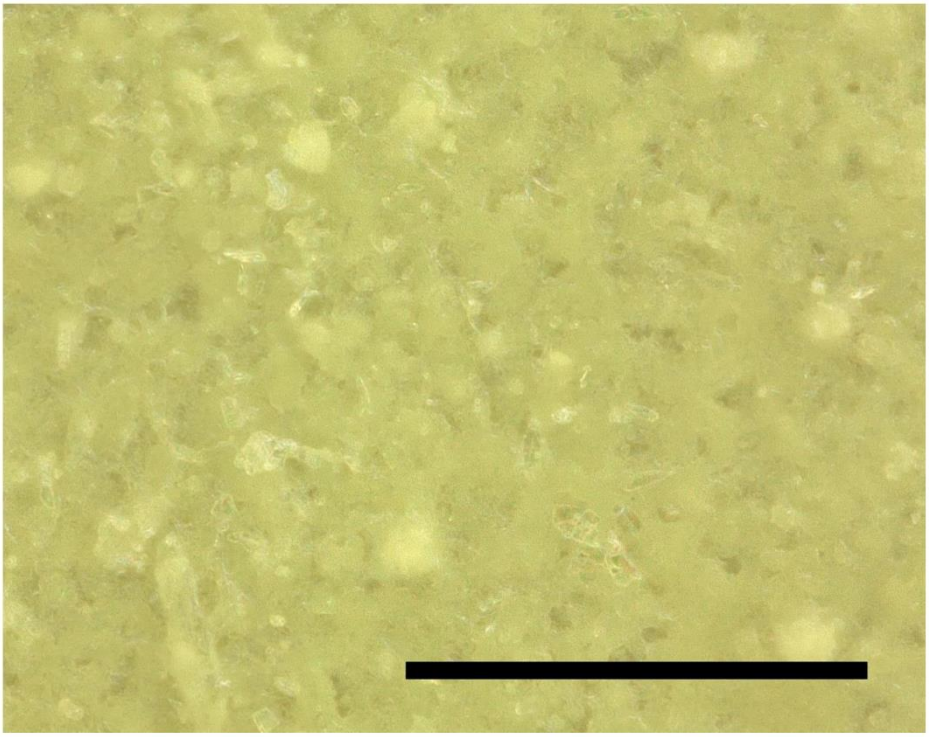

Figure S1: Microscopic image of 9-AA matrix applied to microglia cells. Scale bar: 100 µm.

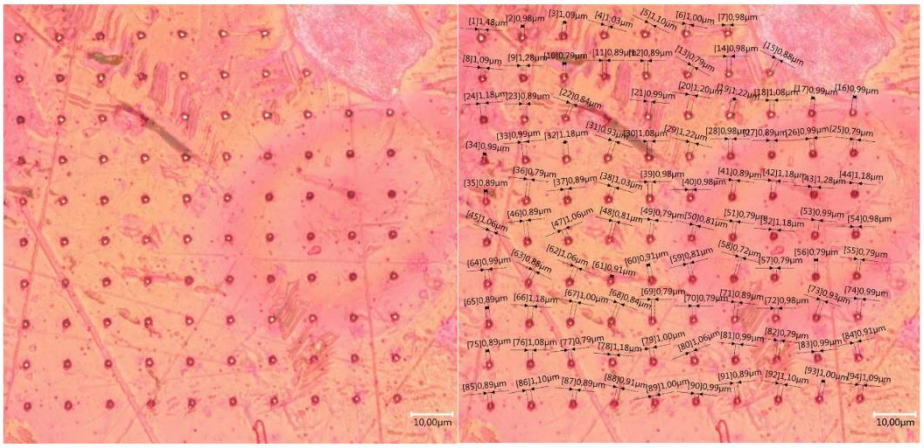

Figure S2: Microscopic image of 100 laser ablation spots in a 10x10 grid acquired with a step size of 10 µm on red dye. Measurements of spot diameter were performed with a digital microscope and showed a mean spot diameter of <1 µm.

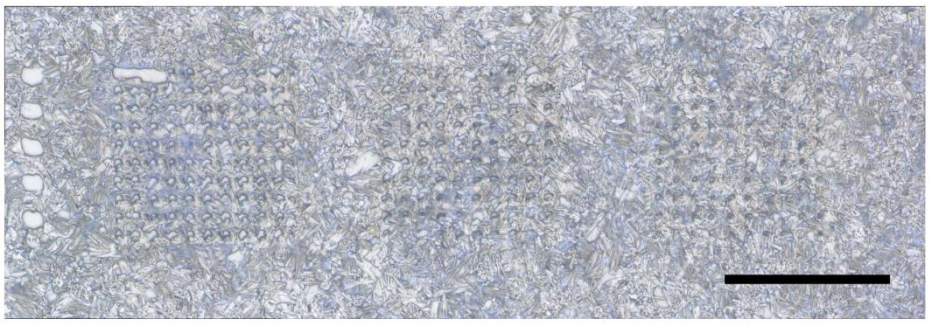

Figure S3: Microscopic images of laser ablation spots on microglia cells covered with DHB matrix at different laser energy settings. Laser energy was decreased from left to right. Irregularities in the spot shape stem from matrix-surface characteristics. Scale bar: 100 µm.

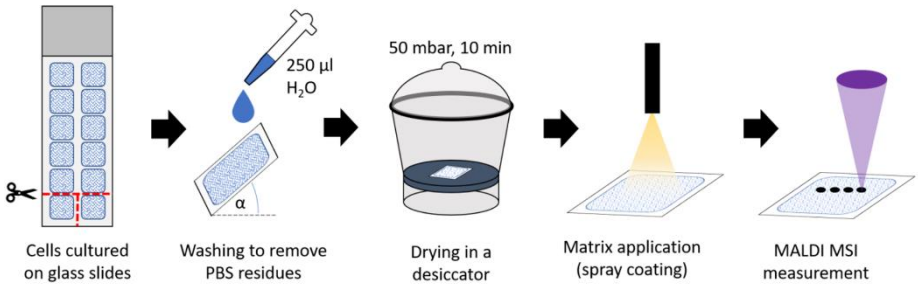

Figure S4: Scheme of the sample preparation workflow of cells grown on glass slides for AP-SMALDI MSI at high lateral resolution.

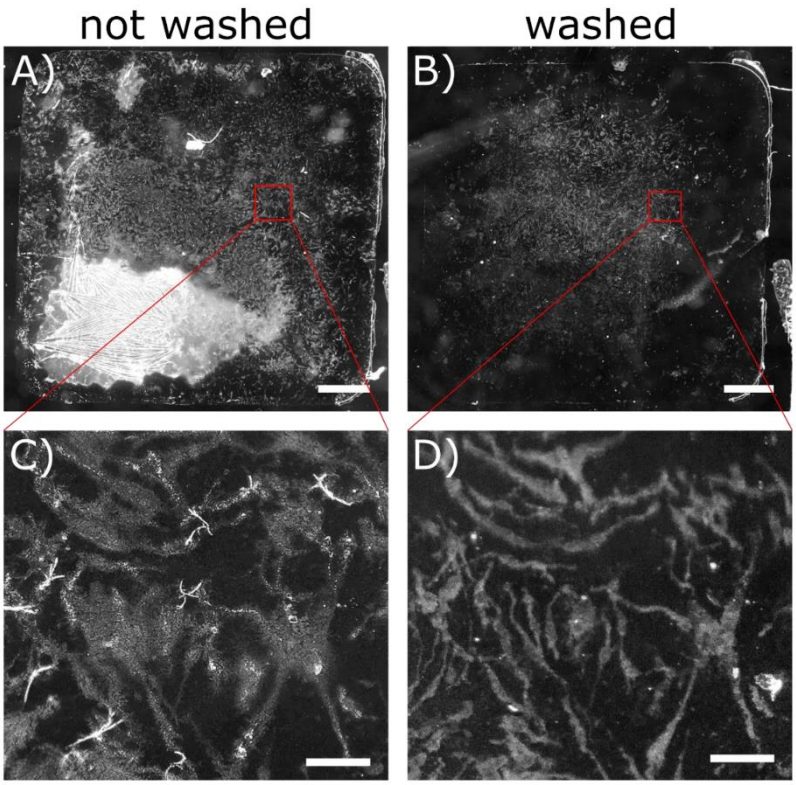

Figure S5: Microscopic images of LPS-stimulated MGL from the OX1 cell line before (A, C) and after washing with deionized water (B, D). Zoom-in area indicated by red rectangles. Unwashed samples were covered with a salt layer of varying thickness originating from culturing in PBS. Sample morphology was preserved after washing (compare C and D). Scale bar: 1 mm (A, B) or 100 µm (C, D).

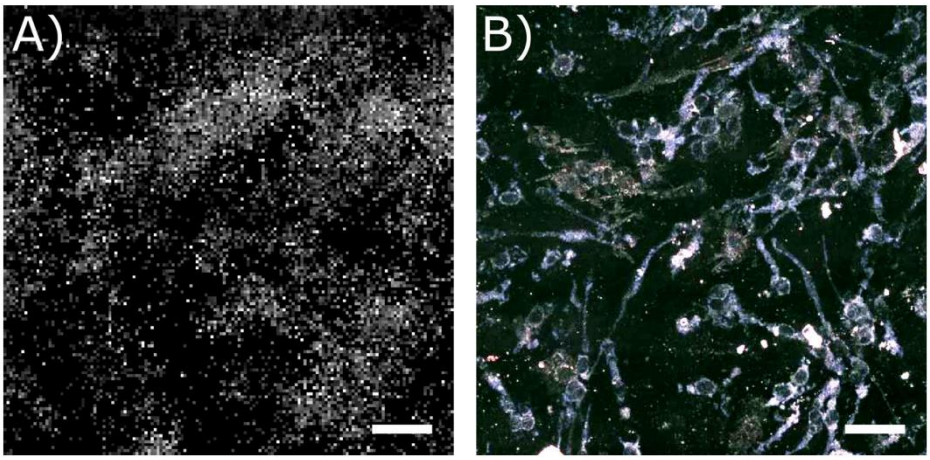

Figure S6: Wash-out effect of analytes from naïve MGL from the B8 cell line with an inappropriate matrix preparation protocol in negative-ion mode. A) AP-SMALDI MSI image of [PE 36:2 – H]⁻ (m/z 742.5392) with 150x150 pixels at 5 µm pixel size showing little to no morphological features. B) Corresponding microscopic image of the area investigated in A). Scale bars: 100 µm.

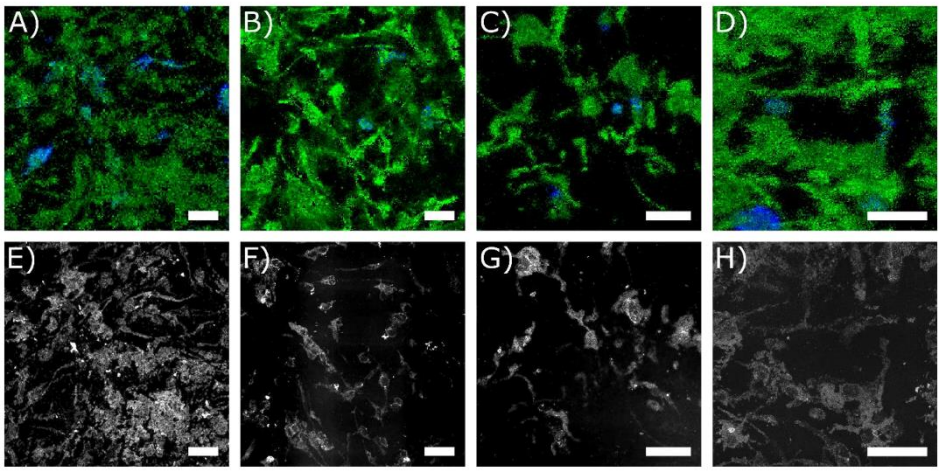

Figure S7: AP-SMALDI MSI images of microglia cells visualizing the distribution of triglycerides represented by $[TG\ 52:2 + Na]^+$ (red, m/z 881.7569) compared to evenly distributed $[PC\ 36:2 + Na]^+$ (green, m/z 808.5827). A): LPS-stimulated D9 MGL cells, 150x150 pixels, 5 µm pixel size. B): LPS-stimulated E2 MGL cells, 250x250 pixels, 3 µm pixel size. C): Naïve D9 MGL cells, 250x250 pixels, 2 µm pixel size. D): LPS-stimulated D9 MGL cells, 250x250 pixels, 1.5 µm pixel size. E)-H): Corresponding microscopic images of the areas investigated. Scale bars: 100 µm.

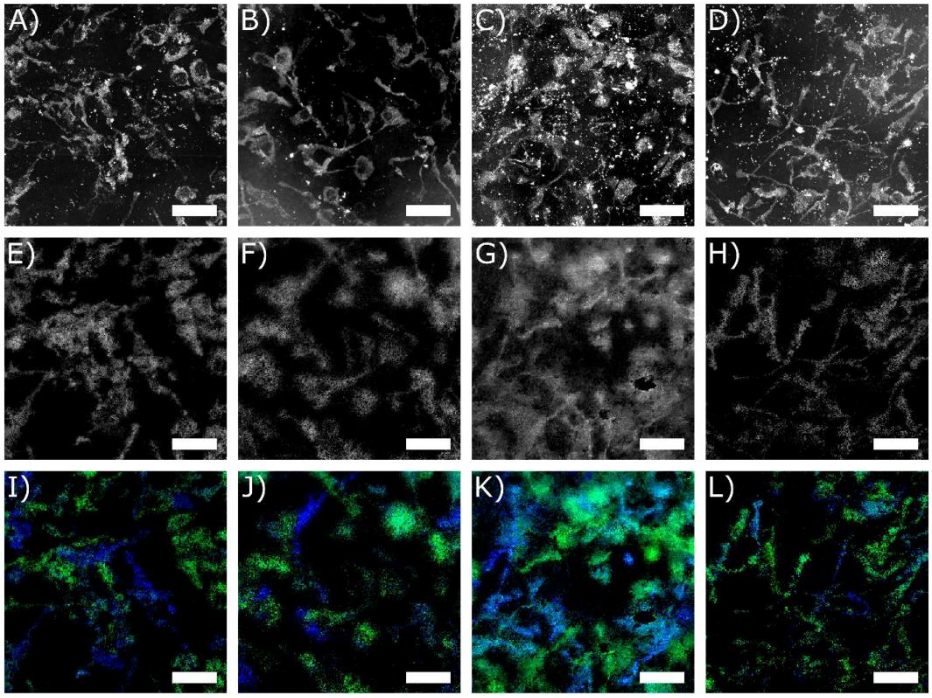

Figure S8: Examples for cell-to-cell heterogeneity found in AP-SMALDI MSI experiments (250x250 pixels, 2 µm pixel size) using negative-ion mode for naïve (A, B, E, F, I, J) and LPS-stimulated (C, D, G, H, K, L) B8 MGL cells. A)-D): Microscopic images of the regions investigated. E)-H): AP-SMALDI MSI images of $[PI\ 38:4 - H]^-$ (m/z 885.5498) as an example for a homogeneously distributed lipid. I)-L): AP-SMALDI MSI images of $[PI\ 38:3 - H]^-$ (m/z 887.5655, red) and $[PI\ 38:5 - H]^-$ (m/z 883.5342, green) showing a heterogeneous distribution of these lipids. Scale bars: 100 µm.

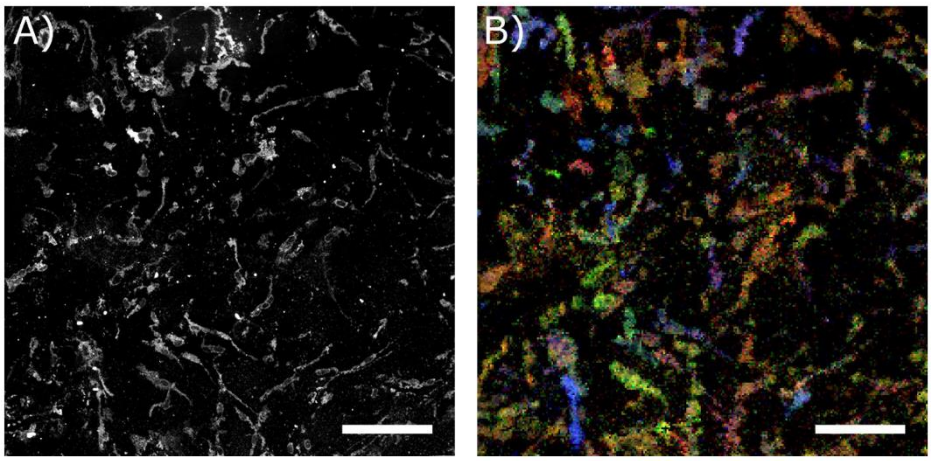

Figure S9: Example for cell-to-cell heterogeneity found in AP-SMALDI MSI experiments (250x250 pixels, 5 µm) using negative ion mode for LPS-stimulated B8 MGL cells. A): Microscopic image of the region investigated. B) AP-SMALDI MSI image of [PI 38:4 - H]$^-$ (m/z 885.5501, red), [PI 38:3 - H]$^-$ (m/z 887.5653, green) and [PI 36:1 - H]$^-$ (m/z 863.5657, blue). Scale bars: 250 µm.

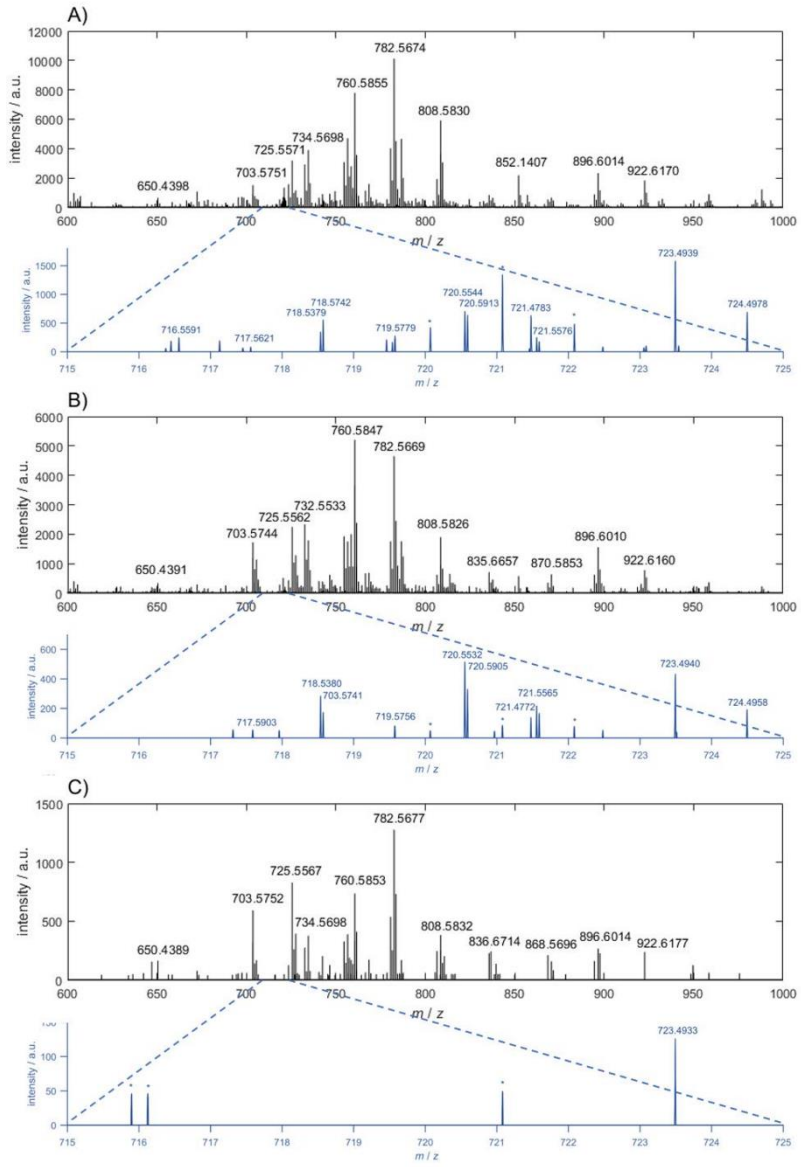

Figure S10: Exemplary single-pixel mass spectra (black, m/z 600 – 1000) from flash-frozen microglia in positive-ion mode at different lateral resolution settings (no fixation). Blue spectra are zoom-ins into a mass window (m/z 715 – 725) with low abundant analytes. Stars indicate matrix-related signals. A) 5 µm pixel size (LPS-stimulated D9 MGL cells), B) 3 µm pixel size (naïve D9 MGL cells), C) 1.5 µm pixel size (naïve E2 MGL cells).

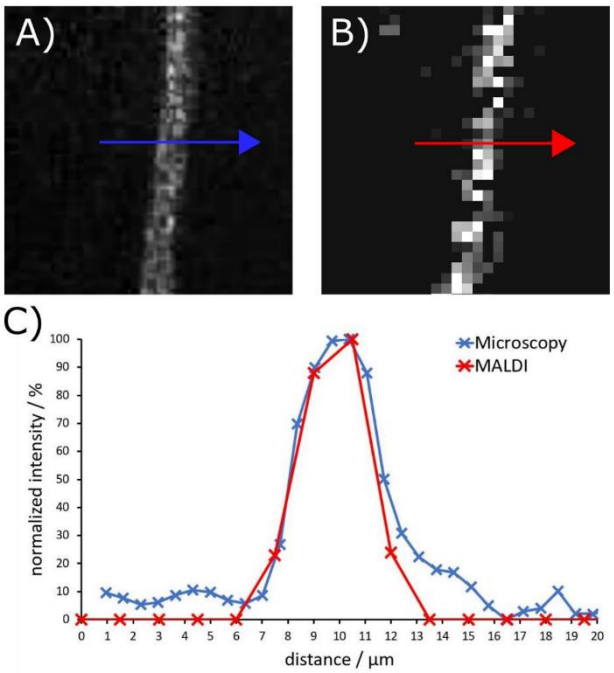

Figure S11: Intensity contrast microglia projections from naïve B8 MGL cells in microscopy and AP-SMALDI MSI on fixed samples. A) Section of a microscopic image of a microglia projection. B) Section of an AP-SMALDI MSI image at 1.5 µm pixel size of PC 34:1 (m/z 896.6140, [M + DHB – H2O + H]$^+$). C) Intensity plot over a microglia projection as indicated by arrows in A) and B) extracted from a microscopy image (blue) and an AP-SMALDI MSI image at 1.5 µm pixel size (red).

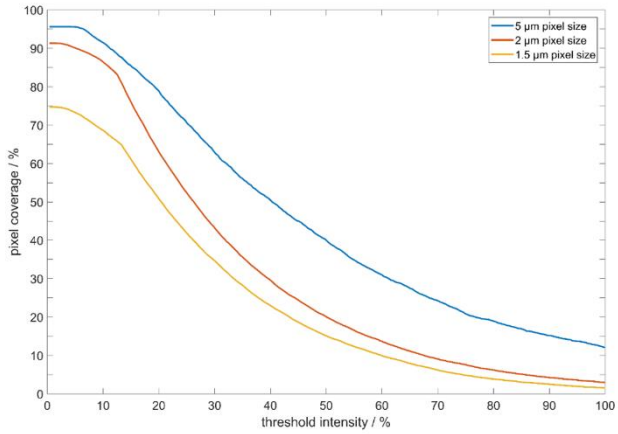

Figure S12: Plot of percentage of pixels, in which the analyte ion signal (exemplary for PC 34:1) is above a given intensity threshold (relative to highest intensity pixel) at different lateral resolution settings. Pixel coverage is normalized to total number of on-cell pixels.

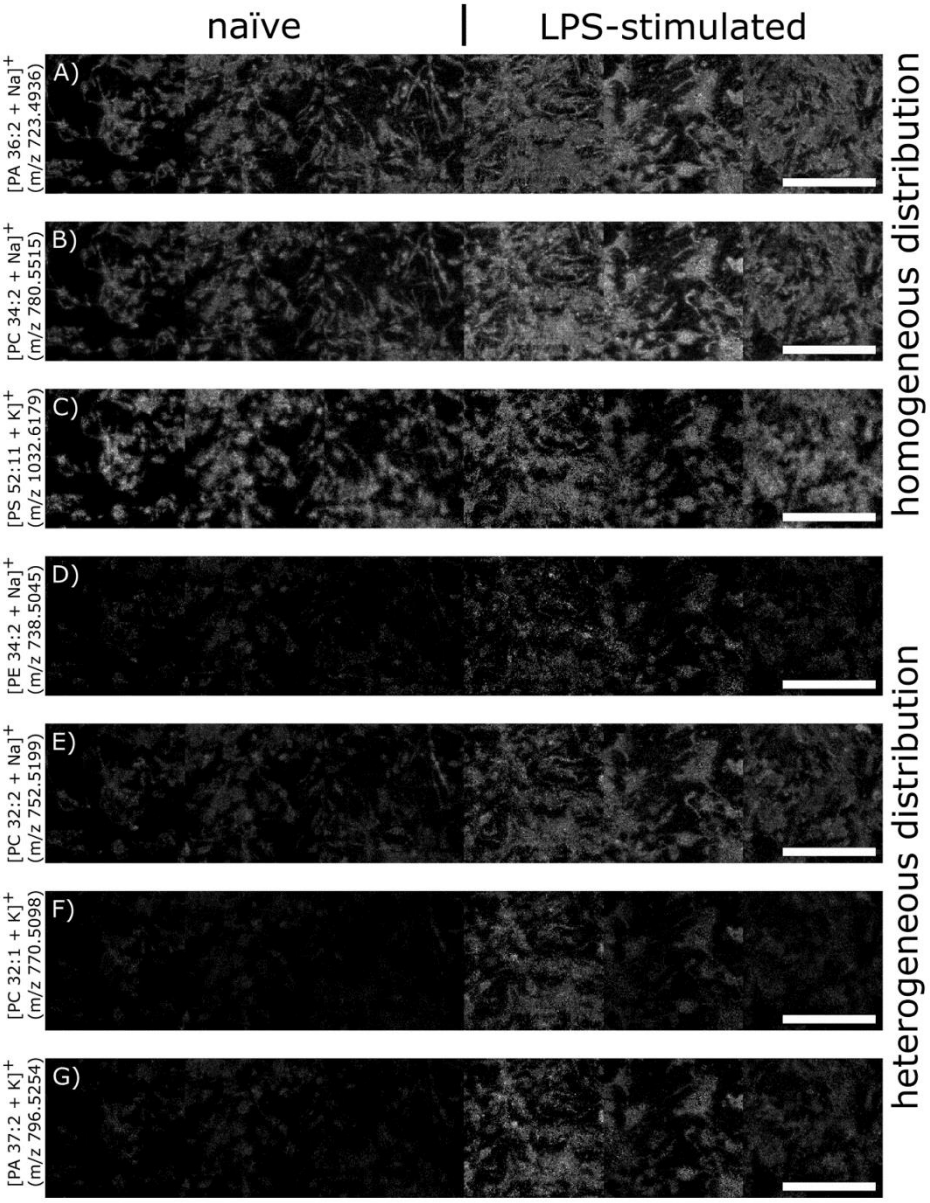

Figure S13: Exemplary AP-SMALDI MSI images of phospholipid signals in the D9 cell line, distributed comparably (A-C) or dissimilarly (D-G) between naïve and LPS-stimulated cells. Each image consists of individual measurements of 3 naïve and 3 LPS-stimulated samples with 150x150 pixels at 5 µm pixel size, respectively. Scale bars: 500 µm.

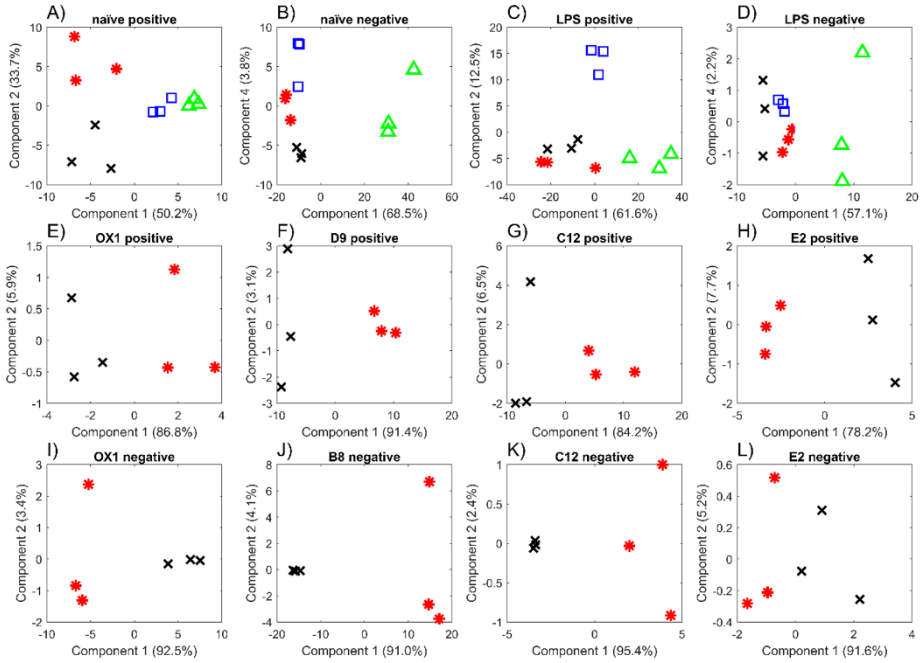

Figure S14: PCA-plots obtained from statistical analysis of AP-SMALDI MSI results at 5 µm pixel size by ANOVA-based multiple-sample test. Three biological replicates of cell cultures grown in separate wells on the same glass slide, each containing a multitude of individual cells, were used for analysis and mass spectrometric signal intensities were averaged over 22,500 mass spectra. P-values were set to 0.01 (A, B, C, D, F, I, J, K) or 0.05 (E, G, H, L), respectively. Color coding: A)-D): OX1 (red, star), D9 (green, triangle positive-ion mode), B8 (green, triangle, negative-ion mode), C12 (blue, square), E2 (black, x). E)-L): naïve (red), LPS-stimulated (black).

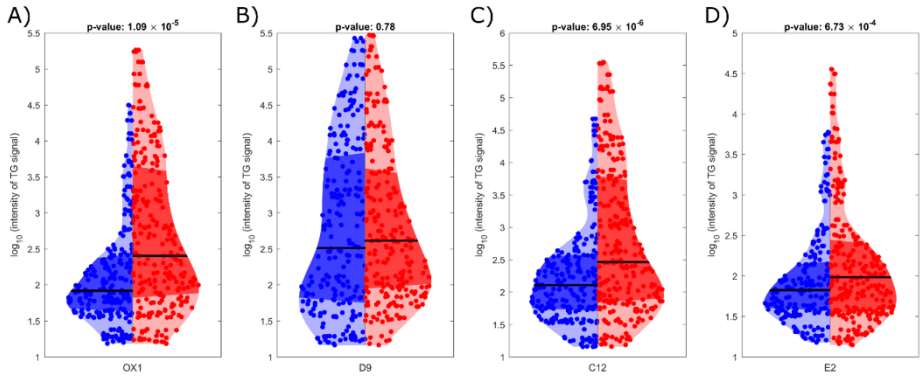

Figure S15: Violin plots of TG-associated signal intensities from a 5 µm pixel size measurement in positive-ion mode of naïve (blue) and LPS-stimulated (red) MGL cells from the OX1 (A), D9 (B), C12 (C) and E2 (D) line, respectively. Each data point corresponds to a TG-associated mass spectrometric signal, averaged from 3 biological replicates. The black line indicates the median. p-Values calculated by double-sided t-test.

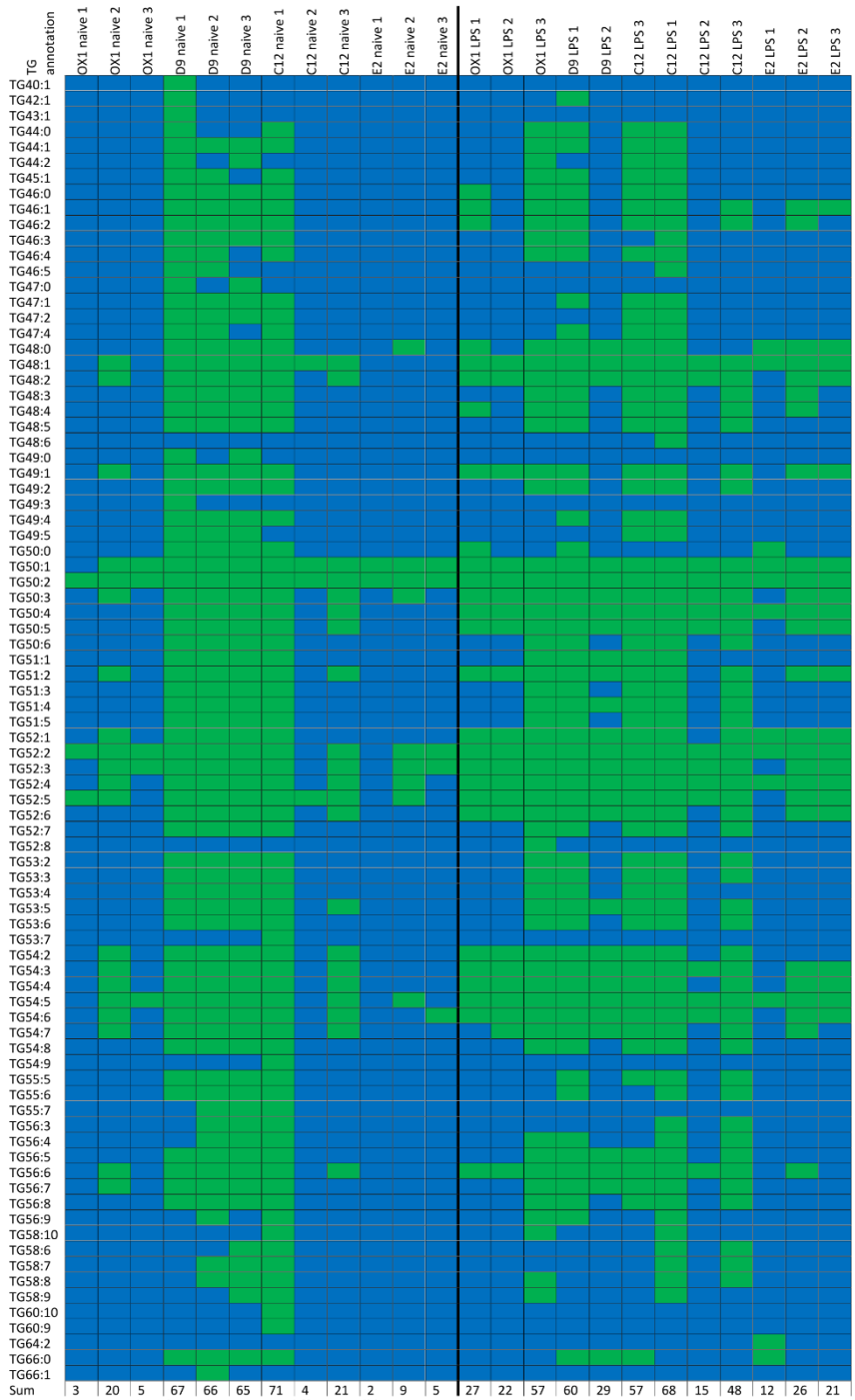

Figure S16: Detected triglyceride species in different cell lines. Green indicates detection, blue indicates no detection in Metaspace using LIPID MAPS database.

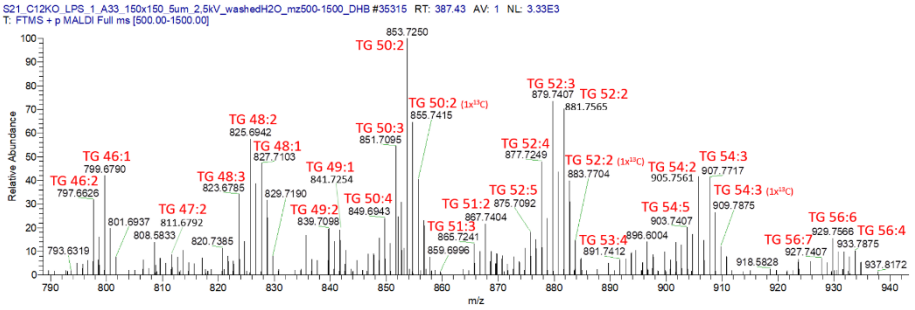

Figure S17: Exemplary single-pixel mass spectrum from LPS-stimulated C12 MGL cells. The mass spectrum was recorded at a position, that is associated with lipid droplets. The most abundant triglyceride species (all [M+Na]⁺) were labelled.

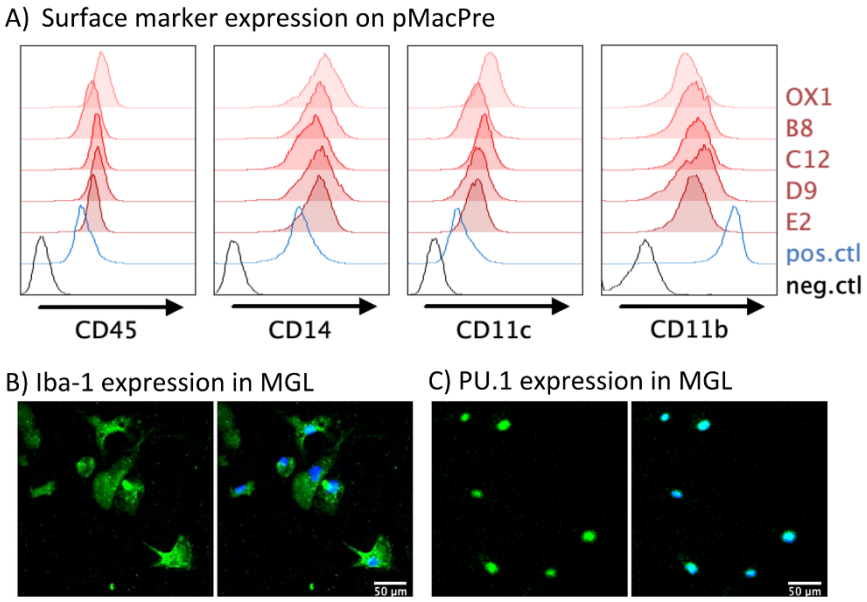

Figure S18: A) Cell surface expression of immune cell marker CD45 and myeloid markers CD14, CD11c and, CD11b in iPSC-derived primitive macrophage precursor (pMacPre) is confirmed by flow cytometry. Negative control: iPSC; positive control: primary blood-derived monocytes. B,C) Representative images of intracellular myeloid markers Iba-1 (green, B) and PU.1 (green, C) in fully differentiated OX1 microglia-like cells. Nuclei were counterstained with DAPI (blue).

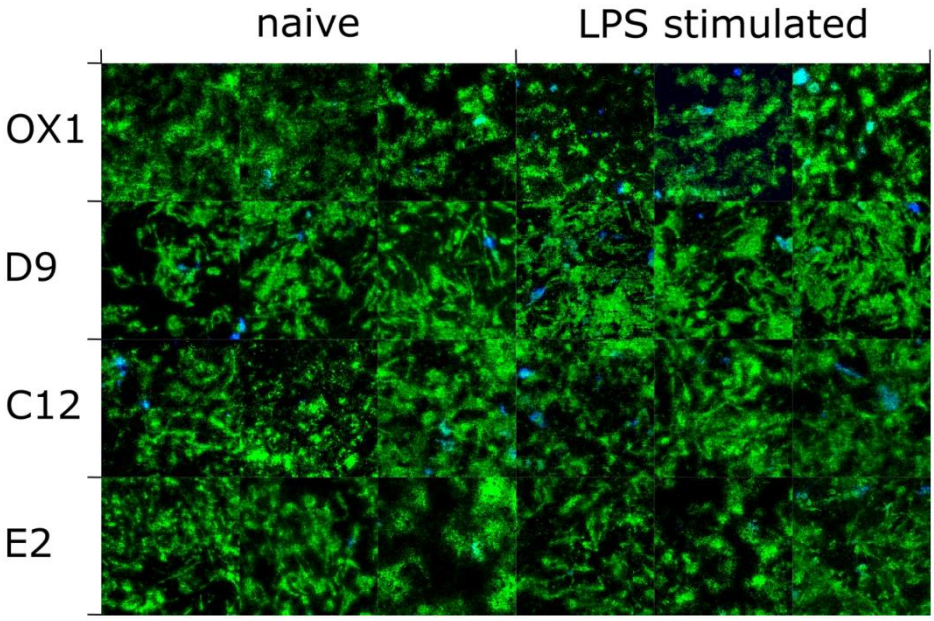

Figure S19: 24 stitched AP-SMALDI MSI images, each 150x150 pixels at 5 µm pixel size, in positive-ion mode of biological triplicates of different cell lines in naïve or LPS-stimulated state showing the distribution of lipid droplets, represented by [TG 52:2 + Na]⁺ (m/z 881.7569, blue), compared to the cellular background, represented by [PC 36:2 + Na]⁺ (m/z 808.5827, green).

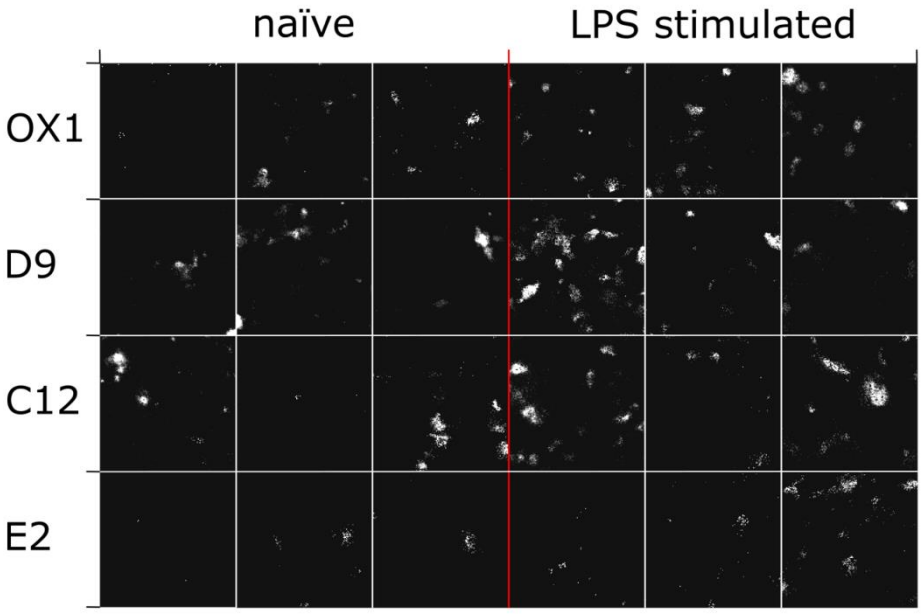

Figure S20: 24 stitched AP-SMALDI MSI images, each 150x150 pixels at 5 µm pixel size, of [TG 52:2 + Na]⁺ in biological triplicates of different cell lines in naïve or LPS-stimulated state. Red line indicates border between naïve and LPS-stimulated cells. White lines indicate borders between different measurements.

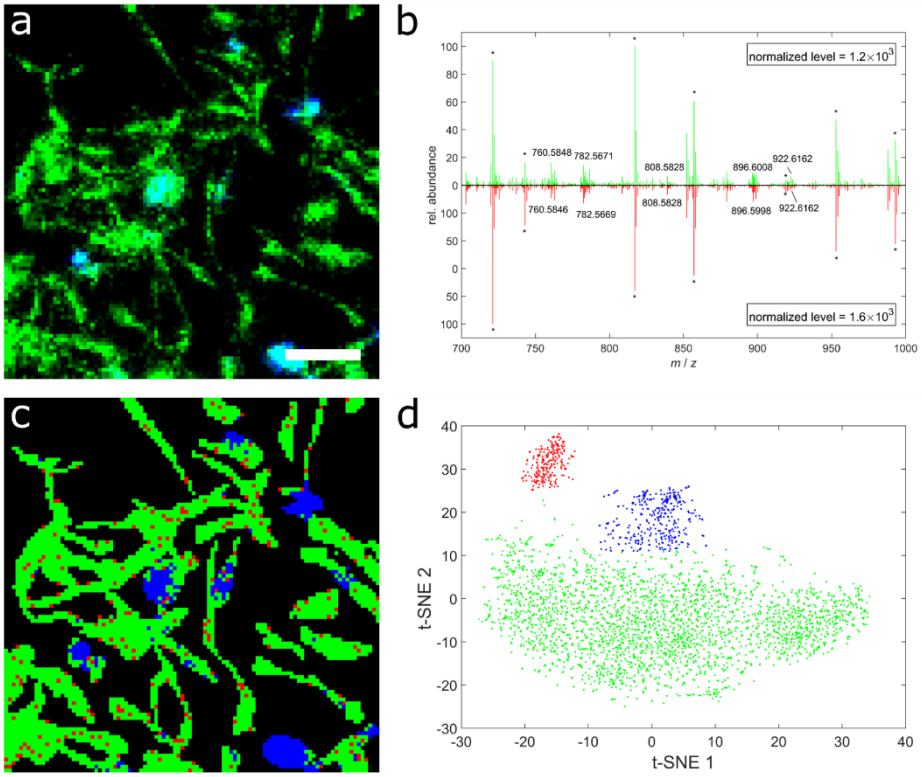

Figure S21: AP-SMALDI MSI and statistical analysis for identification of cells with increased TG production. a): AP-SMALDI MSI image with 100x100 pixels at 5 µm pixel size of fixed LPS-stimulated B8 MGL cells. Color-coding: blue: TG 52:2 (m/z 881.7568, [M + Na]⁺), green: PC 34:1 (m/z 896.6140, [M + DHB – H2O + H]⁺) b): Example of single-pixel mass spectra corresponding to the green or red clusters as identified by pixel-based t-SNE analysis in d. Stars indicate matrix-related signals. c): Pixel-wise classification based on t-SNE analysis of the mass spectrometric data with automated color-coding referring to clusters identified in d. d): Plot of pixel-wise t-SNE analysis of mass spectrometric data (m/z 800-1000) allowing for 3 clusters, while each of the 6511 data points represents an individual mass spectrum. The green cluster nicely outlines the cells in c, the blue cluster identifies pixels with increased triglyceride production and the red cluster is most likely an artifact of statistical analysis, since mass spectra as presented in b are virtually identical. Off-sample signals were excluded from analysis.

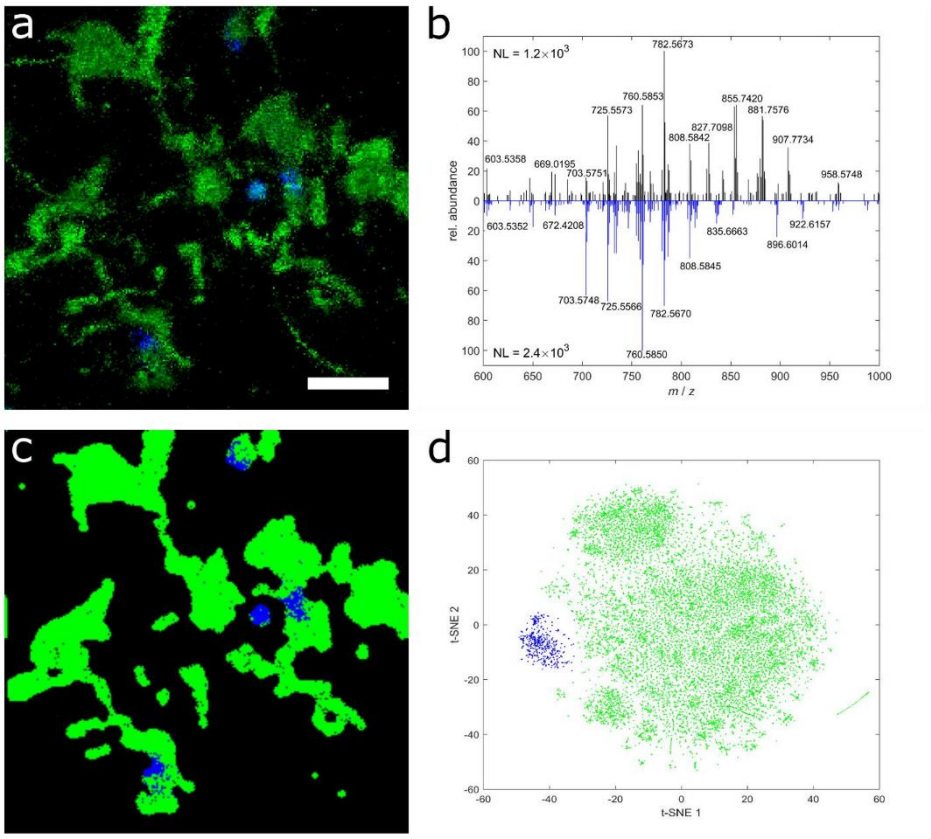

Figure S22 AP-SMALDI MSI and statistical analysis for identification of cells with increased TG production. a): AP-SMALDI MSI image with 250x250 pixels at 2 µm pixel size of naïve D9 cells. Color-coding: blue: TG 52:2 (m/z 881.7568, $[M + Na]^+$), green: PC 36:2 (m/z 808.5827, $[M + Na]^+$). b): Example of single-pixel mass spectra from pixels identified as TG-upregulated (black) or TG-downregulated (blue). c): Pixel-wise classification based on t-SNE analysis of the mass spectrometric data with automated color-coding referring to clusters identified in d. d): Plot of pixel-wise t-SNE analysis of mass spectrometric data (m/z 800-1000) color-coded for clusters identified by hierarchical clustering, while each of the 48041 data points represents an individual mass spectrum. Off-sample signals were excluded from analysis.

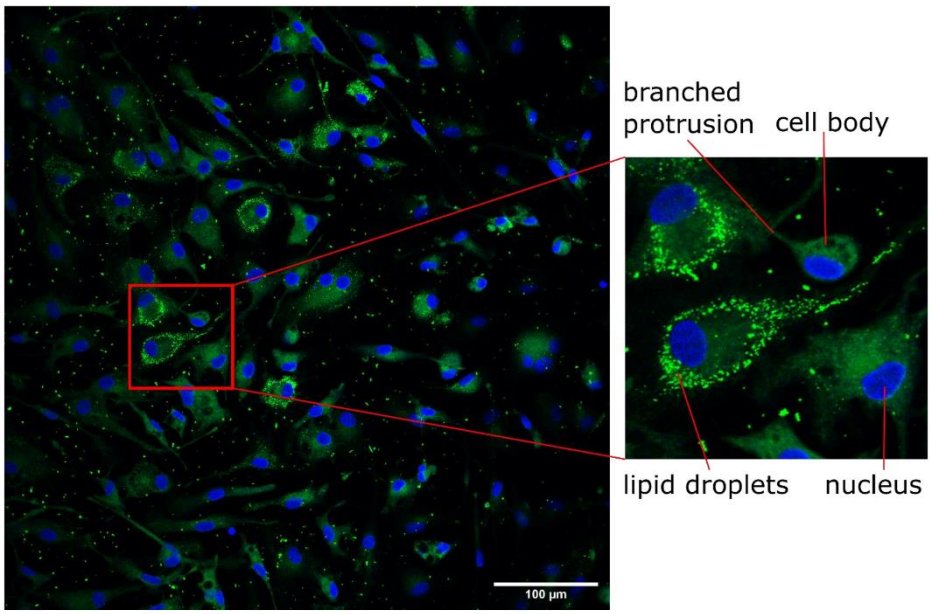

Figure S23: Fluorescence microscopy image of naïve MGL cells of the B8 cell line, stained with BODIPY (green, selective for apolar domains, e.g. lipid droplets) and DAPI (blue, selective for DNA, e.g. cell nuclei), indicating a heterogeneous distribution of lipid droplets. Red lines indicate zoom-in on interesting area.

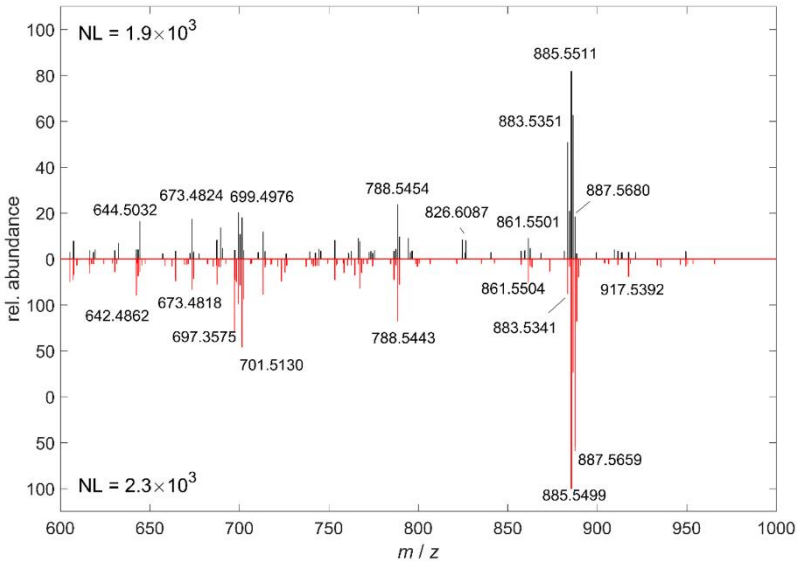

Figure S24: Single-pixel mass spectra of different subpopulations in naïve B8 MGL cells measured in negative-ion mode.

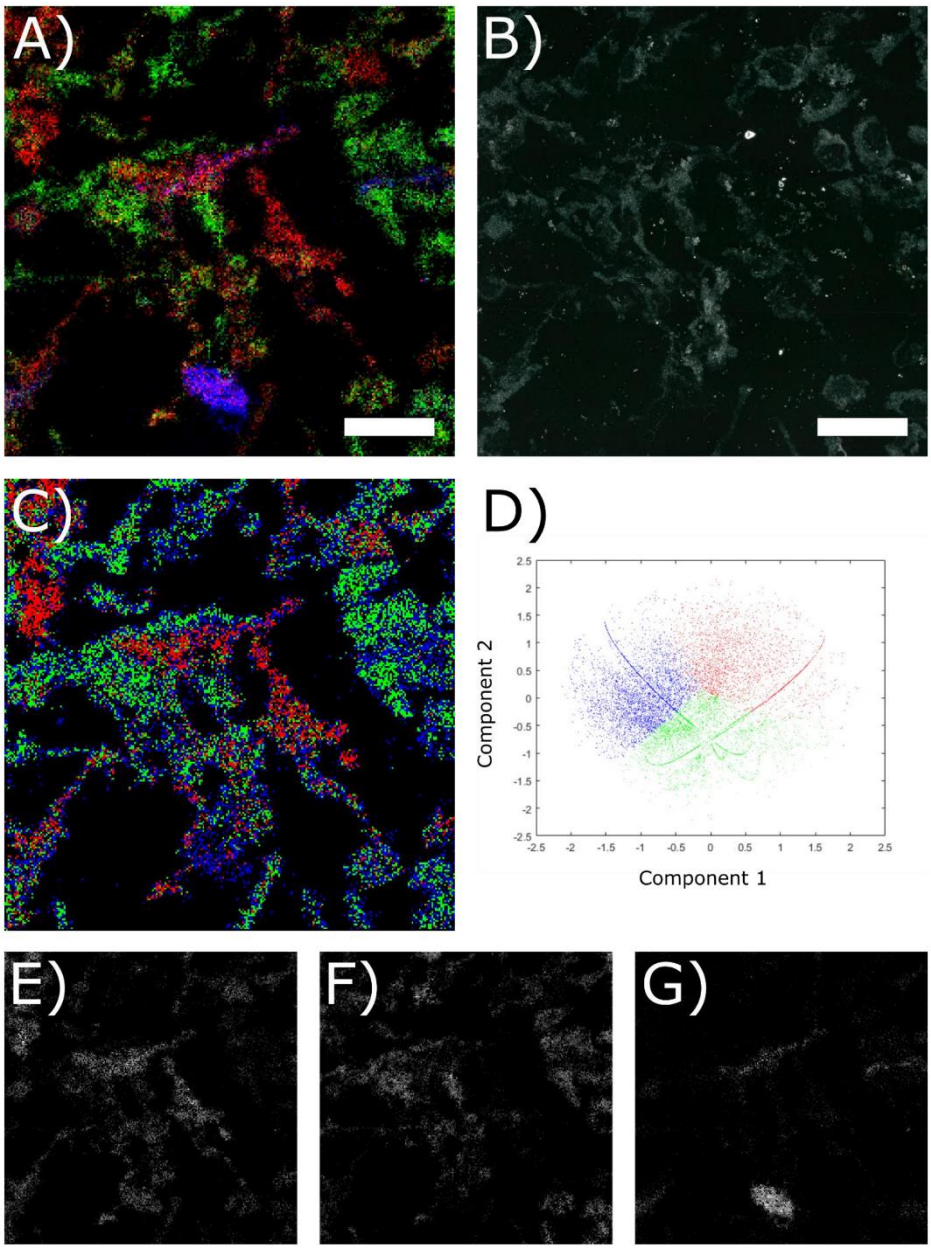

Figure S25: Statistical analysis of a naïve sample from the B8 microglia cell line. A), E), F), G): AP-SMALDI MSI images showing [PI 38:3 - H]⁻ (red or (E), m/z 887.5655), [PI 38:5- H]⁻ (green or (F), m/z 883.5342) and [PI 36:1 - H]⁻ (blue or (G), m/z 863.5491). B): Corresponding microscopic image of the area investigated. C): Pixelwise classification using a k-means algorithm for automated clustering based on mass spectrometric data from m/z 860 – 900. Colors red, green and blue symbolize cluster affiliation. D): Principal component analysis plot of mass spectrometric data, colorized corresponding to clusters identified by k-means algorithm (as shown in C)). Each of the 46051 data points represents an individual mass spectrum. Clusters found by k-means also cluster in principal component analysis.

Table S1: List of lipid annotations for 5 µm pixel size measurements of flash frozen D9 MGL, considering all lipid-related signals, that were found in >1% of all pixels. Annotations were assigned using the LIPID MAPS database allowing for a mass deviation of <5ppm (grey) or <0.05 m/z (others). Color coding indicates consensus with literature-reported annotations by Fitzner and co-workers with deviation to mass measured by our own MALDI MSI experiments being <5 ppm (green), <20 ppm (yellow) or >20 ppm (red). Stars (*) indicate the possibility of the formation of a DHB-adduct for this particular m/z value, which are listed and explained in Table S2.

m/z found	*m/z* calc	LIPID MAPS annotation	adduct	Δ *m/z*	Δppm	Literature annotation
601.5194	601.519	DG O-36:5	[M+H]+	0.0003	0.50	
601.5202	601.519	DG O-36:5	[M+H]+	0.0012	1.99	
603.5351	603.5347	DG O-36:4	[M+H]+	0.0004	0.66	
604.5385	604.5065	Cer 36:1;O2	[M+K]+	0.0319	52.77	Cer 36:1;2
605.4241	605.4259	MGDG 23:0	[M+H]+	0.0018	2.97	
605.5471	605.5479	DG O-34:0	[M+Na]+	0.0008	1.32	
605.5509	605.5503	DG O-36:3	[M+H]+	0.0006	0.99	
606.4134	606.4129	LPS O-25:2	[M+H]+	0.0004	0.66	
608.4289	608.4286	LPS O-25:1	[M+H]+	0.0004	0.66	
615.4963	615.4959	DG 34:2	[M+Na]+	0.0004	0.65	
616.5777	616.5639	Cer 38:1;O2	[M+Na]+	0.0138	22.38	Cer 38:1;2
617.5120	617.5115	DG 34:1	[M+Na]+	0.0005	0.81	
617.5120	617.5115	DG 34:1	[M+Na]+	0.0005	0.81	DAG 16:0;0 18:1;0
618.4131	618.4129	LPS O-26:3	[M+H]+	0.0001	0.16	
620.4288	620.4286	LPS O-26:2	[M+H]+	0.0002	0.32	
622.4082	622.408	DGTA 23:1	[M+K]+	0.0002	0.32	
622.4212	622.4207	LPC O-25:4	[M+Na]+	0.0005	0.80	
622.4445	622.4442	LPS O-26:1	[M+H]+	0.0003	0.48	
623.5031	623.5034	DG O-38:8	[M+H]+	0.0003	0.48	
624.4239	624.4236	DGTA 23:0	[M+K]+	0.0003	0.48	
625.5187	625.519	DG O-38:7	[M+H]+	0.0004	0.64	
627.4945	627.4959	DG 35:3	[M+Na]+	0.0014	2.23	
627.5349	627.5347	DG O-38:6	[M+H]+	0.0002	0.32	
629.5496	629.5503	DG O-38:5	[M+H]+	0.0007	1.11	
629.5508	629.5503	DG O-38:5	[M+H]+	0.0004	0.64	
630.4097	630.4105	LPS O-25:1	[M+Na]+	0.0008	1.27	
630.4109	630.4105	LPS O-25:1	[M+Na]+	0.0004	0.63	
630.4472	630.4469	LPC 24:0	[M+Na]+	0.0003	0.48	
631.4144	631.4123	DG O-36:9	[M+K]+	0.0021	3.33	
631.5662	631.566	DG O-38:4	[M+H]+	0.0002	0.32	
632.4287	632.4286	LPS O-27:3	[M+H]+	0.0001	0.16	
634.4080	634.408	DGTA 24:2	[M+K]+	0.0001	0.16	
634.4445	634.4442	LPS O-27:2	[M+H]+	0.0002	0.32	
636.4238	636.4236	DGTA 24:1	[M+K]+	0.0002	0.31	
636.4363	636.4363	LPC O-26:4	[M+Na]+	0	<0.01	
636.4596	636.4599	LPS O-27:1	[M+H]+	0.0002	0.31	
636.4604	636.4599	LPS O-27:1	[M+H]+	0.0005	0.79	
638.4031	638.4029	DGCC 23:1	[M+K]+	0.0002	0.31	
638.4390	638.4391	LPS 26:0	[M+H]+	0.0001	0.16	
638.4404	638.4393	DGTA 24:0	[M+K]+	0.0011	1.72	
638.4522	638.452	LPC O-26:3	[M+Na]+	0.0002	0.31	
639.4062	639.4079	MGDG 24:1	[M+Na]+	0.0017	2.66	
640.4680	640.4676	LPC O-26:2	[M+Na]+	0.0003	0.47	
641.4716	641.4694	CE 15:4	[M+K]+	0.0021	3.27	
642.4097	642.4105	LPS O-26:2	[M+Na]+	0.0008	1.25	
642.4109	642.4105	LPS O-26:2	[M+Na]+	0.0004	0.62	
642.4839	642.4833	LPC O-26:1	[M+Na]+	0.0006	0.93	
643.4144	643.4123	DG O-37:10	[M+K]+	0.0021	3.26	
643.5275	643.5272	DG 36:2	[M+Na]+	0.0003	0.47	
643.5275	643.5272	DG 36:2	[M+Na]+	0.0003	0.47	DAG 18:0;0 18:2;0
643.5275	643.5272	DG 36:2	[M+Na]+	0.0003	0.47	DAG 18:1;0 18:1;0
644.4265	644.4262	LPS O-26:1	[M+Na]+	0.0003	0.47	
644.4635	644.4626	LPC 25:0	[M+Na]+	0.001	1.55	
644.6091	644.5952	Cer 40:1;O2	[M+Na]+	0.0139	21.56	Cer 40:1;2
645.4295	645.428	DG O-37:9	[M+K]+	0.0016	2.48	
645.4305	645.428	DG O-37:9	[M+K]+	0.0025	3.87	
646.4064	646.4054	LPS 25:0	[M+Na]+	0.0009	1.39	
646.4443	646.4442	LPS O-28:3	[M+H]+	0.0001	0.15	
648.4237	648.4236	DGTA 25:2	[M+K]+	0.0001	0.15	
648.4592	648.4599	LPS O-28:2	[M+H]+	0.0006	0.93	
648.4605	648.4599	LPS O-28:2	[M+H]+	0.0006	0.93	
650.4030	650.4029	DGCC 24:2	[M+K]+	0.0002	0.31	
650.4393	650.4393	DGTA 25:1	[M+K]+	0.0001	0.15	
650.4402	650.4393	DGTA 25:1	[M+K]+	0.0009	1.38	
650.4522	650.452	LPC O-27:4	[M+Na]+	0.0002	0.31	
650.4758	650.4755	LPS O-28:1	[M+H]+	0.0003	0.46	
651.5347	651.5347	DG O-40:8	[M+H]+	0	<0.01	
652.4187	652.4185	DGCC 24:1	[M+K]+	0.0001	0.15	
652.4317	652.4313	LPC 26:3	[M+Na]+	0.0005	0.77	
652.4555	652.4549	DGTA 25:0	[M+K]+	0.0006	0.92	
652.4679	652.4676	LPC O-27:3	[M+Na]+	0.0003	0.46	

653.4228	653.4235	MGDG 25:1	[M+Na]+	0.0007	1.07	
654.4096	654.4105	LPS O-27:3	[M+Na]+	0.0009	1.38	
654.4109	654.4105	LPS O-27:3	[M+Na]+	0.0004	0.61	
654.4342	654.4342	DGCC 24:0	[M+K]+	0	<0.01	
654.4473	654.4469	LPC 26:2	[M+Na]+	0.0004	0.61	
654.4836	654.4833	LPC O-27:2	[M+Na]+	0.0003	0.46	
655.4378	655.4392	MGDG 25:0	[M+Na]+	0.0013	1.98	
655.4675	655.4673	LPA 32:1	[M+Na]+	0.0001	0.15	
656.4053	656.4052	LPC 25:2	[M+K]+	0.0001	0.15	
656.4265	656.4262	LPS O-27:2	[M+Na]+	0.0003	0.46	
656.5726	656.5952	Cer 41:2;O2	[M+Na]+	0.0227	34.57	Cer 41:2;2
657.4087	657.4102	LPG 27:2	[M+Na]+	0.0014	2.13	
657.4291	657.428	DG O-38:10	[M+K]+	0.0012	1.83	
657.4309	657.4337	LPI O-23:0	[M+H]+	0.0028	4.26	
657.4553	657.4572	MGDG 27:2	[M+H]+	0.002	3.04	
658.4056	658.4054	LPS 26:1	[M+Na]+	0.0002	0.30	
658.4422	658.4418	LPS O-27:1	[M+Na]+	0.0003	0.46	
658.4576	658.4572	LPC O-26:1	[M+K]+	0.0004	0.61	
658.5409	658.5535	Cer 40:2;O2	[M+K]+	0.0126	19.13	Cer 40:2;2
659.4091	659.4072	DG 37:9	[M+K]+	0.0018	2.73	
659.4103	659.4072	DG 37:9	[M+K]+	0.0031	4.70	
659.4103	659.4049	PA 30:0	[M+K]+	0.0055	8.34	PA 14:0;0 16:0;0
659.4457	659.4436	DG O-38:9	[M+K]+	0.0021	3.18	
659.5922	659.5949	DG O-38:1	[M+Na]+	0.0026	3.94	
660.4220	660.4211	LPS 26:0	[M+Na]+	0.0009	1.36	
660.4593	660.4599	LPS O-29:3	[M+H]+	0.0006	0.91	
660.4606	660.4599	LPS O-29:3	[M+H]+	0.0007	1.06	
661.4253	661.4229	DG 37:8	[M+K]+	0.0025	3.78	
661.6074	661.6105	DG O-38:0	[M+Na]+	0.0031	4.69	
662.4018	662.4028	PS 27:2	[M+H]+	0.0009	1.36	
662.4390	662.4391	LPS 28:2	[M+H]+	0.0001	0.15	
662.4422	662.4393	DGTA 26:2	[M+K]+	0.0029	4.38	
662.4509	662.452	LPC O-28:5	[M+Na]+	0.0011	1.66	
662.4757	662.4755	LPS O-29:2	[M+H]+	0.0002	0.30	
664.4187	664.4185	DGCC 25:2	[M+K]+	0.0002	0.30	
664.4550	664.4549	DGTA 26:1	[M+K]+	0.0001	0.15	
664.4679	664.4676	LPC O-28:4	[M+Na]+	0.0002	0.30	
664.4915	664.4912	LPS O-29:1	[M+H]+	0.0003	0.45	
665.4225	665.4235	MGDG 26:2	[M+Na]+	0.001	1.50	
665.4714	665.4752	PA 32:0;O	[M+H]+	0.0038	5.71	PA 16:0;0 16:0;0
666.4343	666.4342	DGCC 25:1	[M+K]+	0.0001	0.15	
666.4473	666.4469	LPC 27:3	[M+Na]+	0.0004	0.60	
666.4671	666.4704	LPS 28:0	[M+H]+	0.0033	4.95	
666.4707	666.4706	DGTA 26:0	[M+K]+	0.0001	0.15	
666.4834	666.4833	LPC O-28:3	[M+Na]+	0.0002	0.30	
667.4377	667.4392	MGDG 26:1	[M+Na]+	0.0015	2.25	
668.4265	668.4262	LPS O-28:3	[M+Na]+	0.0003	0.45	
668.4413	668.4416	LPC O-27:3	[M+K]+	0.0003	0.45	
668.4629	668.4626	LPC 27:2	[M+Na]+	0.0004	0.60	
668.4994	668.4989	LPC O-28:2	[M+Na]+	0.0005	0.75	
668.5004	668.5013	LPC O-30:5	[M+H]+	0.001	1.50	
669.4117	669.4126	TG 38:10	[M+Na]+	0.0008	1.20	
669.4312	669.4337	LPI O-24:1	[M+H]+	0.0025	3.73	
669.4467	669.4466	LPG O-29:3	[M+Na]+	0.0001	0.15	
669.4834	669.483	LPA 33:1	[M+Na]+	0.0005	0.75	
669.5028	669.5007	CE 17:4	[M+K]+	0.0021	3.14	
670.4057	670.4054	LPS 27:2	[M+Na]+	0.0002	0.30	
670.4420	670.4418	LPS O-28:2	[M+Na]+	0.0002	0.30	
670.4788	670.4782	LPC 27:1	[M+Na]+	0.0006	0.89	
671.4090	671.4072	DG 38:10	[M+K]+	0.0018	2.68	
671.4105	671.413	LPI 23:0	[M+H]+	0.0025	3.72	
671.4457	671.4436	DG O-39:10	[M+K]+	0.0021	3.13	
671.4623	671.4622	LPG O-29:2	[M+Na]+	0.0001	0.15	
672.4213	672.4211	LPS 27:1	[M+Na]+	0.0002	0.30	
672.4578	672.4575	LPS O-28:1	[M+Na]+	0.0003	0.45	
673.4245	673.4229	DG 38:9	[M+K]+	0.0017	2.52	
673.4614	673.4593	DG O-39:9	[M+K]+	0.0021	3.12	
674.4007	674.4004	PS 26:0	[M+Na]+	0.0003	0.44	
674.4385	674.4391	LPS 29:3	[M+H]+	0.0007	1.04	
674.4755	674.4755	LPS O-30:3	[M+H]+	0.0001	0.15	
674.5831	674.5848	Cer 41:1;O2	[M+K]+	0.0017	2.52	Cer 41:1;2
675.4039	675.4021	TG 37:8	[M+K]+	0.0017	2.52	
675.4417	675.4385	DG 38:8	[M+K]+	0.0032	4.74	
676.4166	676.4184	PS 28:2	[M+H]+	0.0018	2.66	
676.4547	676.4548	LPS 29:2	[M+H]+	0.0001	0.15	
676.4914	676.4912	LPS O-30:2	[M+H]+	0.0002	0.30	
677.4180	677.4178	TG 37:7	[M+K]+	0.0002	0.30	
677.5605	677.5633	CE 17:0	[M+K]+	0.0028	4.13	
678.4342	678.4342	DGCC 26:2	[M+K]+	0	<0.01	
678.4698	678.4704	LPS 29:1	[M+H]+	0.0007	1.03	
678.4706	678.4706	DGTA 27:1	[M+K]+	0.0001	0.15	
678.5068	678.5068	LPS O-30:1	[M+H]+	0	<0.01	
679.4366	679.4392	MGDG 27:2	[M+Na]+	0.0026	3.83	

S22

680.4492	680.4497	DGTA 29:6	[M+Na]+	0.0004	0.59	
680.4505	680.4498	DGCC 26:1	[M+K]+	0.0006	0.88	
680.4629	680.4626	LPC 28:3	[M+Na]+	0.0003	0.44	
680.4989	680.4989	LPC O-29:3	[M+Na]+	0.0001	0.15	
681.4464	681.4466	LPG O-30:4	[M+Na]+	0.0002	0.29	
681.4826	681.483	LPA 34:2	[M+Na]+	0.0003	0.44	
682.4054	682.4054	LPS 28:3	[M+Na]+	0	<0.01	
682.4221	682.4208	LPC 27:3	[M+K]+	0.0012	1.76	
682.4422	682.4418	LPS O-29:3	[M+Na]+	0.0004	0.59	
682.4571	682.4572	LPC O-28:3	[M+K]+	0.0001	0.15	
682.4782	682.4782	LPC 28:2	[M+Na]+	0	<0.01	
683.4461	683.4436	DG O-40:11	[M+K]+	0.0025	3.66	
683.4616	683.4622	LPG O-30:3	[M+Na]+	0.0006	0.88	
683.4742	683.4729	MGDG 29:3	[M+H]+	0.0013	1.90	
683.4742	683.5011	DG 38:4	[M+K]+	0.0270	39.50	DAG 18:0;0 20:4;0
683.4984	683.4986	LPA 34:1	[M+Na]+	0.0002	0.29	
684.4197	684.4211	LPS 28:2	[M+Na]+	0.0014	2.05	
684.4212	684.4211	LPS 28:2	[M+Na]+	0.0001	0.15	
684.4362	684.4365	LPC 27:2	[M+K]+	0.0003	0.44	
684.4574	684.4575	LPS O-29:2	[M+Na]+	0.0001	0.15	
684.4735	684.4729	LPC O-28:2	[M+K]+	0.0006	0.88	
685.4239	685.4229	DG 39:10	[M+K]+	0.001	1.46	
685.4616	685.4593	DG O-40:10	[M+K]+	0.0023	3.36	
685.4769	685.4779	LPG O-30:2	[M+Na]+	0.001	1.46	
685.4769	685.4415	PA 32:1;O	[M+Na]+	0.0354	51.64	PA 16:0;0 16:1;0
686.4007	686.4004	PS 27:1	[M+Na]+	0.0004	0.58	
686.4369	686.4367	LPS 28:1	[M+Na]+	0.0002	0.29	
686.4735	686.4731	LPS O-29:1	[M+Na]+	0.0004	0.58	
686.5678	686.5848	Cer 42:2;O2	[M+K]+	0.0170	24.76	Cer 42:2;2
687.4041	687.4021	TG 38:9	[M+K]+	0.0019	2.76	
687.4395	687.4385	DG 39:9	[M+K]+	0.001	1.45	
687.4407	687.4385	DG 39:9	[M+K]+	0.0022	3.20	
687.4773	687.4749	DG O-40:9	[M+K]+	0.0023	3.35	
687.5786	687.5435	SM 33:2;O2	[M+H]+	0.0351	51.05	SM 33:2;2
688.4161	688.416	PS 27:0	[M+Na]+	0.0001	0.15	
688.4530	688.4524	LPS 28:0	[M+Na]+	0.0006	0.87	
688.4655	688.4676	LPC O-30:6	[M+Na]+	0.0021	3.05	
688.4912	688.4912	LPS O-31:3	[M+H]+	0	<0.01	
688.5835	688.6004	Cer 42:1;O2	[M+K]+	0.0170	24.69	Cer 42:1;2
689.4193	689.4178	TG 38:8	[M+K]+	0.0015	2.18	
689.4203	689.4178	TG 38:8	[M+K]+	0.0025	3.63	
689.4566	689.4542	DG 39:8	[M+K]+	0.0024	3.48	
689.5229	689.5198	MGDG 29:0	[M+H]+	0.0031	4.50	
689.5605	689.5633	CE 18:1	[M+K]+	0.0029	4.21	
689.5605	689.5592	SM 33:1;O2	[M+H]+	0.0013	1.89	SM 33:1;2
690.4334	690.4341	PS 29:2	[M+H]+	0.0006	0.87	
690.4694	690.4704	LPS 30:2	[M+H]+	0.001	1.45	
690.4709	690.4706	DGTA 28:2	[M+K]+	0.0004	0.58	
690.4815	690.4833	LPC O-30:5	[M+Na]+	0.0018	2.61	
690.5432	690.5432	LPC 30:1	[M+H]+	0	<0.01	
691.4283	691.4309	LPG O-31:6	[M+Na]+	0.0026	3.76	
692.4495	692.4497	DGTA 30:7	[M+Na]+	0.0002	0.29	
692.4504	692.4498	DGCC 27:2	[M+K]+	0.0005	0.72	
692.4860	692.4861	LPS 30:1	[M+H]+	0	<0.01	
692.5225	692.5225	LPS O-31:1	[M+H]+	0	<0.01	
692.5225	692.5225	PE 32:0	[M+H]+	0.0000	<0.01	PE 16:0;0 16:0;0
692.5589	692.5589	LPC 30:0	[M+H]+	0	<0.01	
693.4461	693.4466	LPG O-31:5	[M+Na]+	0.0005	0.72	
693.4531	693.4548	MGDG 28:2	[M+Na]+	0.0017	2.45	
694.4469	694.4442	LPS O-32:7	[M+H]+	0.0027	3.89	
694.4654	694.4654	PS 29:0	[M+H]+	0	<0.01	
694.5147	694.5146	LPC O-30:3	[M+Na]+	0.0001	0.14	
695.4622	695.4622	LPG O-31:4	[M+Na]+	0	<0.01	
696.4195	696.4211	LPS 29:3	[M+Na]+	0.0016	2.30	
696.4211	696.4211	LPS 29:3	[M+Na]+	0	<0.01	
696.4570	696.4575	LPS O-30:3	[M+Na]+	0.0004	0.57	
696.5294	696.5302	LPC O-30:2	[M+Na]+	0.0008	1.15	
696.5307	696.5302	LPC O-30:2	[M+Na]+	0.0005	0.72	
697.4244	697.4229	DG 40:11	[M+K]+	0.0015	2.15	
697.4632	697.465	LPI O-26:1	[M+H]+	0.0018	2.58	
697.4632	697.4779	PA 34:1	[M+Na]+	0.0146	20.93	PA 16:0;0 18:1;0
697.4779	697.4779	LPG O-31:3	[M+Na]+	0	<0.01	
698.4011	698.4004	PS 28:2	[M+Na]+	0.0007	1.00	
698.4368	698.4367	LPS 29:2	[M+Na]+	0	<0.01	
698.4784	698.4755	LPS O-32:5	[M+H]+	0.0029	4.15	
699.4396	699.4385	DG 40:10	[M+K]+	0.0011	1.57	
699.4405	699.4385	DG 40:10	[M+K]+	0.002	2.86	
700.4163	700.416	PS 28:1	[M+Na]+	0.0003	0.43	
700.4526	700.4524	LPS 29:1	[M+Na]+	0.0002	0.29	
700.4886	700.4888	LPS O-30:1	[M+Na]+	0.0002	0.29	
700.4907	700.4912	LPS O-32:4	[M+H]+	0.0005	0.71	
700.5254	700.5252	LPC 29:0	[M+Na]+	0.0002	0.29	
701.4189	701.4178	TG 39:9	[M+K]+	0.0011	1.57	

701.4208	701.4235	MGDG 29:5	[M+Na]+	0.0027	3.85	
701.4559	701.4542	DG 40:9	[M+K]+	0.0018	2.57	
701.4795	701.4776	TG 42:11	[M+H]+	0.0019	2.71	
701.4811	701.4776	TG 42:11	[M+H]+	0.0035	4.99	
701.5604	701.5633	CE 19:2	[M+K]+	0.003	4.28	
701.5604	701.5592	SM 34:2;O2	[M+H]+	0.0012	1.71	SM 34:2;2
702.4112	702.4107	LPS 28:1	[M+K]+	0.0005	0.71	
702.4319	702.4317	PS 28:0	[M+Na]+	0.0003	0.43	
702.4680	702.468	LPS 29:0	[M+Na]+	0	<0.01	
702.4708	702.4706	DGTA 29:3	[M+K]+	0.0002	0.28	
702.4844	702.4834	LPC 28:0	[M+K]+	0.0009	1.28	
702.5067	702.5068	LPS O-32:3	[M+H]+	0.0001	0.14	
703.4352	703.4334	TG 39:8	[M+K]+	0.0018	2.56	
703.4734	703.4698	DG 40:8	[M+K]+	0.0035	4.98	
703.5388	703.5355	MGDG 30:0	[M+H]+	0.0033	4.69	
704.4032	704.4052	LPC 29:6	[M+K]+	0.002	2.84	
704.4478	704.4497	PS 30:2	[M+H]+	0.0019	2.70	
704.4861	704.4861	LPS 31:2	[M+H]+	0	<0.01	
704.5226	704.5225	LPS O-32:2	[M+H]+	0.0001	0.14	
704.5423	704.5436	DGTA 30:1	[M+Na]+	0.0013	1.85	
704.5588	704.5589	LPC 31:1	[M+H]+	0.0001	0.14	
704.5588	704.5225	PC 30:1	[M+H]+	0.0363	51.52	PC 14:0;0 16:1;0
704.5615	704.5589	LPC 31:1	[M+H]+	0.0026	3.69	
705.4444	705.4466	LPG O-32:6	[M+Na]+	0.0021	2.98	
705.4890	705.4855	DG 40:7	[M+K]+	0.0035	4.96	
705.5545	705.5581	CE 21:6	[M+Na]+	0.0035	4.96	
705.5897	705.5905	SM 34:0;O2	[M+H]+	0.0008	1.13	SM 34:0;2
705.5914	705.5946	CE 19:0	[M+K]+	0.0032	4.54	
706.4026	706.4054	LPS 30:5	[M+Na]+	0.0029	4.11	
706.4184	706.4208	LPC 29:5	[M+K]+	0.0024	3.40	
706.4653	706.4654	PS 30:1	[M+H]+	0.0001	0.14	
706.5018	706.5019	DGTA 29:1	[M+K]+	0	<0.01	
706.5382	706.5381	LPS O-32:1	[M+H]+	0	<0.01	
706.5573	706.5592	DGTA 30:0	[M+Na]+	0.0019	2.69	
706.5746	706.5745	LPC 31:0	[M+H]+	0.0001	0.14	
707.4620	707.4622	LPG O-32:5	[M+Na]+	0.0002	0.28	
707.4982	707.4986	PA O-36:3	[M+Na]+	0.0005	0.71	
707.5970	707.5973	DG O-44:8	[M+H]+	0.0003	0.42	
708.4576	708.4575	LPS O-31:4	[M+Na]+	0.0001	0.14	
708.5505	708.5538	LPS O-32:0	[M+H]+	0.0032	4.52	
709.4778	709.4779	LPG O-32:4	[M+Na]+	0.0001	0.14	
709.5141	709.5143	PA O-36:2	[M+Na]+	0.0002	0.28	
710.4368	710.4367	LPS 30:3	[M+Na]+	0	<0.01	
710.4734	710.4731	LPS O-31:3	[M+Na]+	0.0003	0.42	
711.4016	711.4021	TG 40:11	[M+K]+	0.0005	0.70	
711.4370	711.4362	LPG O-31:4	[M+K]+	0.0008	1.12	
711.4932	711.4935	LPG O-32:3	[M+Na]+	0.0003	0.42	
711.5051	711.5042	MGDG 31:3	[M+H]+	0.0009	1.26	
712.4162	712.416	PS 29:2	[M+Na]+	0.0002	0.28	
712.4525	712.4524	LPS 30:2	[M+Na]+	0.0001	0.14	
712.4886	712.4888	LPS O-31:2	[M+Na]+	0.0001	0.14	
712.4926	712.4912	LPS O-33:5	[M+H]+	0.0014	1.96	
712.5080	712.4888	PE 32:1	[M+Na]+	0.0193	27.09	PE 16:0;0 16:1;0
712.5253	712.5252	LPC 30:1	[M+Na]+	0.0002	0.28	
713.4529	713.4518	LPG O-31:3	[M+K]+	0.0011	1.54	
713.4972	713.4963	LPI O-27:0	[M+H]+	0.0009	1.26	
713.4972	713.4994	SM 32:1;O2	[M+K]+	0.0022	3.08	SM 32:1;2
713.5194	713.5198	MGDG 31:2	[M+H]+	0.0004	0.56	
713.5209	713.5198	MGDG 31:2	[M+H]+	0.0011	1.54	
714.4112	714.4107	LPS 29:2	[M+K]+	0.0005	0.70	
714.4317	714.4317	PS 29:1	[M+Na]+	0.0001	0.14	
714.4682	714.468	LPS 30:1	[M+Na]+	0.0002	0.28	
714.5046	714.5044	LPS O-31:1	[M+Na]+	0.0002	0.28	
714.5397	714.5408	LPC 30:0	[M+Na]+	0.0011	1.54	
714.5410	714.5408	LPC 30:0	[M+Na]+	0.0002	0.28	
715.4353	715.4334	TG 40:9	[M+K]+	0.0018	2.52	
715.4721	715.4698	DG 41:9	[M+K]+	0.0023	3.21	
715.5082	715.5062	DG O-42:9	[M+K]+	0.0019	2.66	
716.4265	716.4263	LPS 29:1	[M+K]+	0.0002	0.28	
716.4474	716.4473	PS 29:0	[M+Na]+	0.0001	0.14	
716.5223	716.5225	LPS O-33:3	[M+H]+	0.0001	0.14	
716.5223	716.5225	PE 34:2	[M+H]+	0.0001	0.14	PE 16:0;0 18:2;0
716.5223	716.5225	PE 34:2	[M+H]+	0.0001	0.14	PE 16:1;0 18:1;0
716.5589	716.5589	LPC 32:2	[M+H]+	0	<0.01	
717.4482	717.449	PA 38:8	[M+H]+	0.0007	0.98	
717.4510	717.4491	TG 40:8	[M+K]+	0.0019	2.65	
717.5896	717.5905	SM 35:1;O2	[M+H]+	0.0009	1.25	SM 35:1;2
718.4643	718.4653	DGTA 32:8	[M+Na]+	0.001	1.39	
718.5382	718.5381	LPS O-33:2	[M+H]+	0.0001	0.14	
718.5745	718.5745	LPC 32:1	[M+H]+	0	<0.01	
718.5930	718.5745	PC O-32:1	[M+H]+	0.0185	25.74	PC O-16:1;0/16:0;0
719.4594	719.4622	LPG O-33:6	[M+Na]+	0.0028	3.89	
719.4610	719.4622	LPG O-33:6	[M+Na]+	0.0012	1.67	

720.4811	720.4811	DGCC 29:2	[M+K]+	0	<0.01	
720.5539	720.5538	LPS O-33:1	[M+H]+	0.0001	0.14	
720.5896	720.5902	LPC 32:0	[M+H]+	0.0005	0.69	
720.5905	720.5902	LPC 32:0	[M+H]+	0.0004	0.56	
721.4778	721.4779	LPG O-33:5	[M+Na]+	0	<0.01	
722.5564	722.5565	DGCC 32:3	[M+H]+	0.0001	0.14	
722.5564	722.5541	HexCer 34:1;O2	[M+Na]+	0.0023	3.18	HexCer 34:1;2
722.5564	722.5330	PC 30:0;O	[M+H]+	0.0234	32.39	PC 14:0;0 16:0;0
722.5564	722.5330	PC 30:0;O	[M+H]+	0.0234	32.39	PC 15:0;0 15:0;0
723.4778	723.4807	LPI O-28:2	[M+H]+	0.0029	4.01	
723.4936	723.4935	LPG O-33:4	[M+Na]+	0.0001	0.14	
724.4147	724.416	PS 30:3	[M+Na]+	0.0014	1.93	
724.4527	724.4524	LPS 31:3	[M+Na]+	0.0004	0.55	
724.5256	724.5252	LPC 31:2	[M+Na]+	0.0005	0.69	
724.5256	724.5252	PE O-34:2	[M+Na]+	0.0005	0.69	PE O-16:1;0/18:1;0
724.5256	724.5276	PE O-36:5	[M+H]+	0.0019	2.62	PE O-16:1;0/20:4;0
725.4552	725.4542	DG 42:11	[M+K]+	0.001	1.38	
725.4732	725.4728	LPG 32:3	[M+Na]+	0.0004	0.55	
725.4987	725.4963	LPI O-28:1	[M+H]+	0.0024	3.31	
725.5188	725.5198	MGDG 32:3	[M+H]+	0.001	1.38	
725.5219	725.5198	MGDG 32:3	[M+H]+	0.002	2.76	
726.4319	726.4317	PS 30:2	[M+Na]+	0.0003	0.41	
726.4681	726.468	LPS 31:2	[M+Na]+	0.0001	0.14	
726.5046	726.5044	LPS O-32:2	[M+Na]+	0.0001	0.14	
726.5244	726.5279	DGTA 32:4	[M+Na]+	0.0036	4.96	
726.5421	726.5432	LPC 33:4	[M+H]+	0.0011	1.51	
726.5421	726.5432	PE O-36:4	[M+H]+	0.0011	1.51	PE O-16:1;0/20:3;0
727.4715	727.4698	DG 42:10	[M+K]+	0.0017	2.34	
727.5080	727.5062	DG O-43:10	[M+K]+	0.0018	2.47	
727.5136	727.512	LPI O-28:0	[M+H]+	0.0017	2.34	
727.5367	727.5355	MGDG 32:2	[M+H]+	0.0012	1.65	
728.4476	728.4473	PS 30:1	[M+Na]+	0.0003	0.41	
728.4839	728.4837	LPS 31:1	[M+Na]+	0.0002	0.27	
728.5196	728.5201	LPS O-32:1	[M+Na]+	0.0004	0.55	
728.5205	728.5201	LPS O-32:1	[M+Na]+	0.0004	0.55	
728.5387	728.5355	LPC O-31:1	[M+K]+	0.0032	4.39	
728.5406	728.5436	DGTA 32:3	[M+Na]+	0.003	4.12	
728.5573	728.5565	LPC 31:0	[M+Na]+	0.0009	1.24	
728.5609	728.5589	LPC 33:3	[M+H]+	0.002	2.75	
729.4869	729.4855	DG 42:9	[M+K]+	0.0015	2.06	
729.5237	729.5219	DG O-43:9	[M+K]+	0.0018	2.47	
729.5788	729.5792	DG O-44:8	[M+Na]+	0.0004	0.55	
729.5803	729.5794	DG 41:2	[M+K]+	0.0009	1.23	
730.4635	730.463	PS 30:0	[M+Na]+	0.0005	0.68	
730.5250	730.5252	DGCC 33:6	[M+H]+	0.0002	0.27	
730.5382	730.5381	LPS O-34:3	[M+H]+	0.0001	0.14	
730.5761	730.5745	LPC 33:2	[M+H]+	0.0016	2.19	
731.4863	731.4858	BMP 33:3	[M+H]+	0.0006	0.82	
731.6061	731.6061	SM 36:1;O2	[M+H]+	0.0001	0.14	SM 36:1;2
732.4424	732.4446	DGCC 32:9	[M+Na]+	0.0022	3.00	
732.4785	732.481	PS 32:2	[M+H]+	0.0025	3.41	
732.5537	732.5538	LPS O-34:2	[M+H]+	0	<0.01	
732.5893	732.5902	LPC 33:1	[M+H]+	0.0009	1.23	
732.5905	732.5902	LPC 33:1	[M+H]+	0.0004	0.55	
733.4761	733.4779	LPG O-34:6	[M+Na]+	0.0018	2.45	
734.5333	734.5332	DGTA 31:1	[M+K]+	0.0001	0.14	
734.5695	734.5694	LPS O-34:1	[M+H]+	0.0001	0.14	
734.5702	734.5694	LPS O-34:1	[M+H]+	0.0008	1.09	
734.6053	734.6058	LPC 33:0	[M+H]+	0.0005	0.68	
735.4567	735.4571	LPG 33:5	[M+Na]+	0.0004	0.54	
735.4935	735.4935	LPG O-34:5	[M+Na]+	0	<0.01	
735.5353	735.5324	DG 42:6	[M+K]+	0.0029	3.94	
736.4140	736.416	PS 31:4	[M+Na]+	0.002	2.72	
736.4884	736.4888	LPS O-33:4	[M+Na]+	0.0003	0.41	
737.4521	737.4518	LPG O-33:5	[M+K]+	0.0003	0.41	
737.4521	737.4518	PA 36:3	[M+K]+	0.0003	0.41	PA 18:1;0 18:2;0
737.4727	737.4728	LPG 33:4	[M+Na]+	0.0001	0.14	
737.5086	737.5092	LPG O-34:4	[M+Na]+	0.0006	0.81	
737.5786	737.5568	SM 35:2;O2	[M+Na]+	0.0218	29.56	SM 35:2;2
738.4292	738.4317	PS 31:3	[M+Na]+	0.0024	3.25	
738.4306	738.4317	PS 31:3	[M+Na]+	0.001	1.35	
738.4681	738.468	LPS 32:3	[M+Na]+	0.0001	0.14	
738.5045	738.5044	LPS O-33:3	[M+Na]+	0.0001	0.14	
738.5395	738.5408	LPC 32:2	[M+Na]+	0.0013	1.76	
738.5412	738.5408	LPC 32:2	[M+Na]+	0.0004	0.54	
739.4329	739.4333	PA 40:11	[M+H]+	0.0004	0.54	
739.4329	739.4675	PA 36:2	[M+K]+	0.0345	46.66	PA 18:0;0 18:2;0
739.4329	739.4675	PA 36:2	[M+K]+	0.0345	46.66	PA 18:1;0 18:1;0
739.4676	739.4675	LPG O-33:4	[M+K]+	0.0002	0.27	
739.4882	739.4884	LPG 33:3	[M+Na]+	0.0002	0.27	
739.5079	739.5062	DG O-44:11	[M+K]+	0.0016	2.16	
739.5359	739.5355	MGDG 33:3	[M+H]+	0.0004	0.54	
740.4474	740.4473	PS 31:2	[M+Na]+	0.0001	0.14	

740.4843	740.4837	LPS 32:2	[M+Na]+	0.0006	0.81	
740.5196	740.5201	LPS O-33:2	[M+Na]+	0.0005	0.68	
740.5205	740.5201	LPS O-33:2	[M+Na]+	0.0004	0.54	
740.5386	740.5355	LPC O-32:2	[M+K]+	0.0031	4.19	
740.5386	740.5201	PE 34:1	[M+Na]+	0.0185	24.98	PE 16:0;0 18:1;0
740.5386	740.5201	PE 34:1	[M+Na]+	0.0185	24.98	PE 16:1;0 18:0;0
740.5565	740.5565	LPC 32:1	[M+Na]+	0	<0.01	
741.4946	741.4914	MGDG 30:0	[M+K]+	0.0032	4.32	
741.5288	741.5276	LPI O-29:0	[M+H]+	0.0012	1.62	
741.5310	741.5276	LPI O-29:0	[M+H]+	0.0034	4.59	
741.5490	741.5511	MGDG 33:2	[M+H]+	0.0021	2.83	
741.5490	741.5517	SM 34:1;O3	[M+Na]+	0.0027	3.64	SM 34:1;3
741.5490	741.5307	SM 34:1;O2	[M+K]+	0.0183	24.68	SM 34:1;2
742.4631	742.463	PS 31:1	[M+Na]+	0.0002	0.27	
742.4989	742.4993	LPS 32:1	[M+Na]+	0.0005	0.67	
742.4989	742.5017	PC 32:4;O	[M+H]+	0.0029	3.91	PC 15:4;0 17:0;0
742.5007	742.5017	LPS 34:4	[M+H]+	0.0011	1.48	
742.5191	742.5228	DGCC 32:4	[M+Na]+	0.0037	4.98	
742.5204	742.5228	DGCC 32:4	[M+Na]+	0.0024	3.23	
742.5355	742.5357	LPS O-33:1	[M+Na]+	0.0002	0.27	
742.5538	742.5511	LPC O-32:1	[M+K]+	0.0026	3.50	
742.5721	742.5721	LPC 32:0	[M+Na]+	0	<0.01	
743.4593	743.4622	PA 38:6	[M+Na]+	0.0029	3.90	
743.4621	743.4622	PA 38:6	[M+Na]+	0.0001	0.13	
743.5389	743.5375	DG O-44:9	[M+K]+	0.0014	1.88	
744.4786	744.4786	PS 31:0	[M+Na]+	0	<0.01	
744.4941	744.494	LPS O-32:1	[M+K]+	0.0001	0.13	
744.5341	744.5304	LPC 31:0	[M+K]+	0.0037	4.97	
744.5531	744.5538	LPT O-34:3	[M+H]+	0.0007	0.94	
744.5772	744.5773	DGTA 35:5	[M+H]+	0.0001	0.13	
744.5896	744.5902	LPC 34:2	[M+H]+	0.0006	0.81	
744.5906	744.5902	LPC 34:2	[M+H]+	0.0005	0.67	
745.4762	745.4779	PA 38:5	[M+Na]+	0.0017	2.28	
745.5072	745.5014	PG 34:3	[M+H]+	0.0058	7.78	PG 16:1;0 18:2;0
745.5072	745.5014	PG 34:3	[M+H]+	0.0058	7.78	PG 16:2;0 18:1;0
746.4578	746.4602	DGCC 33:9	[M+Na]+	0.0024	3.22	
746.4789	746.4755	PC 34:8	[M+H]+	0.0034	4.55	
746.5090	746.5095	LPC 33:5	[M+Na]+	0.0005	0.67	
746.5109	746.5119	PC O-35:8	[M+H]+	0.001	1.34	
746.5328	746.533	LPS 34:2	[M+H]+	0.0002	0.27	
746.5328	746.5330	PC 32:2;O	[M+H]+	0.0002	0.27	PC 14:0;0 18:2;0
746.5328	746.5330	PC 32:2;O	[M+H]+	0.0002	0.27	PC 16:0;0 16:2;0
746.5328	746.5330	PC 32:2;O	[M+H]+	0.0002	0.27	PC 16:1;0 16:1;0
746.5328	746.5097	PC O-30:0;O	[M+K]+	0.0232	31.08	PC O-14:0;0/16:0;0
746.5328	746.5694	PC 33:1	[M+H]+	0.0366	49.03	PC 15:0;0 18:1;0
746.5328	746.5694	PC 33:1	[M+H]+	0.0366	49.03	PC 16:0;0 17:1;0
746.5328	746.5694	PC 33:1	[M+H]+	0.0366	49.03	PC 16:1;0 17:0;0
746.5328	746.5694	PE 36:1	[M+H]+	0.0366	49.03	PE 18:0;0 18:1;0
746.5694	746.5694	LPT O-34:2	[M+H]+	0.0001	0.13	
746.5703	746.5694	LPT O-34:2	[M+H]+	0.0008	1.07	
746.6058	746.6058	LPC 34:1	[M+H]+	0	<0.01	
747.4253	747.4232	PG 35:9	[M+H]+	0.0021	2.81	
747.4931	747.4935	PA 38:4	[M+Na]+	0.0005	0.67	
748.5484	748.5487	LPS 34:1	[M+H]+	0.0003	0.40	
748.5618	748.5615	LPC O-34:4	[M+Na]+	0.0003	0.40	
748.5854	748.5851	LPT O-34:1	[M+H]+	0.0003	0.40	
749.5092	749.5092	PA 38:3	[M+Na]+	0	<0.01	
749.5103	749.5092	PA 38:3	[M+Na]+	0.0011	1.47	
750.5422	750.5432	PC O-35:6	[M+H]+	0.0011	1.47	
750.5772	750.5772	LPC O-34:3	[M+Na]+	0	<0.01	
*751.5149	751.512	LPI O-30:2	[M+H]+	0.0029	3.86	
751.5251	751.5248	PA 38:2	[M+Na]+	0.0003	0.40	
751.5742	751.5724	SM 36:2;O2	[M+Na]+	0.0018	2.39	SM 36:2;2
751.5742	751.5484	PG 34:0	[M+H]+	0.0259	34.46	PG 16:0;0 18:0;0
751.5810	751.579	CE 23:5	[M+K]+	0.002	2.66	
752.4085	752.4052	PE O-36:10	[M+K]+	0.0033	4.39	
752.4471	752.4473	PS 32:3	[M+Na]+	0.0002	0.27	
752.4841	752.4837	LPS 33:3	[M+Na]+	0.0004	0.53	
752.5194	752.5201	LPS O-34:3	[M+Na]+	0.0006	0.80	
752.5204	752.5201	LPS O-34:3	[M+Na]+	0.0004	0.53	
752.5573	752.5565	LPC 33:2	[M+Na]+	0.0008	1.06	
752.5573	752.5589	PE O-38:5	[M+H]+	0.0016	2.13	PE O-16:1;0/22:4;0
752.5573	752.5589	PE O-38:5	[M+H]+	0.0016	2.13	PE O-18:1;0/20:4;0
752.5573	752.5589	PE O-38:5	[M+H]+	0.0016	2.13	PE O-18:2;0/20:3;0
752.5930	752.5928	LPC O-34:2	[M+Na]+	0.0002	0.27	
753.5237	753.5219	DG O-45:11	[M+K]+	0.0018	2.39	
753.5518	753.5511	MGDG 34:3	[M+H]+	0.0007	0.93	
754.4992	754.4993	LPS 33:2	[M+Na]+	0.0001	0.13	
754.5007	754.5017	LPT 34:5	[M+H]+	0.0011	1.46	
754.5358	754.5357	LPS O-34:2	[M+Na]+	0.0001	0.13	
754.5534	754.5511	LPC O-33:2	[M+K]+	0.0023	3.05	
754.5534	754.5381	PC 34:4	[M+H]+	0.0153	20.28	PC 14:0;0 20:4;0
754.5534	754.5381	PE 37:4	[M+H]+	0.0153	20.28	PE 17:0;0 20:4;0

754.5534	754.5357	PC 32:1	[M+Na]+	0.0177	23.46	PC 14:0;0 18:1;0
754.5534	754.5357	PC 32:1	[M+Na]+	0.0177	23.46	PC 15:0;0 17:1;0
754.5534	754.5357	PC 32:1	[M+Na]+	0.0177	23.46	PC 16:0;0 16:1;0
754.5724	754.5721	LPC 33:1	[M+Na]+	0.0003	0.40	
755.5391	755.5375	DG O-45:10	[M+K]+	0.0016	2.12	
755.5403	755.5375	DG O-45:10	[M+K]+	0.0028	3.71	
755.5671	755.5668	MGDG 34:2	[M+H]+	0.0003	0.40	
756.4784	756.4786	PS 32:1	[M+Na]+	0.0002	0.26	
756.4784	756.4786	PS 32:1	[M+Na]+	0.0002	0.26	PS 16:0;0 16:1;0
756.4944	756.494	LPS O-33:2	[M+K]+	0.0004	0.53	
756.5153	756.515	LPS 33:1	[M+Na]+	0.0003	0.40	
756.5516	756.5514	LPS O-34:1	[M+Na]+	0.0002	0.26	
756.5879	756.5878	LPC 33:0	[M+Na]+	0.0002	0.26	
756.5879	756.5514	PC 32:0	[M+Na]+	0.0365	48.24	PC 14:0;0 18:0;0
756.5879	756.5514	PC 32:0	[M+Na]+	0.0365	48.24	PC 15:0;0 17:0;0
756.5879	756.5514	PC 32:0	[M+Na]+	0.0365	48.24	PC 16:0;0 16:0;0
757.5162	757.5167	PA O-42:9	[M+H]+	0.0005	0.66	
757.5551	757.5532	DG O-45:9	[M+K]+	0.002	2.64	
758.4943	758.4943	PS 32:0	[M+Na]+	0	<0.01	
758.5093	758.5095	LPC 34:6	[M+Na]+	0.0002	0.26	
758.5109	758.5119	PC O-36:9	[M+H]+	0.0011	1.45	
758.5109	758.5097	PC 31:0	[M+K]+	0.0012	1.58	PC 14:0;0 17:0;0
758.5109	758.5097	PC 31:0	[M+K]+	0.0012	1.58	PC 15:0;0 16:0;0
758.5109	758.5097	PE 34:0	[M+K]+	0.0012	1.58	PE 16:0;0 18:0;0
758.5109	758.5330	PE 36:3;O	[M+H]+	0.0222	29.27	PE 16:0;0 20:3;0
758.5109	758.5330	PE 36:3;O	[M+H]+	0.0222	29.27	PE 18:1;0 18:2;0
758.5109	758.5460	PC O-32:0	[M+K]+	0.0352	46.41	PC O-16:0;0/16:0;0
758.5320	758.533	LPT 34:3	[M+H]+	0.001	1.32	
758.5563	758.5565	DGCC 35:6	[M+H]+	0.0003	0.40	
758.5696	758.5694	PC 34:2	[M+H]+	0.0002	0.26	
758.5706	758.5694	PC 34:2	[M+H]+	0.0012	1.58	
759.5139	759.5147	BMP 33:0	[M+Na]+	0.0007	0.92	
759.5139	759.5171	PG 35:3	[M+H]+	0.0031	4.08	PG 17:1;0 18:2;0
759.5585	759.5558	TG 46:10	[M+H]+	0.0027	3.55	
759.6375	759.6374	SM 38:1;O2	[M+H]+	0.0000	<0.01	SM 38:1;2
760.4873	760.4888	LPT O-34:6	[M+Na]+	0.0015	1.97	
760.5481	760.5487	LPT 34:2	[M+H]+	0.0006	0.79	
760.5852	760.5851	PC 34:1	[M+H]+	0.0001	0.13	
762.5028	762.5044	LPT O-34:5	[M+Na]+	0.0017	2.23	
762.5028	762.5044	PE 36:4	[M+Na]+	0.0017	2.23	PE 16:0;0 20:4;0
762.5643	762.5643	LPT 34:1	[M+H]+	0	<0.01	
762.5893	762.5878	DGCC 35:4	[M+H]+	0.0015	1.97	
762.5914	762.5878	DGCC 35:4	[M+H]+	0.0036	4.72	
762.6016	762.6007	PC 34:0	[M+H]+	0.0009	1.18	
763.4671	763.4673	PA O-41:10	[M+Na]+	0.0002	0.26	
763.4881	763.4884	PG O-35:5	[M+Na]+	0.0004	0.52	
763.4881	763.4884	PA 38:4;O	[M+Na]+	0.0004	0.52	PA 18:0;0 20:4;0
763.4881	763.5120	PG 34:2;O	[M+H]+	0.0239	31.30	PG 16:0;0 18:2;0
763.4881	763.5120	PG 34:2;O	[M+H]+	0.0239	31.30	PG 16:1;0 18:1;0
763.5061	763.5062	DG O-46:13	[M+K]+	0.0001	0.13	
763.5676	763.5637	DG 44:6	[M+K]+	0.0038	4.98	
764.5193	764.5201	LPT O-34:4	[M+Na]+	0.0008	1.05	
764.5206	764.5201	LPT O-34:4	[M+Na]+	0.0005	0.65	
764.5572	764.5565	LPC 34:3	[M+Na]+	0.0007	0.92	
764.5932	764.5800	PC 33:0;O	[M+H]+	0.0132	17.26	PC 15:0;0 18:0;0
765.4831	765.4831	PA 38:3	[M+K]+	0	<0.01	
765.5036	765.5041	PG O-35:4	[M+Na]+	0.0004	0.52	
765.5233	765.5219	DG O-46:12	[M+K]+	0.0015	1.96	
765.5233	765.5276	PG 34:1;O	[M+H]+	0.0043	5.62	PG 16:0;0 18:1;0
765.5233	765.5276	PG 34:1;O	[M+H]+	0.0043	5.62	PG 16:1;0 18:0;0
766.4991	766.4993	LPS 34:3	[M+Na]+	0.0003	0.39	
766.5024	766.5019	DGTA 34:6	[M+K]+	0.0005	0.65	
766.5358	766.5357	LPT O-34:3	[M+Na]+	0.0001	0.13	
766.5726	766.5721	LPC 34:2	[M+Na]+	0.0005	0.65	
767.5391	767.5375	DG O-46:11	[M+K]+	0.0015	1.95	
767.5404	767.5433	LPI O-31:1	[M+H]+	0.0029	3.78	
768.4944	768.494	LPS O-34:3	[M+K]+	0.0004	0.52	
768.5151	768.515	LPS 34:2	[M+Na]+	0.0001	0.13	
768.5516	768.5514	LPT O-34:2	[M+Na]+	0.0002	0.26	
768.5880	768.5878	LPC 34:1	[M+Na]+	0.0003	0.39	
769.4767	769.4779	PA 40:7	[M+Na]+	0.0012	1.56	
769.5179	769.5168	DG 45:10	[M+K]+	0.0012	1.56	
769.5179	769.5014	PG 36:5	[M+H]+	0.0165	21.44	PG 16:1;0 20:4;0
769.5179	769.5014	PG 36:5	[M+H]+	0.0165	21.44	PG 16:2;0 20:3;0
769.5549	769.5532	DG O-46:10	[M+K]+	0.0017	2.21	
770.5094	770.5095	PC O-35:7	[M+Na]+	0.0001	0.13	
770.5105	770.5097	LPS O-34:2	[M+K]+	0.0008	1.04	
770.5293	770.5306	LPS 34:1	[M+Na]+	0.0013	1.69	
770.5310	770.5306	LPS 34:1	[M+Na]+	0.0003	0.39	
770.5565	770.5565	DGCC 36:7	[M+H]+	0.0001	0.13	
770.5675	770.567	LPT O-34:1	[M+Na]+	0.0005	0.65	
770.5704	770.5694	PC 35:3	[M+H]+	0.0009	1.17	
770.5940	770.5929	DGTA 37:6	[M+H]+	0.0011	1.43	

770.6054	770.6058	PC O-36:3	[M+H]+	0.0004	0.52	
770.6054	770.6058	PC O-36:3	[M+H]+	0.0004	0.52	PC O-16:0;0/20:3;0
770.6054	770.6058	PC O-36:3	[M+H]+	0.0004	0.52	PC O-18:1;0/18:2;0
771.4927	771.4935	PA 40:6	[M+Na]+	0.0008	1.04	
771.5131	771.5147	BMP 34:1	[M+Na]+	0.0015	1.94	
771.5341	771.5324	DG 45:9	[M+K]+	0.0017	2.20	
771.5341	771.5171	PG 36:4	[M+H]+	0.0170	22.03	PG 16:0;0 20:4;0
771.5341	771.5171	PG 36:4	[M+H]+	0.0170	22.03	PG 16:1;0 20:3;0
771.5341	771.5171	PG 36:4	[M+H]+	0.0170	22.03	PG 18:1;0 18:3;0
771.5341	771.5171	PG 36:4	[M+H]+	0.0170	22.03	PG 18:2;0 18:2;0
771.5694	771.5688	DG O-46:9	[M+K]+	0.0006	0.78	
771.5711	771.5688	DG O-46:9	[M+K]+	0.0023	2.98	
772.5254	772.5253	LPS O-34:1	[M+K]+	0	<0.01	
772.5468	772.5463	LPS 34:0	[M+Na]+	0.0005	0.65	
772.5852	772.5851	PC 35:2	[M+H]+	0.0001	0.13	
772.6216	772.6215	PC O-36:2	[M+H]+	0.0001	0.13	
773.5088	773.5092	PA 40:5	[M+Na]+	0.0004	0.52	
773.5109	773.5116	PA 42:8	[M+H]+	0.0006	0.78	
773.5286	773.5303	BMP 34:0	[M+Na]+	0.0017	2.20	
773.5304	773.5303	BMP 34:0	[M+Na]+	0.0001	0.13	
774.4542	774.4682	PS 32:0	[M+K]+	0.0140	18.08	PS 16:0;0 16:0;0
774.5257	774.528	PS 35:2	[M+H]+	0.0022	2.84	
774.5640	774.5643	PS O-36:2	[M+H]+	0.0003	0.39	
774.5996	774.6007	PC 35:1	[M+H]+	0.0011	1.42	
774.6010	774.6007	PC 35:1	[M+H]+	0.0003	0.39	
775.4575	775.4545	PG 37:9	[M+H]+	0.0031	4.00	
775.5256	775.525	LPG 34:0	[M+K]+	0.0007	0.90	
775.5676	775.5637	DG 45:7	[M+K]+	0.0038	4.90	
*776.4836	776.4837	LPT 34:5	[M+Na]+	0.0001	0.13	
776.5189	776.5201	PC 34:4	[M+Na]+	0.0011	1.42	
776.5210	776.5201	PC 34:4	[M+Na]+	0.0009	1.16	
776.5785	776.58	PS O-36:1	[M+H]+	0.0015	1.93	
777.5964	777.5946	CE 25:6	[M+K]+	0.0018	2.31	
778.5358	778.5357	PC 34:3	[M+Na]+	0.0001	0.13	
778.6104	778.5956	PC 34:0;O	[M+H]+	0.0147	18.88	PC 16:0;0 18:0;0
779.5391	779.5375	DG O-47:12	[M+K]+	0.0016	2.05	
*779.5405	779.5433	LPI O-32:2	[M+H]+	0.0028	3.59	
779.6120	779.6103	CE 25:5	[M+K]+	0.0017	2.18	
780.5149	780.515	LPT 34:3	[M+Na]+	0.0001	0.13	
780.5515	780.5514	PC 34:2	[M+Na]+	0.0001	0.13	
780.5884	780.5878	PC O-35:2	[M+Na]+	0.0007	0.90	
781.5548	781.5532	DG O-47:11	[M+K]+	0.0017	2.18	
782.4944	782.4943	PS 34:2	[M+Na]+	0.0001	0.13	
782.5093	782.5095	PC O-36:8	[M+Na]+	0.0002	0.26	
782.5107	782.5097	LPT O-34:3	[M+K]+	0.001	1.28	
782.5310	782.5306	LPT 34:2	[M+Na]+	0.0004	0.51	
782.5671	782.567	PC 34:1	[M+Na]+	0.0001	0.13	
783.5135	783.5147	PG 35:2	[M+Na]+	0.0012	1.53	
783.5135	783.5147	PG 35:2	[M+Na]+	0.0012	1.53	PG 17:1;0 18:1;0
783.5334	783.5324	DG 46:10	[M+K]+	0.001	1.28	
783.5698	783.5688	DG O-47:10	[M+K]+	0.0009	1.15	
783.5698	783.5777	SM 37:1;O2	[M+K]+	0.0079	10.08	SM 37:1;2
783.5705	783.5688	DG O-47:10	[M+K]+	0.0017	2.17	
783.6350	783.6374	SM 40:3;O2	[M+H]+	0.0025	3.19	SM 40:3;2
784.5093	784.5099	PS 34:1	[M+Na]+	0.0006	0.76	
784.5105	784.5099	PS 34:1	[M+Na]+	0.0006	0.76	
784.5105	784.5099	PS 34:1	[M+Na]+	0.0006	0.76	PS 16:0;0 18:1;0
784.5105	784.5099	PS 34:1	[M+Na]+	0.0006	0.76	PS 16:1;0 18:0;0
784.5258	784.5253	LPT O-34:2	[M+K]+	0.0005	0.64	
784.5462	784.5463	LPT 34:1	[M+Na]+	0.0001	0.13	
784.5695	784.5698	DGCC 35:4	[M+Na]+	0.0003	0.38	
784.5695	784.5617	PC O-34:1	[M+K]+	0.0078	9.94	PC O-18:1;0/16:0;0
784.5695	784.5851	PC O-36:4;O	[M+H]+	0.0156	19.88	PC O-16:0;0/20:4;0
784.5721	784.5722	DGCC 37:7	[M+H]+	0.0001	0.13	
784.5851	784.5851	PC 36:3	[M+H]+	0	<0.01	
785.5131	785.5117	TG 45:9	[M+K]+	0.0014	1.78	
785.5131	785.5303	PG 35:1	[M+Na]+	0.0172	21.90	PG 16:0;0 19:1;0
785.5131	785.5303	PG 35:1	[M+Na]+	0.0172	21.90	PG 17:0;0 18:1;0
785.5289	785.5303	PG 35:1	[M+Na]+	0.0014	1.78	
785.5490	785.5481	DG 46:9	[M+K]+	0.0009	1.15	
785.5490	785.5327	PG 37:4	[M+H]+	0.0163	20.75	PG 17:1;0 20:3;0
785.5490	785.5327	PG 37:4	[M+H]+	0.0163	20.75	PG 18:1;0 19:3;0
785.5508	785.5481	DG 46:9	[M+K]+	0.0028	3.56	
785.5880	785.5845	DG O-47:9	[M+K]+	0.0036	4.58	
785.6531	785.6531	SM 40:2;O2	[M+H]+	0.0000	<0.01	SM 40:2;2
786.4547	786.4834	PE O-38:7	[M+K]+	0.0288	36.62	PE O-16:1;0/22:6;0
786.5033	786.5044	PC 35:6	[M+Na]+	0.0011	1.40	
786.5254	786.5256	PS 34:0	[M+Na]+	0.0001	0.13	
786.5626	786.5619	LPT 34:0	[M+Na]+	0.0007	0.89	
786.5998	786.6007	PC 36:2	[M+H]+	0.0009	1.14	
786.6009	786.6007	PC 36:2	[M+H]+	0.0001	0.13	
787.5065	787.5038	PA O-41:6	[M+K]+	0.0027	3.43	
787.6704	787.6729	CE 25:1	[M+K]+	0.0025	3.17	

788.5183	788.5201	PC 35:5	[M+Na]+	0.0018	2.28	
788.5204	788.5202	LPS 34:0	[M+K]+	0.0001	0.13	
788.5414	788.5436	DGTA 37:8	[M+Na]+	0.0021	2.66	
788.5414	788.5436	PS 36:2	[M+H]+	0.0022	2.79	PS 16:0;0 20:2;0
788.5414	788.5436	PS 36:2	[M+H]+	0.0022	2.79	PS 18:0;0 18:2;0
788.5414	788.5436	PS 36:2	[M+H]+	0.0022	2.79	PS 18:1;0 18:1;0
788.5569	788.5566	LPT O-34:0	[M+K]+	0.0003	0.38	
788.5569	788.5565	PC O-36:5	[M+Na]+	0.0005	0.63	PC O-16:1;0/20:4;0
788.5569	788.5201	PE O-38:6;O	[M+Na]+	0.0368	46.67	PE O-16:1;0/22:5;0
788.5569	788.5201	PE O-38:6;O	[M+Na]+	0.0368	46.67	PE O-18:2;0/20:4;0
788.6068	788.6035	DGCC 37:5	[M+H]+	0.0033	4.18	
788.6166	788.6164	PC 36:1	[M+H]+	0.0002	0.25	
789.5217	789.5195	PA O-41:5	[M+K]+	0.0022	2.79	
789.6192	789.6158	DG O-47:7	[M+K]+	0.0034	4.31	
790.5344	790.5357	PC 35:4	[M+Na]+	0.0013	1.64	
790.5578	790.5593	PS 36:1	[M+H]+	0.0014	1.77	
790.5725	790.5721	PC O-36:4	[M+Na]+	0.0004	0.51	
791.5377	791.5375	DG O-48:13	[M+K]+	0.0002	0.25	
791.5757	791.5797	PG 37:1	[M+H]+	0.0039	4.93	
792.5516	792.5514	PC 35:3	[M+Na]+	0.0002	0.25	
792.5886	792.5878	PC O-36:3	[M+Na]+	0.0008	1.01	
792.5905	792.5902	PC O-38:6	[M+H]+	0.0003	0.38	
793.5549	793.5532	DG O-48:12	[M+K]+	0.0017	2.14	
793.5921	793.5953	PG 37:0	[M+H]+	0.0032	4.03	
794.5295	794.5306	PS O-36:3	[M+Na]+	0.0012	1.51	
794.5295	794.5306	PC 34:3;O	[M+Na]+	0.0012	1.51	PC 14:0;0 20:3;0
794.5295	794.5306	PC 34:3;O	[M+Na]+	0.0012	1.51	PC 16:0;0 18:3;0
794.5295	794.5306	PC 34:3;O	[M+Na]+	0.0012	1.51	PC 16:1;0 18:2;0
794.5295	794.5306	PC 34:3;O	[M+Na]+	0.0012	1.51	PC 16:2;0 18:1;0
794.5309	794.5306	PS O-36:3	[M+Na]+	0.0003	0.38	
794.5672	794.567	PC 35:2	[M+Na]+	0.0002	0.25	
794.6044	794.6034	PC O-36:2	[M+Na]+	0.001	1.26	
795.5340	795.5324	DG 47:11	[M+K]+	0.0016	2.01	
795.5340	795.5171	PG 38:6	[M+H]+	0.0170	21.37	PG 18:1;0 20:5;0
795.5340	795.5171	PG 38:6	[M+H]+	0.0170	21.37	PG 18:2;0 20:4;0
795.5340	795.5147	PG 36:3	[M+Na]+	0.0194	24.39	PG 16:0;0 20:3;0
795.5340	795.5147	PG 36:3	[M+Na]+	0.0194	24.39	PG 16:1;0 20:2;0
795.5340	795.5147	PG 36:3	[M+Na]+	0.0194	24.39	PG 18:1;0 18:2;0
795.5695	795.5688	DG O-48:11	[M+K]+	0.0007	0.88	
795.5695	795.5777	SM 38:2;O2	[M+K]+	0.0081	10.18	SM 38:2;2
795.5708	795.5688	DG O-48:11	[M+K]+	0.002	2.51	
795.6347	795.6350	SM 39:1;O2	[M+Na]+	0.0003	0.38	SM 39:1;2
796.5254	796.5253	PC 34:2	[M+K]+	0.0001	0.13	
796.5461	796.5463	PS O-36:2	[M+Na]+	0.0002	0.25	
796.5830	796.5827	PC 35:1	[M+Na]+	0.0003	0.38	
796.6191	796.6191	PC O-36:1	[M+Na]+	0	<0.01	
796.6191	796.6215	PC O-38:4	[M+H]+	0.0024	3.01	PC O-18:0;0/20:4;0
796.6191	796.6215	PC O-38:4	[M+H]+	0.0024	3.01	PC O-18:1;0/20:3;0
796.6210	796.6215	PC O-38:4	[M+H]+	0.0004	0.50	
797.5287	797.5303	PG 36:2	[M+Na]+	0.0016	2.01	
797.5305	797.5303	PG 36:2	[M+Na]+	0.0002	0.25	
797.5305	797.5303	PG 36:2	[M+Na]+	0.0002	0.25	PG 16:0;0 20:2;0
797.5305	797.5303	PG 36:2	[M+Na]+	0.0002	0.25	PG 16:1;0 20:1;0
797.5305	797.5303	PG 36:2	[M+Na]+	0.0002	0.25	PG 18:0;0 18:2;0
797.5305	797.5303	PG 36:2	[M+Na]+	0.0002	0.25	PG 18:1;0 18:1;0
797.5305	797.5327	PG 38:5	[M+H]+	0.0022	2.76	PG 18:1;0 20:4;0
797.5305	797.5327	PG 38:5	[M+H]+	0.0022	2.76	PG 18:2;0 20:3;0
797.5490	797.5481	DG 47:10	[M+K]+	0.001	1.25	
797.5506	797.5481	DG 47:10	[M+K]+	0.0026	3.26	
797.5863	797.5845	DG O-48:10	[M+K]+	0.0018	2.26	
*798.4658	798.468	PS O-37:8	[M+Na]+	0.0022	2.76	
798.5245	798.5256	PS 35:1	[M+Na]+	0.001	1.25	
798.5245	798.5280	PS 37:4	[M+H]+	0.0034	4.26	PS 17:0;0 20:4;0
798.5245	798.5410	PC 34:1	[M+K]+	0.0164	20.54	PC 16:0;0 18:1;0
798.5245	798.5410	PC 34:1	[M+K]+	0.0164	20.54	PC 16:1;0 18:0;0
798.5245	798.5046	PC 33:2;O	[M+K]+	0.0200	25.05	PC 15:0;0 18:2;0
798.5245	798.5046	PC 33:2;O	[M+K]+	0.0200	25.05	PC 16:1;0 17:1;0
798.5245	798.5046	PE 36:2;O	[M+K]+	0.0200	25.05	PE 18:0;0 18:2;0
798.5245	798.5046	PE 36:2;O	[M+K]+	0.0200	25.05	PE 18:1;0 18:1;0
798.5397	798.5408	PC O-37:7	[M+Na]+	0.0011	1.38	
798.5397	798.5410	PC O-34:2;O	[M+K]+	0.0012	1.50	PC O-16:0;0/18:2;0
798.5397	798.5643	PC 36:4;O	[M+H]+	0.0246	30.81	PC 16:0;0 20:4;0
798.5397	798.5643	PC 36:4;O	[M+H]+	0.0246	30.81	PC 16:1;0 20:3;0
798.5397	798.5643	PC 36:4;O	[M+H]+	0.0246	30.81	PC 18:1;0 18:3;0
798.5397	798.5643	PC 36:4;O	[M+H]+	0.0246	30.81	PC 18:2;0 18:2;0
798.5411	798.541	PC 34:1	[M+K]+	0.0001	0.13	
798.5594	798.5619	PS O-36:1	[M+Na]+	0.0025	3.13	
798.5617	798.5619	PS O-36:1	[M+Na]+	0.0002	0.25	
798.5982	798.5983	PC 35:0	[M+Na]+	0.0002	0.25	
798.6010	798.6007	PC 37:3	[M+H]+	0.0003	0.38	
798.6363	798.6371	PC O-38:3	[M+H]+	0.0008	1.00	
799.5269	799.5272	PA 44:9	[M+H]+	0.0004	0.50	
799.5445	799.546	PG 36:1	[M+Na]+	0.0015	1.88	

799.5650	799.5637	DG 47:9	[M+K]+	0.0013	1.63	
799.5650	799.5484	PG 38:4	[M+H]+	0.0166	20.76	PG 18:0;0 20:4;0
799.5650	799.5484	PG 38:4	[M+H]+	0.0166	20.76	PG 18:1;0 20:3;0
799.5650	799.5484	PG 38:4	[M+H]+	0.0166	20.76	PG 18:2;0 20:2;0
*800.4829	800.4837	PS O-37:7	[M+Na]+	0.0008	1.00	
800.5390	800.5412	PS 35:0	[M+Na]+	0.0022	2.75	
800.5442	800.5437	DGCC 35:4	[M+K]+	0.0004	0.50	
800.5563	800.5565	PC O-37:6	[M+Na]+	0.0002	0.25	
800.5788	800.58	PS O-38:3	[M+H]+	0.0011	1.37	
800.5806	800.5801	DGTA 36:3	[M+K]+	0.0005	0.62	
800.5806	800.5800	PC 36:3;O	[M+H]+	0.0006	0.75	PC 16:0;0 20:3;0
800.5806	800.5800	PC 36:3;O	[M+H]+	0.0006	0.75	PC 16:1;0 20:2;0
800.5806	800.5800	PC 36:3;O	[M+H]+	0.0006	0.75	PC 18:0;0 18:3;0
800.5806	800.5800	PC 36:3;O	[M+H]+	0.0006	0.75	PC 18:1;0 18:2;0
800.6164	800.6164	PC 37:2	[M+H]+	0	<0.01	
801.5429	801.5429	PA 44:8	[M+H]+	0	<0.01	
801.5829	801.5794	DG 47:8	[M+K]+	0.0035	4.37	
801.6192	801.6158	DG O-48:8	[M+K]+	0.0035	4.37	
801.6844	801.6844	SM 41:1;O2	[M+H]+	0.0000	<0.01	SM 41:1;2
*802.4991	802.4993	PS O-37:6	[M+Na]+	0.0002	0.25	
*802.5005	802.4995	PS 34:0	[M+K]+	0.001	1.25	
802.5189	802.5228	DGCC 37:9	[M+Na]+	0.004	4.98	
802.5208	802.5228	DGCC 37:9	[M+Na]+	0.002	2.49	
802.5359	802.5359	LPT 34:0	[M+K]+	0	<0.01	
802.5954	802.5956	PS O-38:2	[M+H]+	0.0003	0.37	
802.5954	802.5956	PC 36:2;O	[M+H]+	0.0003	0.37	PC 16:0;0 20:2;0
802.5954	802.5956	PC 36:2;O	[M+H]+	0.0003	0.37	PC 16:1;0 20:1;0
802.5954	802.5956	PC 36:2;O	[M+H]+	0.0003	0.37	PC 18:0;0 18:2;0
802.5954	802.5956	PC 36:2;O	[M+H]+	0.0003	0.37	PC 18:1;0 18:1;0
803.5028	803.5045	LPI 31:1	[M+Na]+	0.0017	2.12	
803.5389	803.5375	DG O-49:14	[M+K]+	0.0014	1.74	
803.5986	803.595	DG 47:7	[M+K]+	0.0036	4.48	
804.4922	804.4939	PE O-41:11	[M+Na]+	0.0016	1.99	
*804.5145	804.515	PS O-37:5	[M+Na]+	0.0005	0.62	
804.5145	804.5150	PE 38:5;O	[M+Na]+	0.0005	0.62	PE 16:0;0 22:5;0
804.5145	804.5150	PE 38:5;O	[M+Na]+	0.0005	0.62	PE 18:1;0 20:4;0
804.5496	804.5514	PC 36:4	[M+Na]+	0.0017	2.11	
804.5515	804.5514	PC 36:4	[M+Na]+	0.0001	0.12	
*805.5178	805.5168	DG 48:13	[M+K]+	0.001	1.24	
805.5549	805.5565	LPI O-32:0	[M+Na]+	0.0016	1.99	
*806.4920	806.4943	PS 36:4	[M+Na]+	0.0022	2.73	
806.5672	806.567	PC 36:3	[M+Na]+	0.0002	0.25	
807.4954	807.4959	PA 45:12	[M+H]+	0.0005	0.62	
807.5696	807.5688	DG O-49:12	[M+K]+	0.0008	0.99	
807.5708	807.5688	DG O-49:12	[M+K]+	0.0019	2.35	
808.5085	808.5099	PS 36:3	[M+Na]+	0.0014	1.73	
808.5672	808.5698	DGCC 37:6	[M+Na]+	0.0026	3.22	
808.5829	808.5827	PC 36:2	[M+Na]+	0.0003	0.37	
809.5862	809.5845	DG O-49:11	[M+K]+	0.0018	2.22	
809.5862	809.5933	SM 39:2;O2	[M+K]+	0.0071	8.77	SM 39:2;2
809.6497	809.6507	SM 40:1;O2	[M+Na]+	0.0010	1.24	SM 40:1;2
809.6507	809.6531	SM 42:4;O2	[M+H]+	0.0024	2.96	SM 42:4;2
810.5034	810.5044	PC 37:8	[M+Na]+	0.0011	1.36	
810.5253	810.5256	PS 36:2	[M+Na]+	0.0002	0.25	
810.5422	810.5432	PC O-40:11	[M+H]+	0.001	1.23	
810.5621	810.5619	PS O-37:2	[M+Na]+	0.0002	0.25	
810.5885	810.5878	DGCC 39:8	[M+H]+	0.0006	0.74	
810.5977	810.5983	PC 36:1	[M+Na]+	0.0006	0.74	
810.6011	810.6007	PC 38:4	[M+H]+	0.0003	0.37	
810.6011	810.6007	PC 38:4	[M+H]+	0.0003	0.37	PC 16:0;0 22:4;0
810.6011	810.6007	PC 38:4	[M+H]+	0.0003	0.37	PC 18:0;0 20:4;0
810.6011	810.6007	PC 38:4	[M+H]+	0.0003	0.37	PC 18:1;0 20:3;0
810.6011	810.6007	PC 38:4	[M+H]+	0.0003	0.37	PC 18:2;0 20:2;0
810.6540	810.6817	HexCer 42:2;O2	[M+H]+	0.0277	34.17	HexCer 42:2;2
811.5287	811.5273	TG 47:10	[M+K]+	0.0013	1.60	
811.5287	811.5460	PG 37:2	[M+Na]+	0.0173	21.32	PG 18:1;0 19:1;0
811.5307	811.5331	PI 32:0	[M+H]+	0.0024	2.96	
811.5970	811.5977	PA O-42:1	[M+K]+	0.0007	0.86	
811.6024	811.6001	DG O-49:10	[M+K]+	0.0023	2.83	
812.5186	812.5201	PC 37:7	[M+Na]+	0.0015	1.85	
812.5212	812.5202	PS O-36:2	[M+K]+	0.001	1.23	
812.5212	812.5202	PC 34:2;O	[M+K]+	0.0010	1.23	PC 16:0;0 18:2;0
812.5212	812.5202	PC 34:2;O	[M+K]+	0.0010	1.23	PC 16:1;0 18:1;0
812.5212	812.5202	PC 34:2;O	[M+K]+	0.0010	1.23	PC 17:1;0 17:1;0
812.5212	812.5566	PC 35:1	[M+K]+	0.0354	43.57	PC 16:0;0 19:1;0
812.5212	812.5566	PC 35:1	[M+K]+	0.0354	43.57	PC 17:0;0 18:1;0
812.5212	812.5566	PC 35:1	[M+K]+	0.0354	43.57	PC 17:1;0 18:0;0
812.5396	812.5412	PS 36:1	[M+Na]+	0.0016	1.97	
812.5412	812.5412	PS 36:1	[M+Na]+	0	<0.01	
812.6050	812.6035	DGCC 39:7	[M+H]+	0.0015	1.85	
812.6154	812.6164	PC 38:3	[M+H]+	0.0009	1.11	
813.5231	813.5252	LPI O-33:3	[M+Na]+	0.0021	2.58	
813.5445	813.543	TG 47:9	[M+K]+	0.0015	1.84	

813.6186	813.6158	DG O-49:9	[M+K]+	0.0028	3.44	
813.6845	813.6885	CE 27:2	[M+K]+	0.004	4.92	
814.4862	814.4995	PS 35:1	[M+K]+	0.0133	16.33	PS 17:0;0 18:1;0
814.4862	814.4995	PS 35:1	[M+K]+	0.0133	16.33	PS 17:1;0 18:0;0
814.4862	814.4631	PS 34:2;O	[M+K]+	0.0231	28.36	PS 16:0;0 18:2;0
814.4862	814.4631	PS 34:2;O	[M+K]+	0.0231	28.36	PS 16:1;0 18:1;0
814.5348	814.5357	PC 37:6	[M+Na]+	0.001	1.23	
814.5348	814.5357	PE 40:6	[M+Na]+	0.0010	1.23	PE 18:0;0 22:6;0
814.5348	814.5357	PE 40:6	[M+Na]+	0.0010	1.23	PE 18:1;0 22:5;0
814.5566	814.5569	PS 36:0	[M+Na]+	0.0003	0.37	
814.5730	814.5723	PC 35:0	[M+K]+	0.0008	0.98	
814.5935	814.5932	PS O-37:0	[M+Na]+	0.0003	0.37	
814.6322	814.632	PC 38:2	[M+H]+	0.0001	0.12	
814.6322	814.6320	PC 38:2	[M+H]+	0.0001	0.12	PC 16:0;0 22:2;0
814.6322	814.6320	PC 38:2	[M+H]+	0.0001	0.12	PC 18:0;0 20:2;0
814.6322	814.6320	PC 38:2	[M+H]+	0.0001	0.12	PC 18:1;0 20:1;0
815.5381	815.5409	LPI O-33:2	[M+Na]+	0.0028	3.43	
815.5592	815.5586	TG 47:8	[M+K]+	0.0005	0.61	
815.5609	815.5586	TG 47:8	[M+K]+	0.0023	2.82	
815.5609	815.5409	PG 36:1;O	[M+Na]+	0.0201	24.65	PG 16:0;0 20:1;0
815.5609	815.5409	PG 36:1;O	[M+Na]+	0.0201	24.65	PG 18:0;0 18:1;0
815.7007	815.7042	CE 27:1	[M+K]+	0.0034	4.17	
816.5491	816.5514	PC 37:5	[M+Na]+	0.0023	2.82	
816.5513	816.5514	PC 37:5	[M+Na]+	0	<0.01	
816.5513	816.5514	PC 37:5	[M+Na]+	0.0000	<0.01	PC 15:0;0 22:5;0
816.5513	816.5514	PC 37:5	[M+Na]+	0.0000	<0.01	PC 17:1;0 20:4;0
816.5513	816.5514	PE 40:5	[M+Na]+	0.0000	<0.01	PE 18:0;0 22:5;0
816.5513	816.5514	PE 40:5	[M+Na]+	0.0000	<0.01	PE 18:1;0 22:4;0
816.5513	816.5514	PE O-40:6;O	[M+Na]+	0.0000	<0.01	PE O-18:1;0/22:5;0
816.5513	816.5361	PS 35:0;O	[M+Na]+	0.0152	18.61	PS 17:0;0 18:0;0
816.5726	816.5749	PS 38:2	[M+H]+	0.0023	2.82	
816.5881	816.5878	PC O-38:5	[M+Na]+	0.0003	0.37	
816.6084	816.6113	PS O-39:2	[M+H]+	0.0029	3.55	
816.6084	816.6113	PC 37:2;O	[M+H]+	0.0029	3.55	PC 17:0;0 20:2;0
816.6084	816.6113	PC 37:2;O	[M+H]+	0.0029	3.55	PC 18:0;0 19:2;0
816.6084	816.6113	PC 37:2;O	[M+H]+	0.0029	3.55	PC 18:1;0 19:1;0
816.6084	816.5878	PC O-38:5	[M+Na]+	0.0207	25.35	PC O-16:0;0/22:5;0
816.6084	816.5878	PC O-38:5	[M+Na]+	0.0207	25.35	PC O-18:1;0/20:4;0
817.5914	817.5953	PG 39:2	[M+H]+	0.0039	4.77	
817.7069	817.7068	DG O-52:9	[M+H]+	0.0001	0.12	
*818.4939	818.4943	PS 37:5	[M+Na]+	0.0004	0.49	
818.4939	818.4944	PS 34:0;O	[M+K]+	0.0005	0.61	PS 16:0;0 18:0;0
818.4939	818.5097	PC 36:5	[M+K]+	0.0158	19.30	PC 16:0;0 20:5;0
818.4939	818.5097	PC 36:5	[M+K]+	0.0158	19.30	PC 16:1;0 20:4;0
818.4939	818.5097	PE 39:5	[M+K]+	0.0158	19.30	PE 17:0;0 22:5;0
818.4939	818.4733	PE 38:6;O	[M+K]+	0.0206	25.17	PE 16:1;0 22:5;0
818.5670	818.567	PC 37:4	[M+Na]+	0.0001	0.12	
818.5670	818.5670	PC 37:4	[M+Na]+	0.0001	0.12	PC 17:0;0 20:4;0
818.5670	818.5670	PE 40:4	[M+Na]+	0.0001	0.12	PE 18:0;0 22:4;0
818.5670	818.5670	PE O-40:5;O	[M+Na]+	0.0001	0.12	PE O-18:0;0/22:5;0
818.5670	818.5542	PS 37:2;O	[M+H]+	0.0128	15.64	PS 17:0;0 20:2;0
818.5670	818.5542	PS 37:2;O	[M+H]+	0.0128	15.64	PS 18:1;0 19:1;0
818.6039	818.6034	PC O-38:4	[M+Na]+	0.0005	0.61	
*820.4349	820.4314	PE 40:11	[M+K]+	0.0035	4.27	
*820.4912	820.4889	PS O-37:5	[M+K]+	0.0023	2.80	
820.5083	820.5099	PS 37:4	[M+Na]+	0.0016	1.95	
820.5461	820.5463	PS O-38:4	[M+Na]+	0.0002	0.24	
820.5828	820.5827	PC 37:3	[M+Na]+	0.0001	0.12	
820.5828	820.5827	PC 37:3	[M+Na]+	0.0001	0.12	PC 16:0;0 21:3;0
820.5828	820.5827	PC 37:3	[M+Na]+	0.0001	0.12	PC 17:0;0 20:3;0
820.5828	820.5827	PC 37:3	[M+Na]+	0.0001	0.12	PC 18:1;0 19:2;0
820.5828	820.5827	PC 37:3	[M+Na]+	0.0001	0.12	PC 18:2;0 19:1;0
820.5828	820.5827	PE 40:3	[M+Na]+	0.0001	0.12	PE 18:0;0 22:3;0
820.6192	820.6191	PC O-38:3	[M+Na]+	0.0001	0.12	
820.6209	820.6215	PC O-40:6	[M+H]+	0.0006	0.73	
820.6209	820.6215	PC O-40:6	[M+H]+	0.0006	0.73	PC O-18:1;0/22:5;0
821.6235	821.6266	PG 39:0	[M+H]+	0.0031	3.77	
821.6508	821.6507	SM 41:2;O2	[M+Na]+	0.0001	0.12	SM 41:2;2
822.4526	822.4682	PS 36:4	[M+K]+	0.0156	18.97	PS 16:0;0 20:4;0
822.5069	822.5068	PE 43:12	[M+H]+	0.0001	0.12	
822.5069	822.5046	PC 35:4;O	[M+K]+	0.0023	2.80	PC 15:0;0 20:4;0
822.5069	822.5046	PE 38:4;O	[M+K]+	0.0023	2.80	PE 16:0;0 22:4;0
822.5069	822.5046	PE 38:4;O	[M+K]+	0.0023	2.80	PE 18:0;0 20:4;0
822.5069	822.5046	PE 38:4;O	[M+K]+	0.0023	2.80	PE 18:1;0 20:3;0
822.5415	822.541	PC 36:3	[M+K]+	0.0006	0.73	
822.5596	822.5619	PS O-38:3	[M+Na]+	0.0024	2.92	
822.5619	822.5619	PS O-38:3	[M+Na]+	0.0001	0.12	
822.5985	822.5983	PC 37:2	[M+Na]+	0.0001	0.12	
822.6357	822.6347	PC O-38:2	[M+Na]+	0.001	1.22	
822.6357	822.6220	HexCer 40:1;O2	[M+K]+	0.0137	16.65	HexCer 40:1;2
823.5445	823.546	PG 38:3	[M+Na]+	0.0015	1.82	
823.5445	823.5460	PG 38:3	[M+Na]+	0.0015	1.82	PG 18:0;0 20:3;0
823.5445	823.5460	PG 38:3	[M+Na]+	0.0015	1.82	PG 18:1;0 20:2;0

823.5445	823.5460	PG 38:3	[M+Na]+	0.0015	1.82	PG 18:2;0 20:1;0
823.5653	823.5637	DG 49:11	[M+K]+	0.0015	1.82	
823.6026	823.6001	DG O-50:11	[M+K]+	0.0025	3.04	
824.5052	824.5048	PS 36:3;O	[M+Na]+	0.0004	0.49	PS 16:0;0 20:3;0
824.5052	824.5048	PS 36:3;O	[M+Na]+	0.0004	0.49	PS 18:1;0 18:2;0
824.5052	824.5202	PC 35:3;O	[M+K]+	0.0150	18.19	PC 15:0;0 20:3;0
824.5052	824.5202	PC 35:3;O	[M+K]+	0.0150	18.19	PC 17:1;0 18:2;0
824.5052	824.5202	PE 38:3;O	[M+K]+	0.0150	18.19	PE 18:0;0 20:3;0
824.5052	824.5202	PE 38:3;O	[M+K]+	0.0150	18.19	PE 18:1;0 20:2;0
824.5567	824.5566	PC 36:2	[M+K]+	0	<0.01	
824.5772	824.5776	PS O-38:2	[M+Na]+	0.0003	0.36	
824.6518	824.6528	PC O-40:4	[M+H]+	0.0009	1.09	
825.5594	825.5616	PG 38:2	[M+Na]+	0.0022	2.66	
825.5594	825.5252	PG 37:3;O	[M+Na]+	0.0342	41.43	PG 17:1;0 20:2;0
825.5594	825.5252	PG 37:3;O	[M+Na]+	0.0342	41.43	PG 18:1;0 19:2;0
825.5594	825.5252	PG 37:3;O	[M+Na]+	0.0342	41.43	PG 18:2;0 19:1;0
825.5594	825.5124	PI 32:1;O	[M+H]+	0.0471	57.05	PI 14:0;0 18:1;0
825.5594	825.5124	PI 32:1;O	[M+H]+	0.0471	57.05	PI 16:0;0 16:1;0
825.5607	825.5616	PG 38:2	[M+Na]+	0.0009	1.09	
*825.5792	825.5793	PA O-47:10	[M+H]+	0.0001	0.12	
825.5792	825.5616	PG 38:2	[M+Na]+	0.0176	21.32	PG 18:0;0 20:2;0
825.5792	825.5616	PG 38:2	[M+Na]+	0.0176	21.32	PG 18:1;0 20:1;0
825.5810	825.5794	DG 49:10	[M+K]+	0.0017	2.06	
825.6820	825.6844	SM 43:3;O2	[M+H]+	0.0024	2.91	SM 43:3;2
*826.5568	826.5569	PS 37:1	[M+Na]+	0.0001	0.12	
826.5568	826.5569	PS 37:1	[M+Na]+	0.0001	0.12	PS 18:0;0 19:1;0
826.5568	826.5569	PS 37:1	[M+Na]+	0.0001	0.12	PS 18:1;0 19:0;0
826.5568	826.5593	PS 39:4	[M+H]+	0.0025	3.02	PS 17:0;0 22:4;0
826.5568	826.5723	PC 36:1	[M+K]+	0.0155	18.75	PC 16:0;0 20:1;0
826.5568	826.5723	PC 36:1	[M+K]+	0.0155	18.75	PC 18:0;0 18:1;0
826.5568	826.5723	PC O-36:2;O	[M+K]+	0.0155	18.75	PC O-18:1;0/18:1;0
826.5568	826.5359	PC 35:2;O	[M+K]+	0.0209	25.29	PC 15:0;0 20:2;0
826.5568	826.5359	PC 35:2;O	[M+K]+	0.0209	25.29	PC 16:0;0 19:2;0
826.5568	826.5359	PC 35:2;O	[M+K]+	0.0209	25.29	PC 16:1;0 19:1;0
826.5568	826.5359	PC 35:2;O	[M+K]+	0.0209	25.29	PC 17:0;0 18:2;0
826.5568	826.5359	PC 35:2;O	[M+K]+	0.0209	25.29	PC 17:1;0 18:1;0
826.5568	826.5359	PE 38:2;O	[M+K]+	0.0209	25.29	PE 18:0;0 20:2;0
826.5568	826.5359	PE 38:2;O	[M+K]+	0.0209	25.29	PE 18:1;0 20:1;0
826.5568	826.5229	PS 38:5;O	[M+H]+	0.0339	41.01	PS 16:0;0 22:5;0
826.5568	826.5229	PS 38:5;O	[M+H]+	0.0339	41.01	PS 18:1;0 20:4;0
826.5936	826.5932	PS O-38:1	[M+Na]+	0.0003	0.36	
828.5152	828.5151	PS 36:1	[M+K]+	0	<0.01	
828.5152	828.5151	PS 36:1	[M+K]+	0.0000	<0.01	PS 18:0;0 18:1;0
828.5152	828.4788	PS 35:2;O	[M+K]+	0.0364	43.93	PS 17:0;0 18:2;0
*828.5356	828.5385	DGCC 39:10	[M+Na]+	0.0029	3.50	
828.5519	828.5515	PS O-37:1	[M+K]+	0.0004	0.48	
828.5519	828.5514	PC 38:6	[M+Na]+	0.0005	0.60	PC 16:0;0 22:6;0
828.5519	828.5514	PC 38:6	[M+Na]+	0.0005	0.60	PC 16:1;0 22:5;0
828.5519	828.5514	PC 38:6	[M+Na]+	0.0005	0.60	PC 18:2;0 20:4;0
*829.4618	829.4628	LPI 32:3	[M+K]+	0.0009	1.09	
829.5550	829.5565	LPI O-34:2	[M+Na]+	0.0015	1.81	
830.5496	830.546	PC O-38:6	[M+K]+	0.0035	4.21	
830.5496	830.5460	PC O-38:6	[M+K]+	0.0035	4.21	PC O-16:0;0/22:6;0
830.5496	830.5542	PS 38:3;O	[M+H]+	0.0046	5.54	PS 18:0;0 20:3;0
830.5496	830.5542	PS 38:3;O	[M+H]+	0.0046	5.54	PS 18:1;0 20:2;0
830.5496	830.5670	PC 38:5	[M+Na]+	0.0175	21.07	PC 16:0;0 22:5;0
830.5496	830.5670	PC 38:5	[M+Na]+	0.0175	21.07	PC 16:1;0 22:4;0
830.5496	830.5670	PC 38:5	[M+Na]+	0.0175	21.07	PC 18:1;0 20:4;0
830.5496	830.5670	PC 38:5	[M+Na]+	0.0175	21.07	PC 18:2;0 20:3;0
830.5496	830.5694	PC 40:8	[M+H]+	0.0199	23.96	PC 20:4;0 20:4;0
830.5514	830.5541	DGCC 39:9	[M+Na]+	0.0027	3.25	
830.5677	830.5672	PS O-37:0	[M+K]+	0.0005	0.60	
*831.4780	831.4784	LPI 32:2	[M+K]+	0.0004	0.48	
831.5548	831.5534	PG O-42:9	[M+H]+	0.0013	1.56	
831.5696	831.5688	DG O-51:14	[M+K]+	0.0008	0.96	
831.5710	831.5722	LPI O-34:1	[M+Na]+	0.0011	1.32	
832.5075	832.5099	PS 38:5	[M+Na]+	0.0024	2.88	
832.5830	832.5827	PC 38:4	[M+Na]+	0.0003	0.36	
832.5830	832.5851	PC 40:7	[M+H]+	0.0021	2.52	PC 18:1;0 22:6;0
832.5830	832.5851	PC 40:7	[M+H]+	0.0021	2.52	PC 18:2;0 22:5;0
832.5830	832.5851	PC 40:7	[M+H]+	0.0021	2.52	PC 20:3;0 20:4;0
*833.4936	833.4941	LPI 32:1	[M+K]+	0.0005	0.60	
833.5114	833.5117	TG 49:13	[M+K]+	0.0003	0.36	
833.5862	833.5878	LPI O-34:0	[M+Na]+	0.0016	1.92	
833.6508	833.6507	SM 42:3;O2	[M+Na]+	0.0001	0.12	SM 42:3;2
834.5232	834.5256	PS 38:4	[M+Na]+	0.0023	2.76	
834.5841	834.5854	DGCC 39:7	[M+Na]+	0.0013	1.56	
834.5987	834.5983	PC 38:3	[M+Na]+	0.0004	0.48	
834.6006	834.6007	PC 40:6	[M+H]+	0.0002	0.24	
834.6006	834.5983	PC 38:3	[M+Na]+	0.0022	2.64	PC 16:0;0 22:3;0
834.6006	834.5983	PC 38:3	[M+Na]+	0.0022	2.64	PC 18:0;0 20:3;0
834.6006	834.5983	PC 38:3	[M+Na]+	0.0022	2.64	PC 18:1;0 20:2;0
834.6006	834.5983	PC 38:3	[M+Na]+	0.0022	2.64	PC 18:2;0 20:1;0

834.6540	834.6793	HexCer 42:1;O2	[M+Na]+	0.0253	30.31	HexCer 42:1;2
835.5265	835.5272	PA 47:12	[M+H]+	0.0007	0.84	
835.5265	835.5331	PI 34:2	[M+H]+	0.0066	7.90	PI 16:0;0 18:2;0
835.6024	835.6001	DG O-51:12	[M+K]+	0.0023	2.75	
835.6024	835.6090	SM 41:3;O2	[M+K]+	0.0066	7.90	SM 41:3;2
835.6662	835.6663	SM 42:2;O2	[M+Na]+	0.0001	0.12	SM 42:2;2
*836.5418	836.5412	PS 38:3	[M+Na]+	0.0006	0.72	
836.5418	836.5436	PS 40:6	[M+H]+	0.0018	2.15	PS 18:0;0 22:6;0
836.5418	836.5436	PS 40:6	[M+H]+	0.0018	2.15	PS 18:1;0 22:5;0
836.6145	836.614	PC 38:2	[M+Na]+	0.0005	0.60	
837.6180	837.6158	DG O-51:11	[M+K]+	0.0022	2.63	
838.5569	838.5569	PS 38:2	[M+Na]+	0.0001	0.12	
838.5569	838.5569	PS 38:2	[M+Na]+	0.0001	0.12	PS 18:0;0 20:2;0
838.5569	838.5569	PS 38:2	[M+Na]+	0.0001	0.12	PS 18:1;0 20:1;0
838.6289	838.6296	PC 38:1	[M+Na]+	0.0007	0.83	
838.6289	838.6296	PC 38:1	[M+Na]+	0.0007	0.83	PC 16:0;0 22:1;0
838.6289	838.6296	PC 38:1	[M+Na]+	0.0007	0.83	PC 18:0;0 20:1;0
838.6289	838.6320	PC 40:4	[M+H]+	0.0031	3.70	PC 18:0;0 22:4;0
838.6289	838.6320	PC 40:4	[M+H]+	0.0031	3.70	PC 18:1;0 22:3;0
838.6289	838.6320	PC 40:4	[M+H]+	0.0031	3.70	PC 20:1;0 20:3;0
838.6312	838.632	PC 40:4	[M+H]+	0.0008	0.95	
*839.5581	839.5585	PA 47:10	[M+H]+	0.0005	0.60	
839.5612	839.5586	TG 49:10	[M+K]+	0.0025	2.98	
839.5896	839.5925	PA O-46:7	[M+Na]+	0.0029	3.45	
839.5911	839.5925	PA O-46:7	[M+Na]+	0.0015	1.79	
839.6346	839.6314	DG O-51:10	[M+K]+	0.0032	3.81	
839.6884	839.6888	PA O-47:3	[M+H]+	0.0004	0.48	
839.6960	839.7000	SM 44:3;O2	[M+H]+	0.0040	4.76	SM 44:3;2
*840.5732	840.5725	PS 38:1	[M+Na]+	0.0007	0.83	
840.5941	840.5902	PC O-42:10	[M+H]+	0.0039	4.64	
841.5761	841.5743	TG 49:9	[M+K]+	0.0018	2.14	
*841.6066	841.6082	PA O-46:6	[M+Na]+	0.0016	1.90	
*842.5537	842.5541	DGCC 40:10	[M+Na]+	0.0004	0.47	
*842.5884	842.5882	PS 38:0	[M+Na]+	0.0002	0.24	
842.6079	842.6058	PC O-42:9	[M+H]+	0.0021	2.49	
842.6256	842.6245	PS O-39:0	[M+Na]+	0.0011	1.31	
843.5575	843.5534	PG O-43:10	[M+H]+	0.0041	4.86	
845.6743	845.6784	DG O-51:7	[M+K]+	0.0041	4.85	
846.4486	846.4471	PE 42:12	[M+K]+	0.0015	1.77	
846.5253	846.5256	PS 39:5	[M+Na]+	0.0003	0.35	
846.5253	846.5256	PS 39:5	[M+Na]+	0.0003	0.35	PS 17:0;0 22:5;0
846.6777	846.6793	DGCC 39:1	[M+Na]+	0.0017	2.01	
*847.4187	847.4158	PI O-34:8	[M+K]+	0.0029	3.42	
848.5227	848.5202	PS O-39:5	[M+K]+	0.0025	2.95	
849.4330	849.4315	LPI 34:7	[M+K]+	0.0016	1.88	
849.6820	849.6820	SM 43:2;O2	[M+Na]+	0.0000	<0.01	SM 43:2;2
850.4970	850.4993	PS O-41:10	[M+Na]+	0.0023	2.70	
850.4970	850.4995	PS 38:4	[M+K]+	0.0025	2.94	PS 18:0;0 20:4;0
850.4970	850.4995	PS 38:4	[M+K]+	0.0025	2.94	PS 18:1;0 20:3;0
*850.5188	850.5147	PC O-40:10	[M+K]+	0.004	4.70	
851.6616	851.6607	MGDG 41:3	[M+H]+	0.0009	1.06	
851.6616	851.6976	SM 43:1;O2	[M+Na]+	0.0361	42.39	SM 43:1;2
852.6438	852.6453	PC 39:1	[M+Na]+	0.0015	1.76	
*853.4625	853.4628	LPI 34:5	[M+K]+	0.0003	0.35	
853.6558	853.6559	SM 42:1;O2	[M+K]+	0.0001	0.12	SM 42:1;2
853.6768	853.6763	MGDG 41:2	[M+H]+	0.0005	0.59	
853.6768	853.6769	SM 42:1;O3	[M+Na]+	0.0001	0.12	SM 42:1;3
853.7255	853.7256	TG 50:2	[M+Na]+	0	<0.01	
853.7255	853.7256	TG 50:2	[M+Na]+	0.0000	<0.01	TAG 50:2;0
*854.5528	854.5541	DGCC 41:11	[M+Na]+	0.0013	1.52	
*854.5891	854.5882	PS 39:1	[M+Na]+	0.0009	1.05	
*854.5909	854.5907	DGCC 39:5	[M+K]+	0.0003	0.35	
854.6589	854.6609	PC 39:0	[M+Na]+	0.002	2.34	
855.4760	855.4784	LPI 34:4	[M+K]+	0.0025	2.92	
855.5562	855.5534	PG O-44:11	[M+H]+	0.0028	3.27	
855.5860	855.5874	PA 46:6	[M+Na]+	0.0014	1.64	
*856.5683	856.5698	DGCC 41:10	[M+Na]+	0.0015	1.75	
856.5706	856.5698	DGCC 41:10	[M+Na]+	0.0008	0.93	
856.5844	856.5851	PC 42:9	[M+H]+	0.0007	0.82	
856.5844	856.5827	PC 40:6	[M+Na]+	0.0017	1.98	PC 18:0;0 22:6;0
856.5844	856.5827	PC 40:6	[M+Na]+	0.0017	1.98	PC 18:1;0 22:5;0
856.5844	856.5827	PC 40:6	[M+Na]+	0.0017	1.98	PC 18:2;0 22:4;0
856.5844	856.5827	PC 40:6	[M+Na]+	0.0017	1.98	PC 20:2;0 20:4;0
856.5844	856.5827	PC 40:6	[M+Na]+	0.0017	1.98	PC 20:3;0 20:3;0
856.5844	856.5827	PC O-40:7;O	[M+Na]+	0.0017	1.98	PC O-18:1;0/22:6;0
856.5844	856.5674	PS 38:1;O	[M+Na]+	0.0170	19.85	PS 18:0;0 20:1;0
856.5844	856.5674	PS 38:1;O	[M+Na]+	0.0170	19.85	PS 18:1;0 20:0;0
856.6059	856.6062	DGTA 42:9	[M+Na]+	0.0002	0.23	
*857.4937	857.4941	LPI 34:3	[M+K]+	0.0003	0.35	
857.5133	857.515	PI 34:2	[M+Na]+	0.0018	2.10	
857.5721	857.5691	PG O-44:10	[M+H]+	0.0031	3.61	
857.6080	857.6056	TG 50:8	[M+K]+	0.0024	2.80	
858.5983	858.5983	PC 40:5	[M+Na]+	0	<0.01	

*859.5089	859.5097	LPI 34:2	[M+K]+	0.0008	0.93	
*859.5108	859.5097	LPI 34:2	[M+K]+	0.0011	1.28	
859.5108	859.5307	PI 34:1	[M+Na]+	0.0199	23.15	PI 16:0;0 18:1;0
859.5108	859.5307	PI 34:1	[M+Na]+	0.0199	23.15	PI 16:1;0 18:0;0
859.5108	859.5331	PI 36:4	[M+H]+	0.0223	25.94	PI 16:0;0 20:4;0
859.5108	859.5331	PI 36:4	[M+H]+	0.0223	25.94	PI 18:2;0 18:2;0
860.6140	860.614	PC 40:4	[M+Na]+	0.0001	0.12	
860.6140	860.6011	PS 40:2;O	[M+H]+	0.0129	14.99	PS 18:1;0 22:1;0
861.5262	861.5254	LPI 34:1	[M+K]+	0.0009	1.04	
861.5262	861.5488	PI 36:3	[M+H]+	0.0225	26.12	PI 16:0;0 20:3;0
861.5727	861.5756	SQDG 37:2	[M+H]+	0.0029	3.37	
861.6685	861.6708	PA O-47:3	[M+Na]+	0.0022	2.55	
*862.5565	862.5569	PS 40:4	[M+Na]+	0.0004	0.46	
862.5762	862.5723	PC 39:4	[M+K]+	0.0039	4.52	
863.5876	863.5913	SQDG 37:1	[M+H]+	0.0037	4.28	
*864.5728	864.5725	PS 40:3	[M+Na]+	0.0002	0.23	
*866.5538	866.5541	DGCC 42:12	[M+Na]+	0.0004	0.46	
866.5538	866.5518	PS 39:3;O	[M+Na]+	0.0020	2.31	PS 18:0;0 21:3;0
867.5575	867.5534	PG O-45:12	[M+H]+	0.0041	4.73	
867.6230	867.6238	PA O-48:7	[M+Na]+	0.0008	0.92	
*868.5693	868.5698	DGCC 42:11	[M+Na]+	0.0005	0.58	
*868.5705	868.5698	DGCC 42:11	[M+Na]+	0.0007	0.81	
869.5733	869.5691	PG O-45:11	[M+H]+	0.0042	4.83	
*870.5855	870.5854	DGCC 42:10	[M+Na]+	0.0001	0.11	
871.5887	871.5847	PG O-45:10	[M+H]+	0.004	4.59	
871.6908	871.694	DG O-53:8	[M+K]+	0.0032	3.67	
871.6908	871.7151	TG 50:1	[M+K]+	0.0244	27.99	TAG 50:1;0
872.5923	872.593	PC O-41:6	[M+K]+	0.0007	0.80	
873.5336	873.5488	PI 37:4	[M+H]+	0.0152	17.40	PI 17:0;0 20:4;0
*875.4487	875.4471	PI O-36:8	[M+K]+	0.0015	1.71	
*875.5051	875.5046	PI 34:1	[M+K]+	0.0004	0.46	
876.4592	876.4576	PS O-42:12	[M+K]+	0.0015	1.71	
*876.4612	876.4576	PS O-42:12	[M+K]+	0.0035	3.99	
876.5361	876.5361	PS 40:5;O	[M+Na]+	0.0001	0.11	PS 18:0;0 22:5;0
876.5361	876.5361	PS 40:5;O	[M+Na]+	0.0001	0.11	PS 18:1;0 22:4;0
876.5361	876.5515	PC 39:5;O	[M+K]+	0.0155	17.68	PC 17:0;0 22:5;0
876.5361	876.5515	PC 39:5;O	[M+K]+	0.0155	17.68	PC 19:1;0 20:4;0
877.4641	877.4628	PI O-36:7	[M+K]+	0.0014	1.60	
*877.5675	877.5718	PA 48:9	[M+Na]+	0.0043	4.90	
878.5519	878.5518	PS 40:4;O	[M+Na]+	0.0001	0.11	PS 18:0;0 22:4;0
878.5519	878.5672	PC 39:4;O	[M+K]+	0.0153	17.42	PC 17:0;0 22:4;0
878.5519	878.5672	PC 39:4;O	[M+K]+	0.0153	17.42	PC 18:1;0 21:3;0
*878.5715	878.5694	PC 44:12	[M+H]+	0.0021	2.39	
879.5836	879.5874	PA 48:8	[M+Na]+	0.0039	4.43	
879.7412	879.7412	TG 52:3	[M+Na]+	0	<0.01	
879.7412	879.7412	TG 52:3	[M+Na]+	0.0000	<0.01	TAG 52:3;0
*880.5687	880.5698	DGCC 43:12	[M+Na]+	0.0011	1.25	
880.5711	880.5698	DGCC 43:12	[M+Na]+	0.0013	1.48	
880.5711	880.5674	PS 40:3;O	[M+Na]+	0.0037	4.20	PS 18:0;0 22:3;0
*880.6060	880.6062	PS 43:5	[M+H]+	0.0002	0.23	
*881.4920	881.4941	PI O-36:5	[M+K]+	0.002	2.27	
881.5131	881.515	PI 36:4	[M+Na]+	0.002	2.27	
881.7569	881.7569	TG 52:2	[M+Na]+	0	<0.01	
881.7569	881.7569	TG 52:2	[M+Na]+	0.0000	<0.01	TAG 52:2;0
882.5647	882.5645	DGTA 43:11	[M+K]+	0.0002	0.23	
*882.5856	882.5854	DGCC 43:11	[M+Na]+	0.0002	0.23	
*882.6217	882.6219	PS 43:4	[M+H]+	0.0001	0.11	
*883.5075	883.5097	PI O-36:4	[M+K]+	0.0022	2.49	
883.5887	883.5847	PG O-46:11	[M+H]+	0.004	4.53	
883.6253	883.627	MGDG 42:5	[M+Na]+	0.0017	1.92	
883.6513	883.6551	PA O-49:6	[M+Na]+	0.0038	4.30	
884.6052	884.6011	DGCC 43:10	[M+Na]+	0.0041	4.63	
884.6052	884.6011	PS 42:4;O	[M+H]+	0.0041	4.63	PS 18:0;0 24:4;0
*885.5255	885.5254	PI O-36:3	[M+K]+	0.0001	0.11	
885.5463	885.5463	PI 36:2	[M+Na]+	0.0001	0.11	
885.6108	885.6134	PA O-48:6	[M+K]+	0.0026	2.94	
887.5620	887.562	PI 36:1	[M+Na]+	0	<0.01	
890.5521	890.5672	PC 40:5;O	[M+K]+	0.0151	16.96	PC 18:0;0 22:5;0
890.5521	890.5672	PC 40:5;O	[M+K]+	0.0151	16.96	PC 18:1;0 22:4;0
890.5521	890.5672	PC 40:5;O	[M+K]+	0.0151	16.96	PC 20:1;0 20:4;0
*894.5854	894.5854	DGCC 44:12	[M+Na]+	0	<0.01	
894.5854	894.5985	PC 40:3;O	[M+K]+	0.0131	14.64	PC 18:0;0 22:3;0
895.5481	895.5484	PG 46:12	[M+H]+	0.0003	0.33	
895.5888	895.5847	PG O-47:12	[M+H]+	0.0041	4.58	
*896.5997	896.6011	DGCC 44:11	[M+Na]+	0.0014	1.56	
*896.6013	896.6011	DGCC 44:11	[M+Na]+	0.0002	0.22	
897.6046	897.6004	PG O-47:11	[M+H]+	0.0042	4.68	
*898.6077	898.6086	PC O-43:7	[M+K]+	0.0009	1.00	
898.6127	898.6167	DGCC 44:10	[M+Na]+	0.004	4.45	
899.5507	899.5644	PI 39:5	[M+H]+	0.0137	15.23	PI 19:1;0 20:4;0
899.5507	899.5280	PI 38:6;O	[M+H]+	0.0227	25.23	PI 18:2;0 20:4;0
899.6150	899.616	PG O-47:10	[M+H]+	0.001	1.11	
901.5273	901.5285	DGDG 30:1	[M+K]+	0.0012	1.33	

901.5273	901.5203	PI 36:2	[M+K]+	0.0070	7.76	PI 16:0;0 20:2;0
901.5273	901.5203	PI 36:2	[M+K]+	0.0070	7.76	PI 18:0;0 18:2;0
901.5273	901.5203	PI 36:2	[M+K]+	0.0070	7.76	PI 18:1;0 18:1;0
902.5332	902.5308	PS 42:6	[M+K]+	0.0024	2.66	
*902.5492	902.546	PC O-44:12	[M+K]+	0.0032	3.55	
902.5689	902.5672	PS O-43:6	[M+K]+	0.0018	1.99	
902.5706	902.5672	PS O-43:6	[M+K]+	0.0035	3.88	
903.5393	903.5383	MGDG 43:10	[M+K]+	0.001	1.11	
903.5416	903.5442	DGDG 30:0	[M+K]+	0.0026	2.88	
903.5561	903.5569	PI 36:1;O	[M+Na]+	0.0008	0.89	PI 18:0;0 18:1;0
903.5561	903.5593	PI 38:4;O	[M+H]+	0.0033	3.65	PI 16:0;0 22:4;0
903.5561	903.5593	PI 38:4;O	[M+H]+	0.0033	3.65	PI 18:0;0 20:4;0
903.5561	903.5593	PI 38:4;O	[M+H]+	0.0033	3.65	PI 18:1;0 20:3;0
*904.5278	904.5253	PC 43:11	[M+K]+	0.0025	2.76	
904.5462	904.5463	PS O-45:11	[M+Na]+	0.0001	0.11	
904.5845	904.5828	PS O-43:5	[M+K]+	0.0017	1.88	
*904.6057	904.6062	PS 45:7	[M+H]+	0.0005	0.55	
905.5560	905.554	MGDG 43:9	[M+K]+	0.0021	2.32	
*906.6219	906.6219	PS 45:6	[M+H]+	0	<0.01	
*907.5287	907.5307	PI 38:5	[M+Na]+	0.002	2.20	
*907.5307	907.5307	PI 38:5	[M+Na]+	0	<0.01	
907.5307	907.5307	PI 38:5	[M+Na]+	0.0000	<0.01	PI 16:0;0 22:5;0
907.5307	907.5307	PI 38:5	[M+Na]+	0.0000	<0.01	PI 18:1;0 20:4;0
907.5307	907.5307	PI 38:5	[M+Na]+	0.0000	<0.01	PI 18:2;0 20:3;0
907.7723	907.7725	TG 54:3	[M+Na]+	0.0002	0.22	
907.7723	907.7725	TG 54:3	[M+Na]+	0.0002	0.22	TAG 54:3;0
*908.5993	908.6011	DGCC 45:12	[M+Na]+	0.0017	1.87	
*908.6012	908.6011	DGCC 45:12	[M+Na]+	0.0001	0.11	
*908.6374	908.6375	PS 45:5	[M+H]+	0.0001	0.11	
*909.5457	909.5463	PI 38:4	[M+Na]+	0.0007	0.77	
909.5667	909.564	PG 47:12	[M+H]+	0.0027	2.97	
909.6045	909.6004	PG O-48:12	[M+H]+	0.0041	4.51	
*910.6164	910.6167	DGCC 45:11	[M+Na]+	0.0003	0.33	
911.5621	911.562	PI 38:3	[M+Na]+	0.0001	0.11	
911.5621	911.5620	PI 38:3	[M+Na]+	0.0001	0.11	PI 18:0;0 20:3;0
911.5621	911.5620	PI 38:3	[M+Na]+	0.0001	0.11	PI 18:1;0 20:2;0
911.5621	911.5644	PI 40:6	[M+H]+	0.0023	2.52	PI 18:1;0 22:5;0
911.5621	911.5644	PI 40:6	[M+H]+	0.0023	2.52	PI 20:2;0 20:4;0
916.5281	916.5253	PC 44:12	[M+K]+	0.0028	3.06	
918.5439	918.541	PC 44:11	[M+K]+	0.0029	3.16	
*919.5476	919.546	PG 46:11	[M+Na]+	0.0016	1.74	
922.6168	922.6167	DGCC 46:12	[M+Na]+	0.0001	0.11	
*923.5244	923.5199	PG 45:10	[M+K]+	0.0045	4.87	
923.6195	923.616	PG O-49:12	[M+H]+	0.0035	3.79	
923.6206	923.616	PG O-49:12	[M+H]+	0.0045	4.87	
923.6847	923.6864	PA O-52:7	[M+Na]+	0.0018	1.95	
*924.6251	924.6243	PC O-45:8	[M+K]+	0.0008	0.87	
*924.6317	924.6324	DGCC 46:11	[M+Na]+	0.0007	0.76	
924.6880	924.6841	PC O-48:10	[M+H]+	0.0039	4.22	
*925.5380	925.5355	PG 45:9	[M+K]+	0.0025	2.70	
925.5380	925.5437	PI 40:7;O	[M+H]+	0.0056	6.05	PI 20:3;0 20:4;0
925.6275	925.6293	PG O-47:8	[M+Na]+	0.0017	1.84	
*925.6352	925.6317	PG O-49:11	[M+H]+	0.0035	3.78	
*927.5545	927.5512	PG 45:8	[M+K]+	0.0033	3.56	
929.5129	929.5151	PIP 35:2	[M+H]+	0.0022	2.37	
929.5129	929.5152	PI 37:3;O	[M+K]+	0.0023	2.47	PI 17:0;0 20:3;0
929.5129	929.5152	PI 37:3;O	[M+K]+	0.0023	2.47	PI 18:0;0 19:3;0
929.5351	929.5516	PI 38:2	[M+K]+	0.0165	17.75	PI 18:0;0 20:2;0
*930.5440	930.541	PC 45:12	[M+K]+	0.003	3.22	
*930.6218	930.6219	PS 47:8	[M+H]+	0	<0.01	
931.5278	931.5307	PIP 35:1	[M+H]+	0.0029	3.11	
*931.5489	931.546	PG 47:12	[M+Na]+	0.003	3.22	
931.5510	931.5906	PI 40:4;O	[M+H]+	0.0396	42.51	PI 18:0;0 22:4;0
931.5510	931.5906	PI 40:4;O	[M+H]+	0.0396	42.51	PI 18:1;0 22:3;0
*932.5591	932.5566	PC 45:11	[M+K]+	0.0025	2.68	
*932.5607	932.5566	PC 45:11	[M+K]+	0.0041	4.40	
*933.5434	933.5406	PG O-47:12	[M+K]+	0.0028	3.00	
*933.5636	933.5616	PG 47:11	[M+Na]+	0.002	2.14	
935.5820	935.5620	PI 40:5	[M+Na]+	0.0200	21.38	PI 18:0;0 22:5;0
935.5820	935.5620	PI 40:5	[M+Na]+	0.0200	21.38	PI 18:1;0 22:4;0
*939.6155	939.611	PG 49:11	[M+H]+	0.0045	4.79	
944.5590	944.5566	PC 46:12	[M+K]+	0.0024	2.54	
944.5613	944.5566	PC 46:12	[M+K]+	0.0047	4.98	
945.5648	945.5616	PG 48:12	[M+Na]+	0.0032	3.38	
945.5888	945.5911	DGDG 33:0	[M+K]+	0.0023	2.43	
945.5921	945.5911	DGDG 33:0	[M+K]+	0.001	1.06	
*946.5760	946.5723	PC 46:11	[M+K]+	0.0037	3.91	
947.6853	947.6852	SQDG 43:1	[M+H]+	0.0001	0.11	
*949.5592	949.5567	PI O-41:6	[M+K]+	0.0025	2.63	
*949.6995	949.7008	SQDG 43:0	[M+H]+	0.0014	1.47	
*949.7014	949.7008	SQDG 43:0	[M+H]+	0.0006	0.63	
950.6478	950.648	DGCC 48:12	[M+Na]+	0.0002	0.21	
951.7165	951.7177	PA O-54:7	[M+Na]+	0.0012	1.26	

952.7192	952.7154	PC O-50:10	[M+H]+	0.0038	3.99	
*953.7248	953.7205	PG 49:4	[M+H]+	0.0043	4.51	
955.5520	955.5672	PI 40:3	[M+K]+	0.0152	15.91	PI 18:0;0 22:3;0
*958.5762	958.5723	PC 47:12	[M+K]+	0.0039	4.07	
*959.5791	959.5773	PG 49:12	[M+Na]+	0.0019	1.98	
*959.5807	959.5773	PG 49:12	[M+Na]+	0.0035	3.65	
960.5852	960.5879	PC 47:11	[M+K]+	0.0027	2.81	
*961.5964	961.5929	PG 49:11	[M+Na]+	0.0035	3.64	
*969.5113	969.5159	SQDG 43:9	[M+K]+	0.0045	4.64	
*971.5443	971.541	PI O-43:9	[M+K]+	0.0033	3.40	
971.6830	971.6828	SQDG 43:0	[M+Na]+	0.0002	0.21	
975.5538	975.5512	PG 49:12	[M+K]+	0.0026	2.67	
*975.5761	975.5723	PI O-43:7	[M+K]+	0.0038	3.90	
*975.6077	975.6086	PG 50:11	[M+Na]+	0.0009	0.92	
977.6175	977.6172	DGDG 37:4	[M+Na]+	0.0003	0.31	
*977.6229	977.6242	PG 50:10	[M+Na]+	0.0013	1.33	
*978.5665	978.5621	PS 48:10	[M+K]+	0.0044	4.50	
*978.6265	978.6219	PS 51:12	[M+H]+	0.0046	4.70	
979.5129	979.5097	PI O-44:12	[M+K]+	0.0032	3.27	
985.6611	985.6657	PA 56:11	[M+Na]+	0.0046	4.67	
986.6038	986.6036	PC 49:12	[M+K]+	0.0003	0.30	
986.6643	986.6611	PS O-49:6	[M+K]+	0.0032	3.24	
*987.6765	987.6813	PA 56:10	[M+Na]+	0.0048	4.86	

Table S2: List of lipid annotations for 5 µm pixel size measurements of flash frozen D9 MGL, considering all lipid-related signals from Table S1, for which the formation of a DHB-adduct was anticipated. m/z-values were selected based on the assumption, that for a given potential DHB-adduct [M + DHB – H2O + X]⁺, the non-derivatized form [M + X]⁺ must also be present in the sample at Δm/z -136.0160.

m/z measured	Annotation	DHB-Adduct	Δppm
751.5149	DG 36:5	[M+DHB-H2O+H]+	0.97
776.4836	LPC O-26:2	[M+DHB-H2O+Na]+	0.16
779.5405	DG 36:2	[M+DHB-H2O+Na]+	4.35
798.4658	LPC O-28:5	[M+DHB-H2O+Na]+	3.32
800.4829	LPC O-28:4	[M+DHB-H2O+Na]+	1.20
802.4991	LPC O-28:3	[M+DHB-H2O+Na]+	0.30
802.5005	LPC O-28:3	[M+DHB-H2O+Na]+	1.65
804.5145	LPC O-28:2	[M+DHB-H2O+Na]+	0.75
805.5178	CE 17:4	[M+DHB-H2O+K]+	1.49
806.4920	LPC 27:1	[M+DHB-H2O+Na]+	3.28
818.4939	LPC 28:2	[M+DHB-H2O+Na]+	0.59
820.4349	LPS 28:2	[M+DHB-H2O+Na]+	3.36
820.4912	LPC O-28:2	[M+DHB-H2O+K]+	3.36
825.5792	CE 18:1	[M+DHB-H2O+K]+	0.29
826.5568	LPC 30:1	[M+DHB-H2O+H]+	3.62
828.5356	LPS O-31:1	[M+DHB-H2O+H]+	4.19
829.4618	LPG O-31:5	[M+DHB-H2O+Na]+	1.15
831.4780	LPG O-31:4	[M+DHB-H2O+Na]+	0.29
833.4936	LPG O-31:3	[M+DHB-H2O+Na]+	0.43
836.5418	LPC 29:0	[M+DHB-H2O+Na]+	0.86
839.5581	MGDG 30:0	[M+DHB-H2O+H]+	9.24
840.5732	LPC 31:1	[M+DHB-H2O+H]+	2.41
841.6066	CE 19:0	[M+DHB-H2O+K]+	5.81
842.5537	LPS O-32:1	[M+DHB-H2O+H]+	0.71
842.5884	LPC 31:0	[M+DHB-H2O+H]+	3.11
847.4187	TG 40:11	[M+DHB-H2O+K]+	0.70
850.5188	LPS O-31:1	[M+DHB-H2O+Na]+	2.38
853.4625	LPG O-33:7	[M+DHB-H2O+Na]+	0.14
854.5528	LPS O-33:2	[M+DHB-H2O+H]+	1.81
854.5891	LPC 32:1	[M+DHB-H2O+H]+	2.09
854.5909	LPC 32:1	[M+DHB-H2O+H]+	0.56
855.4760	LPG O-33:6	[M+DHB-H2O+Na]+	3.20
856.5683	LPS O-33:1	[M+DHB-H2O+H]+	2.08
856.5706	LPS O-33:1	[M+DHB-H2O+H]+	1.11
856.6059	LPC 32:0	[M+DHB-H2O+H]+	0.42
857.4937	LPG O-33:5	[M+DHB-H2O+Na]+	0.28
859.5089	LPG O-33:4	[M+DHB-H2O+Na]+	0.83
859.5108	DG 43:11	[M+DHB-H2O+Na]+	1.52
862.5565	LPC 31:1	[M+DHB-H2O+Na]+	0.55
864.5728	LPC 31:0	[M+DHB-H2O+Na]+	0.27
866.5538	LPS O-34:3	[M+DHB-H2O+H]+	0.55
868.5693	LPS O-34:2	[M+DHB-H2O+H]+	0.68
868.5705	LPS O-34:2	[M+DHB-H2O+H]+	0.96
870.5855	LPS O-34:1	[M+DHB-H2O+H]+	0.14
875.4487	PA 40:11	[M+DHB-H2O+H]+	0.95
875.5051	LPG 33:3	[M+DHB-H2O+Na]+	0.81
876.4612	PS 31:2	[M+DHB-H2O+Na]+	2.97

877.5675	MGDG 33:2	[M+DHB-H2O+H]+	0.40
878.5715	DGTA 33:3	[M+DHB-H2O+Na]+	4.98
880.5687	LPT O-34:3	[M+DHB-H2O+H]+	1.48
880.5711	LPT O-34:3	[M+DHB-H2O+H]+	1.61
880.6060	LPC 34:2	[M+DHB-H2O+H]+	0.27
881.4920	PA 38:5	[M+DHB-H2O+Na]+	2.55
882.5856	LPT O-34:2	[M+DHB-H2O+H]+	0.27
882.6217	LPC 34:1	[M+DHB-H2O+H]+	0.13
883.5075	PA 38:4	[M+DHB-H2O+Na]+	2.68
885.5255	PA 38:3	[M+DHB-H2O+Na]+	0.40
894.5854	PC 34:2	[M+DHB-H2O+H]+	0.13
896.5997	PC 34:1	[M+DHB-H2O+H]+	1.84
896.6013	PC 34:1	[M+DHB-H2O+H]+	0.13
898.6077	DGCC 35:4	[M+DHB-H2O+H]+	4.98
902.5492	LPT O-34:3	[M+DHB-H2O+Na]+	3.39
904.5278	LPS 34:2	[M+DHB-H2O+Na]+	4.16
904.6057	PC O-36:4	[M+DHB-H2O+H]+	0.65
906.6219	PC O-36:3	[M+DHB-H2O+H]+	0.00
907.5287	BMP 34:1	[M+DHB-H2O+Na]+	2.59
907.5307	BMP 34:1	[M+DHB-H2O+Na]+	0.00
908.5993	LPT O-34:0	[M+DHB-H2O+Na]+	0.78
908.6012	PC 35:2	[M+DHB-H2O+H]+	0.13
908.6374	PC O-36:2	[M+DHB-H2O+H]+	0.13
909.5457	BMP 34:0	[M+DHB-H2O+Na]+	0.90
910.6164	PC 35:1	[M+DHB-H2O+H]+	0.52
916.5281	LPT 34:3	[M+DHB-H2O+Na]+	3.84
918.5439	LPT 34:2	[M+DHB-H2O+Na]+	3.58
919.5476	PA O-44:10	[M+DHB-H2O+H]+	1.02
922.6168	PC 36:2	[M+DHB-H2O+H]+	0.00
923.5244	LPI O-31:2	[M+DHB-H2O+Na]+	1.52
923.6847	CE 25:1	[M+DHB-H2O+K]+	5.46
924.6251	DGCC 37:5	[M+DHB-H2O+H]+	7.10
924.6317	PC 36:1	[M+DHB-H2O+H]+	0.89
925.5380	PA O-41:5	[M+DHB-H2O+K]+	3.17
925.6352	DG O-47:7	[M+DHB-H2O+K]+	4.31
927.5545	DG O-48:13	[M+DHB-H2O+K]+	1.14
930.5440	PS O-36:3	[M+DHB-H2O+Na]+	3.40
930.6218	PC O-38:5	[M+DHB-H2O+H]+	0.00
931.5489	DG 47:11	[M+DHB-H2O+K]+	0.63
932.5591	PS O-36:2	[M+DHB-H2O+Na]+	4.02
932.5607	PS O-36:2	[M+DHB-H2O+Na]+	2.01
933.5434	PG 36:2	[M+DHB-H2O+Na]+	3.64
933.5636	PA O-45:10	[M+DHB-H2O+H]+	0.50
939.6155	DG 47:7	[M+DHB-H2O+K]+	5.48
946.5760	PS O-37:2	[M+DHB-H2O+Na]+	2.47
949.5592	TG 47:9	[M+DHB-H2O+K]+	0.25
949.6995	CE 27:2	[M+DHB-H2O+K]+	6.27
949.7014	CE 27:2	[M+DHB-H2O+K]+	3.93
950.6478	PC 38:2	[M+DHB-H2O+H]+	0.25
951.7165	CE 27:1	[M+DHB-H2O+K]+	4.66
953.7248	DG O-52:9	[M+DHB-H2O+H]+	2.45
958.5762	PS O-38:3	[M+DHB-H2O+Na]+	2.19
959.5791	PA O-47:11	[M+DHB-H2O+H]+	0.61
959.5807	DG 49:11	[M+DHB-H2O+K]+	1.21
961.5964	DG 49:10	[M+DHB-H2O+K]+	1.21
969.5113	LPI 32:1	[M+DHB-H2O+K]+	1.44
971.5443	TG 49:12	[M+DHB-H2O+K]+	1.08
975.5761	TG 49:10	[M+DHB-H2O+K]+	1.67
975.6077	PA O-46:7	[M+DHB-H2O+Na]+	1.07
977.6229	PA O-46:6	[M+DHB-H2O+Na]+	1.54
978.5665	DGCC 40:10	[M+DHB-H2O+Na]+	4.39
978.6265	PC O-42:9	[M+DHB-H2O+H]+	5.46
987.6765	MGDG 41:3	[M+DHB-H2O+H]+	0.23

Data availability

All AP-SMALDI MSI data presented in this study are publicly available at https://metaspace2020.eu/api_auth/review?prj=5b1c7f90-9a9c-11ea-b3af-a7c719c5959c&token=yZpGwB_VOU5Z

References

(1) Palmer, A.; Phapale, P.; Chernyavsky, I.; Lavigne, R.; Fay, D.; Tarasov, A.; Kovalev, V.; Fuchser, J.; Nikolenko, S.; Pineau, C.; Becker, M.; Alexandrov, T. FDR-controlled metabolite annotation for high-resolution imaging mass spectrometry. *Nat. Methods* **2017**, *14*, 57–60.
(2) Aimo, L.; Liechti, R.; Hyka-Nouspikel, N.; Niknejad, A.; Gleizes, A.; Götz, L.; Kuznetsov, D.; David, F. P. A.; van der Goot, F. Gisou; Riezman, H.; Bougueleret, L.; Xenarios, I.; Bridge, A. The SwissLipids knowledgebase for lipid biology. *Bioinformatics* **2015**, *31*, 2860–2866.
(3) Bien, T.; Bessler, S.; Dreisewerd, K.; Soltwisch, J. Transmission-Mode MALDI Mass Spectrometry Imaging of Single Cells: Optimizing Sample Preparation Protocols. *Anal. Chem.* **2021**, *93*, 4513–4520.
(4) Tsai, Y.-H.; Bhandari, D. R.; Garrett, T. J.; Carter, C. S.; Spengler, B.; Yost, R. A. Skeletal muscle fiber analysis by atmospheric pressure scanning microprobe matrix-assisted laser desorption/ionization mass spectrometric imaging at high mass and high spatial resolution. *Proteomics* **2016**, *16*, 1822–1824.
(5) Yang, T.; Gao, D.; Jin, F.; Jiang, Y.; Liu, H. Surface-printed microdot array chips coupled with matrix-assisted laser desorption/ionization mass spectrometry for high-throughput single-cell patterning and phospholipid analysis. *Rapid Commun. Mass Spectrom.* **2016**, *30 Suppl 1*, 73–79.
(6) Goodwin, R. J. A. Sample preparation for mass spectrometry imaging: small mistakes can lead to big consequences. *J. Proteomics* **2012**, *75*, 4893–4911.
(7) Haenseler, W.; Sansom, S. N.; Buchrieser, J.; Newey, S. E.; Moore, C. S.; Nicholls, F. J.; Chintawar, S.; Schnell, C.; Antel, J. P.; Allen, N. D.; Cader, M. Z.; Wade-Martins, R.; James, W. S.; Cowley, S. A. A Highly Efficient Human Pluripotent Stem Cell Microglia Model Displays a Neuronal-Co-culture-Specific Expression Profile and Inflammatory Response. *Stem Cell Rep.* **2017**, *8*, 1727–1742.
(8) Vaughan-Jackson, A.; Stodolak, S.; Ebrahimi, K. H.; Browne, C.; Reardon, P. K.; Pires, E.; Gilbert-Jaramillo, J.; Cowley, S. A.; James, W. S. Differentiation of human induced pluripotent stem cells to authentic macrophages using a defined, serum-free, open-source medium. *Stem Cell Rep.* **2021**, *16*, 1735–1748.
(9) Lund, S.; Christensen, K. V.; Hedtjärn, M.; Mortensen, A. L.; Hagberg, H.; Falsig, J.; Hasseldam, H.; Schrattenholz, A.; Pörzgen, P.; Leist, M. The dynamics of the LPS triggered inflammatory response of murine microglia under different culture and in vivo conditions. *J. Neuroimmunol.* **2006**, *180*, 71–87.

Acknowledgements

I would like to thank Prof. Dr. Bernhard Spengler for the possibility to prepare this doctoral thesis in his research group at the Justus Liebig University in Giessen. Thank you for providing high-level support, instrumentation and surroundings to enable this research and for all the opportunities I had to improve my skills.

Also, I would like to thank Prof. Dr. Sven Heiles for volunteering as a second referee for this thesis and for the continuous support during my research. Thank you for your advice and for sharing your knowledge and experience with me.

I want to thank all colleagues and alumni I worked with in the research group of Prof. Spengler for the pleasant working atmosphere in the institute and for delightful time during conferences or social activities. In particular, I want to thank Dr. Karl-Christian Schäfer, Dr. Stefanie Gerbig and Dr. Dhaka Ram Bhandari for their guidance, their support and their always open ear in my research projects.

I thankfully want to acknowledge the “Fonds der Chemischen Industrie” for granting me the Kekulé fellowship for the research that culminated in this doctoral thesis.

To my family, I want to express my greatest gratitude for making this possible in the first place. Thank you Laura, my beloved wife, for always believing in me and encouraging me to achieve the best I can every day. This would not have been possible without you and your never-ending love and support. Thank you Beate and Carsten, my parents, for providing me the best conditions possible and promoting me to achieve my dreams. All this would not have been possible without your continuous backup and guidance.

Declaration

I declare that I have completed this dissertation single-handedly without the unauthorized help of a second party and only with the assistance acknowledged therein. I have appropriately acknowledged and cited all text passages that are derived verbatim from or are based on the content of published work of others, and all information relating to verbal communications. I consent to the use of an anti-plagiarism software to check my thesis. I have abided by the principles of good scientific conduct laid down in the charter of the Justus Liebig University Giessen "Satzung der Justus-Liebig-Universität Gießen zur Sicherung guter wissenschaftlicher Praxis" in carrying out the investigations described in the dissertation.

_____

Place, date and signature

Curriculum Vitae

The curriculum vitae was removed from the electronic version of this thesis.

Curriculum Vitae

The curriculum vitae was removed from the electronic version of this thesis.

Curriculum Vitae

The curriculum vitae was removed from the electronic version of this thesis.